The Application of Electronic Portal Imaging Devices to Radiotherapy Quality Assurance

Guilin Liu, M.Sc.

ADELAIDE
UNIVERSITY
AUSTRALIA

Thesis submitted for the degree of
Doctor of Philosophy
in the University of Adelaide
Department of Physics and Mathematical Physics

Supervisors:

A/Prof. Tim van Doorn
Dr. Eva Bezak
A/Prof. John R. Patterson

May 2002

Abstract

Routine quality assurance (QA) of a linear accelerator is critical to the effectiveness of radiation treatment for cancer. The studies reported in this thesis demonstrate the potential for using Electronic Portal Imaging Devices (EPIDs) for quality assurance tests with the aim of improving the accuracy and efficiency of radiotherapy QA.

Prior to its application in quality assurance, the characteristics of an EPID need to be investigated. This involves measurements of the amount of build-up material needed for different energies, sensitivity across the major axes of the detector, pixel size and spatial linearity and output characteristic curves with different input doses, dose rates, field sizes, and energies. It has been found that the output pixel values are a linear function of the incident beam monitor units. The field size effects on the EPID are similar to ion chamber measurements at smaller field sizes. However, the pixel values increase more rapidly than ion chamber measurements at larger field sizes due to side scatter from the EPID housing. The imaging system is insensitive to dose rate, but is energy dependent.

The developed QA techniques with EPIDs include mechanical alignment assessment, flatness and symmetry assessment, light and radiation isocentre assessment, photon beam energy constancy check, and light/radiation field coincidence tests. For mechanical alignment assessment, an EPID (BEAMVIEW^{PLUS}) mounted onto a gantry was used to detect and distinguish the possible causes of mechanical misalignments, e.g. source position displacement relative to the collimator rotational axis, collimator jaw asymmetry, and when the rotational axes of the gantry and the collimator did not intersect. As EPIDs have the ability to provide two dimensional dose distribution information, it is possible to investigate the flatness and symmetry within a defined area. A stand-alone EPID, i.e. an Beam Imaging System (BIS710), was used to investigate the flatness and symmetry of the x-ray beams. As it is essential to check the isocentre of the linac for patient set up, mechanical and radiation isocentre were also assessed using the BIS710.

It is concluded that EPIDs can be used for quality assurance after careful measurement of their inherent physical parameters. The study has demonstrated the feasibility of using the EPID to assess mechanical alignment, mechanical and radiation isocentres of a linear accelerator in a quick and efficient way with a higher degree of accuracy achieved as compared to more conventional methods. Instead of determining the flatness and symmetry from major axes only, the EPID allows the beam flatness and symmetry to be assessed within two-dimensional area. The efficiency of using EPIDs to check the energy constancy and light/radiation field coincidence has also been demonstrated. The device can also be used to provide quick dosimetric checks provided that it is calibrated.

DECLARATION

This work contains no material which has been accepted for the award of any other degree or diploma in any university or other tertiary institution an, to the best of my knowledge and belief, contains no material previously published or written by another person, except where due reference has been made in the text.

I give consent to this copy of my thesis, when deposited in the University Library, being available for loan and photocopying.

DATE: 28/05/2002

ACKNOWLEDGMENTS

Firstly, I wish to warmly thank my primary supervisor, Associate Professor Tim van Doorn for his encouragement all the way. Tim's enthusiasm, ideas and solutions to my many problems have been invaluable throughout this project. His knowledge of the radiation physics and experience with students have enabled me to complete this degree, attend conferences and enjoy the research in medical physics.

I am grateful for the supervision and guidance of Dr Eva Bezak. From her joining this department, Eva was helpful and supportive in many ways: reading my thesis and helping me to carry out experiments.

Thanks also to Dr John Patterson for organisational and financial support to help me to attend conferences, provide the software package, and proof reading this thesis.

Peter Greer has been an inspiration and motivation for me during this research. His ability to learn, his incredible work output and experience gave me impetus whenever I needed it. Also thanks go to Jeremy Booth, for his enthusiasm and willingness to share his knowledge and friendship. The other staff of the Medical Physics Department at the Royal Adelaide Hospital have all been very helpful, particularly Dr Sergei Zavgorodni who provided invaluable discussion and help me to finish some of the experiments, Dr Mostafa Heydarian (now at Princess Margaret Hospital, Toronto), who provided invaluable help during my first year of research. As well as the medical physics staff I would like to thank Dr Michael Penniment and Dr Eric Yeoh from the Department of Radiation Oncology, who helped me to receive the travel assistance for attending the international conference on EPIDs and IMRT.

I am unable to fully express my gratitude to my wife Lin for her support and unconditional love during the years of preparing this thesis.

Symbols and Abbreviations

Symbols

D	Absorbed dose
d_{max}	Depth maximum dose build-up
E	Electron or photon energy
E_{en}	Amount of kinetic energy absorbed in the medium
E_{tr}	Amount of kinetic energy transferred to electrons of the medium from a photon interaction
K	Kerma
K_{c}	Collision kerma
R_{50}	Depth of 50% electron isodose distribution
R_{p}	Electron beam practical range
S/ρ	Mass stopping power
μ	Linear attenuation coefficient
μ/ρ	Total mass attenuation coefficient
ϕ	Particle fluence
Ψ	Energy fluence
ρ	Mass density

Abbreviations

AAPM	American Associate of Physicists in Medicine
ACPSEM	Australian College of Physical Sciences & Engineers in Medicine
BIS	A Wellhofer Beam Imaging System
CCD	Charge Coupled Device
EGS4	Electron and Gamma Shower version 4 Monte Carlo simulation code
EPID	Electron Portal Imaging Device

FWHM	Full-width at half maximum
ICRU	International Commission on Radiation Units and Measurements
Linac	Liner accelerator
MeV	Mega-electron Volts
MTF	Modulation Transfer Function
MV	Megavolts
LSF	Line Spread Function
QA	Quality Assurance
TAR	Tissue Air Ratio
TMR	Tissue Maximum Ratio
TPR	Tissue Phantom Ratio
SSD	Source to Surface Distance
VEPID	Video-based Electronic Portal Imaging Device

Preface

The publications and presentations with which the author has been involved with during the course of this research are:

Publications

Liu G, van Doorn T and Bezak E (2000) *Evaluation of the mechanical alignment of a linear accelerator with an electronic portal imaging device (EPID)*, **Australasian Physical & Engineering Sciences in Medicine, 23 (3),** 74-80

Conference Presentations

- Liu G, van Doorn T and Bezak E (2000) *Linear accelerator mechanical and radiation isocentre assessment with an EPID*, **14th National Congress of the Australian Institute of Physics, AIP, Adelaide**

- Liu G, van Doorn T and Bezak E (2000) *Linear accelerator mechanical and radiation isocentre assessment with an EPID*, **Australasian Physical & Engineering Sciences in Medicine, 23 (4),** 170 **(abstract), APESM, Newcastle**

- Liu G, van Doorn T and Bezak E (2000) *Assessment of Flatness and Symmetry with an EPID*, **Proc. of EPI2K, Brussels**

- Liu G, van Doorn T and Bezak E (2000) *The Linear Accelerator Mechanical and Radiation Isocentre Assessment with an Electronic Portal Imaging Device (EPID)*, **Proc. of EPI2K, Brussels**

- Liu G, van Doorn T and Bezak E (2000) *Assessment of Flatness and Symmetry with an EPID*, **Proc. of 2th Beijing Congress in Radiation Physics, Beijing**

- Liu G, van Doorn T and Bezak E (2000) *The Linear Accelerator Mechanical and Radiation Isocentre Assessment with an Electronic Portal Imaging Device (EPID)*, **Proc. of 2th Beijing Congress in Radiation Physics, Beijing**

- van Doorn T, Greer P, Liu G and Schirmer M (1998) *A comparative study of the imaging characteristics of five portal image receptors*, **Radiotherapy and Oncology, 48, (Suppl. 1)**, s110, **17th Annual ESTRO Meeting, Edinburgh**

Papers in preparation

Liu G, van Doorn T and Bezak E, *Assessment of Flatness and Symmetry with an EPID*

Chapter 1

Introduction

1.1. Introduction

The goal of radiotherapy is to cure, or improve the quality of life of, a cancer patient through the accurate delivery of a radiation dose to a presecibed target volume. However, there will always be some uncertainty in the dose delivered. This uncertainty in dose is due to errors and physical limitations that may occur at different steps in the radiotherapy treatment process, as follows:

(a) the determination of patient anatomy; (errors in obtaining patient outlines, patient positioning, defining organs at risk, estimating tissue inhomogeneities, etc);

(b) the definition of the target volume(s) (shapes and location, failure to take into account movements of organs or tissue due to gastric movement and respiration and/or movement of the whole patient etc);

(c) the treatment planning (errors in beam data, beam models, computer software and hardware, etc);

(d) the treatment delivery (errors in machine calibration, patient set-up, improper machine settings, etc);

(e) patient data (identification, diagnosis, treatment prescription, records of previous treatment given, portals of entry, etc) ;

Inaccurate delivery of the radiation can result in either a recurrence of the disease due to an underdose, or serious clinical complications due to overdose. To avoid this, a system of frequent monitoring, known as quality assurance, in radiation delivery has been developed. Quality assurance (QA) in radiotherapy includes all procedures that provide for consistency of the medical prescription and safe fulfillment of that prescription as regards dose to target volume, together with minimal dose to normal tissue, minimal exposure of personnel, and adequate patient monitoring. Quality assurance procedures in radiotherapy have long been in place. The importance of such quality assurance in radiotherapy has been stressed by the World Health Organization (WHO, 1988), American Association of Physicists in Medicine (AAPM, 1995), Australiasian Physical and Engineering Sciences in Medicine (APESM, 1997) and many others. A detailed review of current conventional quality assurance procedures will be presented in the next chapter.

At present, most radiation departments use water tank, “solid water” phantoms and film techniques for QA measurements. The set-up of a water tank is a time consuming procedure, which is not practical for frequent use for a department with a heavy workload. Furthermore, a conventional routine quality assurance program using ion chambers typically just monitors discrete points.

For monitoring of geometrical errors, portal films are used. However, portal oncology films have limitations and are expensive. The limited dynamic range along with the fixed and low contrast of film makes it less than optimal for portal imaging. Also in part, the characteristics of the film and the delays caused by film development make it impractical for setup evaluation during the treatments.

In contrast, electronic portal imaging devices (EPIDs) can acquire images with a few cGy of beam dose during the course of treatment and can display it in almost real time. EPIDs have the potential to monitor patient geometry and movement continuously, so inaccuracies in dose delivery due to geometrical set-up errors can be reduced. They also have the major advantages of providing high display contrast and two-dimensional information.

1.2. Aims of the current research

Even though EPIDs have originally been developed to provide online monitoring of patient positions, efforts have been made in the last decade to implement EPIDs more universally in radiotherapy. The previous studies have concentrated mostly on geometrical verifications such as radiation beam size, shape, and location relative to anatomical structures (van Herk *et al* 1988, Bijhold *et al* 1991, Bel *et al* 1996, Meertens *et al* 1990 and Michalski *et al* 1993). The research presented in this thesis, however, is more concerned with the application of EPIDs to radiotherapy QA techniques namely: mechanical alignment assessment, mechanical and radiation isocentre checks, flatness and symmetry checks and others. This is achieved through a thorough investigation of the characteristics of the EPIDs and through the development of procedures aimed at examination of linac properties and their implementation to routine QA. Computer programs have also been developed to enable an automatic analysis of EPID measurements in QA applications.

The electronic portal imaging devices used for this research thesis are the video-based EPIDs namely, the BEAMVIEW$^{\mathrm{PLUS}}$ (Siemens Medical Systems Inc., Concord, CA) and the BIS 710 (Wellhofer Dosimetrie, Schwarzenbruk, Germany). The research covered by this thesis is described in detail in the next section.

1.3. Thesis outline

The major experimental investigations presented in this thesis are elaborated in Chapters 4, 5, 6 and 7. Chapters 1, 2 and 3 are intended to provide recent literature sources and general background information for the external beam radiotherapy and megavoltage imaging physics.

Chapter 2 introduces the major components of medical linear accelerators used in radiotherapy and provides a review of the current quality assurance procedures which are adopted by a majority of radiotherapy centres. The x-ray and electron beam characteristics of a medical linear accelerator are also described.

Chapter 3 discusses the general aspects of megavoltage imaging and currently available electronic portal imaging techniques, followed by an outline of clinical applications of EPIDs. The basic characteristics of commercially available EPIDs will be compared.

Clinical studies of the comparison of portal film and EPIDs will be discussed and recommended EPID QA procedures will be introduced. It will also be shown how the use of EPID imaging processing can result in improved clinical benefits. In their clinical application, geometrical verification and setup error correction strategies will be introduced. The chapter will conclude with a brief discussion of possible dosimetric applications of EPID, e.g., measurements of transmitted dose and compensator design.

Chapter 4 deals with a detailed study of the characteristics of a stand-alone EPID. To thoroughly understand the EPID, the effect of the parameters such as beam field size, dose rate, photon energy, and CCD sampling time on the detector response will be investigated through computer analysis of the recorded EPID image. The reproducibility, stability, sensitivity measurements and response to scattered radiation will also be examined.

Chapter 5 investigates the efficacy of using an EPID to monitor the flatness and symmetry of a linac x-ray beam, the light and radiation field coincidence, the wedge dose distributions and photon energy constancy. EPIDs have the ability to provide two dimensional relative dose distribution information making it possible to investigate these tasks more efficiently, thereby benefiting QA procedures.

Chapter 6 presents an innovative technique for detection of the mechanical misalignment of a medical linear accelerator using an EPID. The technique is simultaneously sensitive to the three general causes of mechanical misalignment (gantry rotation axis problem, jaw asymmetry problem, source displacement) with almost real-time analysis.

Chapter 7 discusses the implementation of an EPID to the assessment of the medical linear accelerator's mechanical and radiation isocentre with high accuracy and efficiency. With the light/radiation scintillation detector screen of an EPID, the mechanical isocentre can be determined through the linear accelerator’s optical system. The radiation isocentre can be assessed using the radiation detector of the EPID. When compared with conventional methods, the assessment of the position of the mechanical isocentre and radiation isocentre using an EPID can be more accurate, quantitative, simple and fast.

Chapter 8 highlights and summarises the main findings of the work presented in this thesis and possible future research in the field.

Chapter 2

Quality Assurance of Medical Linear Accelerators

2.1. Introduction

An accelerator is a machine used to produce high-energy beams of charged particles for research, medical therapies, and some industrial applications. In a linear accelerator charged particles are accelerated in a straight line, either by means of a steady electrical field or by radiofrequency electric fields. In the latter, the passage of the particle is synchronized with the phase of the accelerating field. For electrons, the linear accelerator has an advantage as it overcomes large energy losses due to synchrotron radiation in ring accelerators such as the betatron. In this thesis, the term 'medical linear accelerator' or 'linac' is used to describe the whole system used to deliver radiation for electron or photon therapy beams. In brief, it consists of a gantry which supports a linear accelerator waveguide and beam defining system along with the patient support system and associated RF and AC power supply and control systems.

Since patient care is always the first priority for radiation therapy, corresponding quality assurance has been introduced and has long been in place. The "quality" of a radiation oncology service can be defined as "the totality of features or characteristics of the radiation oncology service that bear on its ability to satisfy the stated or implied goal of effective patient care" (ISO, 1986). Quality Assurance (QA) of radiation therapy equipment is primarily an ongoing evaluation of functional performance characteristics. There are two essential requirements, (a) it should be performed periodically on all therapy equipment, including the dosimetry and other QA measurement devices; and (b) there should be scheduled regular preventive maintenance monitoring and adjustment of the performance of therapy machines and measurement equipment. The goal of these procedures is to ensure that the performance characteristics (the baseline standard), defined by the physical parameters established during commissioning of the equipment, demonstrate no serious deviations from established standards.

A Quality Assurance program should provide the organisational structure, responsibilities, procedures and resources for assuring the quality of patient management (AAPM, 1994). The reasons for the need of quality assurance in radiotherapy (WHO, 1988) are:

(1) quality assurance minimizes errors in treatment planning and dose delivery and thereby improves the results of therapy by increasing remission rates and decreasing complication and recurrence rates;

(2) quality assurance permits the meaningful inter comparison of results both among radiotherapy centres within a country and internationally by ensuring more uniform and accurate dosimetry and treatment delivery;

(3) the superior performance of modern radiotherapy equipment cannot be fully exploited unless a high degree of accuracy and consistency is reached, that is only possible through quality assurance;

(4) In the developing world, the application of radiotherapy will increase greatly in the near future and quality assurance programs will be necessary to ensure that treatment is of acceptable quality.

To better understand the linac beam properties, this chapter begins with a brief description of the major components of the linear accelerator, followed by a brief introduction to the linac's use for radiation therapy, and a review of current conventional quality assurance procedures.

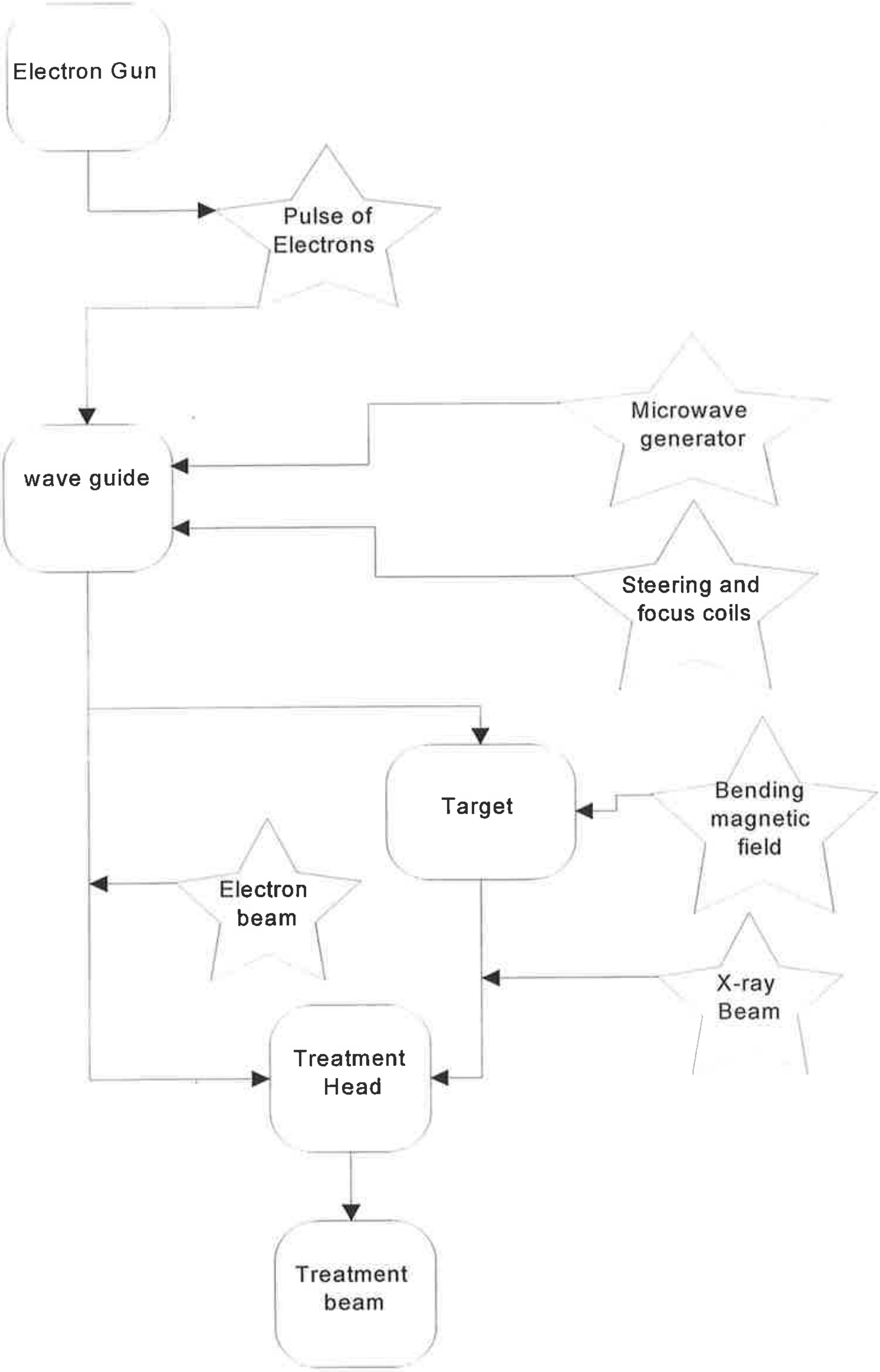

Figure 2.1. A flow chart illustrating the major parts of the accelerator needed for the generation of the radiation beam.

2.2. Major components of the linear accelerator

The major components needed for the generation of radiation beams are identified in the flow chart of Figure 2.1. Further details can be found in Greene and Williams (1997), Metcalfe *et al.* (1997), and Karzmark and Morton (1981).

2.2.1. The microwave generator and waveguide

Microwave generators are used to provide microwave power to accelerate the pulse of electrons from the electron gun. There are two types of microwave generator tubes commonly used in the medical linear accelerators, i.e. the klystron and magnetron.

The frequency of the microwaves produced by the klystron is about 3 GHz, and the corresponding wavelength is about 10 cm. Figure 2.2 shows the number of electrons in a typical pulse sequence (Krieger *et al.* 1989).

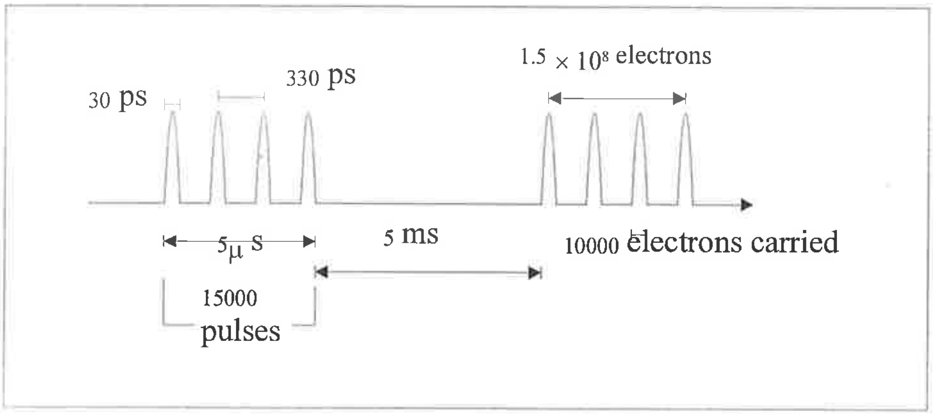

Figure 2.2. Typical microwave pulse sequence showing the approximate number of electrons involved in linac operation (from Krieger and Petzold, 1989).

The accelerating waveguide is used to accelerate electrons to nominal energies. The waveguide is a device which carries electromagnetic waves from one place to another without significant loss in intensity. The length of the waveguide must be a multiple of the wavelength, so waveguides are only practical for electromagnetic waves in the microwave range, with wavelengths, λ, on the scale of a few centimetres. If a microwave oscillation is set up at one end of a waveguide, its electric field causes electric currents to flow in the copper walls. These currents in turn induce new electric and magnetic fields in the waveguide, oscillating with the same frequency as the original microwave. The net effect is that the microwave travels along the copper pipe of radius, a, in the transverse magnetic field with the phase velocity, v_p, (Greene and Williams, 1997):

$$v_p = \frac{c}{\sqrt{1-(\lambda/2.61a)^2}}. \tag{2.1}$$

This velocity represents the movement of the electric field pattern along the guide. This velocity must be known and controlled in order to keep electrons in the accelerating part of the wave.

There are two types of waveguide applied in the medical linear accelerators as accelerator structures, i.e. a travelling waveguide and a standing waveguide. The standing wave system accelerates electrons in a field of constant amplitude while the E field in travelling waveguide system is attenuated as it moves along the guide. The standing waveguide is more efficient for accelerating electrons for the same length of the guide for a given microwave power level (i.e. for a given energy gain and same magnetron power, standing waveguides are shorter in length compared to travelling ones).

2.2.2. Bending magnet

The electron beam has to be actively steered through the accelerator system by the use of two orthogonal dipoles formed by pairs of beam steering coils. Moreover, as the electrons are accelerated through the guide they are subject to forces that will tend to make the beam diverge. Focusing fields required are provided by an additional series of solenoids, known as focusing foils. The electron beam leaving the accelerating structure continues through an evacuated bending magnet system. It is deflected magnetically either so as to strike a target for x-ray therapy or to exit through the treatment head for electron therapy. There are two configurations generally used in medical linear accelerators, i.e. 90° and 270° bending. The radius of curvature of the electron beam is dependent on the electron energy and therefore the 90° bending system acts as an energy spectrometer.

The purpose of the 270° angle bending system is to accomplish achromatic bending so that the electrons will strike the x-ray target or pass through the exit widow at the same point and in the same direction independently of their energy (figure 2.3). When the angular and energy distributions are considered, the low energy component is deflected through a loop of smaller radius and the high energy component is deflected through a loop of larger radius. This ensures that all the electrons with slight difference in energy are focused to one small spot when striking the target, producing thus the x-ray treatment fields with sharper defined edges (Greene and Williams, 1997).

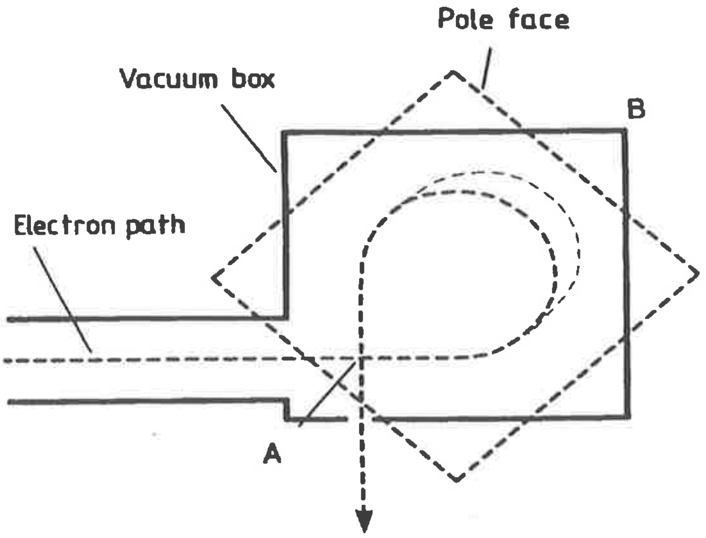

Figure 2.3. A simplified achromatic 270° beam-bending magnet with focusing properties (from Greene and Williams, 1997).

2.2.3. The treatment head

The treatment head is the part of the machine which receives the accelerated electron beam from the waveguide and uses it to generate either an x-ray or an electron beam for treating cancer patients. It contains a number of beam shaping, localising, and monitoring devices. In general it consists of the following (see Figure 2.4):

(1) X-ray target (if x-ray beam is going to be produced)
(2) Primary and secondary collimators plus other field defining systems, such as multileaf collimator
(3) Flattening filter and scatter foils for electron beam
(4) Beam monitor
(5) Wedge filter
(6) Mirror
(7) Accessory ring

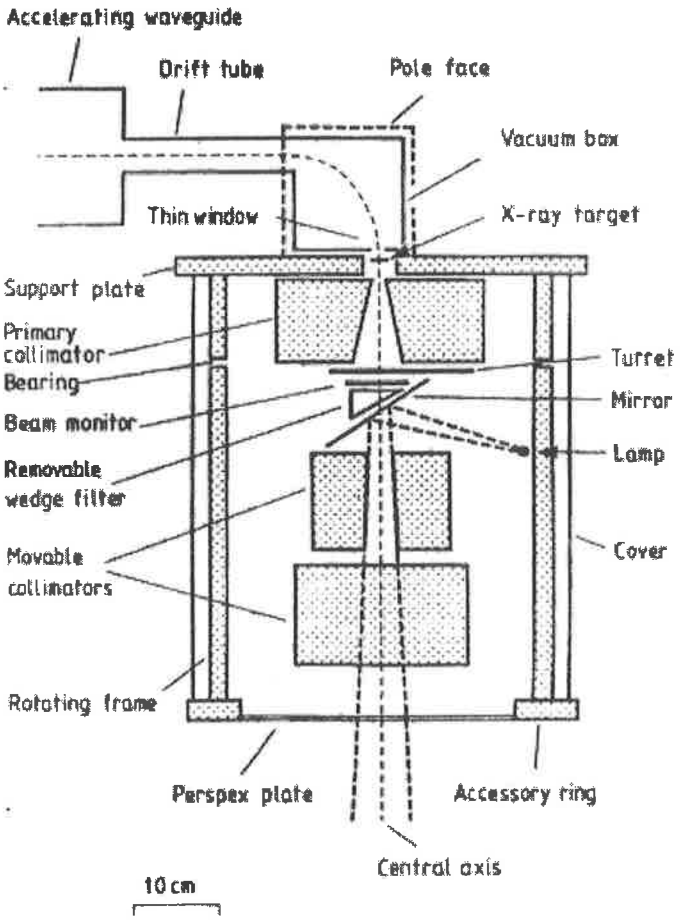

Figure 2.4. The major components of treatment head for the x-ray beam system (from Greene and Williams, 1997).

To produce x-ray beams, accelerated electrons strike a metal target. Transmission targets are employed in medical linear accelerators because in the megavoltage energy range, the photons produced are directed mainly in the same direction as the incoming electrons. The photon spectrum generated depends on the atomic number and the thickness of the target for a given electron energy. Podogorsak *et al* (1975) investigated experimentally the radiation quality and output produced by different targets and concluded that for electron energies up to 10 MeV a thick tungsten target gave the best compromise between good x-ray output and beam penetration, while for higher energies a thick aluminium target should be used.

The primary collimator, usually a lead-tungsten alloy, provides shielding and beam definition. It limits the maximum field size for x-ray therapy. The thicknesses of primary collimator required do not vary greatly over the radiotherapy energy range, in which the mean photon energy is about 1.5-10 MeV. This follows from the slow variation of the attenuation coefficient as a function of photon energy. The actual thicknesses have to be determined empirically to give < 1% transmission and this will not be discussed here. The secondary collimator defines the treatment field size and is designed to move in an arc focused on the target. In order to give a precise measure of field sizes, the amount of backlash that can be tolerated in the collimator movement is very small. In older models, the secondary collimators were designed to move in pairs symmetrically about the axis of the rotation of the beam. For more flexible control, independent collimators which control the four blocks independently were introduced. More recently, multileaf collimators (MLC) were introduced to produce desirable irregular radiation beam shapes. The design and performance of MLCs have been described by many authors (Galvin et al. 1992, Galvin et al. 1993a, 1993b, Brahme, 1993, Das et al. 1998, Galvin 1999).

The unfiltered x-ray beam from a megavoltage generator produces a sharply peaked dose distribution along the central axis of the beam. The dose distribution becomes even more forward peaked for higher energy beams requiring the use of a flattening filter. The filtered beam will produce a relatively flat dose distribution at a certain depth (usually defined at 10 cm water depth). The beam flattening filter also acts as a radiation filter in the traditional sense by changing the radiation spectrum due to differential photon absorption. This is particularly important for heavy elements like lead, for which both soft and high energy x-rays are filtered out. To avoid significant beam softening, a medium-atomic-number material, such as aluminium, is selected for flattening filter production. For these materials, however, some beam hardening effect at the central part of the beam will be introduced. When dosimetry measurements are performed, energy-independent dosimetry detectors such as the ion chamber are not affected by the beam hardening, but energy dependent detectors, such as films, EPIDs etc need to be take beam hardening into account. This will be further discussed in a later chapter.

The beam monitor consists of two transmission ionization chambers which monitor the whole cross sectional area of the radiation beam after it has passed through the flattening filter or scattering foil (described in **Sec. 2.2.5**).

A mirror and a lamp are used to produce a light field which illuminates the field defined by the collimators. The light field simulates the x-ray field and facilitates positioning of patients for treatment. Therefore the light field must coincide with the radiation field in order to deliver the treatment to the intended area. The accessory ring provides a rigid mounting for any necessary mechanical or optical beam direction devices.

Wedge filters are designed to produce a gradient of dose distribution across the treatment field. The wedge angle, while not a full description of the overall effect of the wedge on the dose distribution, is used to quantify the effect of each wedge filter. The wedge angle is defined in IEC report 976 (1989) as the angle through which an isodose curve is tilted at the central axis of the beam at a specified depth and field size. The reference depth, however, is not generally agreed upon and a 10 centimetre depth was recommended (Khan, 1992). The wedge angle definition is illustrated in figure 2.5. It measures how much the isodose curves have been tilted by the wedge filter.

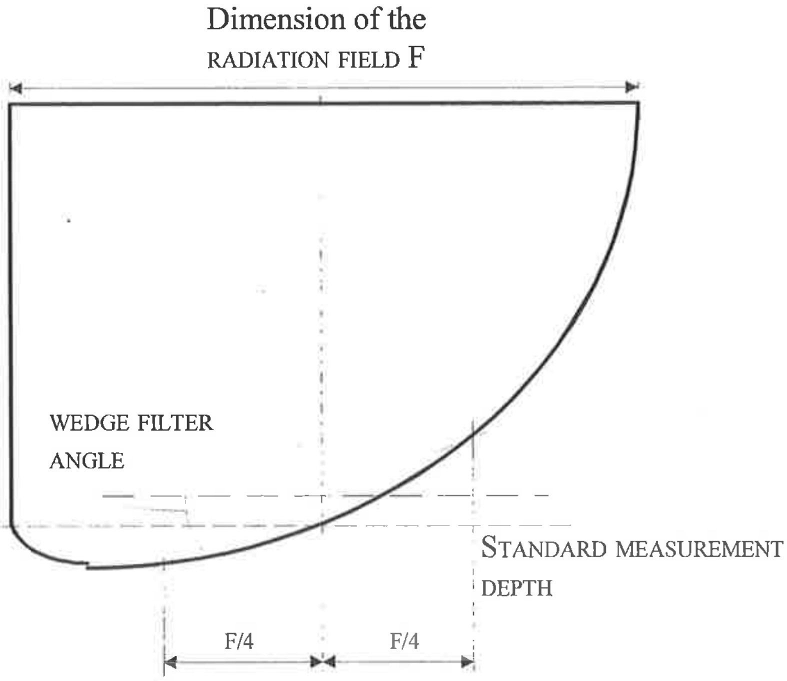

Figure 2.5. Wedge filter definition (IEC 976). The wedge angle is calculated from the beam central axis and the line connecting two points, F/4 distance away from the centre. F is the radiation field size.

In general, there are three types of wedges:

(1) Physical (removable) wedges, which are individually designed to produce a particular required dose distribution at a specified depth in a phantom. The introduction of a wedge produces a reduction in beam transmission. This is accounted for by using wedge transmission factors to correct the dose delivered. Because the physical wedges harden the beam, the depth dose curves for wedged fields are slightly shallower at depth than open field. However, this effect tends to be very small. e.g., less than 2% difference for 6 MV at 30 cm depth (Metcafe *et. al.* 1997).

(2) Universal (motorized) wedges are designed to produce a steeper distribution of dose if needed, and are placed in the beam for a certain portion of the exposure. The final dose distribution is the appropriately weighted average of that obtained with the wedge and the open beam. The wedge angle resulting from the weighted beam is given by:

$$\tan\theta' = \left(\frac{w_2}{w_1 + w_2}\right)\tan\theta, \tag{2.2}$$

where w_1 and w_2 are the beam weights for the unwedged fraction and the wedged fraction, respectively.

(3) Dynamic wedges, which have adopted the same idea as the universal wedge, produce a wedged beam by dynamic motion of the collimators during the irradiation. Dynamic wedge production can be extremely flexible as the wedge profile can be programmed to produce any required shape. Furthermore, as the wedge effect is not produced by the differential attenuation through a filter, the beam is not subject to a change in energy as is the case for physical wedge filters.

2.2.4. Electron scattering foil

Modern medical linear accelerators are used to produce electron beams as well as x-rays. While x-ray beams are used to deliver high doses to deeper targets within the body, electron beams are used to deposit their energy near the body surface. The differences required within the treatment head to produce an electron beam are (a) thin windows instead of a target, (b) scatter foils instead of a flattening filter. The pencil electron beam which emerges from the thin window of the accelerator vacuum system needs to be widened before it can be used for patient treatments. For this reason the scattering foil is introduced. Also the collimator has to be extended to be near the treatment surface because electrons undergo significant scattering in the air. As a result, electron applicator was introduced. High atomic number materials, while appropriate to collimate the x-ray beam, would generate unwanted x-rays when electrons are scattered. Electron beams are therefore collimated by low atomic number materials such as aluminium.

2.3. The mechanical systems

The mechanical systems described here are those used to help to deliver radiotherapy in a more convenient way. The components of the mechanical systems are the gantry, the patient support system and the collimator.

2.3.1. The gantry

The gantry is a rotatable arm on which the waveguide, the focusing and steering coils, the treatment head, and necessary additional shielding are mounted. Due to the large amount of weight, the system as a whole will be subject to elastic deflections, and there will also be play in the bearings for the gantry rotation and for the rotation of the treatment head. As a result, the gantry rotation axis at the isocentre plane (a plane perpendicular to the central beam and 100 cm from the source) is not a unique position in space but will follow a complex path when the gantry is rotated through 360°. The recommended tolerance for this position is a 2 mm diameter sphere (AAPM, 1995) at the isocentre, the ideal intersection point of the rotational axis of the gantry, collimator and couch (it will be further discussed in chapter 7).

2.3.2. The patient support system - treatment couch

The patient support system consists of a treatment couch which can be moved to the required position by vertical, horizontal and rotational movements. In clinical practice it takes a much longer time to set up the patient for treatment than to deliver the radiation dose. Consequently, an efficient utilisation of the equipment requires that the systems for lining up the radiation field with respect to the patient allow the setting up to be done in logical sequence. The principles of the isocentric mounting used for this purpose were described by Howard-Flander and Newbery (1950). In an isocentric mounting, the main rotation axis of the couch passes through the isocentre. The most likely potential error sources for patient set up are (i) the sagging of the couch under patient load and (ii) the rotation axis does not pass through the isocentre during rotation because of loose bearings. These are also the most frequently checked error sources in periodic quality assurance procedures.

2.3.3. The Collimators

The primary and secondary collimators are located in the treatment head as was discussed in section 2.2.4. However, it is important to discuss their mechanical properties since the collimators define the radiation treatment field delivered to patients. Here only the secondary conventional collimators will be mentioned. The collimators are designed to move in an arc focused on the target. The radiation beam axis should coincide with the collimator rotation axis. There is a potential error in that the collimator rotation axis may not stay in a unique direction during its rotation. This can be caused, for example, by the loose guide bars of the outer jaws. The problem will represent itself as a jaw asymmetry especially during the gantry rotation (i.e. the radiation field will not be symmetric relative to the central axis, but will be shifted to one side). QA program recommendations are made for collimator symmetry checks.

2.4. Energy selection

Modern medical linear accelerators produce x-ray beams at more than one energy. The output energy of the linear accelerator is an important quality index of the treatment beam and its constancy should be checked periodically. In this section, the energy selection mechanism will be discussed.

The output x-ray energy depends on these factors:

(1) Electron beam current. When the current increases the electron energy decreases.

(2) The microwave power applied to the waveguide.

(3) The gun cathode voltage. The electron energy will change when the voltage changes.

For a travelling waveguide, variation of the energy of the electron beam can be achieved by changing the frequency of the microwaves. If the accelerator operates at fixed microwave power and frequency, the electric field amplitude is attenuated as the wave passes along the accelerating guide. The rate of attenuation depends on the electron beam current. Consequently, the average electric field acting on an electron, and hence the energy received in passing through the guide, will be reduced as the electron beam current is increased.

For a travelling waveguide, the wave velocity in a travelling wave accelerator is critically dependent on the microwave frequency. Relatively small changes in frequency can be used to produce wide variations in the electron energy. A change in the relationship between the initial electron velocity and the wave velocity in the buncher section in the accelerating guide will alter the position of the bunches on the wavefront. Since it is this position which determines the electric field strength accelerating the electron, the final energy of the electron can be changed.

2.5. The basic physics of radiotherapy with photon and electron beams from a linac

2.5.1. X-ray beam properties

2.5.1.1. The surface dose and dose build up region

The properties of the radiation beams can be measured in a water phantom since water is regarded as the most suitable substitute for soft tissue. The variation in depth dose or the dose distribution within the whole field can be determined by making a sufficient number of measurements with a computer-controlled dosimeter scanning system.

In megavoltage x-ray beams, the maximum dose is at deeper tissue depths instead of at the skin surface as the range of the electrons set in motion is several millimetres, and dose is deposited at depth beneath the patient skin surface (the effect known as skin sparing). This is one of the great advantages of photon beams because most of the tumours occur at a depth, except for skin cancers. However, the surface or near surface dose is not negligible, as electrons are produced from x-rays striking a beam modifying device such as flattening filter, monitor ionization chambers, collimator jaws, blocks and block trays. These electrons have a long range in air, and the lowest energy contamination electrons produce a dose deposition at the surface. The remainder of the incident dose at the surface is due to electrons from backscattered photon interactions in the patient and from electrons produced in the air gap between the linac treatment head and the patient. The angle of incidence of the beam to the skin and the exit dose also contributes significantly to patient surface dose. The surface dose also increases with field size, because the amount of scattered electrons from the beam modifying devices and the air gap increases with the field size.

The region from the surface to the maximum dose depth is called the build up region. In the dose build up region the dose deposited sharply increases. This is predominantly due to the dose deposition by electrons generated in the medium (ref. figure 2.8). Accurate measurement of dose in the build up region requires the use of different detector systems, usually parallel plate chambers and TLD techniques.

2.5.1.2. The percentage depth dose (PDD) curve and the dose profile

The percentage depth dose is the ratio of the dose at a point along the beam axis to the dose at a reference point, generally the dose at maximum depth. The percentage depth dose depends on the depth ***d***, the field size ***f***, the distance ***S*** from the source to the surface (SSD) of the phantom, and the quality of the beam, usually the nominal energy, ***E***. It can be expressed as:

$$\%D(d,f,S,E)=\frac{D(d,f,S,E)}{D(d_{\max},f,S,E)}\times 100. \qquad (2.3)$$

A schematic of the set up for percentage depth dose measurements is shown in figure 2.6. The depth dose curves and dose profile under $d_{\max}$ and 10 cm depth measured for a Siemens KD-2 linear accelerator are presented in figure 2.7 and figure 2.8, respectively. In these studies, the symbol $d_{\max}$, D_{10}, and TPR_{10}^{20} stands for depth at maximum dose, dose under 10 cm water and tissue phantom ratio (TPR) at 20 and 10 cm depth, respectively. TPR is defined as the ratio of the dose at a given point in a phantom to the dose at the same point at a fixed reference depth.

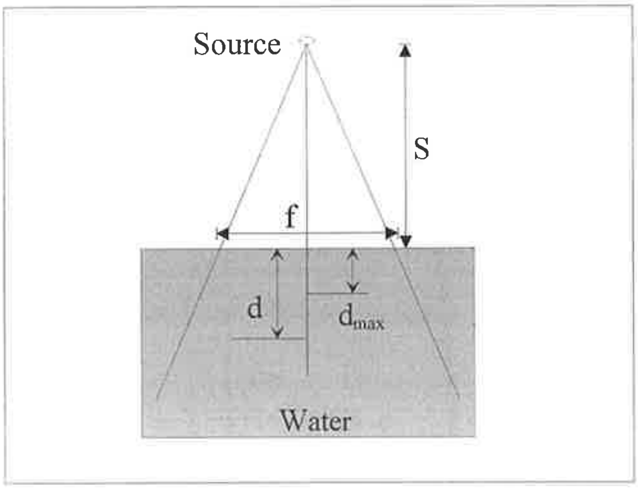

Figure 2.6. Schematics of the set up of the percentage depth dose measurements.

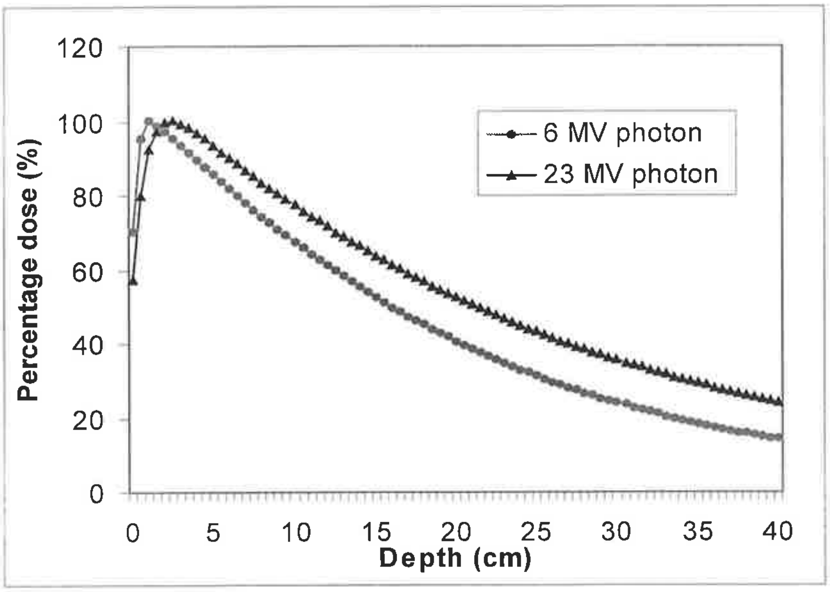

Figure 2.7. Depth dose curve of 6 and 23 MV photons from Siemens KD-2 linac.

Detailed discussions of the relationship of the percentage depth dose with beam energy, field size, and source to surface distance can be found in Johns and Cunningham (1983) and Metcalfe *et al.* (1997). In brief, the depth of penetration increases as the nominal energy increases. The depth dose increases with field size, due to the increase in scatter at larger field sizes. The depth dose falls off faster at a shorter SSD. This can be explained by

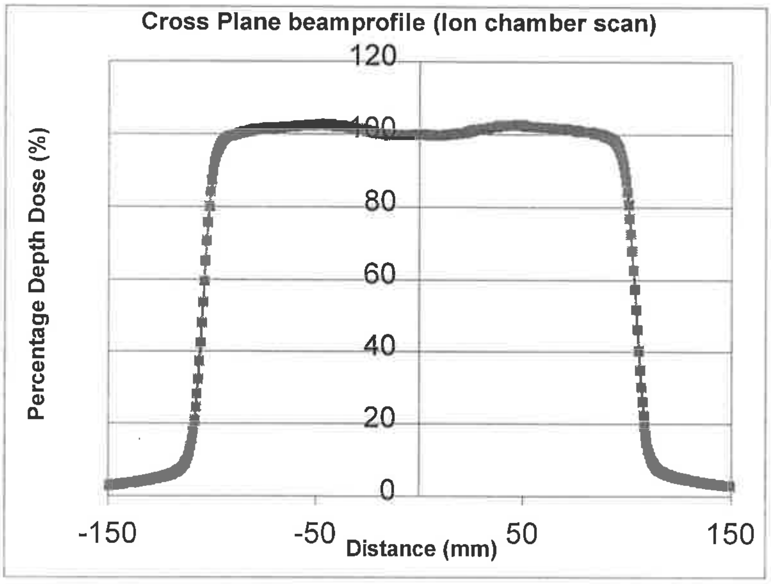

Figure 2.8. The cross plane dose profiles at 10 cm depth measured in water for a Siemens KD-2 linear accelerator and a 6 MV photon beam.

the inverse square law principle, which states that radiation intensity is reduced with the square of the distance from the radiation source. The conversion formula for PDD from one SSD, S_1 to another SSD, S_2, has been given in *the British Journal of Radiology Supplement 17 (BJR)* (Jordan, 1996) as below:

$$\%D(d,f,S_2,E) = \%D(d,f/F,S_1,E) \times \frac{PSF[f/F]}{PSF[f]} F_S^2 \qquad (2.4)$$

where F and F_S are given as

$$F = \frac{S_1+d}{S_1}\frac{S_2}{S_2+d},$$

$$F_S = \frac{S_1+d}{S_1+d_{\max}}\frac{S_2+d_{\max}}{S_2+d},$$

The peak scatter factor (PSF) is the backscatter component at $d_{\max}$. For small variation of SSD the formula can be simplified to equation (2.5) with error less than 1% up to 20 cm depth for 4 MV 150 cm SSD (BJR, Supplement 21, 1997):

$$\%D(d,f,S_2,E) = \%D(d,f/F,S_1,E) \times F_S^2 . \qquad (2.5)$$

Figure 2.7 is an example of percentage depth dose curves measured at Royal Adelaide Hospital (RAH).

The term 'dose profile' is used to describe dose data collected along a plane perpendicular to the beam axis. Dose profiles can be collected at any specified depth and are unique to the depth of collection. The dose profile shown in figure 2.8 has two distinct regions, i.e. the umbral region (central part of the profile) and the penumbral region (near the edges of the profile). At the umbral region the dose is relatively flat because the beam is unaffected by the collimator while at the penumbral region it is. Therefore a large dose gradient fall-off is an obvious characteristic at the penumbral region. The penumbra width of the beam is usually defined as the distance between the 20% and 80% dose contours. Because the dose in the penumbra changes very rapidly, a detector with high spatial resolution is required. Experimental data shows that the p-type diode produces a sharper profile than ion chambers (Metcalfe *et al.* 1997).

The beam profiles measured at a reference depth, e.g. 10 cm, are used to assess the flatness and symmetry of photon beams. In a linear accelerator, the cone structure of the flattening filter may introduce a quality variation across the radiation beam. The beam quality may vary off-axis from the beam centre. This aspect has become of greater importance in recent years with the introduction of asymmetric collimators which allow the treatment beam central axis to differ from the machine central axis, and with the use of two-dimensional dosimetry equipment such as electronic portal imaging devices (EPIDs) for system calibration. In general, the flattening filter design is such that at the beam centre the thicker filter produces hardening of the beam. This effect is compounded by the fact that the photon beam incident on the filter is already softer away from the central axis owing to the nature of bremsstrahlung production. Scattering within the phantom further complicates the situation. Consequently, the beam can be flattened at one depth only (e.g. 10 cm depth), resulting in over-flattening at lesser depths.

When using physical wedges, radiation quality variation across the beam may be evident in the wedge direction owning to the varying thickness of wedge material traversed. The low dose side will receive a greater proportion of scattered radiation than higher dose side, reducing its average energy. This will affect the energy dependent dosimetry equipment such as EPIDs and radiographic films.

2.5.1.3. Tissue-Phantom Ratio

The tissue-phantom ratio (TPR) is defined as the ratio of absorbed dose at any given point to the absorbed dose at the same distance from the source but at a reference depth in the same material phantom. It can be represented by (see figure 2.9)

$$TPR(d, d_{ref}, F, E) = \frac{D_Y}{D_{Y'}} \tag{2.6}$$

TPR depends on the depth d below the surface of the phantom, the field size F of the beam measured at depth d, and the quality of the radiation beam E. TPR does not depend on SSD. The recommended reference depth, d_{ref}, is 5 cm (Khan, 1992). If d_{ref} is equal maximum dose depth, d_{max}, then the quantity TPR gives rise to the tissue-maximum-ratio (TMR), which is defined as the ratio of the dose at a given point in phantom to the dose at the same point at the reference depth of maximum dose. The TPR concept is useful when planning with isocentric beams as dose ratios at different depths are provided directly.

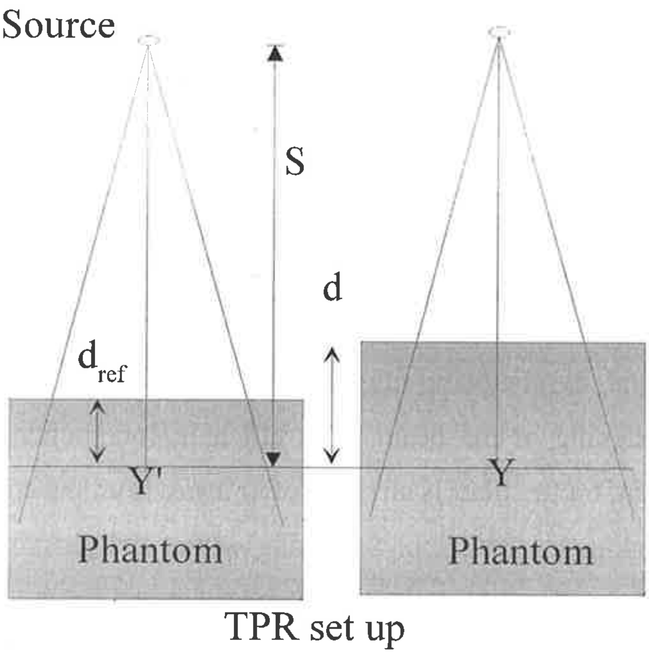

Figure 2.9. Diagrams to illustrate the meaning of tissue-phantom ratio.

2.5.1.4. The quality of Megavoltage x-ray beams

Beam quality relates to the energy spectrum of the bremsstrahlung beam. Assessing beam quality plays a fundamental role in radiation dosimetry, but there has been no completely satisfactory single parameter that can act as a beam quality specifier. As a result, different approaches are applied for different purposes. Essentially three methods have been used:

(a) methods based on quantifying attenuation by the measurement of the two points on a depth ionization curve well beyond $d_{\max}$, (b) methods based on determining a single point on a standard depth ionization curve relative to $d_{\max}$, consisting of either the percentage dose at a standard depth, or the depth of a particular percentage dose, and (c) the nominal accelerating potential. These will be discussed in the following sections.

(a) Methods based on relative attenuation

In order to avoid the problem associated with electron contamination at the depth of maximum dose, most radiation protocols recommended TPR_{10}^{20} value as a quality index (QI), but it has been shown that it is not unique as two beams of different electron energy and filtration may have the same TPR_{10}^{20} but different ionization chamber calibration factors (Owen, 1991).

(b) Methods based on the standard depth dose curve:

The reasons for the changes in PDD with increasing beam energy may be (a) an increase in the depth of maximum dose $d_{\max}$, and (b) a decrease in the rate of attenuation beyond $d_{\max}$. TPR_{10}^{20} reflects only the latter change. The depth of maximum dose, $d_{\max}$, reflects only the former change and it can not be measured very accurately due to the flat peak. A more sensitive parameter would be one that incorporates both the changes in $d_{\max}$ and the subsequent slope of the depth dose curve. Several methods have been proposed: (a) the depth of the 80% dose level ($d_{80\%}$) as the index (BJR, Suppl.17, 1987), but this was not widely accepted (BJR, suppl. 25); (b) percentage depth dose value at 10 cm depth, D_{10} (LaRiviere, 1989). LaRiviere found the relation

$$D_{10}=26.09\log_{10}(MV)+46.78.$$

For dosimetric purposes D_{10} has been very closely related to water-to-air stopping powers. Bot these parameters $d_{80\%}$ and D_{10} are intimately dependent on the measurement of the maximum dose and the presence of electron contamination there. Jordan (1996) argued that $d_{80\%}$ and D_{10} have the relation:

$$d_{80\%} = 0.0039(D_{10} - 63)^2 + 0.18(D_{10} - 63) + 5.8, \tag{2.7}$$

and had two slight advantages over D_{10}: firstly, at beam energies above 20 MV, $d_{80\%}$ moves deeper than 10 cm and continues to increase in depth with energy, so that it is less influenced by electron contamination (although this still influences $d_{\max}$); secondly, at the highest energies, the change in D_{10} with nominal MV becomes progressively less, while d_{80} continues to increase, implying that the latter may be more sensitive to high energies.

(c) Manufacturers use the nominal accelerating potential (NAP) in MV as the quality index. It gives the peak electron energy before electrons strike the target. However, the NAP does not provide much energy spectrum information. Produced x-ray energy spectrum is further modified by the characteristic attenuation curve of the flattening filter material (LaRiviere, 1989).

2.5.2. Electron beam properties

The features of the electron beam that make it a unique therapeutic tool are related to its physical characteristics rather than to any biological effectiveness of electrons. The most attractive characteristic in radiotherapy application is the shape of the percentage depth dose curves (see figure 2.10).

2.5.2.1. The percentage depth dose (PDD) curve and the dose profile

The depth dose curve is equipment dependent, i.e. dependent on the energy spectral and angular electron distributions (e.g. scanning beam accelerators and those with thin scatter foil systems). The PDD curve can be considered broadly in three sections with increasing depth (figure 2.10). Region ***A*** is the build-up region. In this region, there are two important characteristics: one is that the relative surface dose increases with energy as a result of the decrease in mass scattering power with increasing energy. The surface dose is defined as the ratio of the absorbed dose at 0.5 mm depth to the maximum absorbed dose in the beam axis. The other one is that the depth of maximum dose, $d_{\max}$, does not follow a linear relationship with energy and shows significant variation among different types of machines. From figure 2.10 the depth of maximum dose shifts to a deeper depth at medium energy. The next region of the PDD curve (region ***B***) is the dose fall-off along beam axis. The slope decreases with an increase in energy. A convenient measure of this slope adopted from ICRU (1984) is the normalised dose gradient ***G***, where:

$$G = \frac{R_p}{R_p - R_q}, \tag{2.8}$$

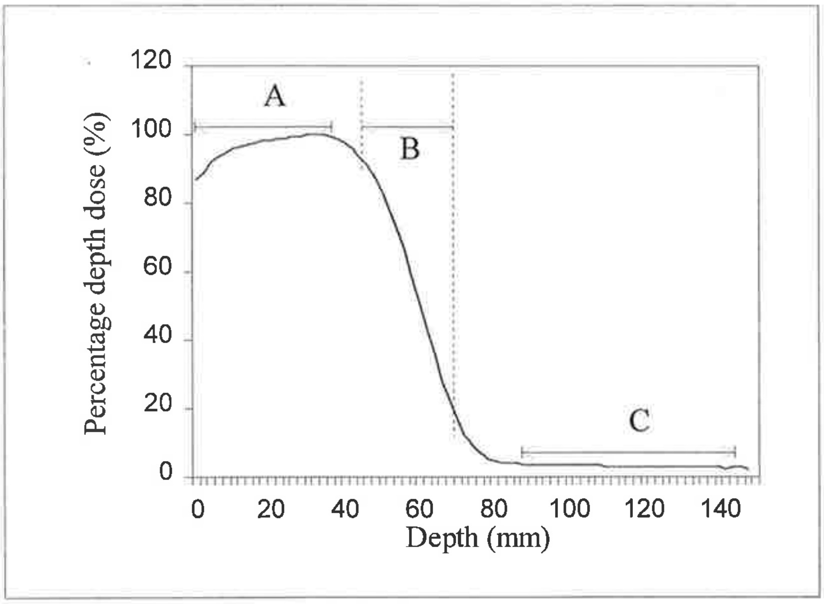

Figure 2.10 A typical electron percentage depth dose curve.

where R_p is the electron practical range and R_q is the depth where the tangent at the steepest point intersects the 100% absorbed dose level. The electron practical range R_p is defined as the intersection point of the tangent to the descending linear portion of the curve (at the point of inflection) and the extrapolated background, as shown in figure 2.10. Typical values of ***G*** lie between 2.0 to 3.0. There is another parameter often used, R_{50}, which is defined as the depth where the absorbed dose has decrease to 50% of its maximum value.

The third region (region ***C***) results from bremsstrahlung contamination which penetrates beyond the electron range. Most of the contamination comes from the scatter foils and it is desirable to reduce this tail.

The depth dose curve changes with many other parameters such as field size, energy, source to surface distance (SDD), and so on. The ranges of scattered electrons are much shorter than those of scattered photons in a x-ray beam of the same energy. Consequently, the effects of scatter on the depth dose curve are mainly seen where the beam diameter is less than the electron range. As the field sizes are reduced, the peak dose moves to the phantom surface and fall-off region, region ***B***, becomes less steep. The effect of SSDs on the depth dose curves has been much less than the influence of the different scattering system present. The main effect of SSDs on the PDD curves is a shift in the position of the depth of the peak dose and the magnitude of the surface dose owing to the loss of low-energy electrons scattered from the collimator. Little effect is observed in the fall-off region (BJR, Suppl. 25, 1997).

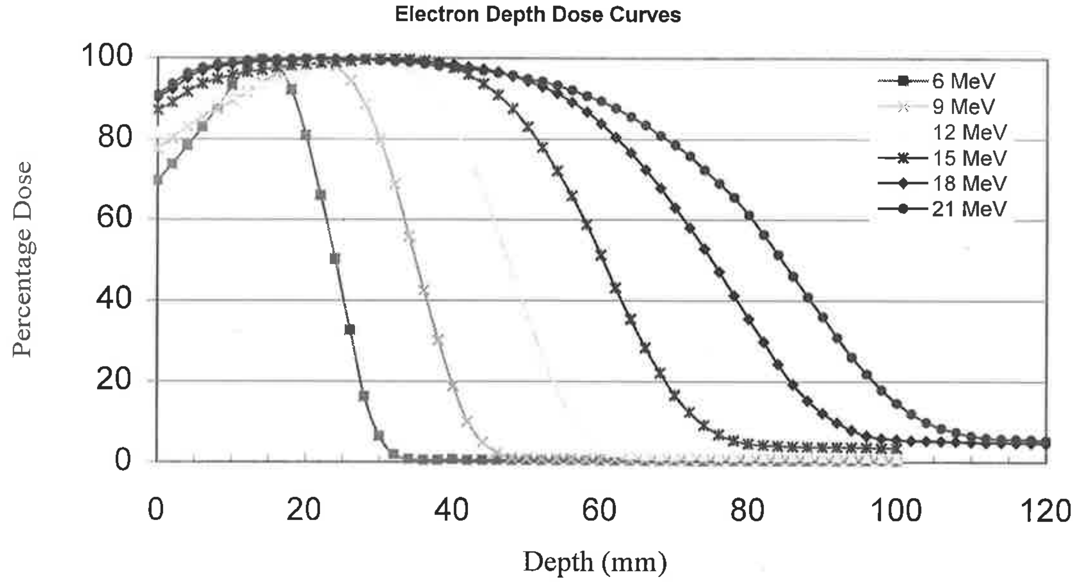

Figure 2.11. The measured electron percentage depth dose curve from a Siemens KD-2 linear accelerator.

The electron beam percentage depth dose measured from a Siemens KD-2 linear accelerator is shown in figure 2.11. The depth (in centimetres) at which electrons deliver a dose to 80% to 90% isodose level, is about one-third to one-quarter of the electron energy in MeV. Clinically, the most useful treatment depth, or the therapeutic range, of electrons is given by the 90% depth dose (Khan, 1992). Unlike x-ray beams, the skin sparing effect with clinical electron beams at higher energy is modest or nonexistent. More detailed information about electron beams is provided by isodose charts. An isodose chart normally gives the dose distribution in the central plane of the radiation beam.

2.5.2.2. The electron beam quality

The distribution of electron energy fluence is shown in figure 2.12. The electron energy before passing through the thin window is almost monoenergetic, after it passes through the exit window, scattering foil, monitor chambers, air and other materials, the electron beam suffers energy degradation and the beam takes on a spectrum of energies. There are a number of ways to determine energy, such as measurement of threshold energy for nuclear reactions; range measurement, half-value dose depth (R_{50}), and measurement of Cerenkov radiation (ICRU report 35, 1984). The electron practical range is the most commonly used parameter to determine the electron beam energy (beam quality), because the practical range is most closely related to the most probable electron energy at the phantom surface $E_{p,0}$. Two equations have been proposed in ICRU report 35 (1984):

$$E_{p,0} = 1.95R_p + 0.48 \qquad (3\text{MeV} \le E_{p,0} \le 25\text{ MeV}) \qquad (2.9)$$

$$E_{P,0} = 0.22 + 1.98R_p + 0.0025R_p^2 \qquad (1\text{MeV} \le E_{p,0} \le 50\text{ MeV}), \qquad (2.10)$$

where R_p is measured in cm for large field size and $E_{p,0}$ in MeV. Equation (2.10) allows for the increasing importance of radiative energy losses beyond 30 MeV.

Another method of energy specification, particularly useful in the dosimetric quantities, is to use the half value dose depth, $R_{50.}$ It is approximately related to the mean energy of the incident spectrum at the phantom surface by:

$$\overline{E}_0(MeV) = 2.33\mathrm{R}_{50}(cm), \qquad (2.11)$$

It is relatively straightforward to interpolate between the depth dose data for large field sizes, and comparison with measured data can be readily made by interpolation to the nearest depth dose curve. The mean energy of the spectrum decreases linearly with depth and can be expressed by the relationship

$$\overline{E}_Z = \overline{E}_0(1 - \frac{z}{R_p}), \qquad (2.12)$$

where z is the depth in phantom.

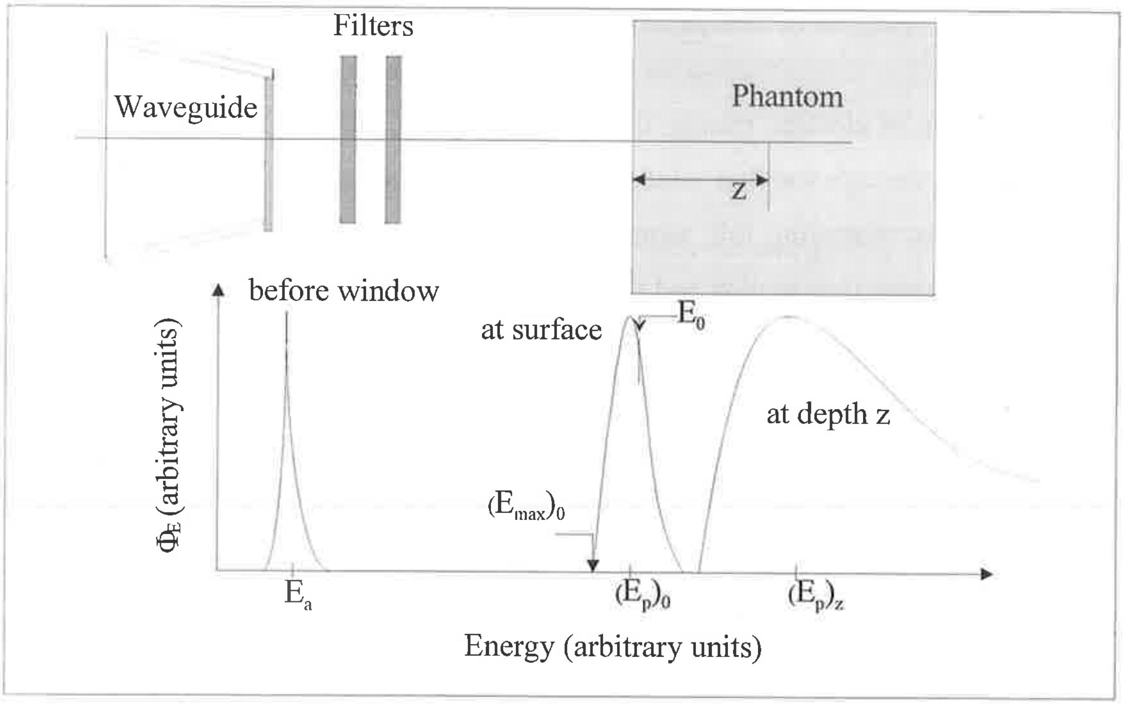

Figure 2.12. Distribution of electron fluence in energy as the beam passes through the collimation system of the accelerator and the phantom (redrawn from Khan, 1992).

The energy constancy should be checked periodically since it affects all the dosimetry parameters of the linear accelerators. The quality assurance procedures will be discussed in later sections.

2.6. Quality assurance of external beam equipment

2.6.1. Introduction

Linear accelerators are the major radiation therapy treatment units. Appendix **A** lists the performance tests, tolerance values and frequencies for medical accelerator units (AAPM, 1994). AAPM TG-40 report recommends that the parameters for daily tests be those which could seriously affect patient positioning and therefore the registration of the radiation field, target volume, patient dose and safety. For monthly tests, more refined testing parameters should be included, which either have a smaller impact on the patient or have a lower likelihood of changing over a month. The report did not recommend weekly tests. It should be noted that the test frequency of a parameter is decided by its deviation from the baseline standard and the constancy of the parameter.

A QA program should be flexible in order to take into account quality, costs, equipment condition, and institutional needs. The tolerance values are action levels and are obtained from the quadratic summation (AAMP, 1984). They were intended to make it possible to achieve an overall dosimetric uncertainty of ± 5% and overall spatial uncertainty of ± 5 mm. It should be noted that just specifying the acceptable levels for individual parameters without considering the cumulative effect is not adequate because detailed recommendations about individual equipment parameters and dosimetric procedures do not guarantee technical quality. These uncertainties are generally perceived as clinical practices (ICRU, 1976).

2.6.2. The test procedures for medical accelerators

The following are typical tests performance during quality assurance. This thesis seeks alternative ways to carry out these checks.

2.6.2.1. Checking of the mechanical and radiation systems

A) Alignment of collimator jaws on the collimator rotation axis

The closure of the collimator jaws on the mechanical axis of the rotation of the collimator should be tested first and, if necessary, adjusted. This could be accomplished by using a front pointer grasped by the all four jaws extending the pointer to the isocenter. Rotation of the collimators will enable the pointer to trace out any misalignment.

B) Collimator rotation axis, central axis of light beam and cross hair coincidence

In clinical practice the mechanical axis of the collimator is presented by the cross hair position, therefore it is necessary to ensure the coincidence of the collimator rotation axis, the central axis of the light beam and the cross hair. This can be done by using a square field to mark (a) the edges of the light field (b) the position of the intersection of the diagonal and (c) the position image of the cross hair. Parts (b) and (c) should coincide. Rotate collimator through 180° and check the coincidence of the new position of the edges. The light field edges are determined to be symmetric about the centre (and adjacent edges must be perpendicular to one another). The light source position is adjusted if necessary (Khan, 1992, AAPM, 1975).

C) Light field and radiation field congruence and coincidence

This test may be divided into two parts: (i) Are the light and x-ray beams symmetrically related to one another for all orientations of the collimator assembly and of the gantry; i.e. does the target (or focal spot) coincide with the effective position of the light source and the geometric back projection of the collimator axis? (ii) Are the dimensions of the light beam, the settings of the collimator dials and the formally defined x-ray beam size coincident at the reference distance? The reference distance is generally source-to-surface distance (SSD).

The light field symmetry can be easily checked by measuring the distances from the crosshairs to the opposite edges, or by checking the edge positions after the collimator rotates by 180°. Open a rectangular field (to reduce confusion), and mark the edges of the light field and the cross hairs. The distances can be measured and checked. Expose two films with collimators rotated by 180° between exposures to verify collimator jaws symmetry. The light field and radiation field coincidence can be checked as follows using ready pack films. Open a rectangular field, mark the edges of the light field and the center, use ready-pack film, cover with sufficient materials to produce electron equilibrium. Make an exposure and develop the film. Visually compare the dose FWHM (Full Width a Half Maximum) with the markers. The displacement should be within 2 mm. Several collimator and gantry angles should be used to check the congruence of light field and radiation field.

D) Determination of mechanical isocenter

The mechanical isocentre is defined as the intersection point of the axis of rotation of the collimator and the axis of the rotation of the gantry (Khan, 1992). Due to its heavy weight, the gantry frame may flex during rotation of the gantry. This may cause the axis of the gantry rotation to move relative to the axis of the collimator rotation, thereby creating an uncertainty in the position of the mechanical isocentre.

Collimator rotation

Attach a piece of graph paper to the flat surface of a plastic sheet and mark an intersection point of two graph lines. Place the paper perpendicular to the axis of the collimator rotation and set the SSD to 100 cm. Using a front pointer attached to the accessory tray, place the centre point of the graph paper at the assumed isocentre. Rotate the collimator with a certain step size, say 30°, and mark the pointer positions. For an acceptable alignment the front pointer positions should stay in a 2 mm diameter circle when the collimator is rotated through its full range.

Gantry rotation

With the front pointer pointed at the mean position determined above, another horizontal pointer is mounted on the treatment couch so that the two pointers coincide as accurately as possible (Figure 2.13). By moving the gantry through 360°, the displacement between the two pointers is visually noted and measured. The recommend tolerance of the mechanical isocentre motion with full gantry rotation is 2 mm. The approximate location of the isocenter can be determined by orienting the gantry at two successive positions at right angles to each other and finding the intersection of the cross hair images.

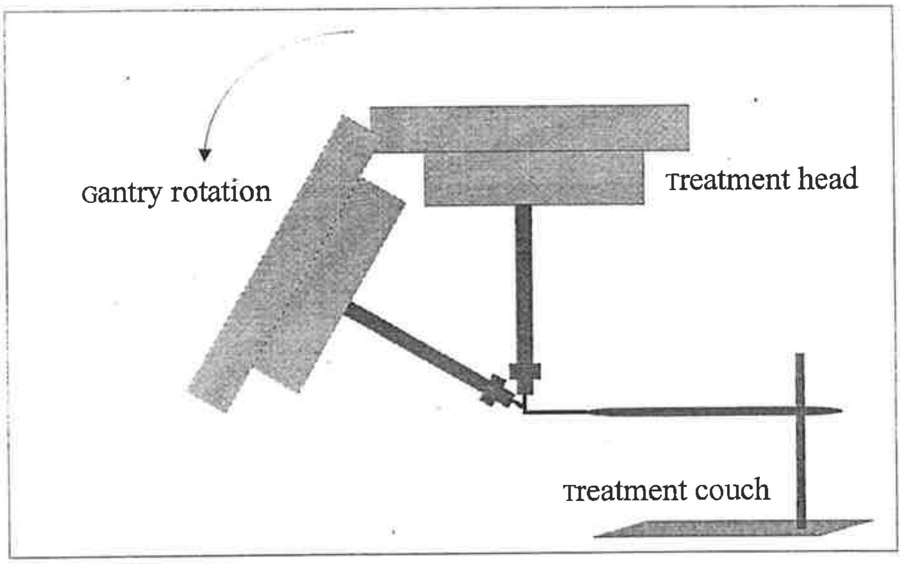

Figure 2.13. Diagram of the setup geometry using front pointers to check the mechanical isocentre.

E. Determination of radiation isocenter

The radiation isocentre is defined as the idealized intersection of the collimator, gantry and couch rotation axes (Nash, *et. al.*, 1994). More practically, the radiation isocentre is specified to be within a sphere (Greene, 1986).

Collimator rotation

With the gantry vertical, place a use ready pack film at 100 cm SSD on the top of the treatment couch. Open upper jaws and close lower jaws to yield a narrow slit of radiation about 0.5mm or less. Place 1cm of solid water as a buildup on the top of the film. By rotating the collimator through a number of different angles, the film is exposed to obtain an optical density of 1. The interval of between angles should be such that the exposures cover the full range of the collimator rotation without overlaps. Close the upper jaws and open the lower jaws and using a new film, repeat the above process. The processed films will show a star shot pattern, with a dark central region (Figure 2.14). Lines may be drawn through the middle of the slit images. The intersections of the lines should be contained in 2.0 mm circle.

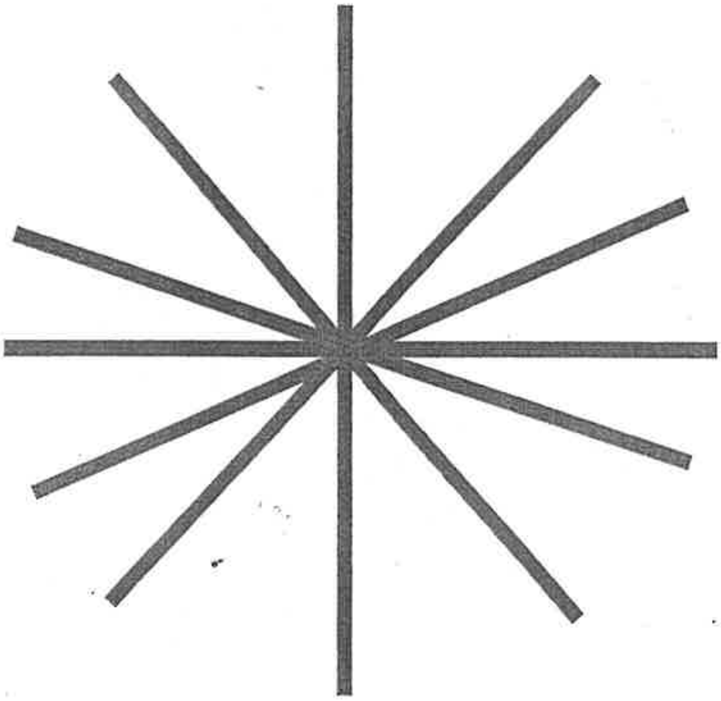

Figure 2.14. A typical star shot pattern from a treatment unit.

Gantry rotation

Place a sandwiched use ready film pack perpendicular to the plane of the couch top in such way that it contains the beam central axis for all the gantry angles. Create a narrow slit beam and make a number of exposures of the film at different gantry angles, avoiding overlaps. Check the star pattern; make sure the intersections lie within a 2 mm-diameter circle.

Treatment couch rotation

Place a film on the table at the source-to-axis distance (SAD). Make a narrow slit beam and place a build up sheet on top of the film. Make seven exposures on the same film rotating the table through 30° between exposures and avoid overlap. The intercept of the centre lines of the images on the developed film should be contained in a circle of 2 mm in diameter.

F) Wedge factors

When wedges are introduced into a beam, the dose in monitor units may be related to the dose at the reference point by means of wedge factors. These are the ratios of the dose measured in a phantom at 10 cm depth with and without the wedge filter in position. The value of the wedge factor clearly depends on the correct positioning of the wedge in the field. This can be conveniently and adequately checked by the routine measurement of the wedge factor.

G) Other mechanical systems

The couch must be tested to ensure that: (1) its flexure in both longitudinal and lateral travel with and without loads are within tolerance (2-5 mm) and (2) with maximum load its sag is not over 2 mm.

2.6.2.2. Checking the radiation systems and beam parameters

A) Beam output constancy

It is advisable to perform the accelerator calibration early in the acceptance testing process, so that long-term stability of the calibration may be tested (AAPM, 1975). The units recorded at the control consol from the linac ionization chambers are known as monitor units (MU). 1 MU may be calibrated to 1 cGy at 100 cm SSD for 10×10 cm^2 field size at maximum dose depth (d_{max}) in water. For a photon beam, set SSD at 100 cm, field size at 10×10 cm, at a depth of 5 cm in a perspex phantom. Serial readings of 200 MU are measured with a Farmer chamber until three consistent readings are obtained for each energy. With correction for temperature and pressure, deviations of up ± 2% are acceptable within 2 or 3 days (AAPM, 1975). For electron beams, the measurements are carried out using a cylindrical chamber for energies larger than 10 MeV. A parallel plate chamber is recommended for energies lower than 10 MeV. A parallel plate chamber must be used for energies lower than 5 MeV.

Set up SSD at 95 cm and field size at 12 × 12 cm for energies less than 20 MeV and field size of 20 × 20, for energy larger than 20 MeV. The recommended (IAEA, 1987) reference chamber depths for different electron energies are listed in table 2.1. The symbol, R_{100}, used in the table is the maximum depth for electrons.

Table 2.1. The recommend chamber depths for electron beam out put constancy check.

Energy (MeV)	$E < 5$	$5 < E < 10$	$10 < E < 20$	$20 < E < 50$
Chamber depth	R_{100}	R_{100} or 1 cm	R_{100} or 2 cm	R_{100} or 3 cm

Consecutive runs of 200 MU are measured with a chamber until three consistent readings are obtained for each energy in turn. The reason one needs to get three consistent readings is because there are four main sources of variation in the observed values of cGy per 100 monitor units (Greene and Williams, 1997):

(1) Variations in the dose distribution inside the radiation field and radiation quality;
(2) Variations in the sensitivity of the monitoring dosimeter system;
(3) Variations in the sensitivity of the field instrument;
(4) Variations in the way the system is set up for calibrations.

Because relatively elaborate systems are used to stabilise the radiation field, the variations are typically under 2%. Variations in the sensitivity of the dose monitoring system can arise from drifts in the electronics or because the monitor chamber is not completely gas-tight, and it is difficult to eliminate or demonstrate very small leaks where the pressure in the ionisation chamber may vary by a few percent over several days. For item (3), regular testing with a radioactive source should be performed to ensure the field instrument is constant to within ± 0.5% over the period of concern. Item (4) is not likely to be a major contributor to the variation because the geometrical errors in setting up the system for calibration do not normally produce changes in the reading of the field instrument of more than 0.1%.

B) Characteristics of dose monitor system

There are generally three aspects that should be checked. (i) linearity and end effect, (ii) the output constancy with gantry angle, (iii) the monitor chamber seal integrity.

(i)The relationship between the measured dose values of dose monitor units (MU) and absorbed dose shall be linear and of the form

$$D = s \times U, \tag{2.13}$$

where D is the absorbed dose, s is the proportionality factor, U is the value of the dose in MU. A series of MU, i.e. 10, 20, 30, … 100 are made, and the output is measured by an ion chamber. The final output value is an average of four or five readings from the chamber. The output of the accelerator is plotted versus the MU. The deviation is calculated between the average readings and values calculated from0 the best linear fit to the measured data (equation 2.13). The recommended maximum deviation should be less that 2% (IEC 977, 1989).

(ii) The machine's output for various gantry angles should be checked by measurement in-air using a detector with appropriate build up. Make four measurements and calculate the average for each 4 arcs, each a 45° arc in a different sector over the full gantry rotation range. Determine the maximum average reading R_1 and minimum reading R_2 and their difference in percentage of their average.

(iii) The monitor chamber seal integrity can be checked by monitoring the outputs versus ambient pressure and temperature. A gross gas leak will show up quickly as a fast response to changes in atmospheric pressure and temperature.

C) Flatness (photon beam)

There are two definitions for radiation field flatness proposed by the International Atomic Energy Agency (IAEA) and the International Electrotechnical Commission (IEC). Both protocols use a measurement depth of 10 cm water. The flatness formula used by the IAEA protocol is defined as:

$$F = \frac{(M - m)}{(M + m)} \times 100\%, \tag{2.14}$$

where $\boldsymbol{M}$ and $\boldsymbol{m}$ are the maximum and minimum dose respectively within the central 80% of the beam profile cross the radiation field. The recommended tolerance is 1.5%.

The IEC protocol adopts a more complicated measurement (IEC 976 & 977, 1989). The beam flatness and symmetry are defined in an area (IEC 976, 1989), as shown in Figure 2.15. The flatness of the X-ray beam is defined by the following formula (IEC 977, 1989) (within a flattened area, under 10 cm of water):

$$\text{Flatness}\,(\%) = \frac{D_{\max}}{D_{\min}} \times 100\%\,, \qquad (2.15)$$

where $D_{\max}$ and $D_{\min}$ are the maximum and minimum doses respectively within the flattened area. The values of d_m and d_d, that determine the flattened area, are defined for different radiation field sizes in Table 2.2 and figure 2.15.

Table 2.2. The values of d_m and d_d for different field size (from IEC 976, 1989).

Square Radiation Field F (in cm)	Dimensions defining the flattened area	
	d_m	d_d
$5 \leq F \leq 10$	1 cm	2 cm
$10 < F \leq 30$	$0.1\,F$	$0.2\,F$
$30 < F$	3 cm	6 cm

The shape of the beam profile at the depth of maximum dose, $d_{\max}$, is very sensitive to changes of the beam energy and is a good quality control indicator. Therefore it is also advisable to have a specification at $d_{\max}$, because the beam profile is sensitive to the energy at $d_{\max}$ and it can be used to check hot spots or horns. These horns should not exceed 105% relative to the central axis value. Generally, a water phantom with a dosimetry scanning system or film are used for these measurements. This procedure can also check that the uniformity index (defined as the ratio of the area enclosed by 90% contour to that by 50% contour in a reference plane) should be greater than 0.8. It should be noted that the beam profile is only calibrated to be flat at one depth plane, because the dose at any point in the field includes a significant component of scattered radiation from other parts of the field.

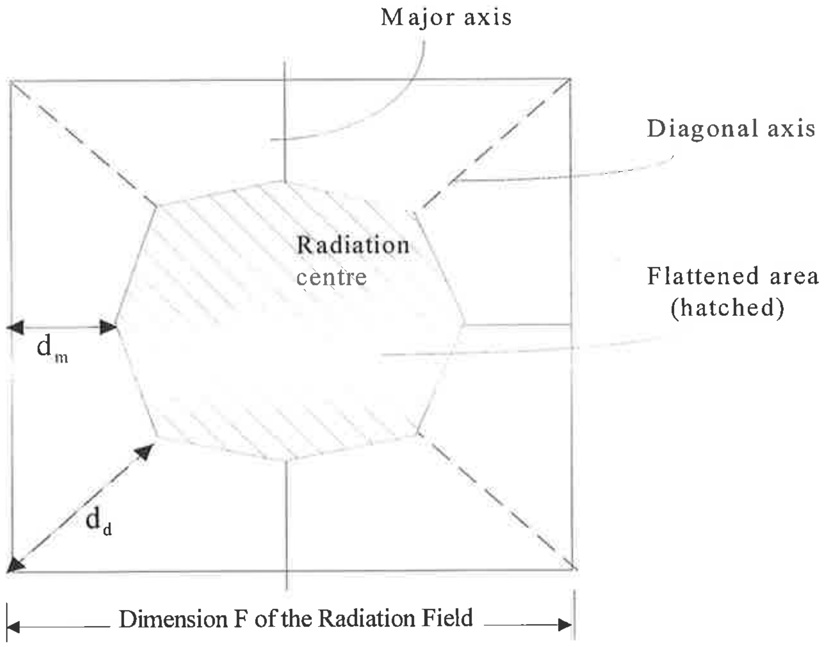

Figure 2.15. Flattened area (shown hatched) within the radiation field. The values of d_m and d_d are defined for different radiation field sizes in IEC, 976.

D) Symmetry (photon beams)

Symmetry is defined as the maximum permissible percentage deviation of the left side dose to the right side dose of the beam profile (see equation 2.16).

$$\text{Symmmetry}(\%) = \left|\frac{D(x)}{D(-x)}\right|_{\max} \times 100\% \,. \tag{2.16}$$

Again, the IAEA protocol definition of the symmetry is calculated from the beam profiles corresponding to 80% absorbed dose. Symmetry is usually specified for both transverse and longitudinal directions, for several field sizes, for specified depths in a phantom, and for several gantry angles. Some manufacturers also specify symmetry along the diagonals of the beams. In the IEC protocol, symmetry is calculated from the flattened area defined in figure 2.15.

E) Penumbra

This is the lateral distance between the 80% and 20% dose lines (of maximum dose) on one side of the beam profile. Film is a sensitive detector for the measurement of the penumbra because of its high spatial resolution, provided that it is exposed in the linear response region.

F) Photon energy constancy check

Despite the lack of a unique energy index, the ratio of doses at two different depths, such as at 20 cm and 10 cm (D_{10}^{20}) or 10 cm and **d**$_{max}$, is still adopted by many radiation centres as a convenient check on the photon energy constancy.

G) Electron energy constancy check

There are several methods to determine the electron energy. The methods use the practical range R_p and half-value depth R_{50} for the electron beams which have been introduced earlier. Again there is no unique parameter accepted as an index for expressing energy. Here two other methods will be introduced.

Table 2.3. Example data for electron energy constancy check (Varian clinic 2500 manual, 1995).

Nominal Energy (MeV)	Depth in routine phantom (mm)	Additional perspex (mm)	d_1 (mm)	Additional perspex (mm)	d_2 (mm)	Expected ratio R1/R2
6	10	4.4	14.4	4.40	18.80	1.30
9	10	10.0	20.0	10.65	30.65	1.97
12	10	20.8	28.8	15.05	43.85	2.43
15	50	Nil	50.0	10.00	60.00	2.172
18	50	4.4	54.4	18.80	73.20	2.904
22	50	4.4	54.4	29.45	83.85	2.242

(1) Depth dose ratio methods

This method is based on the constancy of the ratio of doses at the two different depths. These ratios are sensitive to the energy changes. The ratios are measured at different depths for different energies: the data are shown in Table 2.3. The chambers are set at a depth in a routine phantom measurement, i.e. either at 1.0 or 5.0 cm for low and high energies. Without a change of SSD, the chamber readings, R_1 and R_2, from two additional depths, d_1 and d_2, are recorded and the ratios are calculated. The expected data from the commissioning procedures are given for comparison.

(2) Practical range measurement method

This method is based on a linear relationship between the established practical range and the mean beam energy at the phantom surface. The relationship of practical range and electron energy is schematically shown in figure 2.16a. By plotting the mean incident energy against the depths associated with the linear portion of depth ionization curves, a continuous series of linearity intervals is produced (see figure 2.16b). Two depths, d_1 and d_2, that are symmetric about the centre of the interval (depth at 70% dose ($\mathbf{d}_{70\%}$) and 15% dose ($\mathbf{d}_{15\%}$)) for a specific mean incident energy are chosen (Pisciotta, 1992). Measurements can be made at these two depths and the electron practical range for that energy can be calculated.

The equation for the linear portion of the ionization curves can be written:

$$I = k \times d + b. \qquad (2.17)$$

If we take the readings of d_1 and d_2 from the curves (in theory), I_1 I_2, then

$$k = (I_2 - I_1) / (d_2 - d_1), \qquad (2.18)$$

$$b = I_1 - k \times d_1, \qquad (2.19)$$

where k and b are the slope and *y* intercept, respectively. The *x* intercept can be determined from:

$$X_R' = -b/m. \qquad (2.20)$$

The difference along x-axis between the x intercept, X_R' and the practical range for any given electron beam energy is predetermined from standard ionization curve as an offset. The practical range R_p is

$$R_p = X_R'\text{-offset}. \qquad (2.21)$$

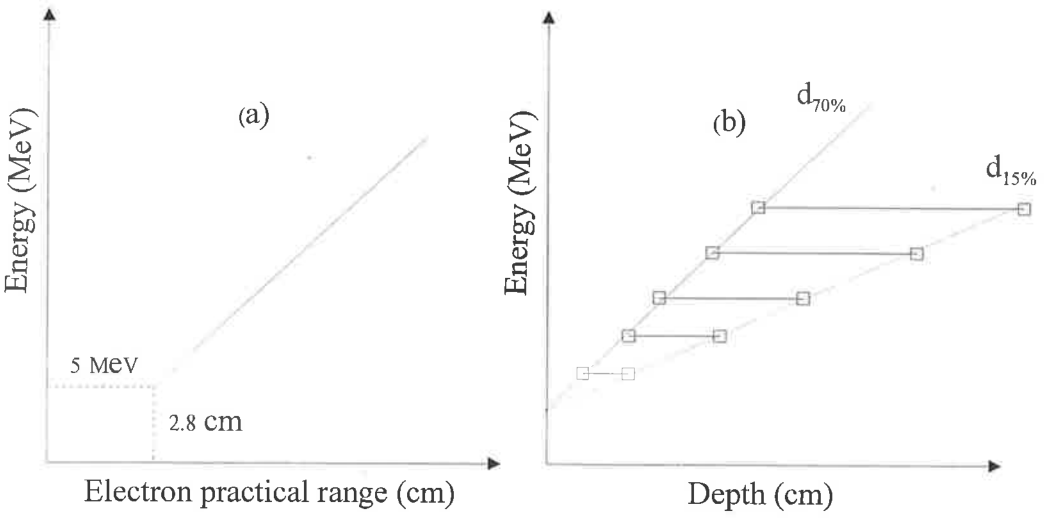

Figure 2.16. (a) The relationship of practical range, and (b) Linearity interval depth levels.

The selected measurement depths are governed by

(a) A minimum difference of 15% in the percent ionization in water at the two depths.

(b) The position of the two measurement depths should be as close as possible to the centre of the linear intervals (between 15%-70%).

I) Electron beam flatness

The ICRU 35 specifies electron beam flatness in terms of a uniformity index. This is defined in a reference plane and at a reference depth as the ratio of the area where the dose exceeds 90% of its value at the central axis to the geometric beam cross-sectional area at the phantom surface. The uniformity index should exceed a given fraction (eg. 0.80 for a 10×10 cm^2 field size at the depth of maximum dose) (IAEA, 1987). In addition, the dose at any arbitrary point in the reference plane should not exceed a prescribed value of the central axis value (eg ± 5%).

The IEC 976 protocol suggests (see figure 2.17) that the electron flatness should check (a) the maximum distance between the 90% isodose contour and the edge of projection of the geometrical field on both major axes at a standard depth. (b) The maximum distance between the 80% isodose contour and the edge of the projection of the geometrical field on both major axes at base depth. (c) the maximum distance between the 90% isodose contour and the corner of the edge of projection of the geometrical field on bisectors of the corner

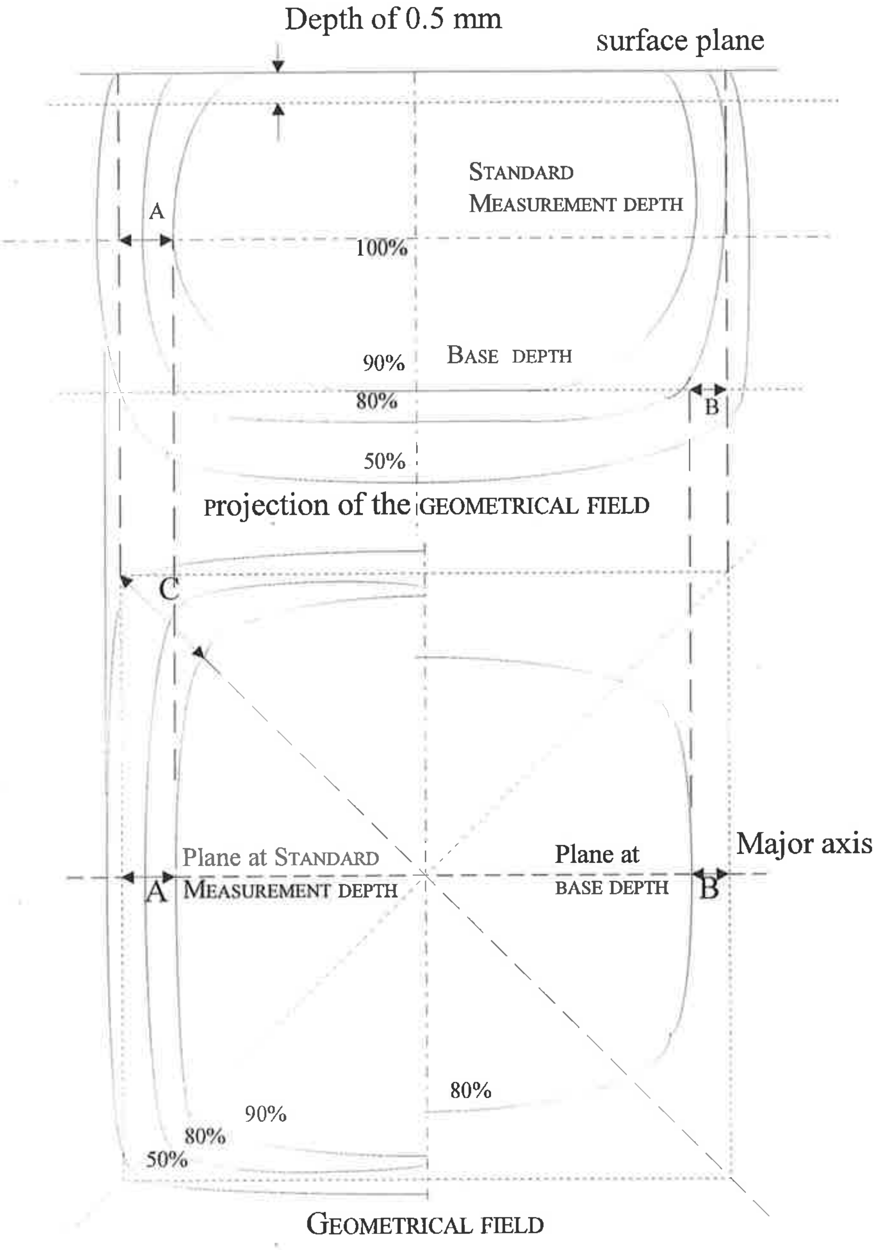

Figure 2.17. Electron beam flatness and symmetry tests (from IEC 976).

at standard depth. The standard depth and base depth are defined as one half of the penetrative quality and the 90% dose depth at 10×10 cm^2 field, respectively (IEC 976, 1989). The penetrative quality is the depth of the 80% isodose line on the central axis.

The AAPM (AAPM, 1995) recommends that the flatness of the electron field be specified in a reference plane perpendicular to the central axis, at the depth of the 95% isodose contour beyond the depth of dose maximum. The variation in the dose relative to the central axis should not exceed 5% over an area confined within lines of 2 cm inside the geometric edge of a field equal to or larger than 10×10 cm^2.

2.7. Conclusion

Radiation therapy has been a useful method of treating cancer for more than sixty years. Its development has been dependent on the availability of suitable radiation sources and the means of measuring radiation dose. Linear accelerators have become the most popular device among the three most used types of radiation sources: cobalt 60, betatrons and linear accelerators. This chapter has outlined the basic technology of a typical linear accelerator, the basic beam characteristics of the output beams and the most common used quality assurance procedures.

The test procedures described above are the main tests that should be performed for the quality assurance of a medical linear accelerator. However, there are some variations in techniques used by different radiotherapy centres. The following chapters will describe how some of these tests might be assessed with an electronic portal imaging device (EPID) with the aim of improving the accuracy and efficiency of QA checks.

Chapter 3

Megavoltage Imaging and Electronic Portal Imaging Devices

3.1. Introduction

Medical imaging is an important diagnostic tool. There are a variety of medical imaging techniques, each image a different physical or physiological property of the patient's body. This chapter is concentrated on images produced by megavoltage energy beams. In particular, portal imaging refers to imaging of the radiotherapy treatment field to verify the geometric (and potentially dosimetric) accuracy of the treatment. In this case, images are acquired to show the geometric placement of the treatment fields relative to bony anatomical landmarks. Images are compared to reference images showing the intended beam placement. Field displacement errors can be then determined either by quantitative measurements or visual assessment. If the portal images are in digital form then they can also be processed to improve image quality. The devices that produce digital portal images are called Electronic Portal Imaging Devices (EPIDs).

This chapter begins with a discussion of the basic theory of image formation with emphasis on imaging at megavoltage energies followed by a description of specific imaging devices developed for megavoltage imaging. The basic technique used for digital imaging is then introduced. Finally, the chapter discusses the utilization of portal images for clinical applications such as treatment verification including the quantitative measurement of beam placement, correction strategies to reduce errors in beam placement and dosimetric applications of EPIDs. A review of previous investigations on the use of EPIDs for linear accelerator quality assurance is given at the end of this chapter.

3.2. Basic image formation theory

Although the physical and biochemical processes being imaged and the mechanism by which images are formed differ between different modalities, it is possible to develop a general mathematical description of the imaging process. From this, a methodology for understanding and analysing the performance of an imaging system can be derived, largely independent of the physical details of the imaging process.

3.2.1. The Image Equation

An object to be imaged is represented by a three-dimensional function $f(x, y, z)$, where the value of this function can be thought of as a brightness or intensity value in the image. Physically this may be the dose distribution at each point in space, or the density of photons and so on. If two separated objects, f_1 and f_2, are presented to an image system and images g produced, then:

$$g = (Ag_1 + Bg_2) = T(Af_1) + T(Bf_2) = AT(f_1) + BT(f_2), \qquad (3.1)$$

where T is the imaging process operator, A and B are brightness scale factors, g_1 and g_2 are the images of the two objects produced separately by the imaging system. This equation means that the image of both objects together is the same as adding the images of the individual objects. Such a system is said to be linear. In fact a few medical imaging systems such as film, CT and MRI, are actually linear. However, linearity has such useful properties that it is assumed to hold, at least for part of the imaging process. The most important feature of linearity is that it allows the image of a complex object to be decomposed into the summation of the images of a set of simple objects. The objects are point objects represented mathematically by the delta (δ) function. This function has properties:

$$\iiint \delta(x - x_0, y - y_0, z - z_0)dxdydz = 1, \tag{3.2}$$

and

$$f(x, y, z) = \iiint f(\xi, \eta, \zeta)\delta(x - \xi, y - \eta, z - \zeta)d\xi d\eta d\zeta . \tag{3.3}$$

Now the image g is given by

$$g = T(f) = T(\iiint f(\xi, \eta, \zeta)\delta(x - \xi, y - \eta, z - \zeta)d\xi d\eta d\zeta). \tag{3.4}$$

The right-hand side of this equation is similar to equation (3.1), where f is interpreted as a scaling factor at the point (ξ,η,ζ) and δ as an object function situated at the point (ξ,η,ζ). It then follows from the linearity definition of equation (3.1) that:

$$g(x, y, z) = \iiint f(\xi, \eta, \zeta)T(\delta(x - \xi, y - \eta, z - \zeta))d\xi d\eta d\zeta_{\zeta} . \tag{3.5}$$

The expression $T(\delta(x - \xi, y - \eta, z - \zeta))$ represents the result of imaging a point object. This can be written as

$$h(x - \xi, y - \eta, z - \zeta; \xi, \eta, \zeta) = T(\delta(x - \xi, y - \eta, z - \zeta)). \tag{3.6}$$

Inserting h into equation (3.5) gives the superposition integral or the image equation:

$$g(x, y, z) = \iiint f(\xi, \eta, \zeta)h(x - \xi, y - \eta, z - \zeta; \xi, \eta, \zeta)d\xi d\eta d\zeta . \tag{3.7}$$

We can only handle the mathematics of the image if we make simplifying assumptions. One assumption is that the shape of h is independent the position. Then the image equation reduces to

$$g(x, y, z) = \iiint f(\xi, \eta, \zeta)h(x - \xi, y - \eta, z - \zeta)d\xi d\eta d\zeta . \tag{3.8}$$

This equation is known as the convolution equation written as

$$g = f \otimes h, \tag{3.9}$$

h is the image of a point object. Unlike the δ function, *h* will be spread to a smaller or greater extend around each point (ξ,η,ζ) and this leads to one of the common names for *h*: the *point spread function* (PSF). If we know the PSF and the imaging system is position independent, then we can fully characterize the imaging system by using the convolution integral.

While in the spatial domain the image equation can be written as (3.9), in the frequency domain, the image equation can be written as:

$$G = F \times H, \tag{3.10}$$

where H(ξ,η,ζ) is the Fourier transform of the impulse response, and is known as the *modulation transfer function* (MTF) of the imaging system.

The image equations discussed above are for general image information. The images to be discussed in this chapter are radiographic images. The radiographic image is formed by the interaction of a distribution of x-ray photons with a detector characterised by an absorption coefficient μ(x,y,z). The distribution of photons is either primary photons that are transmitted through the patient without interacting, or secondary photons that result from interactions within the patient. The secondary photons are deflected from their initial direction and carry little useful imaging information. The primary photons measure the probability of the photons passing through the patient without interacting. The most important image characteristics such as contrast, noise, and spatial resolution for film and EPIDs will discussed in the following sections.

3.2.2. Contrast and signal-to-noise ratio

3.2.2.1. Contrast

Here contrast means the subject contrast which is the difference in attenuation between an anatomical object embedded in a medium and the background. This results in a difference in the number of x-ray quanta reaching the detector behind the object compared to the un-attenuated background. The linear attenuation coefficients of bone and soft-tissue (water) vary with incident photon energy. Photoelectric interactions predominate for all materials at sufficiently low photon energies, for energies up to 50 keV. From 60 to 90 keV both Compton and photoelectric interactions are important. As the energy increases to 200 keV and above, the photoelectric interactions falls off more rapidly than the Compton effect and the latter eventually takes over as the dominant process. When photon energies reach several MeV the pair production process becomes the greatest contributor to photon interactions. The mass attenuation coefficients for bone and water as a function of photon energy are shown in Figure 3.1. From the figure, attenuation is high for bone at the low energies due to photoelectric absorption. This is strongly dependent on atomic number, and hence bone absorbs much more strongly than tissue (water) due to the difference in atomic number. However as the energy increases, the predominant interaction process becomes Compton scattering which is largely independent of atomic number, and dependent on electron density. Thus the attenuation difference between bone and tissue is small and less than the attenuation difference between air and tissue, due to the greater density difference.

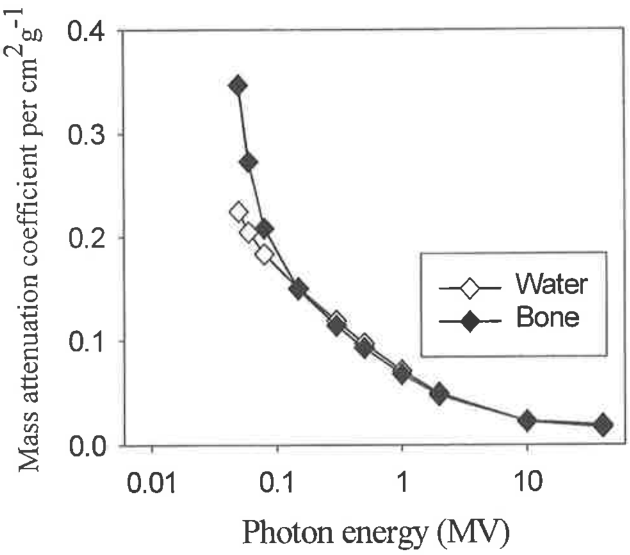

Figure 3.1. Mass attenuation coefficients of water and bone as a function of photon energy (data from *Johns and Cunningham*, 1983).

A simplified analysis to examine the image formation process has been developed by Motz and Danos (1978) where the detectability of a small anatomical structure embedded within a homogeneous body is determined. The model restricts the estimation of signal-to-noise ratio (SNR) to primary subject contrast, statistical noise and scatter. Consider a homogeneous medium of thickness L, linear attenuation coefficient μ, and the mass density

ρ (see figure 3.2). On average the transmitted x-ray fluence $n_t = n_u + n_s$ at a given point, P, is detected as image background. Where n_u is the un-scattered fluence and n_s is the scattered fluence. Then the scattered fraction $F = n_s / n_t$

$$n_u = n\exp(-\mu\rho l). \tag{3.11}$$

Embedded within the medium there is a structure of thickness L_x and attenuation coefficient μ_x such that n' total quanta are detected behind the anatomical object, at point p'. Then

$$n_u' = n\exp(-\Delta - \mu\rho l). \tag{3.12}$$

where $\Delta = L_x(\mu_x - \mu)$ represents the attenuation difference between the anatomic structure and the background. If on average n photons are detected as the background then the subject contrast (ratio of the signal difference between the anatomical structure and the background, to the mean carrier signal) can be expressed as

$$C = 2|n - n'|/(n + n'). \tag{3.13}$$

This can be rewritten as (Motz and Danos, 1978):

$$C = \frac{2(1 - e^{-\Delta})}{1 + e^{-\Delta} + 2F/(1 - F)}, \tag{3.14}$$

Subject contrast therefore increases as this attenuation difference Δ increases, or if the scatter fraction F decreases.

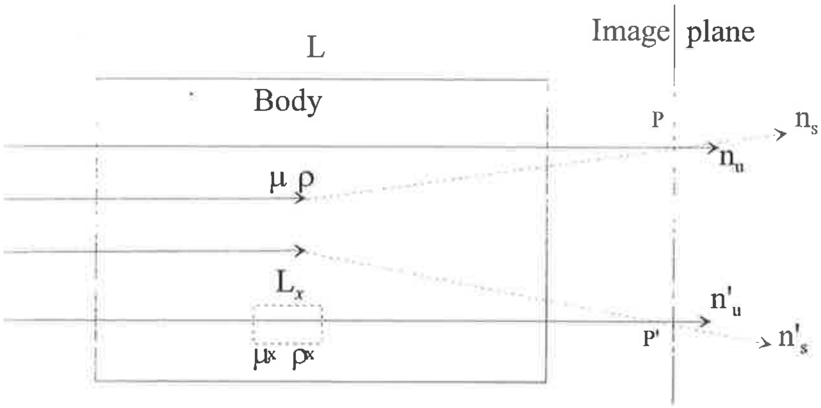

Figure 3.2. Diagram of x-ray transmission through simple body structure with unknown component having length L_x, density ρ_x, and attenuation coefficient μ_x (from Motz and Danos, 1978).

Due to the small difference in attenuation coefficient between bone and soft tissue (see figure 3.1), subject contrast is very low at megavoltage photon energies; it is 10-20 times less than at diagnostic energies. For a 1 cm thick bone structure within a 20 cm thick water medium, the subject contrast decreases from 18.5% at 50 keV to 1.4% at 2 MeV (Boyer *et al.*; 1992b). This is illustrated in figure 3.3 where the contrast *C* for a 1 cm bone structure and a 1 cm air cavity in a 20 cm thick water phantom is plotted as a function of monoenergetic incident photon energy. This contrast was calculated using Equation 3.14 from the tabulated attenuation coefficients for bone, air and water as a function of energy (*Johns* and *Cunningham*, 1983).

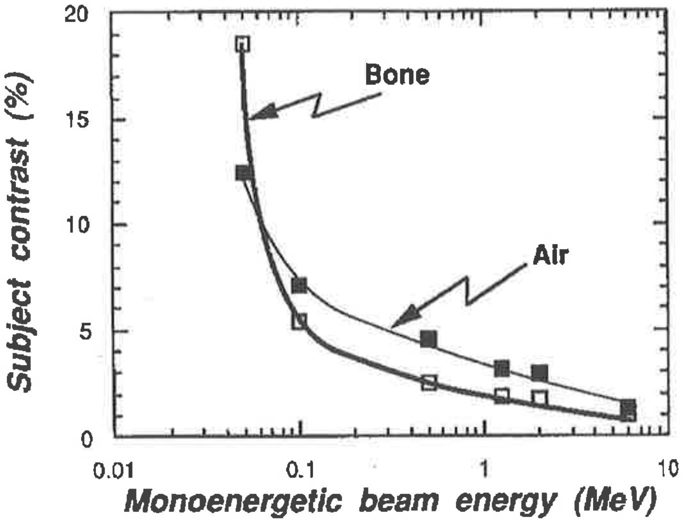

Figure 3.3. Subject contrast, *C*, as a function of monoenergetic beam energy for a 1 cm bone structure and a 1 cm air cavity embedded in a 20 cm thick water phantom (adapted from Boyer *et al.* 1992).

3.2.2.2. Signal-to-noise ratio

An important quantity that is closely related to image information content is the signal-to-noise ratio. This can be expressed as the ratio of the signal difference between the structure and the background to the statistical noise associated with detection of the quanta (Motz and Danos, 1978):

$$SNR = \left|(n - n')\right| / \sqrt{n + n'} . \tag{3.15}$$

Motz and Danos (1978) have shown that this can be written as:

$$SNR = \left[A\Phi\eta e^{-\mu L}\left(1 + e^{-\Delta} + \frac{2F}{1-F}\right)\right]^{\frac{1}{2}} \cdot \frac{C}{2}, \tag{3.16}$$

where A is the area of the anatomical object, Φ is the photon fluence incident on the phantom, and η is the x-ray quantum efficiency of the detector. The SNR will therefore improve as the size of the structure increases, the subject contrast C increases and the number of x-ray quanta, utilized for image formation, increases.

Much larger numbers of x-ray quanta interact with the radiation detector in megavoltage imaging due to higher doses given, the penetrating power of the radiation and the lack of any grids, as in diagnostic radiology, to attenuate the transmitted radiation (Boyer *et al.* 1992). The SNR is calculated from equation (3.16) for the 1 cm object in the 20 cm phantom, assuming a dose of 0.05 cGy for the low energy image, and a 10 cGy dose for the high energy image. The result is illustrated in Figure 3.4. It shows that the SNR does not drop precipitously as the subject contrast decreases with increasing energy. This also means that an increases in dose (numbers of x-ray quanta) can compensate for the lower subject contrast, and the object should be equally detectable at 50 keV or 1.25 MeV. However, this model does not account for loss of spatial resolution or detector noise. The only way to determine what effect those quantities have on the megavoltage imaging performance is to evaluate the spatial resolution, noise and signal-to-noise properties of the megavoltage imaging systems quantitatively.

3.2.3. Spatial resolution

A Gaussian point spread function (PSF) can be described by measuring the full-width at half-maximum height (FWHM) which is often taken as a measure of the resolution. The concept of resolution comes from the idea that if two point projects are close together, their images will merge together in a way which makes it impossible, at least visually, to determine that two discrete objects are present. As the objects are moved apart, a point will come at which it is clear that there are two objects because two peaks of intensity appear. In practice, the exact distance apart that two objects need to be before they can be distinguished will depend on the shape of the point spread function (PSF).

There are other ways of assessing resolution, each of which leads to a definition not always compatible with the FWHM definition. For example, one other common definition is to image an object consisting of a set of parallel lines and to determine how close the lines have to be before they can no longer be seen as separate lines. The resolution is then expressed as the number of line pairs per unit length in one dimension. Spatial resolution of a radiation detector can also be characterised by the detector's modulation transfer function MTF(*f*). The response of the radiation detector to a narrow radiation beam, which is known as the line spread function (LFS), is determined by the spread of the signal caused by angular distribution of secondary electrons in the detector. Spatial resolution should not be confused with image resolution, bit resolution, monitor resolution and output resolution.

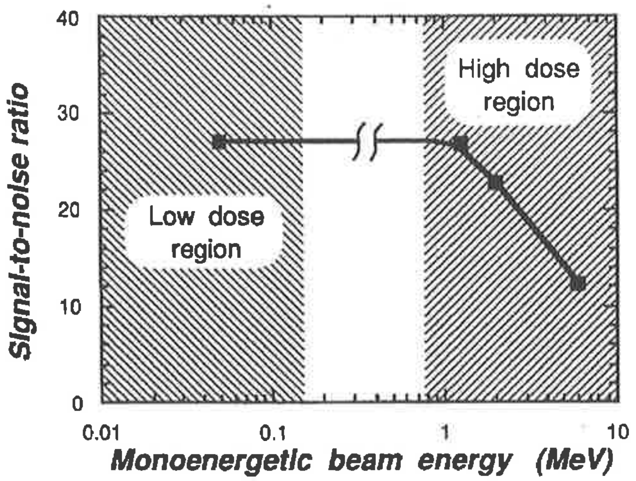

Figure 3.4. Signal to noise ratio expected for a 1 cm bony object embedded in a 20 cm thick water medium for exposures typical of diagnostic radiology (low dose region, 0.05 cGy) and radiation therapy (high dose region, 10 cGy) (from Boyer *et al.* 1992).

Image resolution refers to the spacing of pixels in the image and is measured in pixels per inch (ppi) or per unit length. The higher the resolution, the more pixels there are in the image. Higher resolutions allow for more detail and subtle color transitions in an image.

Bit resolution, or pixel depth, is a measurement of the number of bits of stored information per pixel. Bit resolution determines how much color information is available for each pixel in the file. Greater pixel depth means more available colors and more accurate color representation in the digital image. For example, a pixel with a bit depth of 1 has two possible values: on and off. A pixel with a bit depth of 8 has 2^8, or 256, possible values; and a pixel with a bit depth of 24 has 2^{24}, or 16 million possible values. Common values for pixel depth range from 1 to 24 bits per pixel.

Monitor resolution defines the number of dots or pixels per unit length of output. It is commonly measured in dots per inch (dpi) or pixels per inch (ppi). The device resolution of an IBM-compatible monitor is typically 96 dpi. The monitor resolution determines the size of the displayed image and should not be confused with the image resolution, which reflects the spacing of the pixels in the image. For example, an image with a resolution of 144 ppi is displayed at twice its actual size on a 72-dpi monitor (only 72 of the 144 pixels can be displayed in one inch on the monitor). The same image would be only slightly larger than its original size on a 120 dpi monitor because 120 of the 144 pixels can be displayed in each inch.

Output resolution refers to the number of dots per inch (dpi) that the output device, such as an imagesetter or laser printer, produces. Laser printers usually have output resolutions of 300 to 600 dpi. High-end imagesetters can print at 1200 dpi, 2400 dpi, or higher.

3.2.4. Noise

There are two major contributions to the noise in an image (a) quantum mottle i.e., the photon number fluctuations in signal, and (b) system noise (e.g. film). Statistical variation in the number of x-ray photons forming each point in the image leads to mottling of the image (Johns, 1982). Quanta mottle cannot be completely eliminated. It can be reduced by increasing the number of x-ray photons that form the image, by introducing unsharpness in the image receptor and hence blurring the mottle, or by reducing the detector contrast and hence making it less visible. Fluctuations in the signal will also occur due to the properties of the x-ray detection system. This latter noise is a function of spatial frequency and can be expressed in terms of the Wiener spectrum or noise power spectrum (NPS(f)) function. The spatial frequency, f, is defined as the reciprocal of the spatial period of the fluctuation component, often measured in lines/mm. The mean-square deviation of a signal from its mean value is the variance, and the analysis of these fluctuations into spatial frequency components gives the NPS(*f*) (Boyer *et al.* 1992).

3.2.5. Detective quantum efficiency

The detective quantum efficiency (DQE(*f*)) indicates the signal-noise-ratio transfer characteristic of an imaging system as a function of spatial frequency. The DQE is defined as (Doi *et al.*, 1982):

$$DQE(f) = \left[\frac{SNR_{out}(f)}{SNR_{in}(f)}\right]^2 . \qquad (3.17)$$

Equation (3.17) can be rewritten as (Doi *et al.*, 1982):

$$DQE(f) = K^2 \frac{MTF^2(f)}{\Phi} NPS^2(f), \qquad (3.18)$$

where K is a constant (for a digital imaging system where response is directly proportional to exposure K = unity). The DQE(*f*), which gives a measurement of how efficiently the imaging system responds to the photons (i.e. image information), is reduced if the imaging system (a) cause a loss of spatial resolution (i.e. reduces the MTF(*f*)), (b) adds system noise (i.e. increase NPS(*f*)), or (c) does not efficiently detect all of the x-ray quanta impinging on it (Boyer *et al.* 1992).

Munro *et al.* (1990) investigated the metal plate/phosphor detector DQE(*f*) irradiated by 1.25 MeV ^{60}Co, 6 MV and 18 MV beams and showed that the x-ray quantum efficiency is less than 2%. The x-ray quantum efficiency is low, since only 5% to 7% of the photons impinging on the detector interact within it, and only a fraction of x-ray interactions result in the release of an electron that causes scintillation in the phosphor. This has implications for all portal imaging systems except the 'crystal array' detector developed by Swindell and his colleagues. Therefore Munro *et al.* came to the conclusion to use a metal plate attached to some other material as an x-ray detector. Since the x-ray detectors are not improving, although the recording devices are improving, we will reach a limit on the image quality unless there is a fundamental improvement in the process of portal imaging.

3.2.6. Factors influencing the image quality

The factors which influence the image quality include subject contrast; display contrast, x-ray scatter, x-ray source size, image magnification, spatial resolution and quantum efficiency of the imaging system.

Subject contrast decreases as the energy of the incident x-ray beam increases. However, since the information content of an image, i.e. signal to noise ratio, depends not only on subject contrast, but also on the total number of x-ray quanta used to form the image, increasing the number of x-ray quanta used to form the image can compensate for the loss in subject contrast as the energy of the x-ray beam is increased. Motz and Danos' model does suggest that large numbers of x-ray quanta should be used to acquire portal images. In turn this suggests that the imaging devices that are suitable for portal imaging should:

- Have a high x-ray quantum efficiency
- Cover the entire field of view so that all the quanta have the potential to contribute to the image.
- Add no additional noise to the final image.

In the case of films, the major source of noise is the film granularity rather than x-ray quantum mottle. Film records most of the incoming information, however image information may be lost due to the limited display contrast range. Noise in the human eye-brain system then becomes more important, because both the signal and the noise in portal films may be small (Munro, 1990). The solution is to increase the display contrast. High gamma film i.e. larger display contrast should be used (the gamma of the film is the slope of the straight-line portion of the H-D characteristic curve).

In case of EPIDs, high display contrast is easy to accomplish merely by "windowing and levelling" the digital images and this is one of their major advantages compared with film. Film has had such poor display characteristic that EPIDs were perceived to have better image quality because they displayed and recorded imaging information better (Munro, 1997).

Source size affects the spatial resolution as well as the image magnification. The image formation can be written as a convolution of the source function and the object transmission functions projected onto the image plane. Increased magnification increases the geometrical penumbra, thus increasing the effect of the source size on spatial resolution. However it decreases the blurring due to the detector. Therefore, an optimum magnification distance, which maximizes the resolution of the imaging system, can be derived. This has been found to be 70-100 cm below the patient for an electronic portal imaging device (Bissonnette, 1994). For film which has a narrower detector response, the optimal magnification is just below the patient to minimize the reduction in resolution due to the source.

X-ray scatter can degrade image quality in two ways: for film (with fixed display capability) x-ray scatter will reduce subject contrast in the image. For EPIDs, the loss in subject contrast can be compensated for by increasing the display contrast, but the extra quantum noise due to scattered photons cannot be eliminated. Thus the scattered photons reduce the SNR. The number of scattered photons reaching the EPID depends on (a) the energy of the beam; (b) the gap between the patient and the EPID; (c) the field size; (d) and the thickness of the patient.

3.3. Megavoltage imaging technologies

Megavoltage images have traditionally been acquired with radiographic film/screen combinations designed specifically for portal imaging. However, there are limitations to the use of portal film such as the low image quality which is due in part to the small difference in attenuation between bone and soft tissues at high beam energies (that is, low subject contrast). Furthermore, the delays caused by film development make real time portal film imaging impractical during the treatment. In the last few decades, a great deal of effort has been devoted to developing new equipment, i.e. electronic portal imaging devices. These include scanning linear arrays of diodes (Taborsky *et al.*, 1982) and scintillating crystals (Morton *et al.*, 1991), video-camera based systems (Baily *et al.*, 1980; Leong, 1986; Shalev *et al.*, 1989; Visser *et al.*, 1990; Munro *et al.*, 1990; Wong *et al.*, 1990), matrix ion-chamber systems (Meertens *et al.*, 1985), and flat-panel arrays (Antonuk *et al.*, 1990; Zhao and Rowlands, 1992). In the next few sections, the different type of

EPIDs will be introduced in brief, more details can be found in Boyer's (Boyer, 1992) review paper.

3.3.1. Video-camera based EPIDs

Video-camera electronic portal imaging devices (VEPIDs) consist of a metal plate with the underside coated with a fluorescent phosphor screen to produce visible photons. A 45° mirror deflects some of the light onto a video camera. The major potential advantages of VEPIDs are that (a) all of the radiation exiting from the patient has the potential to generate a signal in the EPID, i.e. the detector views the entire area of the irradiated screen; (b) the spatial resolution can be high, depending upon the thickness of the screen; (c) the system can generate an image quickly. Images can also be acquired rapidly, at up to 30 frames per second. However a major limitation to the design is that only a very small fraction of the light is captured by the lens (0.01-0.1%) and focussed onto the camera (Munro *et al.*; 1990). That will reduce the image quality at two ways:

(a) If a photon interacts in x-ray detector and none of the light generated by this action reaches TV camera, then no measurable signal is produced;
(b) If only a small part of signal is produced in the TV camera then noise generated by the preamplifier and other electronics may be quite large compared to the small signal.

Therefore the development of these device has concentrated on improving the light collection efficiency by increasing the output of the phosphor, increasing the aperture of the lens and increasing the detection efficiency of the camera. However, the thicker screen will improve the quality of the images, but suffers from the loss of spatial resolution and blemishes. Increasing the lens size to increase the light collection efficiency may decrease spatial resolution causing non-uniform brightness and image distortions. These will be discussed further in the following sections.

The noise in the camera has also been minimised by using charge-coupled devices (CCD) cameras and cooling the camera electronics. When cooled, the CCD cameras are extremely low noise devices.

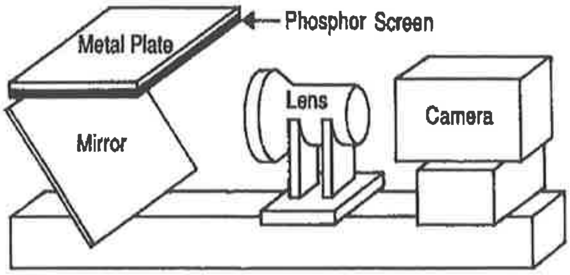

Figure 3.5. Schematic of a video-based EPID (From Boyer et al. 1992).

3.3.1.1. Detector screen

In this section the influence (advantages and disadvantages) of EPID screen thickness on quality of the image will be discussed. The effect of radiation scattered from the patient will also be examined.

There are several types of video-based EPIDs using a structural design similar to figure 3.5. They differ mainly in the details of the metal/phosphor screen and in the selection of the video camera. This section will introduce published works on spatial resolution measurement, metal/phosphor screen thickness optimization, detector noise analysis and scatter effect to the imager. Munro *et al.* (1990) examined the performance of a video-camera based portal imaging system. They measured the overall modulate transfer function (MTF) of the fluoroscopic imaging system as well as independently measuring the modulation transfer function (MTF) of the metal plate/phosphor with film. Thus the contribution to the image blurring from the optical chain, camera and frame-grabber could be deduced. Five thicknesses of phosphor from 50 to 400 mg/cm^2 were tested and the MTFs decreased with increasing phosphor thickness. The MTFs for the system as a whole were significantly lower than for the detector alone. It was also dependent on the orientation of the slit to the raster scan direction, and was lower when parallel to the scan. To study the noise power spectrum (*NPS*), Munro *et al.* (1990) compared an incandescent source, illuminating the video camera (camera noise only), with light from x-rays impinging on the detector (quantum noise). No significant difference was found hence other types of noises are dominant. They suggest that this is not due to the camera but to light quanta noise due to the poor optical efficiency of the optical chain. Increasing the light collection efficiency by increasing phosphor thickness, lens aperture, use of larger camera, and light amplification could result in a six-fold increase in light detected per x-ray quanta.

Munro *et al.* (1990) concluded some component of the fluoroscopic imaging system dominates the spatial resolution rather than the lateral spread of the light and electrons in the phosphor layer of the detector. The TV camera and frame grabber have negligible effect on the MTF: while the magnification of the lens increases the spatial resolution, the frame grabber reduces the spatial resolution. The frame grabber video input filter limits the bandwidth and removes the high-frequency components that would cause aliasing. The frame grabber samples a 512 × 512 pixel matrix, preventing the camera from operating in its high spatial resolution mode.

Wowk *et al.* (1994) varied the thickness of the phosphor layer and the metal plate to examine the dependence of light output and resolution on these parameters. Phosphor thicknesses from 100 to 500 mg/cm^2 were placed on brass plates from 1 to 5 mm thick. The light output was measured with a light photometer. The modulation transfer functions were measured with a high magnification video technique. Light output was found to increase approximately linearly with phosphor thicknesses up to 500 mg/cm^2 as shown in figure 3.7. Spatial resolution decreased exponentially with phosphor thickness up to 750 mg/cm^2, where a minimum was reached. The line spread function (LSF) had a narrow central peak followed by a broad exponential tail (see figure 3.6). However, the measured phosphor LSF is much wider than that expected from electron spread within the phosphor. Wowk et al. concluded that light photon scattering, not electron scattering, dominates the central peak width of the thick phosphor screens.

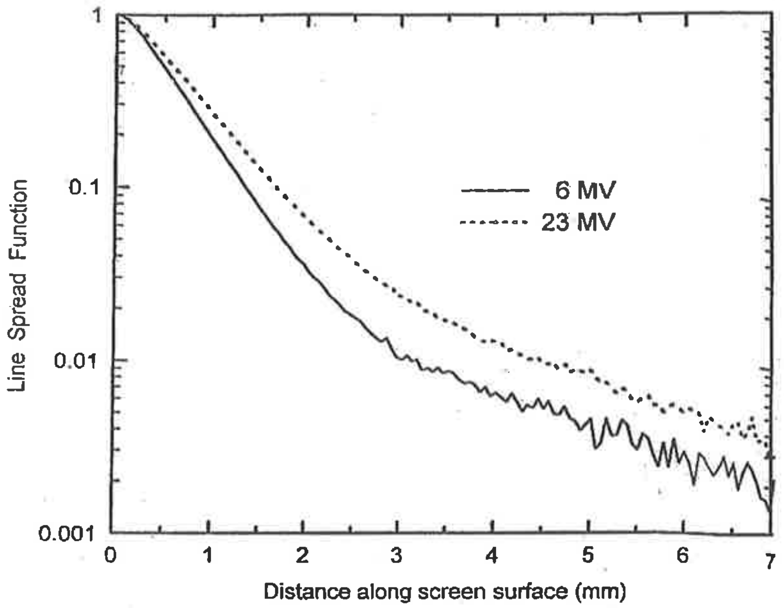

Figure 3.6. Line spread functions for 500 mg cm^{-2} phosphor on 1.25 mm brass. The central peak of scattered light photons, and wide exponential tail produced by bremsstrahlung x rays are clearly evident (redrawn from Wowk *et al.* 1994).

From these results, Wowk et al assumed that most of the noise is generated by light photon statistics, and an expression for the detective quantum efficiency, DQE(f), as a function of phosphor thickness was developed. It was found that a 1000 mg/cm^2 thick phosphor was optimal for spatial frequencies below 0.15 mm^{-1}. The optimal thickness decreases for higher spatial frequencies. The metal plate thickness was found to have a smaller effect on system performance, with 2 mm brass optimal for a dual energy linear accelerator.

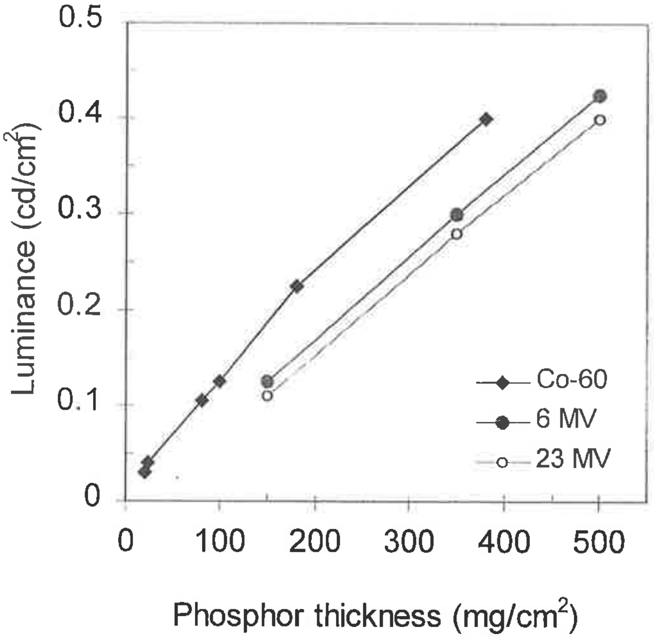

Figure 3.7. Luminance of a Gd_2O_2S screen irradiated by ^{60}Co, 6 and 23 MV photon beams. The data are normalized to an incident dose rate of 100 *cGy/min* (redrawn from Wowk *et al.* 1994).

Bissonnette *et al.* (1997) calculated the optimal phosphor thickness by determining the DQE(*f*) of a video-camera based system and used this to determine indices of displayed and perceived image quality for two types of object: a pelvis object and a point-like object. Eight phosphor thicknesses from 67 to 947 mg/cm^2 were tested. The maximal indices of image quality were obtained for screen thicknesses between 358 and 947 mg/cm^2. The results showed that the optimal thickness depended on the imaging task, with the higher indices for pelvic structures obtained with thicker screens than for a point object. This is because the information is concentrated at lower spatial frequencies where degradation with thicker screens is modest. However, overall there were only modest improvements in quality for phosphor screens thicker than 350-400 mg/cm^2.

Radcliffe *et al.* (1993) used Monte Carlo methods to study the effects of different thicknesses of phosphor and metal plate on the detection efficiency and deposited energy. They found the detection efficiency and deposited energy is roughly linear as a function of phosphor thickness. When the phosphor thickness is 500 mg/cm^2, the contribution of the metal to the detection efficiency is 25% and 40% at 6 MV and 23 MV, respectively.

Beyond a copper thickness of 0.5 mm at 6 MV and 3 mm at 23 MV, the copper has no effect on the deposited energy. Once the metal is sufficiently thick that the phosphor is close to electronic equilibrium throughout its thickness, the metal has no further role to play. They also modelled the optical photon transport out of the screen. It was found that the screen brightness increases with the phosphor thickness and the absorption of the phosphor has a minor effect until the thickness reaches about 500 mg/cm^2. Their evaluations of the signal-to-noise ratio (SNR) for screens concluded that the metal/phosphor screens commercially available on VEPIDs were more than adequate to image bony anatomy down to contrast levels of 1%. The general inability of such systems to perform at this level may be due to additional noise sources such as camera target noise, screen non-uniformity, and digitization noise.

However, apart from the benefits, there are also problems with increasing phosphor or plate thickness. As well as the degradation in spatial resolution with phosphor thickness, thicker phosphor screens may introduce blemishes into the image. These can be corrected for, but the imaging systems suffer from slope as the gantry rotates meaning the camera is not always focused onto the same area of the phosphor, thus making corrections for fixed spatial artifacts difficult (Wowk et al 1994).

Another problem is the influence of the scatter from the patient and energy of the incident beam on the metal/phosphor detector. Monte Carlo simulations have been widely used to investigate this. As the incident beam energy is increased above approximately 1 MV, bremsstrahlung and positron annihilation processes become more prevalent. These produce x-rays which contribute to the low energy component of the scatter spectrum. At megavoltage energies, the scatter spectrum is of significantly lower energy than that of the primary component.

Jaffray *et al.* (1994) used Monte Carlo methods to study the physical characteristics of x-rays scattered by the patient and so reaching the image detector. Their results show that for a specific geometry, the scatter fraction can vary by an order of magnitude, depending on the sensitivity of the imaging detector. The metal/phosphor detectors are sensitive to the lower energy scatter radiation, due to the phosphor high sensitivity at low energy.

Consequently, the scattered radiation contributes to noise and low contrast of the imaging system.

Jaffray *et al.* (1995) studied the x-ray energy absorption and quantum noise in a megavoltage metal/phosphor detector. They concluded the x-ray absorption noise reduces the detective quantum efficiency (DQE) of metal/phosphor detector by as much as 50% at megavoltage energies (1-10 MeV). The metal conversion plate commonly used in megavoltage imaging enhances the DQE of the phosphor screen by increasing the quantum absorption efficiency and reduces the magnitude of x-ray absorption noise.

Yeboah *et al.* (2000) used a Monte Carlo method to investigate the spectral characteristics and exit dose of photon beams scattered from a water phantom and reaching a metal/phosphor portal imaging detector. Their results show that the radiation equilibrium is lost in the air gap and this effect becomes more pronounced as the width of the air gap increases with the low and intermediated-energy scattered photons being affected most. For a specific geometry, a 30 cm air gap decreased the intensity of the lower- and intermediate-energy scattered photons at the detector entrance by up to 90% and 100%, respectively, with a minimum impact to the high energy component.

3.3.1.2. Magnification factor

The source-to-detector distance (SDD), which determines the magnification, is another factor which affects the image quality. There is some controversy as to the ideal values of the SDD. A small field of view is a common problem suffered by all types of EPIDs. Therefore placing the EPID close to the source, e.g. at the isocentre, gives a larger field of view, but it also increases the scatter/primary ratio which reduces the image quality of the system. A small clearance also increases the risk of contact with the patient or treatment couch during the gantry rotation. Placing it further away improves the spatial resolution at the expense of the field of view, and the larger air gap reduces the scatter component of the incident radiation. Bissonnette (1992) showed that the optimal magnification (SDD/100) was about 2 for maximum signal transfer and about 1.5-1.7 for maximum transfer of the signal-to-noise ratio (SNR). The magnification factors of the commercial available EPIDs are 1.4 for Beamview^{PLUS}, 1.6 for SRI-100, and adjustable for both Theraview and Portal Vision.

3.3.1.3. Optical system

The optical chain contributes to the spatial resolution reduction due to its poor efficiency (Munro *et al.,* 1990). The efficiency of the lens can be expressed (Boyer *et al.*, 1992):

$$\varepsilon_{lens} = k\left\lfloor \tau M^2 / (1+M)^2 f^2 \right\rfloor, \tag{3.19}$$

where τ is the lens transmission factor (generally $\tau \approx 0.92$); M is the lens magnification factor, defined as the size of the virtual image on the video-camera divided by the size of the image on the x-ray detector ($M \leq 1$); k is a solid angle factor equal to 1/16 assuming that the light emitted from a point on the phosphor is emitted isotropically into 4π steradians; and f is the *f*-number (focal length/diameter of the lens). Increasing the size of the camera or light sensor will increase M, improve the efficiency of the optical system and hence improve the DQE. Large aperture lenses would increase light collection efficiency, however these suffer from spherical aberration. Large aperture lenses may also suffer from vignetting loss of rays which results in images that are brighter at the centre of the lens, and barrel distortion which causes straight lines to appear as curves. This is undesirable for portal imaging where the image may yield a geometrically inaccurate patient position.

The video-based EPIDs suffer from optical scatter from the optical chain known as optical glare or optical cross talk. Therefore extra precautions must be taken when this kind of EPID is used for dosimetry measurements. Partridge *et al.* (1999) studied the optical scatter for two different video-based EPIDs and developed a technique, an anti-scatter grid, to remove scattered light. The model they used assumes that the major source of optical scatter is multiple reflections between the scintillation screen and the 45° mirror within the imager. They conclude that the model can predict the scatter signal within 1.5% accuracy compared with measured results. Therefore, a correction can be made by removing the optical scatter from the measured image signal. For large radiation fields, the optical scatter contributes over 20% of the primary signal scintillation light intensity to the centre of the field. The use of physical antiscatter grids presents a simple alternative to deconvolution methods of reducing optical scattering for dosimetric portal imaging; however, ~25% of the signal over the field of view is lost. This further reduces the light collection efficiency and thus cannot be expected to give a large improvement in image quality.

The presence of the large mirror in a video-camera base EPID introduces implementation problems in much treatment geometry, however the design can enable the detector assembly to be retracted. Replacing the mirror with a two-dimensional array of fibre-optic image reducers has been demonstrated (Wong *et al.,* 1990), however, these have not been developed commercially. The disadvantages of the system are:

- the output image is distorted because of the small fibre output dimensions;
- the light must have a smaller angle than the acceptance angle. That means some of the light cannot contribute to the images.

Another disadvantage of the video-camera based systems is their bulkiness necessitated by the housing for the mirror. This can hamper patient setup. Fibre-optical systems have been developed to couple the camera to the phosphor.

3.3.1.4. Cameras and frame grabber

The use of CCD cameras has been found to result in an improvement in image quality, particularly when the cameras are cooled to reduce electronic noise in the camera (Jaffray *et al.*, 1996). Several types of video camera are being used in EPIDs that include a CCD with an image amplifier, SIT (silicon intensity target) camera, ISOCON, ST silicon target tube, NEWVICON. Shalev (1995) compared the cameras response with faceplate illuminance. The result showed (see Figure 3.8) that the CCD camera has the lowest illuminance response (about 5×10^{-5} foot candle (fc)) and the NewVicon camera has the highest response illuminance (about 3.3×10^{-2} fc). The thicker phosphor screens provide a brighter image. The light emitted by a Gd_2O_2S screen is predominantly at 545 nm green wavelength. Shalev (1995) also plotted the quantum efficiency vs wavelength, the NewVicon has an eight-fold advantage over the SIT camera (Fig. 3.9), and it has a superior contrast to SIT.

To determine the physical quantities governing image quality, Althof *et al.* (1996) developed a model describing the signal and noise propagation through a CCD camera-based fluoroscopic EPID. They found that camera read-out noise is the largest contributor to noise. They calculated for a new cooled 512×512 pixel CCD camera with negligible read-out noise and high quantum efficiency, that the imager would be quantum noise limited (low spatial resolution) at clinical imaging doses of 1-4 MU. Cameras are now available with 2048×2048 pixels which should improve spatial resolution.

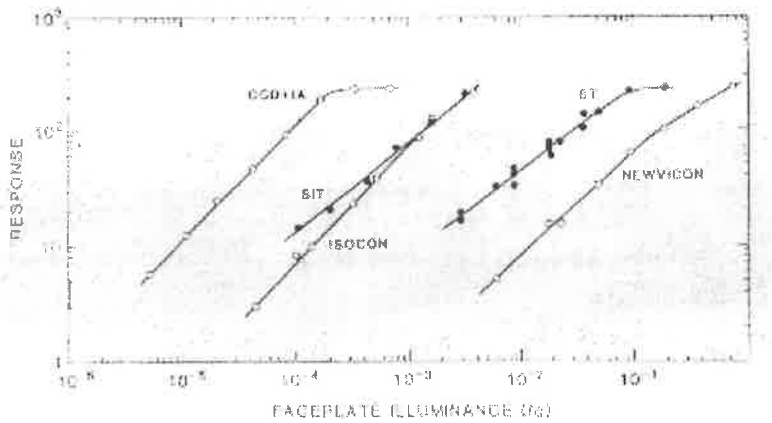

Figure 3.8. Response curves for several video cameras: SIT, silicon-intensified target; IA, image amplifier; ST, silicon target (from Shalev, 1995).

The frame grabber limits the size of data matrix, and prevents the camera from operating in its high spatial resolution mode. This was investigated by Swindell *et al.* (1991), who theoretically studied the number of frame grabber bits required for digital accuracy. The precise value for the signal-to-noise-ratio (DSNR) for threshold visibility has not yet been established. In their study, the value 10 of DSNR was chosen to represent the minimum DSNR in a radiological image. Their results are given in figure 3.10 where the number of the bits to see a certain thickness of bone embedded in tissue was shown as a function of bone thickness and DSNR. They concluded that a 12-bit analog-to-digital (AD) converter would readily allow a 5 mm thick section of bone to be visualised, although Swindell *et al.* (1991) confirmed that a 10-bit system would perform reasonably well for bone thickness above 10 mm.

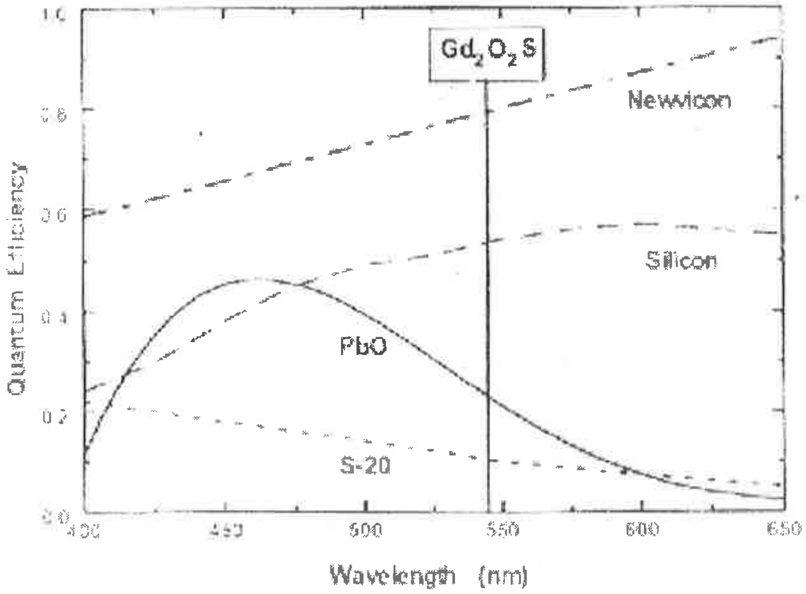

Figure 3.9. Quantum efficiency of Newvicon, CCD (Sillicon), Plumbicon (PbO), and SIT (S-20) video cameras. The light emitted by a Gd_2O_2S screen is predominantly at 545 nm (from Shalev, 1995).

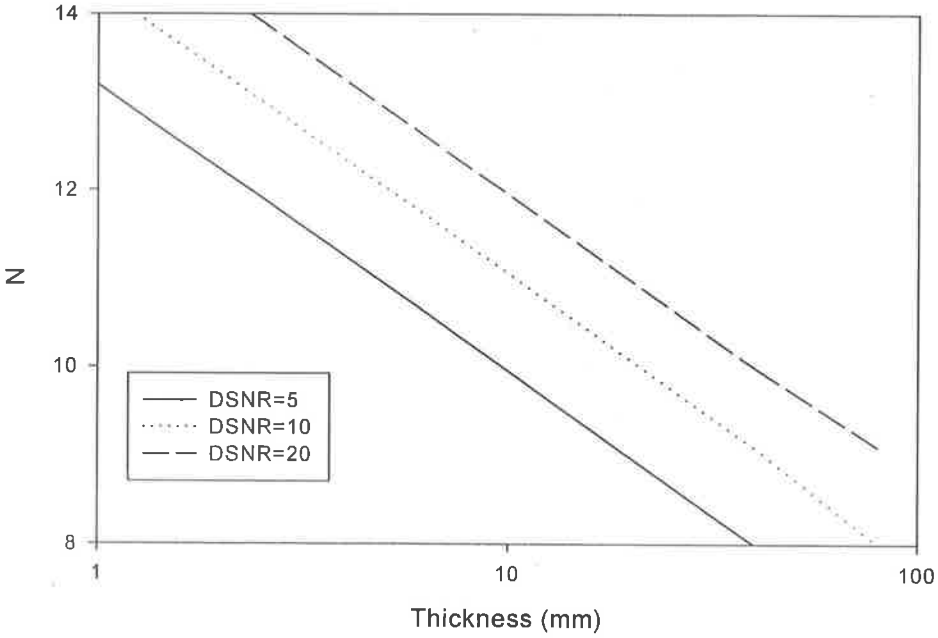

Figure 3.10. The number of bits, N, required to digitise the image for a patient thickness T=250 mm and μ_1=0.049 mm^{-1}. Abscissa is the thickness of bone (μ_2= 0.0083 mm^{-1}) just visible for different values of DSNR (redrawn from Swindell *et al.* 1991).

3.3.2. Matrix-ion chamber array

This type of commercially available EPID was first developed by Meertens *et al.*, (1985) and van Herk and Meertens (1988). This system shown in figure 3.11 employs ion transport in a liquid. The EPID consists of (a) a "camera" cassette and (b) the control unit. The " camera" cassette consists of a 256-channel electrometer system, a 256-channel high voltage switch system and control electronics. The detector consists of two sets of 256 strip electrodes perpendicular to each other. The electrodes lie on the inner surfaces of two printed circuit boards, separated by a 0.8 mm gap filled with liquid film (Iso-octane, spectroscopically pure Merck) which serves as the ionization medium. One set of electrodes is connected to a high-voltage supply, and the other is connected to sensitive electrometers. At the cross-point of the electrodes, a small ionisation chamber is formed. There is a 1 mm steel plate in front of the upper board which acts as the main radiation build-up material. The liquid is ionized when it is irradiated. To obtain one image, the ionization matrix is scanned row by row, by successively switching the high voltage (HV) to different voltage electrodes and measuring the currents in all the 256 column electrodes. As the A/D conversion time is ~ 4 μs, a single row can be read-out in 1 ms. The active area of the matrix is 32.5 × 32.5 cm. The outputs of the electrometers are multiplexed to a single amplifier and digitized in the control unit.

When the HV is switched to a row, a transient pulse is induced in the electrometers. Thus each row cycle consists of a wait-time for this pulse followed by readout of the 256 electrometers. The HV in the latest faster model of this detector is 500 V (van Herk *et al.*, 1995). The HV cycle time based on two cycles of the accelerator 360 Hz timing pulse is 5.6 ms, comprising of a waiting time of 3 ms, and the remainder is signal readout time. In this time the currents of each ionization chamber are measured ten times, and the value can be averaged. The total frame acquisition time is therefore ~1.4 s (which is a result of multiplication of 256 electrometers by 5.6 ms pulse time). The total frame acquisition time For older models the total frame acquisition time is ~ 3s (Boyer *et al.*). Signal readout is synchronised with the pulse timing of the accelerator to obtain smooth images without artifacts due to radiation pulse variation. Several frames can be averaged depending on the time available, and the dose rate delivered.

Due to the relatively long read out time, it is only possible to use this device for dose rate measurements, instead of measuring the integrated dose directly. The relation between output pixel values PV, i.e. ionization current, and dose rate is given by Essers, *et al.* (1995) as follows:

$$PV = G(\dot{D}) = a * \dot{D}^{\frac{1}{2}} + b * \dot{D}, \tag{3.20}$$

where a and b are parameters with units $(min/cGy)^{1/2}$ and min/cGy, respectively. G is the gray level and is a function of dose rate. For practical reasons, typical a and b values of an EPID are determined by measuring the average dose response curve for 5 × 5 pixels in the centre of the EPID. At low dose rates the dependence is accurately described by a square root relation while at high dose rates the linear term becomes more important. The square root term is determined by the ionization of the liquid and the recombination of the ions in the liquid. Application of the high voltage to the chambers disturbs the ion concentration, resulting in the linear term.

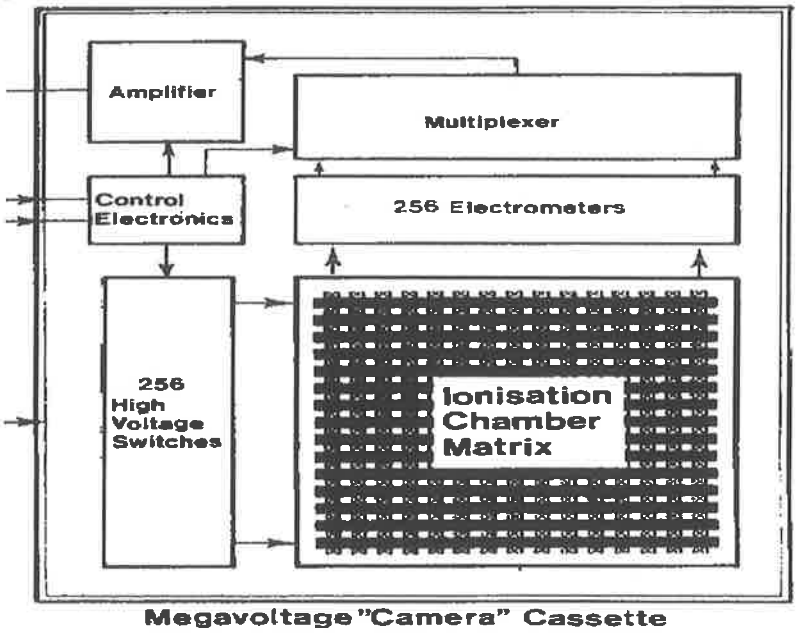

Figure 3.11. Matrix-ion chamber array EPID (from van Herk, 1987)

The variation of free ion pair concentration $n(t)$ with time when no high voltage is applied on the liquid chambers of the EPID is given by van Herk (van Herk, 1991):

$$\frac{dn(t)}{dt} = N_{in}(t) - \alpha n(t)^2 , \tag{3.20}$$

where $N_{in}(t)$ is the ionisation rate, and α is the recombination coefficient, or $\alpha n(t)^2$ is the loss of ions due to volume recombination. When irradiated, the number of ions formed increases until equilibrium is reached between ion-pair formation and ion-pair recombination. This equilibrium occurs after ~ 0.5 s of irradiation and forms a latent image in the ion-chamber matrix. Irradiating for longer periods does not increase the size of the signal once the equilibrium is reached. The signal measured does not depend greatly on the dose-rate when the HV is applied (van Herk *et al.*, 1995). Belloaard *et al.* (1996) gave the solution of equation (3.21) for continuous and pulsed radiation. In the case of continuous radiation $N_{in}(t)$ is proportional to the dose rate, which is now a constant in time. The equilibrium ion concentration is found by taking *dn(t)/dt* equal to zero:

$$n\ (t) = \sqrt{N_{in}(t) / \alpha} \; . \tag{3.21}$$

For pulsed radiation the average concentration is given approximately by

$$n_{avg} = (N'_{in} / \alpha \Delta t)^{1/2} - [\frac{3}{8} \alpha^{1/2} \Delta t^{1/2} N_{in}^{'3/2}] + \cdots , \tag{3.22}$$

where N'_{in} is the production of free ions per volume per pulse, Δt is time between two pulses. The dose rate, $\dot{D}$, is proportional to $N'_{in}/\Delta t$, thus the second term is proportional to $\dot{D}^{1.5} \Delta t^2$. Therefore, it is concluded that the average ion concentration, in practice, is proportional to the square root of the dose rate for both continuous and pulsed radiation.

The major drawback to the scanning design is the quantum utilisation, as only one row of the image is recorded at a time. Scanning also means the device cannot be used to image dynamically changing beam intensity or field size.

Imperfect electrode shapes, different gains of the individual electrometers, and a slight variation in detector distance result in different sensitivities of the individual ionization chambers. For imaging purposes, this is corrected by dividing each pixel value I_{ij} by a flat irradiation (flood-field) pixel value, $I_{ij,flat}$.

For regular calibration of the cassette, background images b_{ij} without radiation are taken to determine the offsets for the chambers (dark-field), and flood-field images $I_{ij,flat}$ are acquired for the chamber sensitivities. The flood field images on the accelerator are achieved by irradiation of the cassette with pulsed beam. The image acquisition is synchronized with the radiation pulses. The corrected image is therefore

$$I_{ij} = \left(I_{ij}^{*} - b_{ij}\right) / \left(I_{fij} - b_{ij}\right), \tag{3.23}$$

where I_{ij}^{*} is the raw uncorrected image. The variation in chamber sensitivities is due to electrode shape differences, electrode surface inhomogeneities, and local thickness variations of the liquid layer.

A major advantage of this EPID design over the video-based EPIDs is that it is compact. Other advantages are that the images are spatially correct, having no geometric distortions. The EPID detector has no moving parts, reducing the likelihood of mechanical problems. However the cassette contains a large quantity of electronics just peripheral to the ionisation chamber matrix, and these are susceptible to radiation damage, either from direct or scattered radiation. This means the cassettes have a limited lifetime.

3.3.3. Scanning linear arrays (solid state system)

A non-optical approach has been developed by Taborsky and his colleagues (1982). This system uses a linear array of 255 diodes with a centre-to-centre spacing of 2 mm that scanned the image in 2 mm increments using a stepping motor. A 1.1 mm thick lead plate covering the diode array acts as build up layer. As the array only covers a small portion of the field the doses required to form an image are large. Spatial resolution is lower, due to the larger diode spacing than a finer detail system such as fluoroscopy camera devices. Morton *et al.*, (1991) produced a linear array of scintillating crystals ($ZnWO_4$), each 5 × 5 × 25 mm in size. The crystals are arranged in a double row, 64 crystals per row with each row offset by half the crystal width to reduce the sampling interval. The x-rays interact and create high-energy electrons that pass through the volume of these crystals resulting in the creation of visible photons that are detected by photodiodes. As the crystals are optically transparent they can be long (25 mm) and hence the detection efficiency for the x-ray photons is very high, ~50% for 6 MV. The high quantum efficiency of the system allows the image to be produced with high subject contrast. However the spatial resolution is low. This type of scanning portal imaging device is not currently available commercially.

3.3.4. Flat-panel devices

Flat-panel based x-ray imaging is an emerging new technology which could be used to significantly improve the quality of on-line portal imagers. There are two main types of flat-panel solid state imaging devices being developed for megavoltage imaging. These are amorphous silicon photodiode arrays (Antonuk *et al.,* 1992), and amorphous selenium photoconductor arrays (Zhao and Rowlands, 1992). While each of these flat-panel devices have similarities, they also have important properties that distinguish them from each other. In the following sections these two types of flat-panel portal imaging device will be discussed.

3.3.4.1. Amorphous selenium array

The amorphous selenium portal imaging device consists of a layer of amorphous selenium deposited onto a copper or aluminium plate (Wong, *et al*., 1996). The metal acts as an electrode and a transparent electrode (indium tin oxide) is deposited on the other side. Before irradiation the selenium layer is charged to create a uniform field ~10^7 V/m across the layer. Upon irradiation x-rays interact in the metal plate and the selenium to create electron/hole pairs which migrate to the electrodes. They partially discharge the E field to create a voltage pattern on the readout electrode which is proportional to the incident x-ray fluence. This pattern is stable for a long time period. The image is read out by using a scanning line of electrostatic probes or a scanning laser beam. However, the readout of the current amorphous selenium involves bulky, slow and delicate scanning equipment. An active matrix readout is being developed using a 2D matrix of thin film transistors (Zhao and Rowlands, 1993). The thin film transistors are named *active matrix arrays* due to the presence of a large number of active devices. These active matrix arrays evolved from the fabrication and lithographic delineation of large area hydrogenated amorphous silicon (a-Si:H) films developed in the early nineties. The active matrix array is a self-scanned readout structure of general applicability. It has been used to readout x-ray images created either in phosphor layers or photoconductor layers. In combination with a phosphor (which gives off light on interaction with x-rays), the active matrix also uses photodiodes at each pixel in the array to convert the light to charge which is stored on the array. This is called the `indirect conversion flat panel imaging'. It is also used in combination with a photoconductor which releases charge when x-rays interact with it, and this charge is collected on electrodes at each pixel of the active matrix array. This is called the direct conversion flat panel imaging system. The amorphous silicon array will be introduced in the next section. In both the indirect and direct conversion approaches, a latent image representing the incident x-rays is stored as charge on the active matrix array. The spatial resolution of the selenium flat-panel is extremely high (Que and Rowlands, 1995), and is mainly due to the lateral spread of high-energy electrons and to beam divergence. The x-ray quantum efficiency of the selenium is expected to be lower than that of the silicon, given the current thickness of the selenium layers.

3.3.4.2. Amorphous Silicon Array

Amorphous silicon array detectors comprise a 1.5 mm thick copper plate, a gadolinium oxysulfide phosphor screen, a phototype of an amorphous silicon flat-panel light sensor, and associated readout electronics (see figure 3.12). Each flat-panel light sensor consists of a photodiode, and two Thin-Film Transistors (TFTs). The circuits are composed of amorphous silicon which is extremely resistant to radiation damage (Antonuk *et al.*; 1990). They act in the same manner as a large area TV camera, collecting the emitted light from the phosphor layer, but can be placed in direct contact with the metal plate and phosphor, being only ~ 1 mm thick. The photodiode detects the light and the TFTs control the readout of the signal. The light discharges the diode which has a bias voltage applied. During readout the TFTs are made conducting by another voltage pulse. The current then flows from the photodiode to an external amplifier. By activating the TFTs one row at a time, with the TFTs in one column connected to a common external amplifier, the signal can be read out one row a time, until the entire array is recorded, at 10-50 frames per second. About 30% of the visible photons are detected and therefore this overcomes the light collection efficiency problems of the video-camera as well as the bulkiness. The spatial resolution of the array has been found to be determined by the finite pixel size (Yorkston *et* *al.*, 1994; Munro and Bouius, 1998). There is no spreading of the light within the sensor itself. Munro and Bouius (1998) studied a 96×96 mm array with pixel size 0.75×0.75 mm, and showed that the array was x-ray quantum limited. The x-ray noise power spectrum was found to be up to 100 times greater than the noise power added by the electronics of the array. They also found that the response of the array was linear with dose rate. Disadvantages of the array were variations in the dark-current of the pixels, and a non-uniform sensitivity. These effects are believed to be due to migration of oxygen or water through the silicon material. The problem should be solved by large-scale manufacturing processes. The readout electronics adjacent to the matrix needs to be radiation insensitive, and synchronised with the radiation pulsing. As the time to readout a frame is much larger than the interval between radiation pulses (~ 3 ms), the pulses during the readout causes artifacts on the images. These pulsation artifacts can be distracting when one is trying to visualise low contrast structures.

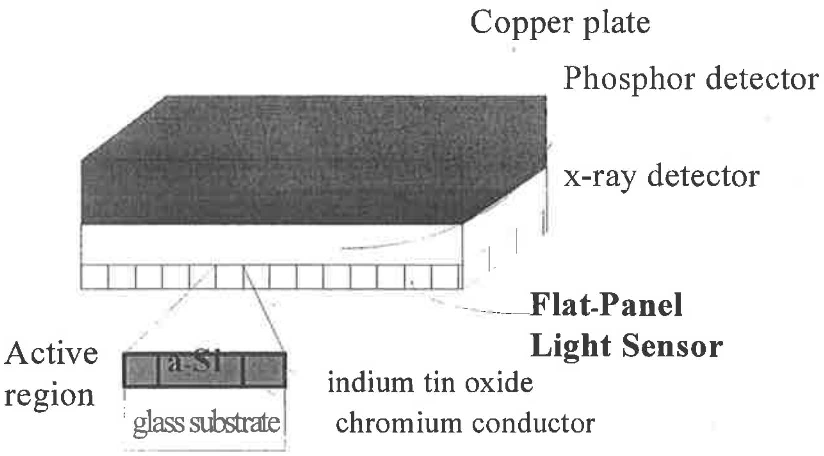

Figure 3.12. A schematic of the amorphous silicon EPID (from Munro et al., 1998).

3.3.5. Comparison of EPIDs

A comparison between commercially available EPIDs may be useful in the selection of new equipment, although normally the purchase of a new linear accelerator will be based on the other considerations. However, if portal imaging is a high priority, and special capabilities are required, careful evaluation of EPIDs parameters may be required. Shalev (1996) compared four systems which were commercially available at that time. Table 3.1

shows a summary of some technical parameters. Of course, several years have already passed, suppliers might have upgraded their products with new developments in hardware and software.

The spatial resolution f_{50} (see more detail in the next section) data were published by Shalev *et al.* (1997). The measurements were made at centres in Canada, the US, Europe, Australia, New Zealand on EPIDs from five different suppliers. The results are given in Table 3.2.

Table 3.1. Comparison of commercially available EPIDs (from Shalev, 1996).

EPID model	Portal Vision	SRI-100	Theraview/ Target View	Beamview^{PLUS}
Supplier	Varian	Philips	Infimed	Siemens
Type	SLIC	VEPID	VEPID	VEPID
Detector	Ion chambers	Gd_2O_2S	Gd_2O_2S	Gd_2O_2S
SDD (cm)	Variable	160	variable	140
Detector size (cm)	32.5 x 32.5	40 x 30	40 x 40	41 x 33
FOV at isocenter (cm)	23 x 23*	25 x 19	28 x 28*	30 x 24
Enclosure	Robotic arm	Rigid, demountable	Motorized vertical and horizontal	Collapsible
Camera	-	CCD	Plumbicon	Newvicom
Detector matrix	256 x 256	512 x 256	512 x 512	512 x 480
Display matrix (pixels)	256 x 256	512 x 512	512 x 512	512 x 480
ADC (bits)	12	8	8	8
Pixel size (mm)	1.27 x 1.27	0.78 x 1.17	0.78 x 0.78	0.65 x 0.52
Platform	PC	PC	SPARCstation	SPARCstation
Movies / Time lapse	Yes / Yes	No/No	Yes / Yes	Yes / Yes

Software tools	Comprehensive	Limited	Comprehensive	Limited
Check field size & shape	Yes	No	Yes	No
Image registration	Yes	No	Yes	No
Image size (bytes)	132,096	131,584	262,336	246,910
Compression available?	Yes	No	No	No

*Field of view is variable. Value given for SDD=140 cm.

Table 3.2. Summary of f_{50} values at different beam energies.

EPID model	Portal Vision	SRI-100	Theraview/ Target View	Beamview^{PLUS}	Eliav
f_{50} at isocenter (lp/mm @ 6MV)	0.258 ± 0.008	0.180 ± 0.014	0.231 ± 0.013	0.214 ± 0.027	0.352
f_{50} at isocenter (lp/mm @ 10-25 MV)	0.251 ± 0.007	0.179 ± 0.014	0.218 ± 0.011	0.192 ± 0.027	0.255

The higher the spatial resolution the better the performance of the imaging system. According to table 3.2, Eliav (Medical Imaging Systems Ltd, Haifa, Israel) and Portal vision EPID models have superior image quality compared to the other models.

3.3.6. Quality assurance (QA) of EPIDs

One of the major aims of EPIDs is to improve the geometric accuracy of radiation treatment. It is important not introduce a field set-up placement error. Like any other radiation equipment, EPIDs should have their performance such as mechanical accuracy, camera offset and gain, calibration and other dosimetric parameters periodically checked. The two most important criteria to check are the geometric accuracy of the EPIDs and the image quality (Low *et al.* 1996). The geometric accuracy is important for video-based EPIDs, which can exhibit the geometric distortions due to lens distortion. Most EPID vendors provide the 'Las Vegas" test phantom for measuring image quality (Kubo *et al.*

1996). Designed for a different purpose, this subjective test is insensitive to small changes in noise or spatial resolution. The main reason for a change in spatial resolution or contrast is a change in the sensitivity of the individual pixels.

Kirby (1995) developed a multipurpose phantom with 1mm lead in Perspex to check the test phantom image and monitor the change in spatial or contrast resolution over time. Rajapakshe *et al.* (1996) developed a quantitative, objective test phantom, the QC-3 phantom (see Figure 3.13), in order to test the image quality. It consists of five bar pattern with spatial frequencies of 0.1, 0.2 0.25, 0.4, and 0.75 lp/mm. The bar patterns can be assembled for specific purposes. There are six regions with uniform absorber 15mm thick, ranging from 15 mm plastic to 15 mm lead. These are used to measure the Signal-to Noise Ratio. In order to compare the image quality, two consecutive images were acquired for each imaging system and the spatial resolution and contrast to noise ratio (CNR) were calculated for each system. Spatial resolution is defined by $f_{50,}$ which is the frequency for 50% of the relative modulation transfer function (RMFT). The contrast is measured from the brightest and darkest regions and the noise, σ, is obtained from the two test images. The two images are subtracted and the standard deviation is obtained from the difference, thus avoiding the contributions from fixed pattern noise (Shalev, 1997).

The phantom has been applied extensively for acceptance tests, commissioning and QA testing of portal imaging devices. An example of the result is shown in **Sec. 3.3.5** Table 3.2.

A QA program should also include image processing, the integrity of patient data, etc. A list of recommended tests and their frequency for EPID systems were given by Rajapakshe *et al.* (2000) (see table 3.3):

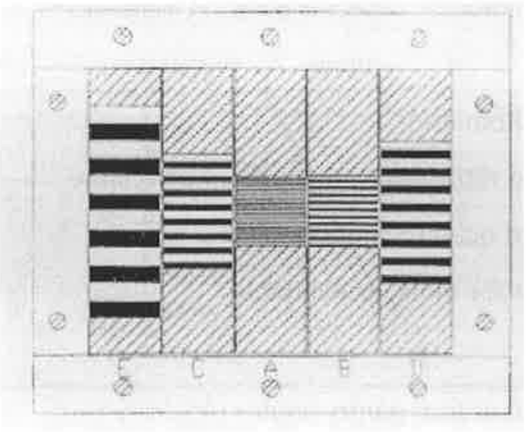

Figure 3.13. A schematic diagram of the QC-3 phantom (from Rajapakshe *et al.*1996).

Table 3.3. Recommended tests and frequency for EPID systems (from Rajapakshe *et al.* 2000).

Test	Description	Frequency
Safety	Collision interlocks*	Daily
	Mechanical integrity*	Weekly
	Electrical safety *	Semi-annual
Mechanical	Lateral positional accuracy of detector*	Daily
	Vertical positional accuracy of detector*	Weekly
	Stability of mirrors, camera and shielding (if present)	Semi-annual
Image acquisition	Single, double and movie acquisition modes	Monthly
	Calibration for dark/open fields *	Monthly #
	Dose required for all acquisition modes	Semi-annual
Image Quality	Spatial resolution at isocentre*	Daily
	Noise level (beam off and on)	Monthly
	Dose response curve	Monthly
	Spatial distortion*	Monthly
	Artefacts *	Monthly

Isocentre indicator, detector position indicator*	Monthly
Accuracy of image registration tools (manual/automatic)	Monthly Semi-annual
Storage and retrieval accuracy, backup/restore	Semi-annual
Accuracy of on-screen measurement tools*	Semi-annual
Other software tools, as available	

* tests should be carried out at four gantry angles (0°, 90°, 180°, 270°)

frequency may be specified by vendor.

3.3.7. Portal films

Three improvements to portal imaging have been made, retaining the use of film as detector: (a) the use of a film digitizer, (b) the use of a metal converter plate, (c) the use of gamma multiplication (Webb, 1993). More recently, film has become a practical tool for the measurement of dose distribution (Burch *et al.*, 1997 Mayer *et al.*, 1997 Perera *et al.* 1998, Gagel *et al.*, 2000).

3.3.7.1. Film Characteristic Curve

The opacity of a film may be expressed in terms of the fractional transmittance, T, to light

$$T = I/I_0 = \exp(-D)\,, \tag{3.24}$$

where I is the transmitted light intensity for an incident intensity of I_0. The optical density (OD), D, of the film is then

$$D = -\log(T)\,. \tag{3.25}$$

The characteristic Hurter-Driffield (H-D) curve of a film expresses the relation between the density of a film and the log of the exposure (Figure 3.14), which is the standard format to display the properties of a film:

$$T = I/I_0 = \exp(-D)\,, \tag{3.24}$$

where I is the transmitted light intensity for an incident intensity of I_0. The optical density (OD), D, of the film is then

$$D = -\log(T)\,. \tag{3.25}$$

The characteristic Hurter-Driffield (H-D) curve of a film expresses the relation between the density of a film and the log of the exposure (Figure 3.14), which is the standard format to display the properties of a film:

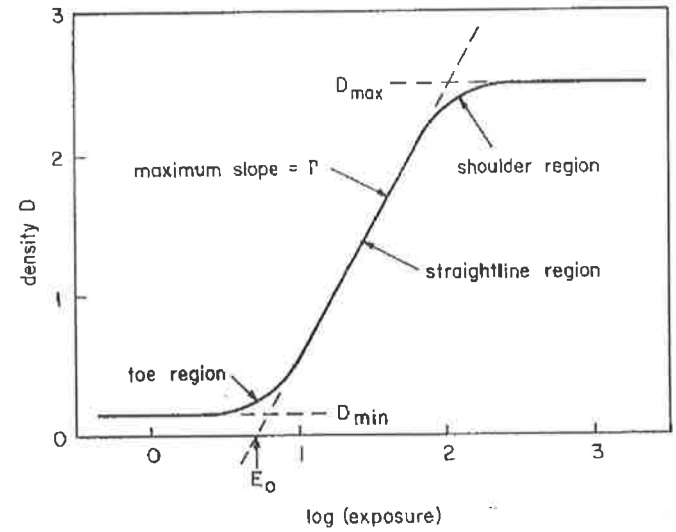

Figure 3.14. Idealized film characteristic H-D curve for a typical film emulsion. The normal range is the "straight line region" of slope Γ, where the density increases linearly with the log of the exposure. The tails near zero and maximum are due to fogging and saturation respectively.

The minimum detectable difference in the exposure depends on the slope of H-D curve, known as the gamma, Γ, of the film. Suppose two parts of a film receive primary dose P_1 and P_2 and the same scatter dose S, then the dose contrast is

$$C = (P_2 + S)/(P_1 + S)\,. \tag{3.26}$$

If $\Delta P = P_2 - P_1$ and $P = P_1$ equation (3.27) can be derived as

$$C = 1 + \frac{\Delta P}{P}\left(\frac{1}{1 + S/P}\right) . \qquad (3.27)$$

This gives a film-density contrast as

$$\Delta D = \Gamma \log(C) \ , \qquad (3.28)$$

The equation indicates that films enhance the contrast of the imaged object by Γ multiplication. The sharper the slopes of H-D curve, the larger the contrast enhancement.

3.3.7.2. Influence of metal screen

Metal screens are generally used with film for portal imaging. The portal film image is not formed directly from the incident megavoltage photon beam, but rather from the stimulated electron emission in the vicinity of the radiographic film. If no screens are used, the major source of electrons is from within the patient near the exit surface (since electrons of *n* MeV travel only *n*/2 cm in tissue). This obliquely scattered radiation detracts from the desired image by increasing blur and reducing the contrast. Increasing the thickness of the plate reduces resolution as the electrons can scatter more laterally, however, if it is not thick enough obliquely scattered electrons from the patient will not be absorbed and degrade image quality. Hence high-density plates are required and copper of about 1 mm or lead of 0.8 mm thickness is usually recommended for megavoltage screens. Droege and Bjarngard (1979) point out that the metal screen cannot increase the effective gamma but does increase the overall contrast by reducing the scatter to primary ratio.

Since there is usually little photon radiation scattered back to the film from structures beyond, a rear metal screen usually has little effect on the image contrast. However the rear screen increases the *speed* of the system with high Z materials (Williamson *et al.*, 1981). This backscattering backward and forward between the front and rear plates can produce a 'crossover' thus resulting in a loss of resolution, although this is not significant when double-emulsion films are used. The rear screen significantly increases the weight of the cassette, so more commonly a low Z rear screen is used which minimises backscatter.

One method of increasing portal film contrast would be to use a high contrast film in the region of its highest gamma. Studies by Reinstein *et al.* (1984) shows the best optical range is from 1.6 to 2.0. Roberts (1995) investigated the commonly available films for their suitability for megavoltage portal imaging. The film speed (represented by film dose which produces unit optical density), gamma and latitude have been determined. The latitude is defined as the film's useful dynamic range, *i.e.* the width, in units of $\log_{10}$(dose), of the straight line portion of the H-D curve. These results are show in Table 3.4.

Table 3.4. The parameters of commercially available film (from Roberts, 1995).

Film	Optimum film dose(cGy)	Gamma (Γ)	Latitude
CEA TVS	40.7	4.4	0.35
CEA TLF	19.1	3.6	0.4
Agfa Ortho STG2	4.7	3.6	0.4
Fuji HRG	6.2	3.1	0.4
Kodak XV	50.1	2.9	0.6
Fuji MIMA	6.3	2.8	0.5
Kodak EG	2.5	2.7	0.4
Agfa HTA	3.5	2.7	0.3
Konica MGH	5.0	2.7	0.4
Agfa RP1	1.5	2.6	0.5
Du Pont Cronex 10s	4.0	2.6	0.5
Kodak XS	2.4	2.5	0.5
Kodak TMATG	2.5	2.5	0.4
Kodak MINR	4.6	2.5	0.4
Kodak ORTHO-G	4.5	2.3	0.4
Kodak MINRH	3.6	2.2	0.5
Agfa MR3	4.2	2.1	0.6
Kodak XL	1.7	2.0	0.5
Kodak TL	3.6	2.0	0.5
DU Pont U.V	1.5	1.9	0.5
Kodak MinR PE205	12.3	1.8	0.4

Robert (1995) concluded:

(a) The CEA films (CEA Medical Imaging Products, UK) are highly recommended for portal imaging since they have the highest Γ.

(b) The CEA TLF films are suitable for localization imaging.

(c) The CEA TVS and Kodak XV films are useful for verification images.

Munro *et al.* (1987a) measured the MTF of metal plate/film and they concluded that scattered photons in the metal plate contribute mainly to the broad low magnitude tails in the LSFs. This causes a drop in the MTF at low spatial frequencies. The MTFs were found to give good spatial resolution, greater than a diagnostic MTF at high spatial frequencies. Therefore the lack of resolution in megavoltage imaging is not due to the film/plate system but to other factors.

3.3.8. Dosimetric Properties of Film

Recently film has become a practical tool for the measurement of dose distributions. Film as a dosimeter has the following advantages:

(1) an enormous reduction in measuring time due to the simultaneous measurements for all points of the film;

(2) a very high spatial resolution;

(3) the possibility of simultaneous dose measurements in full planes in heterogeneous solid phantoms compared with TLDs, ion chambers and diodes;

(4) repetitive readout. It provides a permanent record of dosimetric measurements;

(5) film may be customized in various sizes and shapes to fit any dosimetric applications(suitable for curved and cylindrical surfaces);

(6) In the case of relative dose measurements, the optical density is proportional to the dose without any correction since the collision stopping power ratio of emulsion to water varies slowly with electron energy;

However, they have disadvantages:

(1) Photon energy dependence. The relatively high sensitivity at low photon energies (especially near the silver K-edge, 25 kV) complicates the evaluation of photon beams having significant low energy contribution to the spectrum (Mayer, 1997). The x-ray beam energy distribution can shift toward high energies as the beam traverses the

irradiated medium, the relative number of low energy scattered photons increases with both the depth and field size for megavoltage beams. It is thought the film sensitivity varies with both parameters (Burch, 1997, Williamson, 1981);

(2) film plane orientation. Different film orientations give different results;

(3) processing conditions, the temperature and the chemistry changes;

(4) inter- and intra film density variation. There are two types of variations: those in the emulsion coating due to differences in thickness of coating material and also those due to manufacturing variations from one batch of emulation to another as well as within a single film;

(5) sensitometric non-linearity and inhomogeneity due to trapped air pockets inside the film. Non-reproducible or at least questionable reproducibility;

(6) the time dependence of readout (for radiochromic film), the readout value is tending to be stable after few hours to a few days, 15% increase in OD was observed after four hours (Zhu, 1997);

3.3.9. Comparison of EPIDs with portal films

Extensive studies have been made to compare the image quality of the EPIDs with portal films (Hammond *et al.*, 1997, Kruse *et al.*, 2000, Gagel *ea al.*, 2000).

Hammond *et al.* (1997) compared the image quality from EPIDs and films using objective measurements, which measured the spatial resolution and object contrast for a Las Vegas phantom, and subjective evaluation, which were subjective response of a group to field accuracy and set up errors of portal images. Their objective measurement results showed that film has the potential for better image quality, i.e. has better resolution and object contrast. Their subjective study showed that EPIDs provided the same or better visual image quality as films.

Kruse *et al.* used a three-phase study to compare the EPIDs and portal films. They first measured the clarity of anatomical landmarks in both EPID and film images, then examined oncologists' level of confidence in reviewing the same EPID and portal film, and finally the oncologists' ability to detect and report quantitative setup errors was measured with both film and EPID portals. Their results show that (a) for image quality measurements, the lateral pelvis is the only site for which each landmark is consistently less visible in the EPID images, (b) for confidence-of-view measurements, the users were less confident in their EPID views by an average of 0.5 points on a scale of 1 to 5, (c) for accuracy of measurements, the physician can detect rotational errors and smaller translational shifts using EPIDs. Gagel *et al* also compared the Siemens Beamview EPID and portal film images of three different tumour entities, lung, prostate, and rectum. Their results show the electronic portal image was rated significantly more "visible" than portal film images.

3.4. EPID Image processing and analysis

3.4.1. Introduction

In this section instead of discussing the theory of image processing, we shall study how use of the EPID image processing can result in improved clinical usefulness. Typically, image processing involves manipulating digital images to reduce noise and distortions and to emphasise certain aspects of the image; and facilitating interactive or automated analysis of images. A price is paid for nearly all preprocessing techniques. Noise reduction methods, for instance, are often paid for with a loss in sharpness, whereas sharpness-enhancing techniques are often paid for with an increase of noise. It is considered best to maximise images quality at the beginning of the imaging chain: at the acquisition stage. Regular quality assurance and system calibration should therefore be an essential aspect of the clinical use of an EPID.

Even when the system is optimally tuned and maintained, physical processes put a lower boundary on the quality of portal images as described above. To make portal images clinically more useful, many methods have been proposed and implemented in the past ten to fifteen years to emphasise the structures that are clinically relevant, and to reduce the prominence of other structures. Some of the early methods were based on modelling of the physical image degradation and correcting for it (Meertens *et al.,* 1988). Other techniques are based on calculation of optimal contrast settings, using radiation field edge detection (Bijhold *et al.,* 1991), the enhancement of high spatial frequencies by unsharp masking and band-pass filtering (van Herk *et al.*, 1993). Also adaptive histogram equalisation and more recently statistical and fuzzy enhancement techniques (Krell *et al.*, 1998, Hilt *et al.*, 1999) have been used.

Most techniques mentioned above are aimed at visual enhancement of portal images, rather than enhancement for the purpose of automated analysis. Effective visual enhancement for display purposes is required to catch quickly gross set up errors such as missing or improperly installed blocks, errors in the multi-leaf-collimator (MLC) system, and gross patient displacements. Unfortunately, the tumor is hardly ever visible in portal images, which makes it difficult to assess proper placement of the radiation field. Consequently, in the design of portal image processing methods, the focus is shifted to other structures having approximately known locations with respect to the tumor, e.g. surrounding bony structures. One cannot easily design an effective image processing method without a clear prior understanding of the image structure that one wishes to enhance. The radiation field edge, for instance, requires application of a flank detector, whereas the contours of bony structures often require application of a ridge detector (more details about the detectors can be found in Gilhuijs *et* al., 1995), because of the transmission through the hollow morphological structure of bones. Especially now that EPID technology is advancing towards the physical limitations, it is likely that optimal image processing methods become more strongly dependent on site, dose rate, and beam energy.

Analysis of portal images involves geometrical comparison of corresponding features in portal images and in reference images. These features include beam shaping elements (such as blocks or MLC leafs) and projections of bony structures or seed implants. The reference image is either another portal image selected from one of the earlier treatment sessions, a simulator image obtained during simulation of the treatment, or a Digitally Reconstructed Radiograph (DRR) calculated from the (planning) CT data.

3.4.2. Verification of patient setup

Inaccuracies in any steps, tolerances in mechanical and optical components, anatomical and physiological changes in the patient, movement of internal organs, insufficient immobilisation, and human error can lead to a discrepancy between the prescribed volumetric dose distribution and the dose distribution that is actually delivered over a *al.*, 1997, Gilhuijs *et al.*, 1996, Bansal *et al.*, 1999). Identifying and registering these features is discussed in section 3.4.4. Examples of point features are projections of fiducials from bony anatomy or radio-opaque markers. Examples of curve features are edges or ridges in the projection of bony anatomy or generalised gray value media axes. Template features are usually rectangular regions of pixel values.

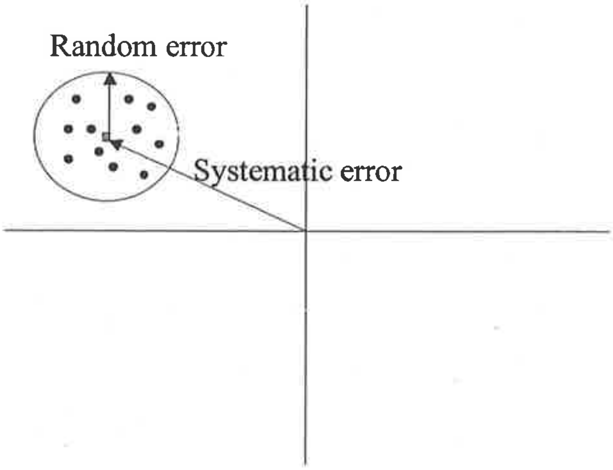

Figure 3.15. Diagram to illustrate systematic and random errors in field placement. The mean position is the systematic error and the random errors are fluctuations about this mean.

The methods mentioned above so far are based on image alignment in two dimensions (2-D). Because the position and orientation of a patient are, however, three-dimensional concepts, the comparison of portal with reference images in 2-D sometimes yields insufficient information to establish a complete correction of the setup in 3-D. For example, rotations of the patient along axes that are not perpendicular to the image plane (out-of-plane rotations) cannot be quantified. Secondly, analysis in 2-D only provides accurate results of patient translations when the errors in rotation are small. For instance, out-of-plane rotations of the pelvis larger than 2 degrees in the treatment of the prostate may cause dosimetrically significant misinterpretation of the position of the isocentre inside the patient (Hanley *et al.*, 1995; Bijhold *et al.*, 1991b; Remeijer *et al.*, 2000). Thirdly, geometrical degeneracy in the alignment of rotation symmetrical objects like the femoral heads may cause ambiguous alignment in 2-D from a single view.

The methods mentioned above so far are based on image alignment in two dimensions (2-D). Because the position and orientation of a patient are, however, three-dimensional concepts, the comparison of portal with reference images in 2-D sometimes yields insufficient information to establish a complete correction of the setup in 3-D. For example, rotations of the patient along axes that are not perpendicular to the image plane (out-of-plane rotations) cannot be quantified. Secondly, analysis in 2-D only provides accurate results of patient translations when the errors in rotation are small. For instance, out-of-plane rotations of the pelvis larger than 2 degrees in the treatment of the prostate may cause dosimetrically significant misinterpretation of the position of the isocentre inside the patient (Hanley *et al.,* 1995; Bijhold *et al.,* 1991b; Remeijer *et al.,* 2000). Thirdly, geometrical degeneracy in the alignment of rotation symmetrical objects like the femoral heads may cause ambiguous alignment in 2-D from a single view.

3.4.3 Verification of radiation field shape

Detection of the radiation field edges is required for two purposes: (a) to verify the shape of the irradiation beam, (b) to establish a coordinate system common to both reference and portal image in which to express deviations in patient setup. Several image processing methods have been reported which extract the edges of the radiation field from portal images, e.g. Bijhold *et al.,* 1991a; Wang and Fallone, 1995; Eilertsen *et al.,* 1994, Petrascu *et al.,* 2000.

With the advance of MLC technology, methods are being developed to accurately detect leaf positions, e.g. Zhou and Verhey, 1994; Eilertsen, 1997. Although MLC systems generally have their own feed-back control systems, there is an increasing interest in independent online verification of proper leaf positioning using portal imaging, e.g. James *et al.,* 2000. Other methods for the verification of beam shaping elements are based on geometrical moments (Bijhold *et al.,* 1992), chamfer matching (Gilhuijs and van Herk, 1993), and elliptic Fourier transform (Gao *et al.,* 1999). Techniques have been developed by several groups (Vigneault *et al.,* 1997, Gilhuijs *et al.,* 1996, Bansal *et al.,* 1999) to quantify the setup of patients in 3-D from one or more multiple views.

The increasing use of small beam intensity modulated fields (e.g. by use of MLC technology) provides an interesting challenge for the verification of patient setup from portal images. The modulation process produces portal images with limited or distorted views of the projected patient anatomy. Other challenges will be portal imaging feed-back mechanisms for gated radiation therapy in order to cope effectively with organ motion during the treatment. The largest challenge, however, is to narrow the existing gap between image processing research and the daily clinical routine.

3.4.4. Image registration

If we want to determine the set-up error we must face the task of registering the simulator and portal images. One problem is to find a common frame of reference for both images. The comparison of the portal images and reference images is generally based on alignment of corresponding image features.

The accuracy of the point-based methods depends on the ability to identify corresponding fiducial landmarks, either between portal and reference image (2-D), or between images obtained in different beam directions (3-D). In the latter case, the methods are mostly based on an analytical solution of the 3-D co-ordinates of the points from multiple projections (Eilertsen, 1997).

Curve features may be extracted from the images by the use of sophisticated image processing filters, or be defined using a drawing tool. Curve features are expected to be less sensitive to random errors in the localization. The boundary of the radiation field is an important curve feature, and software tools have been developed by several groups to extract this feature for automated verification of the shape of the radiation field. Sometimes the field edge is also used as a geometrical reference when the position of the EPID is unknown and variable. In 2-D, the most common alignment technique is to first transfer the reference image curves to the portal image, and subsequently, manually or automatically, correctly position these curves on top of the corresponding portal image feature. In 3-D, several techniques have been reported to align curve features from projection images with CT data, requiring limited or no user interaction (Remeijer *et al.*, 2000, Eilertsen, 2000).

The template features are regions of pixel values that may be defined by a given boundary condition or pixel classification scheme. Template features provide more information for image alignment than point or curve features and may consequently be applicable to a larger range of treatment sites in the future. Typically, regions of interest (ROI) are interactively indicated in the reference image. ROIs may also be defined automatically using a combination of image processing techniques to enhance and extract pixel domains that represent a specific morphology or statistical property. The corresponding regions are automatically recovered in the portal image. Most methods reported for the alignment of templates are based on maximization of the cross-correlation function between one or more templates in the reference and portal image. Maximum correlation corresponds, however, only to the preferred match when the template and the search image have comparable contrast, e.g. when two portal images are used.

Table 3.5. EPIDs manufacturers' basic image registration methods (from Eilertsen, 2000).

Manufacturers	EPID/Sytem	Registration feature	Registration method
Calbon	Therview/Target	Curves	Manual alignment
Elekta	Iview	Points	Measure distance using ruler
Masthead Imaging	PIPSpro	Points or curves	Visual inspection
Siemens	Beamview	Points	Chamfer matching, moments, manual alignment
Varian	PortalVision	Curves	Chamfer matching, manual alignment

To increase analysis speed and provide an user friendly environment, many of the developed techniques have been integrated into comprehensive image processing and registration systems. Some systems provide the means to fully automate the set-up verification procedures, as well as offer facilities for combining analysis results of multiple treatment fractions and fields. At present, there is a great diversity among the techniques and level of sophistication implemented in the commercially available systems (see Table 3.5).

3.5. Clinical uses

3.5.1. Geometrical verification and setup error correction

Patient treatment verification plays a vital role in the management of patients receiving radiation treatment. Portal radiography is the conventional method of verifying the accuracy of megavoltage radiation treatments. Three types of portal radiography can be used:

Localization radiographs: are required with a brief exposure of a few monitor units, examined before the remaining of treatment is delivered. These permit the identification and correction of gross field position errors.

Verification radiographs: are exposed over the entire treatment and are less sensitive, errors can only be corrected on the following treatment. Image quality may be reduced if there is a significant patient movement.

Double exposure radiographs: in which a short exposure of a large unblocked field is followed by a second exposure to the actual treatment field. This has the advantage of showing anatomical features outside the field boundaries, which are often very useful in identifying patient positioning, but frequent use is limited by the radiation tolerance of exposed normal tissues.

Electronic portal imaging devices (EPIDs) can acquire images in a similar manner, including localization images, verification images, and double exposure images. Therefore the geometry of the treatment can be assessed (see S.3.4) and the correction strategies can be designed. There are generally two basically different approaches, i.e. *on-line* (intra-fractional) correction and *off-line* (inter-fractional) correction.

3.5.1.1. On-line corrections

These strategies involve the acquisition of portal images after giving at first a small portion of the dose. The initial portal image is analysed and compared with the reference image to identify any displacements. This method aims to remove both random and systematic components of the field placement errors. Ezz *et al.* (1992) examined this approach and found that patient positioning was improved. However visual inspection was used to determine the positioning of the patient. De Neve *et al.* (1993) similarly visually compared a portal image acquired at the start of the treatment with a reference image, and corrected the patient position by remote movement of the couch from outside the room. They found that adjustments were performed on 55% of fields and that treatment times were increased on average by 46%.

Luchka and Shalev (1996) reported the treatment of an obese patient with megavoltage simulation and intra-treatment corrections. With the interventions, only 2% of the displacements were more than 10 mm compared to ~10% without interventions. As random variation is generally small for the population of patients, and intra-treatment corrections expensive in time, obese patients or patients with poor reproducibility of positioning may become the focus of this correction implementation.

On-line corrections impose considerable clinical workload. It is only justifiable when high setup accuracy is required and when large random deviations are present which cannot be reduced in any other way.

3.5.1.2. Off-line corrections

With *off-line* (inter-fractional) corrections, portal images are evaluated after each treatment session. In this way an EPID is basically a film replacement. Typically, during the first few treatment sessions portal images are acquired and the result is evaluated. The systematic error is estimated by calculating the average of resulting deviations of these first few sessions. However, the random displacements are not corrected.

Due to the presence of day-to-day motion of the patient, the measurement made of patient position only yields an estimate of the true mean position of the patient over the entire course. Elementary sampling statistics apply to this situation. After a number of measurements n, the mean value of field placement $\bar{d}_n$ is found and this is a sample mean from a population of treatment placements for the patient. The true mean Δ can only be determined with total confidence by measuring of the patient's position at every fraction. If many samples of size n were taken, the distribution of sample means ($\bar{d}_n$) found would itself have mean Δ (the mean position or systematic error) and standard deviation $\sigma_p/\sqrt{n}$ (standard error of the mean; SE) where σ_p is the standard deviation of the displacements for all the fractions. A finite population correction should also be included, as the number of fractions is generally small.

If only n measurements have been made for the patient then σ_p is unknown. If random motion for all patients is the same ($\sigma_p = \sigma$) then the σ measured from a population of patients can be used. This then enables a 95% confidence interval for the true mean position of the patient to be found from the sampled mean position as

$$\bar{d}_n \pm 1.96\sigma/\sqrt{n}. \tag{3.29}$$

The finite population correction should also be included, giving

$$\bar{d}_n \pm 1.96\sigma/\sqrt{n} \cdot \sqrt{1-n/N}, \tag{3.30}$$

where N is the total number of fractions. This confidence interval will include the patient's true mean position Δ on 95% of occasions. It decreases in size as the number of measurements n increases. If the random movement is not the same for all patients then the standard deviation of the sample of n measurements S is used as an estimate of σ_p. The confidence interval for the true mean position is then larger (due to the greater uncertainty in σ_p) and constructed from the t-distribution

$$\bar{d}_n \pm t_{n-1}(0.025)S/\sqrt{n}\cdot\sqrt{1-n/N} \tag{3.31}$$

From the measured patient positions a 95% confidence interval for the true mean position is produced. If this confidence interval does not include the (0,0) or reference position then a systematic error is present (at the 95% confidence region) and the patient position should be corrected.

An essential in the off-line procedure is the choice of the action level. A too tight action level might result in unnecessary corrections, while a too wide action level might not yield the desired setup accuracy. The choice of the action level is closely related to the magnitude of random deviations. Therefore the procedure can only be applied effectively if some *a priori* estimate of the distributions of setup deviations is made. It is also a prerequisite that random deviations are roughly equal for all patients.

The "Shrinking Action Level" (SAL) method (Bijhold *et al.*, 1992, Bel *et al.*, 1993, 1996) has been widely adopted. The approach of Bel *et al.*(1993) is to make a decision as fast as possible, and as few decisions as possible. They use the ratio of $\alpha/\sqrt{n}$ (α is directly proportional to the standard deviation: $\alpha = f\,\sigma$, where f is the proportionality constant) as the confidence limit or action level for identifying a systematic error. For n = 1,2,... N_{max} the maximum value of $\bar{d}_n$ (the estimate of systematic error) that will be measured is $\alpha/\sqrt{N_{max}}$. Bel at al (1993) found $f = 2$ and $N_{max} = 2$ gave good results. This is approximately a 95% confidence interval, and only two measurements are performed if the first measurement or the average of the first and second are within the confidence interval. The size of the confidence interval for the systematic error is reset if a correction is made, i.e. $n = 1$ after a correction. When random errors are greater than or equal to the systematic error unnecessary corrections will be made, i.e the random error will be corrected. The parameter (α, N_{max}) can be used to balance workload with accuracy. More recently de Boer *et al.* (2000) proposed an alternative to SAL, i.e. a "No Action Level", method which has only one parameter, N_m. The systematic error is estimated by simply averaging the first N_m measurements. This error is subsequently corrected for the next fraction.

Compared to an on-line procedure, an off-line procedure requires much less clinical workload. It is clear that the off-line procedure is most effective when the random deviations are small due to, for instance, good patient immobilization. Obviously, correction (if it is needed) only can be effective from the next fraction.

3.5.2. Dosimetric application

The dosimetric application of EPIDs requires the pixel values in the images to be a quantitative function of the dose delivered to the EPID. The dose response of the EPID must be known and the system used should be sufficiently stable to allow reproducible, quantitative measurements. Their use for dosimetric purposes has been investigated in the last few years. These dosimetric applications fall into two main categories: measurements of transmitted dose (i.e. two-dimensional dose maps) (Leong 1986, Yin *et al* 1994, Heijimen *et al* 1995, Kirby and Williams 1995, Beollaard *et al* 1996, McNutt *et al* 1996) and the design of compensators to achieve the desired dose (Yin *et al* 1994, Roback and Gerbi 1995).

3.5.2.1. Transit dosimetry

The pixel values of an EPID system can be calibrated against dose in a number of ways including (a) calculation of the dose in air on the detector surface (Yin *et al.* 1994), (b) ion chamber measurements in water at the depth of maximum (Zhu *et al.* 1995), and (c) ion chamber measurements in air at the dose maximum within a cylindrical mini-phantom (Essers *et al.* 1995, Boellaard *et al.* 1996).

For the liquid-filled ionization chamber systems the ionization current and the dose rate can be described by a combination of a linear and a quadratic term. These methods will now be discussed in detail.

Yin *et al.* (1994) investigated a liquid filled ionization chamber system. They found that the pixel values are not a linear function of the incident radiation intensity. The response of the imaging device to the incident energy is comparable for different photon energies. The difference can be explained by the build up thickness which varies different for different energies applied. The long-term stability is fairly constant, the relative standard deviation is less than 1.3% for all the measurement points. The characteristic curves for different gantry angles are almost identical. The curves tend to increase with the field size, because of the increased scatter radiation from the collimators and components of the imager.

Zhu *et al.* (1995) also found that pixel value versus absolute dose has a non-linear response and the sensitivity of the EPID is field-size independent. A two-month period stability measurement shows less than 1.0% relative standard deviation.

Essers *et al.* (1995) investigated the accuracy of the EPID transmission dose rate, comparing the measurement with an ion chamber in a mini-phantom and ion chamber under d_{max} within a solid water plate. They found the ratio of dose rate to EPID and to an ion chamber under 1.6 mm depth of 2.5 cm thick phantom plate is equal unit within 0.3%. The ratio of dose rate of EPID to an ion chamber within the mini-phantom decreases with field size. Because the ratio of EPID/Ion chamber with Perspex plate is almost equal to one, it is likely that the field size dependence is mainly due to by the scatter in the detector. They demonstrated additional build up layers are necessary for dosimetry purposes.

The influence of phantom scatter on EPID signals was determined by comparing EPID transmission and mini-phantom transmission dose rate for various phantom situations. They found at some distance, most of the photon scatter will not be detected by a transmission detector. At 55 cm or more, a very small fraction of the secondary photons is present and the transmission dose rate is an almost constant 67% of the exit dose. The ratio of transmission to exit dose rate initially decreases rapidly with increasing field size; increasing phantom thickness and increasing phantom detector distance and remains at a constant value with further increase in field size phantom thickness, and detector distance.

Boellaard *et al.* (1996) demonstrated the EPID dose response can be fitted with equation (3.20) to within 1% (measurement with the additional build up layer). They determined the build up thickness by getting the maximum EPID pixel readings for two applied energies, 8 MV and 25 MV. The line spread functions were measured to investigate the effects of the additional build up layer on the image quality. It showed no significant difference from without additional build up layers. The results from two methods, i.e. change the dose rate and add different thickness of phantom, fitted with equation (3.18) within 1%. This means that the influence of the beam hardening on the response of the EPID with an additional build-up layer is negligible.

For video-based systems, the EPID signal is generally a linear function of the delivered dose. Leong (1986) investigated the video-based EPID system' dosimetric performance.

He found a linear response within 100cGy/min - 500cGy/min. Also the response to the wedged fields was similar to the film response.

Heijimen et al. (1995) investigated a video-based EPID response as a function of applied monitor units, absorbed thickness and field size. They found the pixel value/portal dose is constant, observed deviations was 0.5% and was field size dependent. They also demonstrated a day-to-day variation in EPID response (within 38 days) was within 0.4% (1 SD).

Kirby and Williams (1995) used a Philips SRI-100 system to investigate the exit dose response. A linear response to monitor units at different depth and detector to exit surface distances was found. The response was detector to exit-distance dependent and also field size dependent.

The optical chain scatter causes a great problem in dosimetry application for video-based EPIDs, and a deconvolution with an empirically derived optical kernel has been proposed.

In all cases mentioned above, an accuracy of a few percent is achievable. In the side of patient dosimetry, however, the calibration against dose at a fixed location relative to the patient might be a shortcoming. In general, the behavior of dose deposition as a function of energy of the incident photons in the portal imaging device and in the calibration device leads to different dose responses. In this situation it is difficult to quantify accuracy of portal dose measurements. It is therefore important to study the dosimetric properties of the imaging detector and the calibration devices. Keller *et al.* (1998) investigated the dose deposited in the portal imaging detector and in the calibration device, i.e. in a water phantom using Monte Carlo simulation. They found that at the depth of maximum dose, there is a large absolute difference between water and detector doses above an incident energy of 4 MV but only a small difference in the most frequent energy range of the beam spectra. For a 6 MV beam, a 3.8% absolute dose difference between detector and water has been found at 1.5 cm water depth. They conclude that the dose response of a portal imaging detector differs from that in a homogeneous water phantom as a function of incident photon energy. In addition the dose response is in general dependent on the location in the portal plane due to the changing beam quality across x-ray beams of a linear accelerator. Therefore, the calibration of the EPID to a water dose at one point leads to a distinct dose at other points in the beam area.

3.5.2.2. Compensator design and quality assurance

The EPID can be calibrated to yield the relationship between image intensity and the radiological thickness. This information is used in conjunction with a model of the patient anatomy to design a compensator. After production of a compensator, an EPID can be used to verify the actual thickness or the dose distribution realised.

Yin *et al.* (1994b) investigated the problem of using a liquid filled ion chamber array EPID to automate the design of compensators for lung inhomogeneity correction. The compensator thickness was determined in order to provide a uniform gray-level distribution in the region of the portal image to be compensated. The phantom study for the lung inhomogeneity indicated that the EPID is potentially useful for compensator design in certain treatment situations. Roback and Gerbi (1995) also demonstrated that missing tissue compensators could be designed and verified using an EPID.

3.6. Application of EPID in linac quality assurance

Kirby and Williams (1995) used a video-based EPID to investigate the capability of determining 6 MV photon beam field flatness. Field flatness was also determined by an in-air scanner in a 1.5 cm deep tissue equivalent phantom block. The EPID readings were averaged within a region of interest of 1 cm × 1 cm along the Gun-target direction in order to compare with the readings from in-air scanner which scan interval is 1 cm. A point by point comparison between the in-air scanner readings and the EPID system readings produced a series of correction factors. The corrected EPID was then used to measure an unflattened field produced by using the secondary steering current circuits of the linac. The results were compared with those obtained from the in-air scanner under the same abnormal steering conditions. Their results shows the EPID system can detect flatness changes of 2% and the overall within 1.5% of that measured from an in-air scanner.

Kirby (1995) designed a phantom to check the coincidence of the light and radiation fields along with check of the field size measuring capabilities of an EPID. The phantom consists a double layer of lead solder wire inlaid into a depth of 2 mm Perspex plate. The lead wires (1 mm diameter) are arranged to produce a square pattern of 40 mm spacing and the distances were marked on the surface for light field alignment. Then the radiation field sizes can be checked against the light field sizes.

Luchka *et al.* (1996) reported a semiautomatic test which provides an objective and quantitative measure of any misalignment between the light and radiation fields. A specially designed phantom with four 1/16" diameter tungsten angled pins allowing beam divergence being imaged with an EPID to test the light and radiation fields coincidence. PC based programs have been used to locate the positions of the pin which represent the light filed. The phantom image was analysed to determine the radiation field 50% dose contour and then compared with the pin positions. The displacement was calculated and displayed on the PC screen and final decision "Go" or "No Go " were made.

Curtin-Savard and Podgorsak (1997) showed the possibility of using an EPID (a) to verify the centre of the MLC field coincidence with its axis of rotation, (b) to measure MLC transmission, (c) to measure the width of the penumbra, (d) to verify the compensator.

Ma *et al* (1997, 1998) used a Wellhofer Beam Imaging System to verify applicability for measurement of the light and radiation field coincidence, electron energy constancy, x-ray beam flatness and symmetry, and collimator and couch rotation axes. The suitability for the flatness and symmetry evaluation was tested by measuring the systematic flatness and symmetry variations from 3% to 30%, produced by custom-made aluminium wedges. Comparison measurements were made against a radiation beam analyser device (RBA-5, Gammex RMI) and it was concluded that BIS 710 was more sensitive to the flatness and symmetry variations. However, the authors, only analysed the crossplane and inplane directions, which is similar to conventional techniques.

3.7. Summary

Electronic portal imaging techniques have been well developed in the last few years. This chapter reviewed the current available EPIDs and addressed the major properties of each type of EPIDs. Furthermore this chapter, (1) compared the image quality of EPIDs with radiotherapy films, (2) summarized the recommended EPID quality assurance procedures, (3) discussed the EPID image processing techniques and clinical applications such as patient setup verification and dosimetric applications. In the following chapters new techniques for routine QA with an EPID, as developed in this program of study, will be described.

Chapter 4

Characteristics of an Electronic Portal Imaging Device

4.1. Introduction

On-line portal imaging systems have been developed to acquire digital images during radiotherapy treatments. Most on-line portal imaging studies have concentrated on verification of the setup geometry, such as the radiation beam size, shape and location relative to anatomical structures (van Herk *et al* 1988, Bijhold *et al* 1991b, Bel *et al* 1996, Meertens *et al* 1990 and Michalski *et al* 1993). Also, their use for dosimetric purposes has been investigated in the last few years. These dosimetric applications fall into two main categories: the measurement of transmitted dose (i.e. two-dimensional dose maps) (Kirby *et al* 1995, Beollaard *et al* 1996, McNutt *et al* 1996) and the design of compensators to achieve the desired dose (Yin *et al* 1994, Roback and Gerbi 1995).

On-line imaging systems can also be used effectively to measure some beam parameters required for treatment planning and equipment quality control (Curtin-Savard *et al* 1997). Most published studies on quality control have sought to verify the isocentre position, interleaf transmission of the MLC, and dose distribution profiles.

As mentioned in previous chapters, only a limited number of papers have been published applying EPIDs to medical linear accelerator quality assurance (Kirby and Williams 1993, Luchka *et al* 1996, Ma *et al* 1997,1998).

In the current work, the application of EPID systems to periodic checks of flatness and symmetry of radiation beam, linac mechanical alignment, light and radiation filed coincidence have been investigated. In the first step, the EPID's performance has been studied; with measured characteristics of the BIS 710 system being discussed in the following sections. In the second step, new procedures for routine QA checks have been developed that will be discussed in the following chapters.

The characteristics of the BIS 710 system discussed in the following sections have been analysed for the region of interest (ROI) of 10 × 10 pixel^2 unless specified otherwise.

4.2. The characteristics of an EPID

4.2.1. The beam imaging system - BIS 710

The Wellhofer Dosimetrie BIS 710 (see user's guide, 1998) is a video-based electronic portal imaging device or EPID. It consists of a gadolinium (Gd_2O_2S) fluorescent phosphor screen preceded by a 1.0 mm copper layer, a CCD camera, 45° mirror, and a frame grabber with a 10 bit depth image. The camera has an effective 500 × 500 pixel array which can view an area on the phosphor of 30× 30 cm^2. The optical assembly and the camera are covered with a curved foil at the beam entry direction to protect the image device from dirt.

The signal standard of the CCD camera is CCIR, i.e. 50 frames/second. The system software provides an adjustable sampling time and sampling number. The sampling time is the integration time of the CCD matrix e.g. a sampling time of 960 ms will integrate 48 video frames, pre-ADC (Analog to Digital Converter) to form one image. The sampling number is the number of averaged or integrated digitised images post-ADC. A typical setup with 960 ms sampling time and a sampling number of 16 will average 16 images with each image consisting of over 48 summed video frames pre-ADC (see Figure 4.1). As summing function was included in the system software, the final BIS image can also be produced by integration (rather than averaging) of the sampling number of images. The user can select either the averaging or integrating mode of BIS 710 as required. The range of values that can be used for sampling time will be discussed in section 4.2.8. and there is no limit for the sampling number.

4.2.2. The sensitivity correction for BIS 710 output images

The pixel elements in the BIS 710 output image need to be processed with a correction image (provided by the manufacturer) and a dark (background) image. When taking scintillation images, the following system-relevant parameters need to be considered: (a) decreasing light intensity between the centre and edges of the optical system, (b) inhomogeneity of the scintillator (c) sensitivity differences of the CCD matrix, and (d) the dark current of the CCD camera. The manufacturer provides an individual correction image for each BIS 710 system. This image was measured using a well-designed uniform X-ray beam geometry to account for the differences of individual pixel sensitivity of the scintillator screen (*Wellhofer Dosimetrie, 1998*). A background image was measured with the same parameter settings as for the measured radiation image and was acquired just before the measured radiation image. The calibration formula for a measured image is:

$$P(i,j) = [P_0(i,j) - P_b(i,j)] \times P_c(i,j)/4096, \qquad (4.1)$$

where $P(i,j)$ is the corrected image, $P_0(i,j)$ is the measured image, and $P_b(i,j)$ is the dark image, $P_c(i,j)$ is the correction image. This correction method is different from the commonly used method shown in equation (4.2).

$$P(i,j) = [P_0(i,j) - P_b(i,j)]/P_c(i,j). \qquad (4.2)$$

Equation (4.1) provides a fixed scaling and normalise the pixel output values of the corrected radiation images. Therefore it makes different measurement radiation images comparable to each other (*Wellhofer Dosimetrie, 1998*).

4.2.3. Reproducibility of the BIS 710

Reproducibility is an important characteristic for dose measurement equipment. The reproducibility of the BIS 710 was measured by acquiring ten consecutive flood radiation images with the same settings, i.e. sampling time was 960 ms and sampling number was 16. The reproducibility is determined as a coefficient of variation using the formula (IEC, 1989a):

$$s = \frac{100}{\bar{R}}\sqrt{\sum_{i=1}^{n}\frac{(\bar{R}-R_i)^2}{n-1}}, \tag{4.3}$$

where R_i is the average output pixel value measured from the BIS 710 image within a ROI. The ROI was also being used to obtain the average pixel values from the same geometric location. $\bar{R}$ is the average of R_i from the acquired ten consecutive flood radiation images and n is the number of image acquisitions. A reproducibility of ±0.5% of the pixel output values of ROI has been determined from our measurement using equation (4.3). Different parameter settings will cause slightly different reproducibility values. The above measurements result was obtained for pixel output values of 800 ~ 900 which was recommended by the manufacturer.

4.2.4. Pixel size and spatial linearity measurements

Pixel size needs to be calculated for verifying the radiation field size as well as for defining the flatness and symmetry area within the radiation fields. The pixel size (at the isocentric plane) can be obtained by comparing the physical field size (which is given by the digital scales) and the measured field size in pixel numbers. The spatial linearity, which can also identify any image distortion, is checked by measuring a range of different field sizes. To measure the pixel size in the horizontal or vertical axis of the BIS 710, images were acquired for different field sizes from 2×2 cm^2 to 25×25 cm^2 at 100 cm SSD. The pixel values from the ROI around the beam centre was taken as the 100% energy fluence value. The radiation field edges were defined as 50% of this value. From the field edge positions, radiation field sizes in image pixel numbers were obtained and plotted against their nominal physical field sizes (as given by linac digital scales). The horizontal or vertical direction pixel size could be determined from the slope of the fitted line.

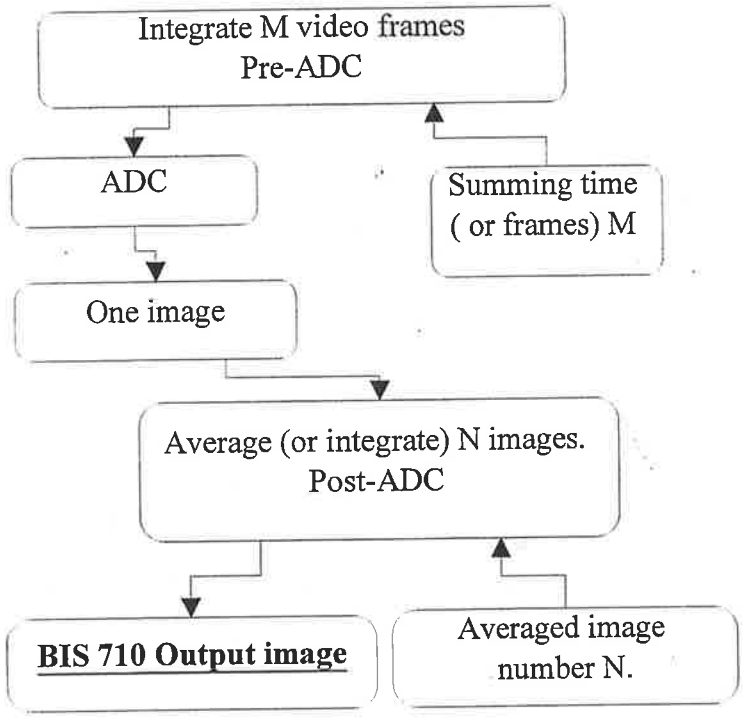

Figure 4.1. The flow chart shows how summing M video frames and averaging (or integrating) N images produces a BIS 710 output image.

The field sizes are calculated from the left or top 50% dose contour to the right or bottom side 50% dose contour of the inplane/crossplane beam profiles. Because of the linear response of pixel value vs dose (see section 4.26), the 50% pixel value contour was used as the 50% dose contour to calculate the field sizes. The number of pixels for different field sizes was determined. The results are plotted in Figure 4.2. The horizontal or vertical pixel size is determined from the slope of the fitted line. From Figure 4.2, the inplane and crossplane pixel size were measured to be 0.598 ± 0.003 mm/pixel and 0.603 ± 0.003 mm/pixel at the isocentre plane, respectively. These results agreed within 0.5% with the manufacturer's value of 0.6 mm/pixel. The fitted straight lines also confirmed that the spatial linearity is very good and there are no detectable image distortions.

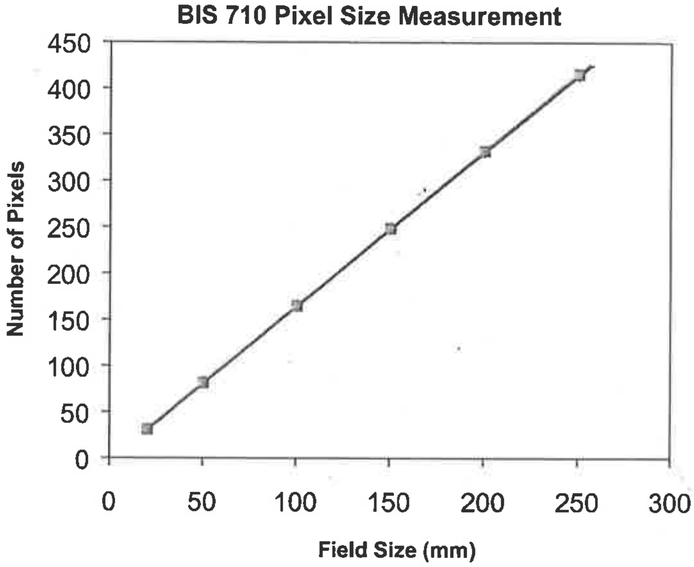

Figure 4.2. The BIS 710 pixel size measurements. ◆ crossplane data, and ● inplane data. The two data sets cannot be distinguished. Field sizes were given by the digital scales.

4.2.5. Noise measurements and set-up parameter optimisation

A dark image provides noise information from the whole system since no radiation signal is present when it is acquired. The dark image is measured with the accelerator switched off and with the typical settings which will produce an pixel output value of 800 ~ 900 with the radiation beam on, in this case a sampling time of 960 ms and an average of 16 images. Evaluation of the pixel value histogram will give a measure of the noise distribution and level for the system.

Inspection of the dark image histogram (shown in Figure 4.3) shows a Gaussian distribution of the total noise with a mean pixel value (PV) of 3.8 and a standard deviation 3.3 pixel values. Unlike some correction procedures, where a fixed DC level is subtracted (which cannot subtract this kind of distribution noise effectively), the image is corrected pixel by pixel (shown in equation 4.1). The measured dark signal (3.8 ± 3.3 PV) is less than 0.5% of the signal (about 828 PV) of a radiation beam image with the same setup parameters.

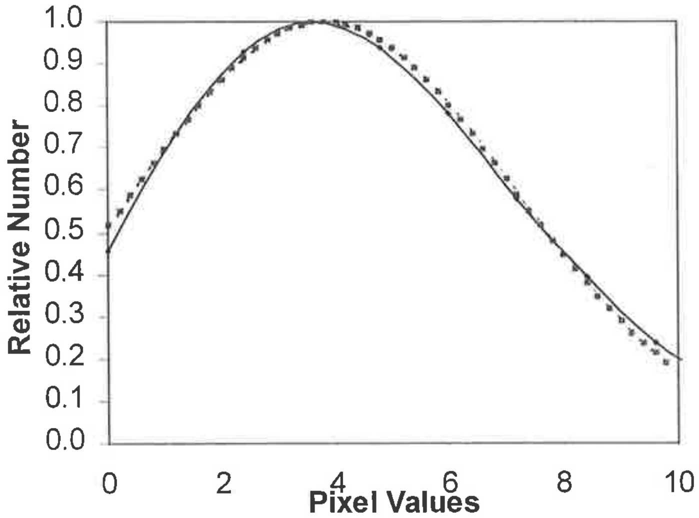

Figure 4.3. The dark image signal analysis result. The solid line shows the measured dark image histogram. The dotted line is the fitted Gaussian distribution.

Analysis of the pixel output values of a series of images with different sampling numbers will provide information about output pixel value dependence on the number of the image samples collected for the same sampling time. A series of flood field images were acquired to investigate the uncertainties in the pixel output value. Images were acquired by varying the sample number, i.e. the images were acquired for different times. The noise in each image was assessed by determining the standard deviation in ROIs of increasing size.

Table 4.1 shows that there is no significant difference in the standard deviation when the sampling number is greater than 25. The standard deviation (SD) does not get smaller with increasing the ROI size. That is because of the non-uniformity of the beam. Consequently, images in this work were acquired with a sampling number of 25 and sampling time 960 ms unless specified otherwise.

4.2.6. Dose and dose rate response curves of the BIS 710

The BIS 710 pixel output value was measured as a function of monitor units, using a 6 MV x-ray beam from a Siemens KD-2 with a build up polymethyl methacrylate (PMMA) phantom provided by the manufacturer. The source to surface distance was 100 cm, and field size used was 10×10 cm^2. The system must be set into the integration mode to allow cumulation of pixel value with dose. However, the BIS 710 digitises to 10 bits depth while the cumulative image is saved at 16 bits depth. Integration of too many images will therefore cause pixel overflow (the value will roll over to 0).

Table 4.1. Variation in pixel values within a ROI of an image for various levels of spatial and temporal averaging.

Sampling Number	Size of the ROI in pixels 10 × 10 (%)	20 × 20 (%)	50 × 50 (%)	100 × 100 (%)
1	0.9	1.0	1.1	1.4
4	0.6	0.7	0.8	1.2
9	0.5	0.6	0.8	1.1
16	0.4	0.5	0.7	1.1
25	0.5	0.4	0.6	1.1
36	0.4	0.4	0.6	1.0

A sampling time of 960 ms was chosen for the measurements; no pixel value overflow was observed for this time selection. Since synchronisation of the radiation beam and the imaging system cannot be achieved, the BIS 710 was switched on before the beam was turned on and finished acquiring after the beam was turned off. All the video frames were added to form a final image. Two dose rates, 200 MU/min and 100 MU/min, were used to test the dose rate dependence. The pixel output values were calculated from the ROI around the beam centre. The pixel values were plotted against the monitor units in Figure 4.4.

Figure 4.4 shows that output values of the BIS 710 depend linearly on monitor units for 6 MV photon energy. This result agrees with the result of Ma *et. al.* 1997. It also shows that the BIS 710 output is slightly dependent on dose rate (maximum 2.5% decrease for a 2 Gy irradiation dose with 200 MU/min compared to 100 MU/min dose rate). The Varian accelerator 21EX installed at Royal Adelaide Hospital produces x-ray beams with 6 dose rates and allows a comprehensive test of the dose rate dependence of the BIS system. Images were acquired with dose rate of 100 MU/min to 600 MU/min and with the same settings for all other parameters. 200 MU were delivered to each image. The pixel values were calculated from a ROI (10 × 10 pixels) around the radiation field centre. The results are shown in Figure 4.5 and it confirms that the BIS system is slightly dose rate dependent with a decrease of 2.5% from 100 MU/min to 600 MU/min.

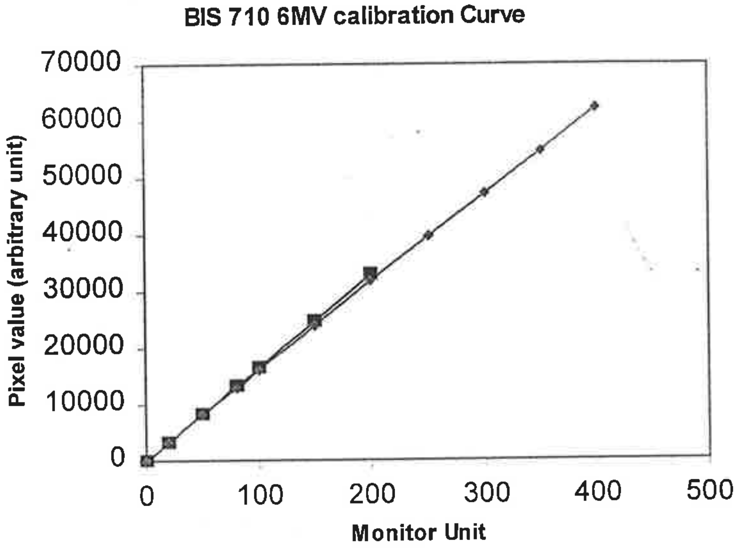

Figure 4.4. Pixel value vs monitor units, for 6 MV photon energies, ■100 MU/min, ◆ 200 MU/min.

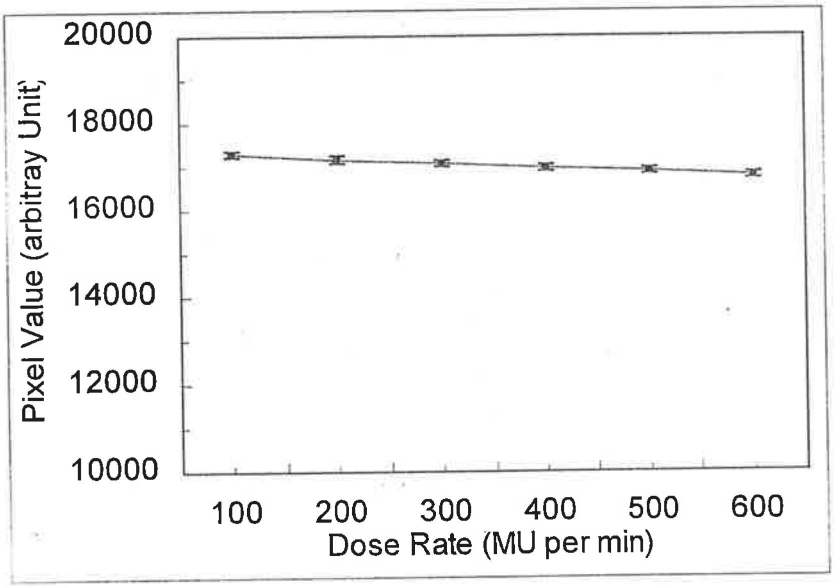

Figure 4.5. Dose rate dependence of measurements taken with BIS 710 and a VARIAN 21EX linac. 200 MU were delivered.

4.2.7. Build-up layer measurements for maximum out put signals

The intrinsic BIS 710 detector (1mm Cu plus scintillation layer) thickness is insufficient to reach electronic equilibrium at the position of Gd_2O_2S layer (middle plane) for megavoltage x-ray beams. If the BIS 710 is used without extra buildup material, its detector is situated in the dose build up region. Therefore, the fluctuation of its output value is more dependent on electrons and low energy scattered photons, produced in the treatment head. Therefore an additional build-up layer is required. The required amount of the build-up material was determined by varying the thickness of material on top of the copper in steps of 2 mm until a maximum pixel reading was obtained. The required amount of additional build-up material was measured for each X-ray energy from a Siemens KD-2 medical linear accelerator (6 and 23 MV), at 100 cm source-to-surface distance and 10 × 10 cm^2 field.

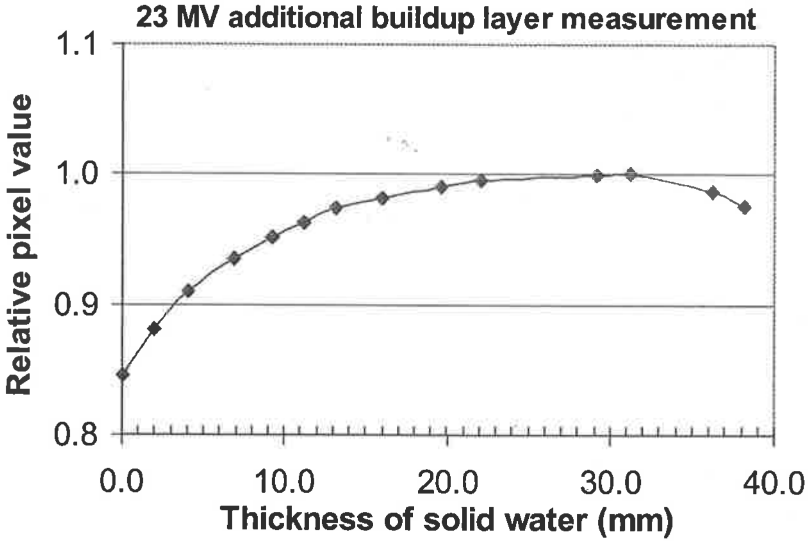

Figure 4.6. BIS 710 additional build-up layer (solid water) measurements. (Note: The error bars for the data plotted in this figure are smaller than the size of the points.)

In Figure 4.6, the relative pixel value readings are shown as a function of additional buildup layer thickness (solid water) for the 23 MV measurements. A maximum pixel value reading is found at a buildup thickness of 32 mm of solid water. For the 6 MV photon beam, a buildup layer thickness of 10 mm solid water is required for dosimetry measurements. The required amount of additional build up layer is close to the expected value for known maximum dose depth for these energies.

4.2.8. The effect of the sampling time on the pixel output value

The BIS 710 system software provides for a variable integration time for the CCD matrix. A different sampling time will result in different pixel output values. A larger sampling time produces a larger pixel output value. In order to take advantage of the dynamic range of the bit depth, a sampling time is selected which produces a pixel output value about 800~900. It is essential for dosimetry purposes that pixel output values are comparable for different settings of the acquisition parameters. In order to investigate the relationship between pixel output values and sampling time, a series of images with different sampling times, from 480 ms to 2400 ms, were acquired. The field size was 10 × 10 cm, the SSD was 100cm and 200 MU was delivered for each image. The pixel values were calculated from the ROI in the centre of the radiation fields. The pixel values were then plotted against the sampling time.

The pixel output values versus the sampling time are shown in Figure 4.7. Below 1.8 s there is a linear relation between the sampling time and pixel output values, and a non-linear response is found for sampling times larger than 1.8 s. The manufacturer claimed that for sampling times larger than 1s there is no linear relation between the pixel output value and sampling time (*BIS 710 User's Manual*). Correspondingly, sampling times shorter than 1.8 s should be selected if the BIS 710 is used for dosimetry purposes. For these times, the relative pixel values can be compared by applying a linear correction factor (which can be derived from Figure 4.7).

4.2.9. Energy response

Since the beam energy spectrum will change after the beam passes through a thickness of phantom before reaching the imaging system and modern linacs produce multiples beam energies, it is necessary to know the energy response of the system. Two X-ray energies, 6 MV and 23 MV, from the Siemens KD-2 linear accelerator and a 4MV x-ray beam from a Varian 4/100 were used to investigate the energy dependence of the system. In order to minimise the noise effect and avoid bit depth saturation, images were acquired for different monitor units varying from 20 to 400 MU to obtain response curves from different incident energies.

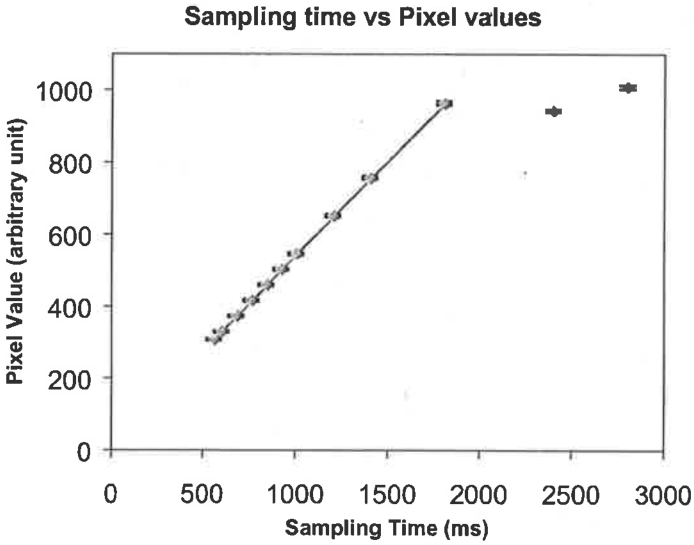

Figure 4.7. The effect of sampling time on pixel values. Below 1.8 s the pixel output values are a linear function of sampling time.

The output characteristic curves were obtained for 4, 6 and 23 MV X-ray energies. A corresponding thickness of additional build-up material, measured as described in the previous section, was applied for each beam energy. The results are plotted in Figure 4.8 below.

Figure 4.8 shows that the BIS 710 response is slightly energy dependent, with about a 13% increase in response at 400 MU from 4 MV to 23 MV photon energies. There are some concerns about the EPID image quality change after the beam passes through the additional build up layer. Boellaard *et. al* (1996) showed that for photon beam energy less than 8 MV there was no significant difference in the image quality between measurements with and without additional build up layers, however for the 25 MV beam there was a small difference. Since the beam energy will change only a small amount after passing through the additional build-up layer, the beam hardening caused by the additional build-up layer is negligible. The BIS 710 output is directly related to the beam energy fluence (Ma *et. al.*, 1998). Consequently, it can be used to measure the absorbed dose.

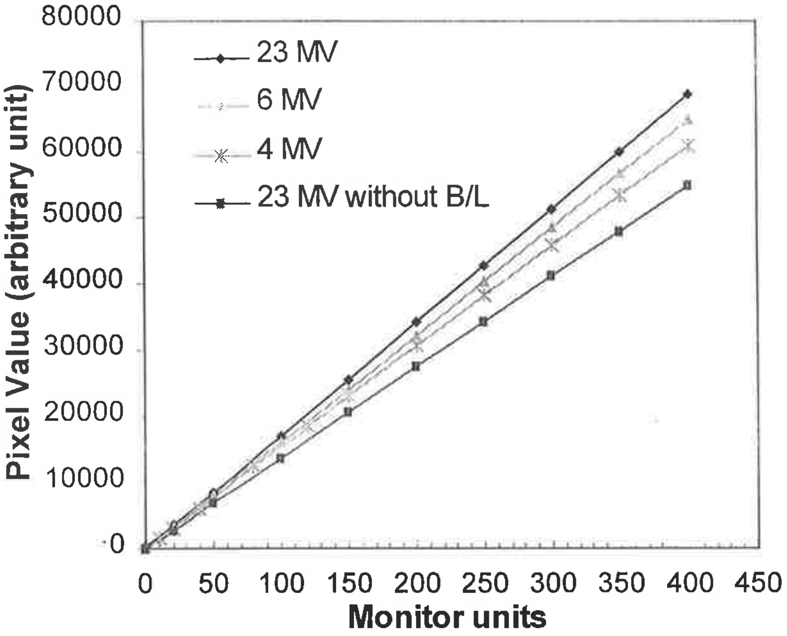

Figure 4.8. BIS 710 energy response with three photon energies from linacs. * 4 MV photon at 200 MU/min, ▲ 6 MV photon at 200 MU/min, ◆ and ■ 23 MV photon at 300 MU/min with and without build up layer.

For comparison, Figure 4.8 also shows the BIS response at 23 MV without additional build-up material. The pixel output values were smaller than for 6 MV energy with additional build-up material. This is because the detector is located in the dose build-up region where a lower dose is deposited.

4.2.10. BIS 710 field size response for a fixed monitor unit

In order to investigate the dependence of the pixel output value of the BIS 710 on the field size (for the same number of radiation monitor units), images were acquired for field sizes from 5 × 5 cm^2 to 25 × 25 cm^2 and delivered with the same numbers of monitor units (say 200 MU). The SSD was 100 cm and dose rate was 200 MU/min . The mean pixel values from a 10 × 10 pixels region in the field centre were calculated and ion chamber readings within solid water phantom were recorded in order to make a comparison. Only 1 cm of solid water was used under the ion chamber to minimize the backscatter to make the measurement comparable with BIS measurement. The results from both measurements were plotted against the field size.

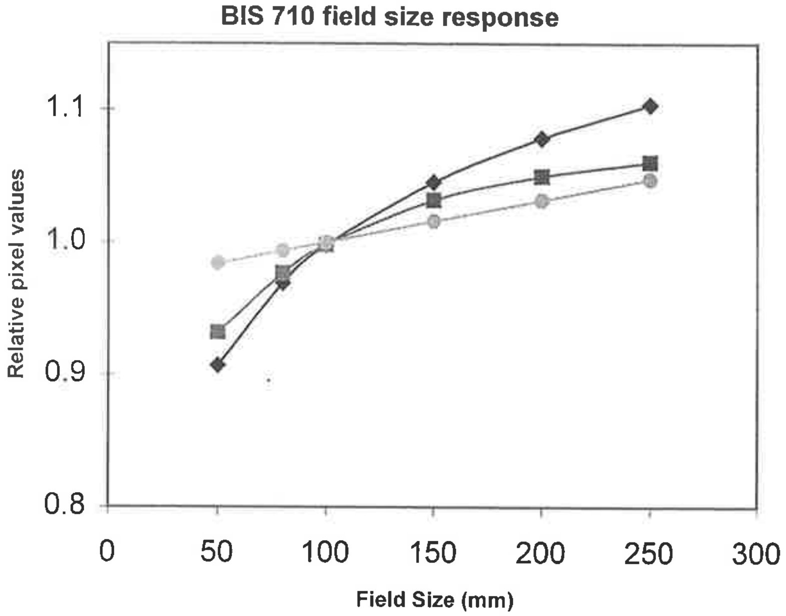

Figure 4.9. The BIS 710 response with field size. ◆ the BIS results. ■ the ion chamber readings within phantom. ● the ratio of the BIS pixel value and the ion chamber dose readings (all results are for 6 MV).

Figure 4.9 shows the relative pixel values for different field sizes varying from 5 × 5 to 25 × 25 cm^2 with the source to detector distance 100 cm at d_{max}. The relative dose measured in solid water using an ion chamber is also presented in Figure 4.9. Both data sets were normalised to a field size 10 × 10 cm^2. The data show that there is a rapid increase in the scatter contribution to pixel value and dose for increasing field size of less than 10 × 10 cm^2. It also shows that at larger field sizes, the pixel values of BIS 710 increase more rapidly with increasing field size than doses measured by an ion chamber in a phantom. This was assumed to be caused in part by scatter within the phosphor layer and the side scatter from the BIS 710 housing walls. To confirm this, further measurements were performed to assess the influence and sources of scattered radiation. The details and results of these are discussed in section 5.2. Therefore, the scatter component contributes more to the measured dose for the BIS 710 than for an ion chamber measured in a phantom. That also means the output of BIS 710 is quite dependent on field size, with a 5.6% increase in response from field of 5 × 5 to 25 × 25 cm^2. More detailed about BIS and scatter radiation can be found in section 5.2 chapter 5.

4.2.11. Comparison of the image quality by using a QC-3 phantom

As the BIS 710 is a relatively new imaging system, it is useful to compare its properties with the previously manufactured EPID systems in order to assess its advantages. A commercially available portal imaging quality control phantom (QC-3) was used to assess the imaging quality of the BIS 710 system and BEAMVIEW^{PLUS} (Siemens Medical Systems, Inc. Oncology Care Systems). The QC-3 phantom was designed by Rajapakshe et al. (1996); it consists of five sets of high-contrast rectangular bars with spatial frequencies of 0.1, 0.2, 0.25, 0.4, and 0.75 lp/mm.

In order to compare the image quality, two consecutive images were acquired (200 MU and 100 cm SSD) for each imaging system and the spatial resolution and contrast to noise ratio (CNR) were calculated for each system. Spatial resolution is defined by f_{50}, which is the frequency for 50% RMFT (relative modulation transfer function). The contrast is measured from the brightest and darkest regions and the noise, σ, is obtained from the two test images. The two images are subtracted and the standard deviation is obtained from the difference, thus avoiding the contributions from fixed pattern noise (Shalev, 1997). The commercial available software portal imaging processing system (PIPS, Masthead Imaging Corporation, Nanaimo, BC, Canada) was used to analysis the images.

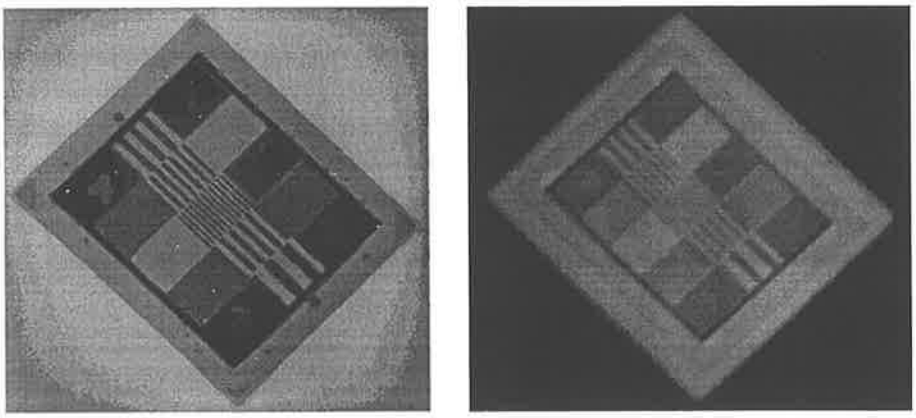

(a) (b)

Figure 4.10. Quality control test phantom images. (a) BIS 710 image, (b) Beamview image (both images were acquired with an additional build-up layer).

The typical BEAMVIEW^{PLUS} spatial resolution is about 0.214 ± 0.027 lp/mm (Shalev, 1997). The results of the quality control test analyzed by PIPS for our BEAMVIEW^{PLUS} system and BIS 710 are shown in Table 4.2. The images of the phantom acquired with the BIS 710 and BEAMVIEW^{PLUS} are shown in Figure 4.10.

Table 4.2 shows that Beamview plus has a higher contrast/noise ratio. However, the BIS 710 has better spatial resolution.

Table 4.2 Comparison of the quality control test phantom results for BEAMVIEW^{PLUS} and BIS 710 system.

	BEAMVIEW^{PLUS}	BIS 710 without Additional Buildup Layer	BIS 710 with Additional Buildup Layer
Contrast/Noise Ratio	145	55	72
Spatial Resolution	0.210 lp/mm	0.357 lp/mm	0.399 lp/mm
Noise Level	0.35	0.63	0.43

When the BIS 710 is used with a build up layer, there are approximately 20% and 10% increases in the contrast/noise ratio and spatial resolution, respectively.

The BIS 710 image quality from two photon energies, 6 and 23 MV, were also compared with each other. The data shows that the system resolution at 6 MV is better than at 23 MV X-ray energies. This has been observed previously (Rajapakshe et al. 1996) and is a result of the larger physical beam penumbra at higher energies and increased transmission through the bar pattern.

4.2.12. Sensitivity measurements

To compensate for the parameters which affect the scintillation images (ref. S4.2.2), a correction image was measured and supplied by the manufacturer. However, the sensitivity of the BIS 710 detector may still vary from pixel to pixel. To measure the sensitivity within the detector, a small radiation field was formed and a series of images were acquired by moving the BIS 710 detector along the cross plane and the inplane directions. All images were corrected with both the correction image and the dark image. A small field, i.e. 2.5 × 2.5 cm^2, was used because it introduces only a small amount of scattered radiation produced in the treatment head as well as scatter from the BIS 710. Therefore, the dose delivered to the detector should be the same and the pixel values will demonstrate the sensitivity at different parts of the detector. The results are presented in figure 4.12. The pixel values were calculated from a ROI of 10 × 10 pixels (0.6 × 0.6 cm) around the beam centre. Uncertainties are based on the standard deviation of the pixels in the ROI. Cross plane means the direction without the camera tube and lens housing (see figure 4.11).

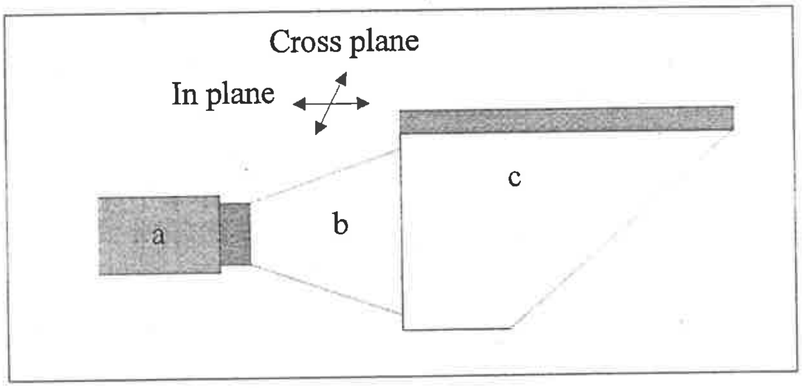

Figure 4.11. Schematic of the image device components: *a)* camera and lens housing, *b)* cone, *c)* scintillator mirror system.

Figure 4.12 shows that the BIS 710 detector sensitivity varies over the area of the detector, with the difference being 2.1% from center to edge part of the detector in the cross plane. However, the difference in the inplane direction is up to 5.2% from the centre to edge parts with the centre part being more sensitive. It means that the correction image provided by the manufacturer is inadequate to provide a uniform response because the measurement conditions are different from when the correction image was measured. This may be explained by the cross-talk effects and because the cover (under the detector screen) is curved. The different responses from the inplane and cross plane may be explained by the curved foil (between scintillator and mirror) preventing some of these cross-talk effects while in plane there is no curve cover foil.

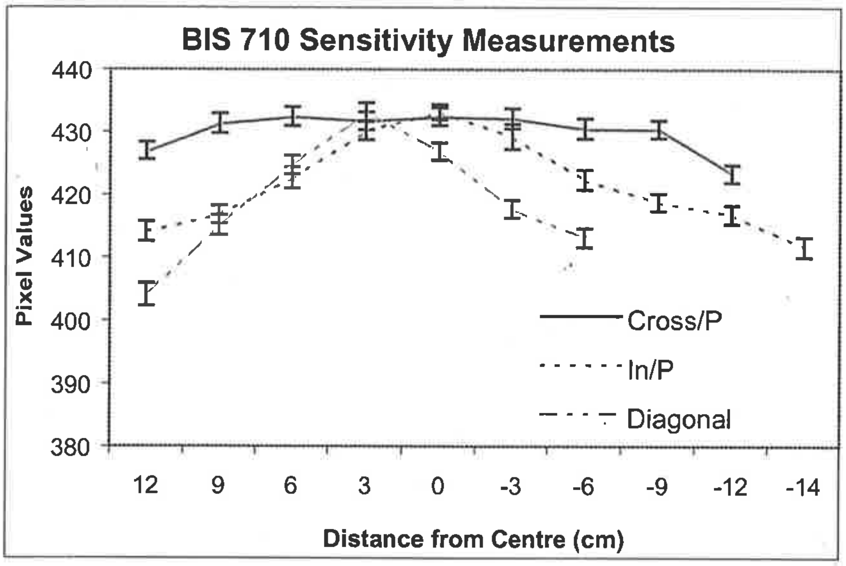

Figure 4.12. BIS 710 detector sensitivity measurements using a small radiation field along the cross plane, inplane and diagonal directions.

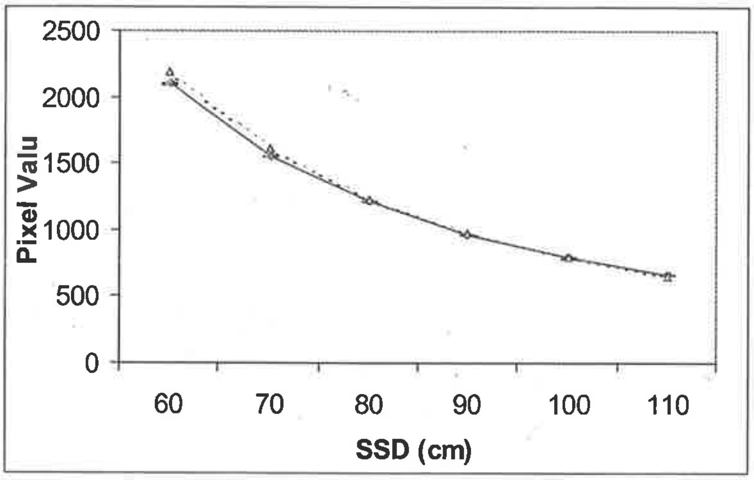

Figure 4.13. The BIS 710 pixel output values vary with SSD. Dash line is calculated results using inverse square law results and solid line is BIS measurement results. The BIS 710 response deviates from inverse square law at small SSDs.

4.2.13. Pixel value changes with SSD

The pixel values were measured with varied SSD. The results are shown in figure 4.13. The pixel values calculated from the inverse square law (using SSD equal 100 cm as a reference point) are also shown. There is 4.3% discrepancy between the measured and calculated (from inverse square law) values at SSD 60 cm, meaning that it is inadequate to apply the inverse square law to the BIS 710 output values at smaller SSDs.

4.2.14. BIS 710 scatter response

Because the scatter conditions between the BIS 710 measurements and an ion chamber measurements are always different, it is useful to compare the BIS and ion chamber response for the scattered radiation. An experiment was carried out by varying the distance from the exit surface of 20 cm solid water phantom to the detector surface. The detector to source distance is fixed to 150 cm. Ion chamber measurements were taken with the ion chamber placed at depth of maximum dose in a 40 × 40 cm solid water plate (1 cm of solid water behind the ion chamber to minimize the backscatter) while BIS detector was covered with additional build up layer measured in section 4.5.2.6. The beam energy is 6 MV photon. The setup geometry is shown in figure 4.14. The results (see figure 4.15) show that BIS is more sensitive to the scatter radiation. The ion chamber readings are re-scaled and normalised to the reading at 100 cm SSD (source to solid water phantom surface/entrance).

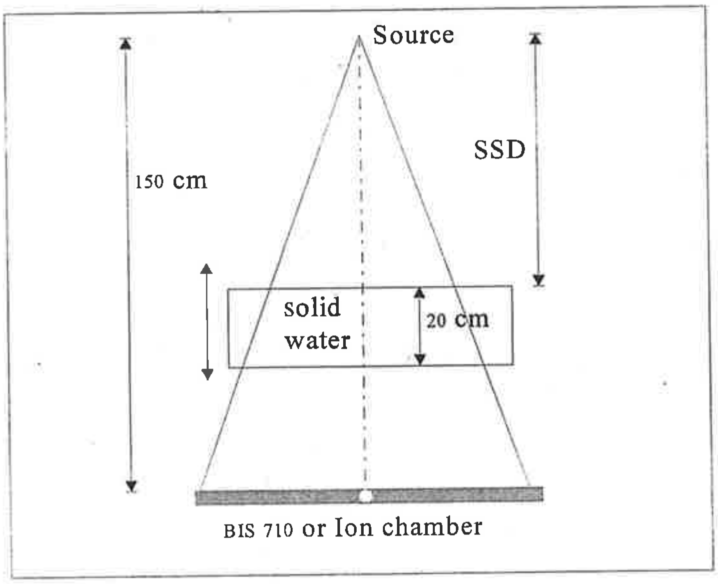

Figure 4.14. The setup geometry of BIS 710 scanter response measurements. Field size of 10 × 10 cm, and 200 MU were used.

The results show that BIS 710 has significantly higher response at a larger SSD (smaller phantom exit surface to BIS 710 detector distance) while at smaller SSDs the BIS 710 has a similar response with an ion chamber. It is concluded that the BIS 710 is more sensitive to the scattered radiation energies (below 1 MV) since the amount of scatter from the solid water phantom is the only difference for different SSDs. Therefore, it is assumed that BIS 710 system is more sensitive to lower energies. Experiments and simple Monte Carlo calculations investigating this will be discussed in the following chapter.

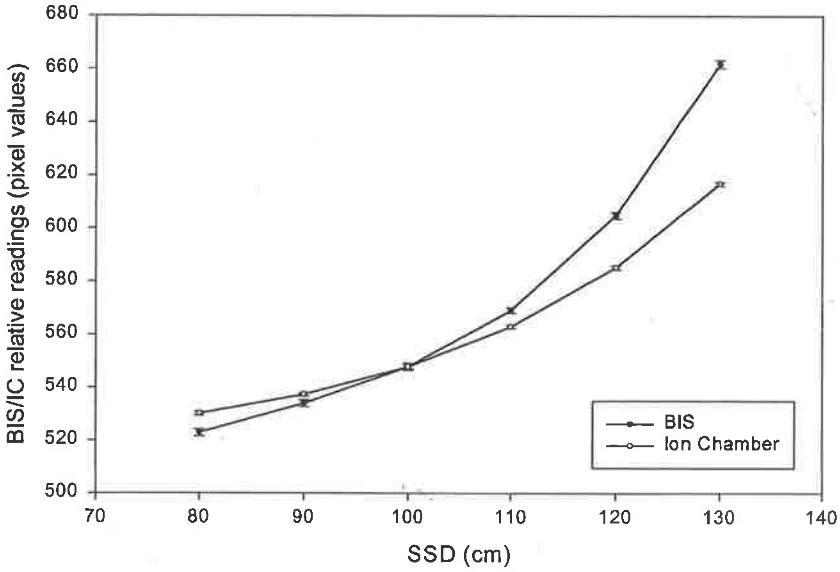

Figure 4.15. BIS scatter sensitivity measurements. A 20 cm solid water was used and the SSD were measured from source to surface of the block. Larger SSDs mean smaller distances from phantom exit surface to the detectors.

4.3. Summary and conclusions

The input/output characteristics of the BIS 710 have been investigated to better understand its basic imaging properties, with the aim of developing periodic quality assurance applications using the imaging device. The dose response curves describe the relationship between the incident energy fluence on the detector and pixel output values. The effect on the beam parameters, such as beam field size, dose rate, photon energy, and sampling times have been investigated in a ROI of 10 × 10 pixels around the central beam axis. The results demonstrate that the pixel output value is a linear function of the monitor units, which is typical for video based portal imaging system (Leong 1986, Kirby and Williams 1993). The field size effect of the BIS 710 is similar to ion chamber measurements at smaller field sizes. However, the pixel output values increase more rapidly at larger field sizes. The system is insensitive to dose rate, but is energy dependent. A linear relationship has been shown for different sampling times under 1.8 seconds. The image quality has also been investigated with the commercially available test phantom and software. A substantially higher spatial resolution was found compared with another portal imaging system (BEAMVIEW^{PLUS}) which is also installed at our centre. However, the contrast and noise levels were lower than that of the BEAMVIEW^{PLUS} system.

Chapter 5

Radiation Quality Assurance Checks with an Electronic Portal Imaging Device

5.1. Introduction

EPIDs have been used effectively to measure some beam parameters required for treatment planning and equipment quality control (Curtin-Savard *et al* 1997). However, previous studies on quality control have concentrated on verifying the isocentre position, interleaf transmission of the MLC, and dose distribution profiles (Bel *et al* 1996 and Michalski *et al* 1993). A few papers have reported the use of an on-line imaging system for periodic radiation quality assurance of medical linear accelerators, such as light field and radiation field coincidence, radiation field flatness and symmetry, and energy constancy (Kirby *et al* 1993, Lute *et al* 1996 and Ma *et al* 1997,1998). For light field and radiation field coincidence check, most commonly described conventional methods use films to examine congruence by marking the light field edges on the film before it is irradiated. The use of linear ion chamber or diode array with predefined field sizes is also reported. Generally, a comprehensive radiation field flatness and symmetry check involves the setup of a computer-controlled water scanning system. For routine consistency checks, a one-dimension ion chamber or diode array can be used, while for x-ray energy consistency checks, the depth-dose ratio at two different depths is commonly used.

An on-line imaging system may provide a solution to the task of quickly checking the light field and radiation field coincidence, beam flatness and symmetry, and beam energy constancy. It has the ability to provide two dimensional dose distribution information that makes it possible to investigate these tasks more completely.

Luchka *et al* (1996) have investigated the use of an electronic portal imaging device (EPID) to test the light and radiation field coincidence with a predefined light field size phantom. Kirby and Williams (1993) have investigated the use of a video-based EPID (RS-100) to test the field flatness and symmetry in diagonal directions. Ma *et al* (1997,1998) used an video-based EPID system to verify a prescribed intensity modulated X-ray beam pattern and applied a video-based imaging system to routine quality assurance such as radiation field flatness, symmetry, light/radiation field congruence, energy constancy and mechanical checks. In their second paper, they used a Wellhofer Beam Imaging System (BIS 710) (Wellhofer Dosimetrie, Schwarzenbruk, Germany) to investigate whether it can be used to check the light and radiation field congruence, electron energy constancy, x-ray beam flatness and symmetry, and collimator and couch rotation axes. In this study, the validity of using a BIS 710 to check the flatness and symmetry was tested by measuring the systematic flatness and symmetry variance from 3% to 30%, which were produced by custom-made aluminium wedges. Comparison measurements were carried out using a radiation beam analyser device. It was concluded that the BIS 710 is more sensitive to the flatness and symmetry variance. However, in this paper the authors did not directly investigate raw BIS 710 images for flatness and symmetry checks. Furthermore, they just checked the crossplane and inplane directions which is similar to conventional techniques.

The BIS 710 is a relatively new beam imaging system and in chapter 4, the characteristics of the BIS 710system have been investigated. Its use for (i) periodic quality assurance of X-ray field flatness and symmetry within a pre-defined area of BIS 710 images at a certain depth, (ii) the light and radiation field coincidence, (iii) x-ray beam energy constancy check, and (iv) measurement of the enhanced dynamic wedge dose distribution will be studied in this chapter.

5.2. Beam flatness and symmetry measurements using BIS 710

A conventional method to investigate beam flatness and symmetry is to setup a computer-controlled scanning water tank system to measure the absolute values of the beam flatness and symmetry at the reference depth. The setup procedure is time consuming and therefore is not ideal for routine quality assurance. For quality assurance purposes, a one dimensional detector array or specially designed phantom is commonly used. However, these devices (including a water scanning system) provide results for just a few specific directions (inplane, crossplane, and along the diagonal axis). On the other hand, an EPID system has the potential to determine a two-dimensional iso-dose map from one exposure (image). It can therefore provide the beam flatness and symmetry information in a defined area. The beam flatness and symmetry definitions in this study are adopted from the IEC protocol (ref. Chapter 2).

Preliminary investigation showed that 8% flatness was measured using the BIS 710 images for radiation field sizes larger than 25 × 25 cm^2, although the ion chamber water tank scan result gave ~3%. The measurements were carried out at 100 cm SSD, maximum dose depth and images were corrected with the correction image. Figure 5.1 shows the crossplane beam profile measured by BIS 710 with 6 MV photon beam at 25 × 25 cm^2 filed size from a Siemens KD-2 linear accelerator. Two horns are apparent near the edges, ~ 8% higher than the central axis dose, showing a deviation from beam flatness.

The different response between the BIS 710 and ion chamber measurements may be caused by: (i) side scatter radiation from the metal wall of the BIS 710 housing for larger field sizes; (ii) light scattering effects within the optical chain of the EPID; and (iii) energy dependent response of the BIS 710 detector.

To investigate the cause of the difference between the BIS and ion chamber profiles (ref. Figure 5.1), a Monte Carlo simulation using EGS4 code has been performed to study the energy response of the BIS 710 scintillation detector. The simulation geometry is shown in figure 5.2.

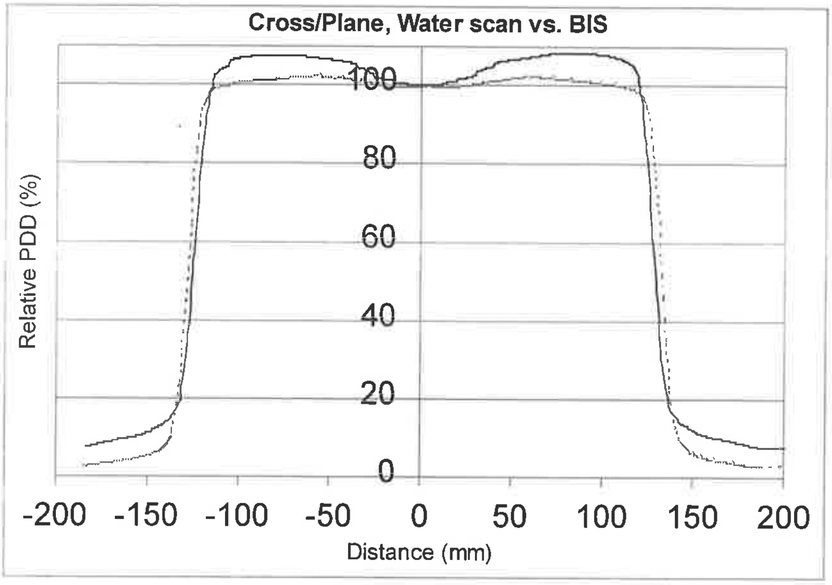

Figure 5.1. The BIS 710 crossplane beam profile (solid line) and ion chamber measurement (dotted line). Two horns are apparent near the edges, showing a deviation from beam flatness. The data was measured for 6 MV x-ray beam and 100 cm SSD at maximum dose depth.

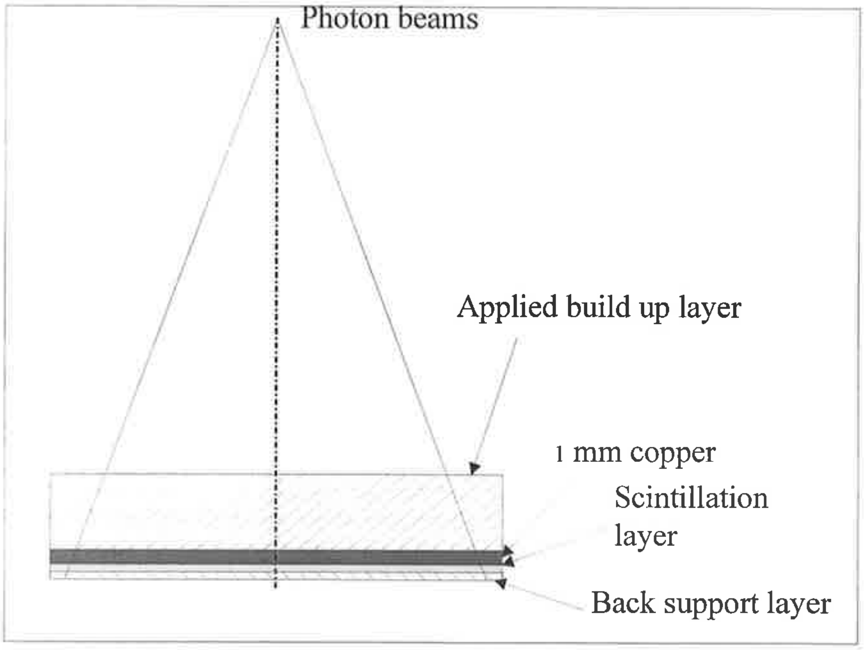

Figure 5.2. The setup geometry for Monte Carlo simulation of the BIS 710 detector energy responses.

The simulation was carried out with monoenergetic photon beams. The field size was 25 × 25 cm^2 and the pixel size was 0.5 × 0.5 cm^2. The code is modified from commonly available EGS4 *XYZDOSE* software with the divergent beam (Nelson *et al.*, 1985). The PRESTA algorithm was used. The parameters used in EGS4 code to control the transport of charged particles were PCUT, ECUT, AP, and AE. PCUT and ECUT represent the minimum total energy of photons and electrons transported. AP and AE represent the energy thresholds for creation of secondary photons and electrons, respectively. For the simulation reported in this study, PCUT = AP = 10 keV and ECUT = AE = 521 keV. These values were chosen to allow accurate modelling of charged particle transport within detector volumes (Andreo, 1991). The relative deposited doses at the back support layer were calculated from the beam central axis and the data are shown in figure 5.3. The simulation demonstrate that the BIS 710 detector response is energy dependent, increasing with energy greater than 1 MeV and decreasing with less than 1 MeV. A similar result has been reported for another metal/phosphor detector (Jaffray *et. al.*, 1995). As the incident energy increases up to 0.5 MeV, Compton scatter starts to dominate, resulting in a large fraction of the interactions occurring in the copper layer. This reduces the probability that an interacting x-ray will deposit energy in the phosphor layer. However, when the energy exceeds 1 MeV, the range of Compton recoil electrons generated in the copper layer is sufficient to escape the copper layer and deposit energy in the phosphor layer.

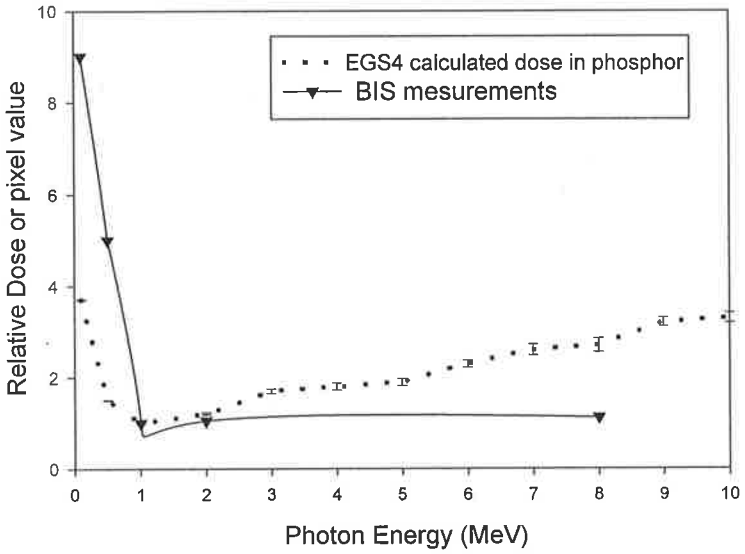

Figure 5.3. The Monte Carlo simulation and measurements results for the BIS 710 detector screen energy response.

To verify the Monte Carlo simulation, the BIS detector was exposed with 50 cGy dose with 4, 6, 23 MV photon beams. The appropriate additional build up materials have been used for each energy (see chapter 4). A Nucletron brachytherapy system with Ir^{192} source with mean energy of 400 keV has also been used to irradiate the BIS 710 detector. The source was held 25.4 cm above the detector and the current source strength was 3.687 $cGym^2h^{-1}$. An image was acquired with a 24 s exposure. The pixel value for depositing 50 cGy to the detector could be derived from ROI of 10 × 10 pixel around the centre of the image. To achieve another low energy calibration, a superficial unit which produces a x-ray beam with a mean energy of ~ 60 keV was also used to check the BIS 710 energy response. The results are given in table 5.1 and indicate that the BIS 710 detector is 9 and 5 more times sensitive to 0.06 and 0.4 MV photon than 4 MV photon. It can be concluded that BIS 710 detector is much more sensitive to low radiation energy although care must be taken not misinterpret these results due to the slightly different setup geometry between the lower energy and linac beam measurements. This suggests that the BIS 710 detector is more sensitive to scattered radiation energy from phantom measurements (ref. Chapter 4). This could be used to explain why there are horns in the BIS 710 profile measurements, because there are more low energy photons near the beam edge after the beam passes through the flattening filter. The energy response discrepancy between the simulation and the measurement results could be explained in part by the fact that the beam energy used for simulation is monoenergetic beam while the measurements were made from polyenergetic beams from the linac and by energy dependent response of BIS detector (higher sensitivity to low energy x-rays). The measurement and the calculation deal with two different quantities. While the latter calculated deposited dose to the detector, the former provides output pixel values. However, pixel values are directly proportional to the dose. Therefore the results of both (measurement and simulation) can be related. For a more rigorous investigation, a calculation should be performed using convolved on/off axis spectra for a linac beam. This is however beyond the scope of this thesis.

Table 5.1. The results of BIS 710 detector response with energy. The data were normalised to 4 MV readings.

Energy (MV)	0.06	0.4	4	6	23
Effective energy* (MeV)	0.06	0.4	1	2	8
Relative PV	9.00 ± 0.03	5.10 ± 0.02	1.000 ± 0.004	1.048 ± 0.004	1.116 ± 0.005

*Effective energy for superficial x-rays was estimated from Johns and Cunningham. Effective energy of linac beams was calculated as 1/3 of the peak energy.

In order to investigate further the reasons for the 'horns' produced in the BIS 710 images the following tests were undertaken with films as the image recorder: (a) the gadolinium (Gd_2O_2S) fluorescent phosphor screen was removed from BIS 710 assembly and replaced with a ready pack film in order to investigate the effects of radiation backscattered from the EPID housing, (b) film was positioned on the couch and covered with BIS 710 gadolinium (Gd_2O_2S) fluorescent phosphor screen in order to estimate the effects of the scatter radiation of the detector screen itself, and (c) film was positioned on the couch with 0.5 cm build up solid water and without any backscatter materials to provide a reference image. In all cases, the films were irradiated with 50 MU, 6 MV x-ray beam. Comparison of the results from (a) and (c) experiments will show the effect of the backscatter radiation from the EPID housing. The results from (b) will show if the 'horns' are produced in the BIS 710 radiation detector.

Comparison of profiles from the films indicate:

(i) There is no detectable difference between (a) and (c) that means there is no or little effects from the EPID housing backscatter radiations.

(ii) There is no detectable difference between the radiation beam profile under the BIS 710 radiation detector and without detector except a broader penumbra.

(iii) The maximum off axis ratio on all films was comparable with that from the ion chamber profiles in water.

From the above results, it can be concluded that there is no or minimal effect from the BIS 710 housing backscatter radiation and the BIS 710 radiation detector itself is not the reason for the 'horns'. This would indicate that it is the design of the optical system within the BIS 710 housing that gives rise to the 'horns' as well as higher response to low radiation energy of BIS 710 detector.

Corrections for the above mentioned effects must be made in order to use the BIS 710 for measurement of flatness and symmetry. Film was chosen to provide a 2-D correction array for a range of field sizes, likely to be used for QA tests, for BIS 710 images because of the difficulty of getting 2-D ion chamber array scans. The BIS 710 system was setup to acquire images at d_{max} (maximum dose depth) for each X-ray beam energy and field sizes. Film images were taken at the same time using the same geometry. Film images were digitized, background-subtracted and saved. The film images and the BIS 710 images were aligned by the centres and the inplane and crossplane profiles and their ratios were saved as correction arrays. Subsequently acquired BIS 710 images (after the application of the correction array) can be used to investigate the flatness and symmetry of the radiation field.

A computer program was written to locate a defined area automatically (Figure 5.4) and calculate the flatness and symmetry within the area using formulas 2.3 and 2.4 (ref. Chapter 2), respectively. The results of beam flatness and symmetry of a 6 MV photon beam from a Siemens KD-2 linac are presented in Table 5.2. Unlike conventional methods that calculate the flatness and symmetry from the main axes (in/cross plane, diagonal) this procedure will assess the flatness and symmetry within the defined area. Table 5.2 shows that the results from BIS 710 (after correction) and film agree well within 1.2%. It demonstrates that this technique can easily pick up the "cold" and "hot" spots in the defined area, therefore it provides more information about radiation field flatness and symmetry.

Table 5.2. Results of a flatness and symmetry check for 6 MV photon beam with radiation field size 25 × 25 cm, expressed as percentages.

6 MV Photon	Inplane Flatness (%)	Inplane Symmetry (%)	Crossplane Flatness (%)	Crossplane Symmetry (%)	Flattened area Flatness (%)	Flattened area Symmetry (%)
BIS 710 (uncorrected)	5.30	0.79	7.20	0.98	8.62	1.12
BIS 710 (corrected)	2.77	0.70	1.91	0.46	2.85	1.01
Film	2.51	0.60	2.25	0.53	2.79	1.12
Ion Chamber	3.20	0.90	3.10	0.50	n/a	n/a

As flatness and symmetry measurements from film and ion chambers are comparable in this instance, films provide a reasonably accurate correction matrix for BIS 710 images. As a secondary standard device, the BIS 710 can be used to monitor the X-ray beam flatness and symmetry. When it shows that flatness or symmetry are outside specified limits, the computer controlled water scanning system can be used to provide more accurate measurements. As mentioned in section 3.8, film is energy dependent and in order to use it for calculation of correction matrix for BIS images, it has to be properly calibrated.

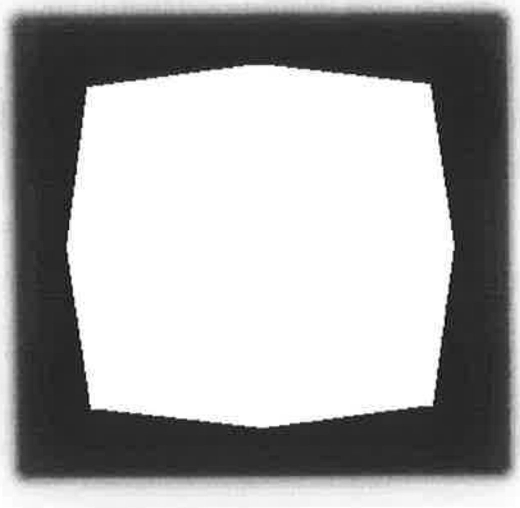

Figure 5.4. A BIS 710 image with a defined flatness and symmetry area automatically located by a computer program.

5.3. Radiation field and light field coincidence

The radiation field has a finite-size penumbra and must be specified at a particular dose level, usually 50% of the dose on the central axis, and a particular distance from the source, usually at the isocentre. The International Commission for Radiological Units and measurements (ICRU, 1976) defines the distance between 50% dose levels as the field size. It is measured at the depth of maximum dose at isocentre. Because both the light field and radiation field have a penumbra and moreover the penumbra of the x-ray field is not the same for all field sizes, the x-ray field size, the optical field size and the collimator scales may differ by several millimeters (up to 5 mm for the largest fields). This is recognised in the IEC's particular requirements for performance. The guide to functional performance values allows 2 mm or 1% discrepancies between the light field and the indicated field size, and 3 mm or 1.5% between the x-ray field and indicated field size, for fields up to 20 cm (IEC 977, 1989).

As an option on the BIS 710system, a so-called light field and radiation field scintillator is available. This scintillator is made from Lanex Fast (front) mounted on a 2 mm Perspex plate and it can acquire light field images as well as radiation images. A pair of light/radiation images was acquired, the nominal field size being 20×20 cm^2. The edges of the light and radiation fields have been detected automatically by computer analysis and the result is shown in figure 5.5. The radiation field edges were presented by the 50% intensity contour, and the light field edges were presented by the 25% intensity contour. According to the manufacturer, that intensity contour is chosen for quantitative analysis of the light field that matches its real physical size (e.g., measured on the graph paper). The light field contour used should be assessed carefully for different type of machines. The light and radiation fields coincide well, i.e. within 2 pixels (1.2 mm), except in the upper right corner and middle of the left edges. The reason for the discrepancies is that the light field intensity is not uniform and the upper right corner is darker since the detected light field edges shrink inside, while in the middle of the left edge, the intensity is higher and the detected light field edge expands outside. BIS 710 is not itself the source of non-uniformity, as uniform light images were measured for a uniform light source.

The results of BIS measurements were found to be in agreement with film measurements within ±1mm.

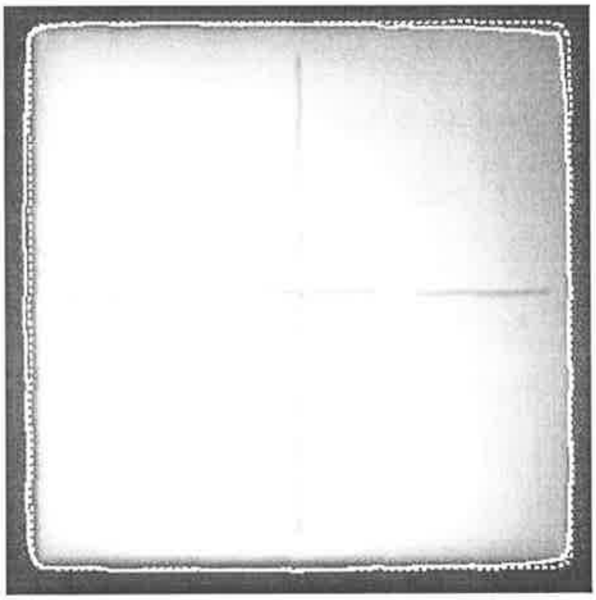

Figure 5.5. Example image of the light field and radiation field coincidence check using the BIS 710. The solid line is the edge of the light field, and the dotted line is the 50% intensity contour of the radiation field.

5.4. Radiation beam energy constancy checks

Although there are arguments about what is the best index for the beam energy, D_{10}^{20} is still commonly used in many cancer centres to check the x-ray energy constancy (ref. Chapter 2). It is hard to use an EPID to measure D_{10}^{20}, however, a set up similar to measurements of TPR_{10}^{20} can be achieved (see figure 5.6), except for there is no backscattered radiation. The ratio of pixel values from a ROI within both regions ***A*** (10 cm) and ***B*** (20 cm) can be derived. An approximate ratio of TPR_{10}^{20} from a BIS 710 image can be calculated for the ratio of pixel values from region ***B*** and ***A***. The base line can be established for the future monitoring. The measured results are presented in table 5.3. The 4 MV beam is from a VARIAN 4/100 linac and the 6 MV and 23 MV beams are produced from a VARIAN 21 EX linac and the ratios are unique for every linacs. The field size used was 15 × 15, source to EPID distance was 100 cm, and distance of ROI off axis was 1 cm. The uncertainty level could be reduced by summing a larger number of image frames. Although the data from the BIS 710 and ion chamber measurements are not the same, the aim of the measurement is to set-up a baseline for future consistency checks. The measurement parameters and set-up geometry can be saved and used for future checks to monitor the photon beam energies constancy. For repeated measurements, provided that the geometry of the measurement setup is the same, the results should be reproducible within 0.5% (see section 4.2.3).

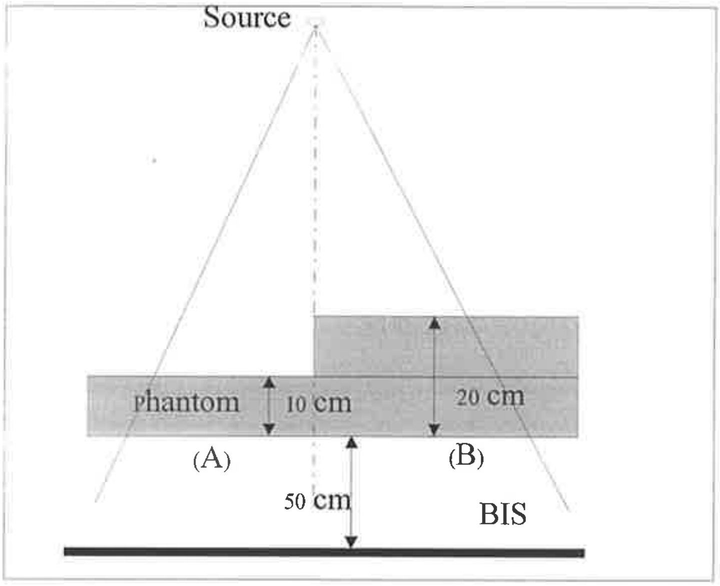

Figure 5.6. Diagram for using the BIS 710 to measure a tissue phantom ratio TPR_{10}^{20}.

Table 5.3. Tissue phantom ratio TPR_{20}^{10} measured with three photon energy beams available in Royal Adelaide Hospital.

	4 MV	6 MV	23 MV
TPR_{20}^{10} (Ion chamber)	0.679	0.694	0.818
TPR_{20}^{10} (BIS 710)	0.647 ± 0.005	0.661 ± 0.005	0.780 ± 0.005

5.5. Wedge dose distribution measurements

Wedge dose distribution data were collected for treatment planning system during the treatment unit commissioning procedure. For enhanced dynamic wedges (EDW), the dose distributions will be continuously monitored during the clinical use of machine. Conventionally, films or water tank scanning systems are used to check the dose distribution and the wedge factors. Since EPIDs provide real time two-dimensional digital images, a faster technique for measuring the dose distributions using an EPID can be achieved.

Dose distributions for two types of wedge, physical wedges and enhanced dynamic wedges have been measured with the BIS 710. In the case of physical wedges, the detector of BIS 710 was positioned at about 5 cm water equivalent depth and at 100 cm SSD. Images were acquired with 100 MU delivered from a KD-2 linac 6 MV photon beam. Profiles perpendicular to the central axis were extracted from the dose distributions for 15°, 30°, 45°, and 60° wedges. The profiles are presented in figure 5.7 and the water tank scanning system results under the same set-up conditions are also plotted in the same figure for comparison. The figure indicates that the dose distributions from the two techniques agree within 1% which means it is reliable to monitor the physical wedge dose distributions with the BIS 710. The better agreement of BIS measurements with ion chamber ones for physical wedge measurements compared to open field measurements can be due to the spectral change of the beam reaching the detector screen. In case of wedges, the soft lower energy component is filtered out and will not influence BIS response.

Some modern linacs are equipped with a 'dynamic wedge' capability in which a jaw sweeps across the beam to produce a wedge like dose distribution. During enhanced dynamic wedge (EDW) commissioning, generally a one-dimensional ion chamber array is used to measure the dose distribution. The dose distribution can be measured and checked with a two-dimensional dose detector such as EPIDs and films for periodic checks. The BIS 710 system has been used to measure the dose distributions of the EDW for a QA check. Dose distribution of wedge angles 10°, 15°, 20°, 30°, 45° and 60° were measured at 5 cm depth in solid water on top of the BIS 710 detector. The open field image was also acquired at the same time to check the symmetry of the field for the correction of the EDW profiles.

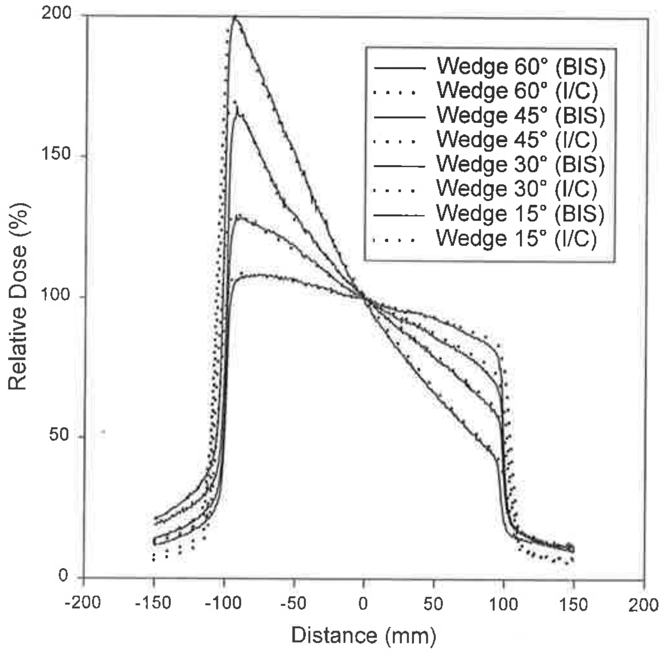

Figure 5.7. The physical wedge dose distributions measure from the BIS 710 (solid lines) and ion chambers (dotted lines) for a Siemens KD-2 linac.

EDW profiles in the unwedged direction were checked. As the profiles were not significantly asymmetric, no correction of the wedged profiles was required. The results with Varian 21 EX linac are presented in table 5.4. Examples of EDW dose distributions are shown in figure 5.8 and the vertical lines present 1/4 field size distance and the central beam axis. The wedge angles were calculated using the IEC definition (IEC989, 1989). For comparison, the film measurement results are also presented in the Table 5.4, and the ion chamber array measurements for 60° wedge were also presented in figure 5.8. There is a larger discrepancy between the BIS 710 and ion chamber array measurements near the edges of the wedge. One of possible reasons for the discrepancies might be the lower spatial resolution for ion chamber array measurements because of the large dose gradient near the edges. Also BIS 710 is more sensitive to lower energy radiation which is mostly irradiated towards the edges of the radiation field. Table 5.4 shows the BIS 710 measurements have a better agreement with the nominal wedge angles than film measurement, with agreement within 2.5%. This demonstrates that it is adequate to use BIS 710 system for routine QA of EDW (constancy check).

Table 5.4. Enhanced dynamic wedge dose distribution measurements with BIS 710 and films.

Wedge angle	10°	15°	20°	30°	45°	60°
Film*	11°	15°	24°	31°	47°	58°
BIS (± 0.5°)	10.2°	14.7°	20.3°	29.7°	44.2°	58.7°

*Reported CAP results (Varian 21 EX CAP data, Department of Medical physics Royal Adelaide Hospital, 2000).

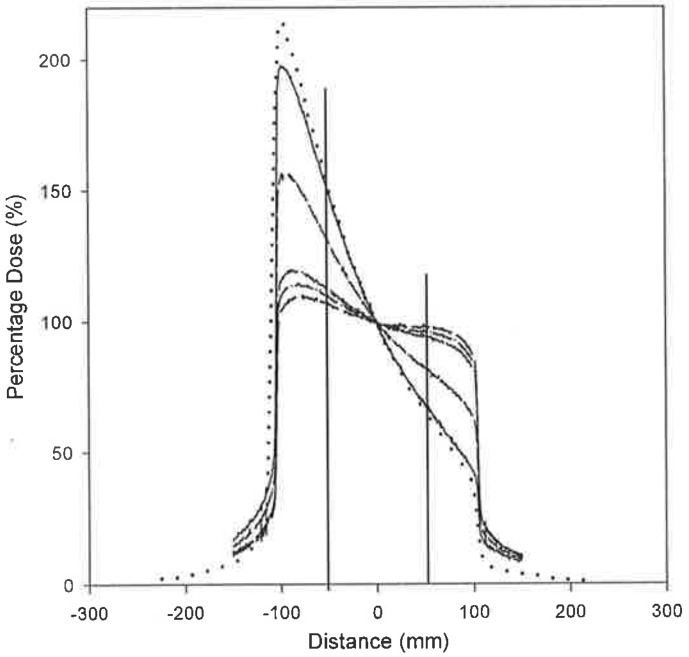

Figure 5.8. Enhanced dynamic wedges dose distributions measured with BIS 710 (solid lines) and ion chamber array (dotted line). Data were normalised at beam central axis.

5.6. Summary and conclusions

The flatness and symmetry calculations from the BIS 710 images show that it can provide more information about the beam flatness and symmetry than a simple calculation of flatness and symmetry from the major axes. This enables it to be used as a secondary device to monitor the X-ray beam flatness and symmetry provided it is properly calibrated.

The combined light and radiation sensitive scintillator detector provides digital and more quantitative measurements which enable light and radiation field coincidence to be checked. However, because the light intensity is not uniform, the light field edges are hard to be detected accurately. Nevertheless it does provide a useful and quick check for light and radiation coincidence and the method compares well with film technique. Its use for checking x-ray energy constancy, and enhanced dynamic wedge dose distributions provide a new and simple approach for routine quality assurance. The x-ray energy constancy check provides a similar check with the ion chamber techniques of checking D_{10}^{20} ratio, but with a faster digitised result. The enhanced dynamic wedge dose distributions measurements with BIS 710 can be used for fast routine QA check provided they are calibrated with the gold standard devices. All the BIS 710 measurements mentioned above assume the BIS 710 measurements are consistent with time, therefore, the long term trend in performance should be established for BIS 710 and then the results can be corrected if there is any discrepancy from the device itself.

Chapter 6

Evaluation of the Mechanical Alignment of a Linear Accelerator with an Electronic Portal Imaging Device

6.1. Introduction

The correct mechanical alignment of a linear accelerator is an important link in the chain of requirements to deliver the prescribed dose to the patient. Consequently, a comprehensive quality assurance program for radiotherapy linear accelerators should include tests capable of detecting and measuring the sources of misalignment. Several such tests have been described in the last few decades (Essenberg and Koziarsky, 1972, AAPM, 1975, Boyer, 1979, Lutz, *et al.* 1982). Every radiotherapy centre lists mechanical alignment checks as one of the quality assurance procedures. The determination of the rotation axes of the collimator, and gantry and the collimator jaw symmetry must be accurate and unambiguous since both the radiation field and positioning aids are aligned to those parameters. A faulty gantry rotation bearing can cause a gantry rotation axis problem. Loose guide bars of the outer jaws can cause jaw asymmetry problems, while bending magnet misalignment will result in a source displacement (Lutz, *et al.* 1982). The combined effect of these alignment parameters on the displacement of two opposing fields should not exceed the value of 2 mm in order to consider the mechanical alignment of the radiotherapy unit acceptable (AAPM, 1975).

The quality assurance procedure for mechanical alignment needs to be both accurate and simple. The time taken to carry out the procedure needs to be short and the equipment requirement should be minimal. Radiographic film was used in most of the previously reported QA methods (Essenberg and Koziarsky, 1972, AAPM, 1975, Boyer, 1979, Lutz, *et al.* 1982) for mechanical alignment tests. Also, these techniques are either not simultaneously sensitive to the three general causes of misalignment mentioned above, or further complicated tests are needed to distinguish between the problems. In this chapter, a procedure is described where all of the mechanical alignment parameters can be measured using digitised images from an Electronic Portal Imaging Device (EPID) with almost real-time analysis. The procedure includes only two major steps and is independent of the light and radiation field congruence. In the first step, two markers are placed on top of the EPID housing and on the treatment couch and two images are acquired for gantry positions 180° apart. Mechanical misalignment of the linear accelerator can be identified when positions of the markers and their distances to the beam centre on both images are compared. In the second step, another two images are acquired at collimator angles 180° apart. By comparing the positions of the beam centre on both images, the three potential sources of misalignment can be distinguished. This procedure can be made suitable for implementation into the routine quality assurance of linear accelerators.

6.2. Split-field test and other conventional tests

6.2.1 Split-field test

The AAPM (1975) *Code of Practice for X-ray Therapy Linear Accelerator* has described the test methods for the mechanical alignment (see Chapter 2). However, these tests are not sensitive to all three general causes of mechanical alignment: (1) source displacement, (2) collimator asymmetry, and (3) shift of either collimator axis or gantry rotational axis.

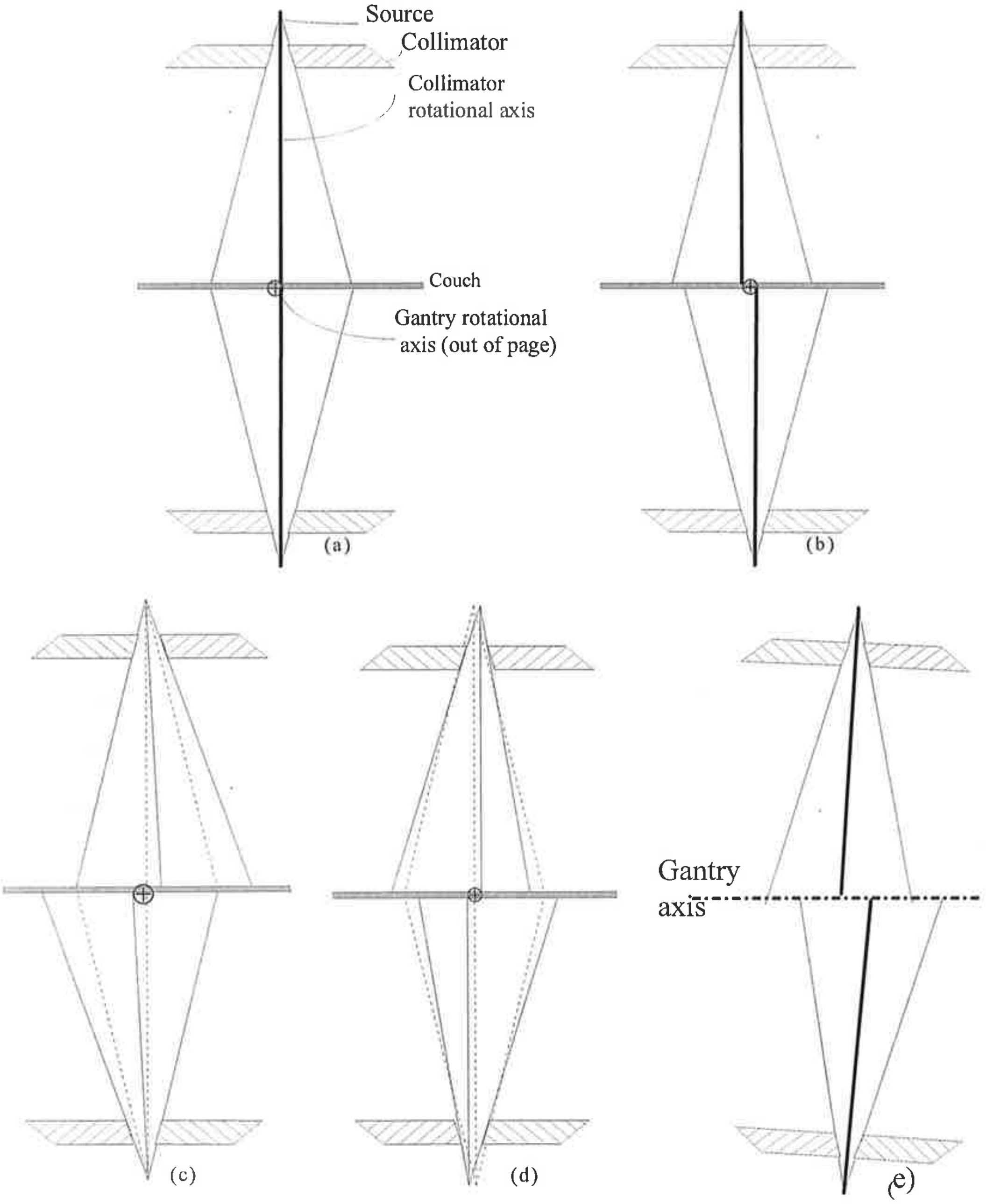

Figure 6.1. Correct (a) and incorrect (b-e) alignments as shown by two opposite fields. A lateral shift can be caused by (b) non-intersecting collimator and gantry rotational axes, (c) asymmetric collimator jaws, or (d) a lateral source displacement. A longitudinal shift between the fields can be due to (e) the flexing treatment head supports (Lutz, 1982).

Assuming that a coincidence between light field and radiation field is maintained, alignment errors will not show up on individual fields set up to skin marks, but will appear in multiple field treatments using different gantry or collimator angles. Figure 6.1 illustrates the effect for a pair of parallel-opposed fields, of which one is set up to skin marks and the other is determined by rotating the gantry by 180°. When the alignment is correct (Fig. 6.1a), the collimator jaws are symmetric about their axis of rotation and the electron beam impinges on the target along the axis of collimator rotation. This axis intersects the gantry rotational axis in a well-defined mechanical isocentre. Each of Fig. 6.1b, 1c and 1d illustrates the effects of the three general problems mentioned above. In each case the result is a shift between the fields in the lateral direction, i.e. along the line perpendicular to both gantry and collimator rotational axes.

A split-field test method was recommended by AAPM (1984) for routine quality assurance due to its relatively rapid and simple execution. The test was developed by Lutz, *et al.* (1982) and consists of the double-exposure of a film, sandwiched between build-up sheets, to two radiation fields, at a gantry angle of 180° apart. The set up geometry is shown schematically in Figure 6.2. As shown in Figure 6.3, a square field is first exposed from above with half the field, say region 2, blocked and then irradiated from below to expose region 2, with region 1 blocked. With modern teletherapy machines, an asymmetric field can be formed easily. A relative shift of the two images is indicative of a mechanical misalignment. If a misalignment is shown by the test, one can then proceed to investigate its cause by checking the individual mechanical alignment parameters. The major disadvantages are (a) it cannot identify the sources of the problems and (b) it is not possible to quantitatively relate the shift to source misalignment or jaw asymmetry. Therefore whether or not to perform the further tests remains uncertain.

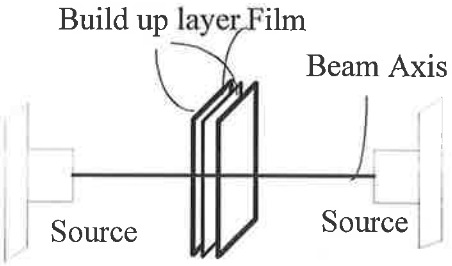

Figure 6.2. A schematic of split-field test set up geometry.

If the decision is made that mechanical misalignment problems exist, then further tests should be performed to isolate the causes of misalignment.

Such tests include checks of all the general causes of mechanical misalignment mentioned above. The jaw symmetry test can be done by setting the gantry head in the upright position, and double exposing a film at collimator angles 180° apart with half of the field blocked with lead for each exposure. The film should be positioned at the isocentre plane and not be moved during the exposures. If the radiation field edges line up on developed film, the collimators are symmetric relative to the axis of the collimator rotation.

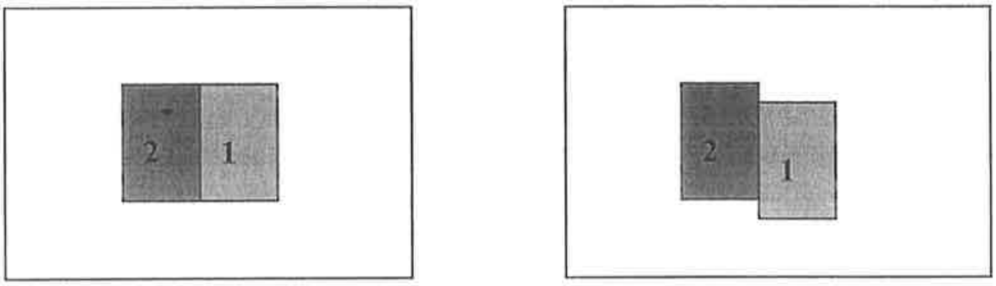

(a) Correct alignment (b) Alignment problem

Figure 6.3 Diagram of a simplified split-field test (from Lutz, 1982)

6.2.2. Conventional tests to distinguish the mechanical misalignment

The source position relative to the axis of collimator rotation can be determined by finding the centre of the radiation field relative to the axis of collimator rotation at an extended distance. The radiation field centre can be determined from an irradiated film by finding the midpoint of the 50% dose on two opposite edges. The film is double- exposed at collimator angles 180° apart to eliminate the jaw asymmetry problems. The axis of the collimator rotation can be determined using a punch apparatus. The punch apparatus is rigidly clamped to the collimator assembly. As the collimator rotates through its full range, a circle of punch marks is made on the same film. The centre of the circle of the punch marks can be found and compared to the radiation centre. If the two centres coincide, the source position is on the axis of collimator rotation. If the two centres do not coincide, the distance from the effective source position to the axis of collimator rotation can be calculated from the separation of the two centres on the film. The lateral displacement D_{lat} of the source to the axis of collimator rotation is given by (Lutz et *al.*, 1982):

$$D_{lat} = \frac{Xf}{F} - f , \tag{6.1}$$

where f is the focus-to-collimator distance, F is the focus-to-film distance and X is the lateral displacement of the two centres.

A test of the coincidence of collimator and gantry rotation axes can be done by using the same punch apparatus. The coincidence of the two centres of the punch marks from collimator and gantry rotations will indicate whether the gantry and collimator axes intersect. If the two centres, constructed from the punch marks, lie along a line in longitudinal direction, the gantry and collimator axes intersect. Otherwise a misalignment problem exists. Another method to test this is by using front pointers as described in chapter 2.

The major disadvantages of the split test are (a) dependence on the light and radiation field coincidence, (e.g. jaw symmetry test), and (b) it cannot check the sagging of the treatment head support, illustrated by figure 6.1 (e). Those latter causes the collimator rotational axis to bend toward the gantry when the treatment head is in the upright position. Furthermore, films are used to record the results. Although film has long been used in radiotherapy, it has inherent problems such as processing time requirements and retrospective analysis (needing digitisation).

6.3. The EPID system - BEAMVIEW^{PLUS}

The portal imaging system used in this work is the 'Beamview Plus' Electronic Portal Imaging Device (see Figure 6.4) manufactured by Siemens.

It consists of (a) detector (screen), (b) 45° mirror, (c) camera, (d) camera control unit (CCU) and (e) computer and frame grabber. The metal/fluorescent combination provides the basic radiation detector element. The detector screen consisting of 1mm copper coated with Gd_2O_2S layer. The copper plate filters secondary electrons produced in the body of the patient (which would reduce the image contrast) and provides a build-up layer thus increasing sensitivity and signal to noise ratio of the system (Radcliffe *et al.*, 1993). Furthermore, it converts the incident photons into secondary electrons, which forms the image on the fluorescent screen. The 45° front-surfaced mirror allows the Newvicon® video camera to be placed outside of the direct photon beam, thus decreasing the risk of radiation damage to the electronic components. The video camera captures the image in a near-real time, 30 frames per second, and applies it to the imaging sub-system via an EIA

RS-170 video interface. The lens apparatus is f/1.4. As mentioned in chapter 3, a larger lens causes image distortion. The detector assembly is mounted on the gantry below the level of the couch and rotates with the gantry to any treatment angle.

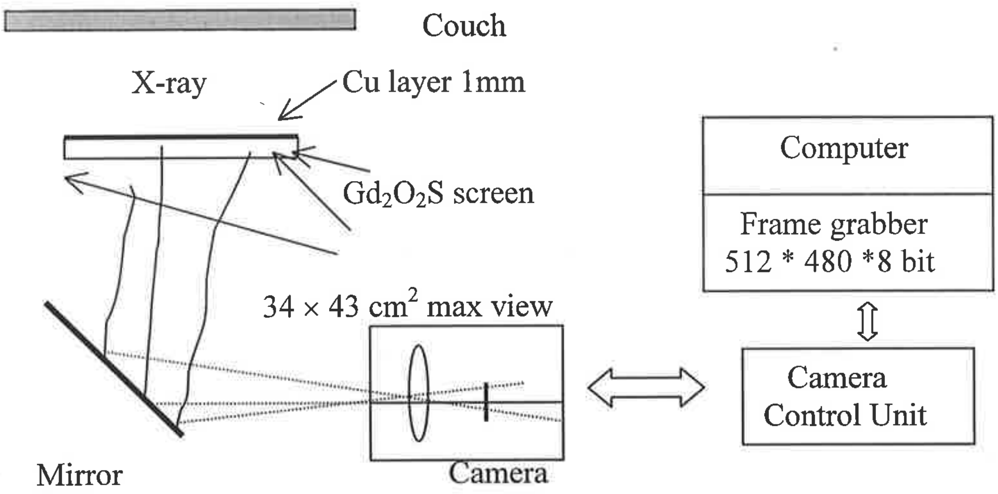

Figure 6.4. A schematic diagram of Siemens' BEAMVIEW^{PLUS} System.

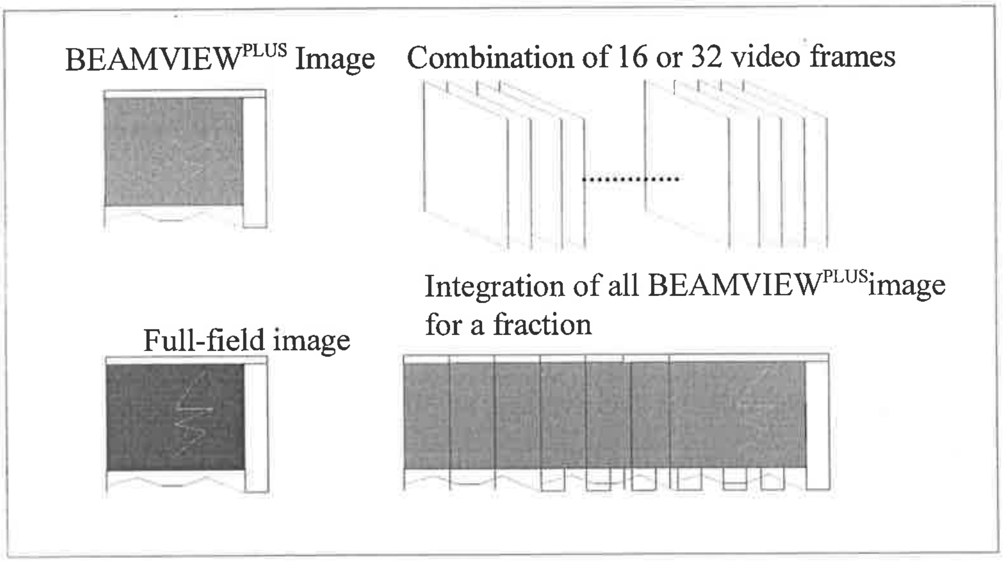

Figure 6.5. A schematic of BEAMVIEW^{PLUS} image.

In order to improve the signal-noise-ratio, video based EPIDs images are generally averaged over a certain number of frames. The BEAMVIEW^{PLUS} image is summing either 16 video frames or 32 frames (pre-programmed). The full-field image is an integration of all BEAMVIEW^{PLUS} images for an entire fraction. This is illustrated in figure 6.5. The upper panel is a BEAMVIEW^{PLUS} image which is summing 16 or 36 frames. The lower panel is a full field BEAMVIEW^{PLUS} image. The images used in this investigation are full field images with 1 Gy dose delivered for the whole fraction. This will give a signal-noise-ratio ~ 150.

6.4. Beam centre localization method

The radiation field centre in this chapter is defined as the intersection point of two perpendicular bisector lines. Each bisector line is formed by connecting the midpoints of two inplane and crossplane profiles respectively. A midpoint is the half distance between the 50% dose contours (see figure 6.6). The midpoint is determined by the same concept as the IEC used to define the field size. The radiation beam centres are generally checked by exposing film and delineating the radiation field edges or by using ion chamber scanning along the major axes to find the 50% dose. In our case, the Beamview Plus images record the relative pixel values instead of dose values. The typical video camera based EPIDs have a linear relationship between the incident dose and output pixel values (Leong, 1986, Kirby and Williams, 1993, 1995). The beam profiles are symmetrical about the midpoint of the profile therefore the midpoints of crossplane and inplane profiles can be determined from the 50% pixel values of the profiles. The 50% Pixel Values (PV) were determined by the following formula:

$$50\%\ \mathrm{PV} = (100\%\ \mathrm{PV} - \mathrm{Background\ PV})/2 + \mathrm{Background\ PV}, \qquad (6.2)$$

where the 100% pixel value is the average of 30 × 30 pixels in the central part of the radiation beam and the background PV was calculated as the mean of 10 × 10 pixels from the outside of the beam.

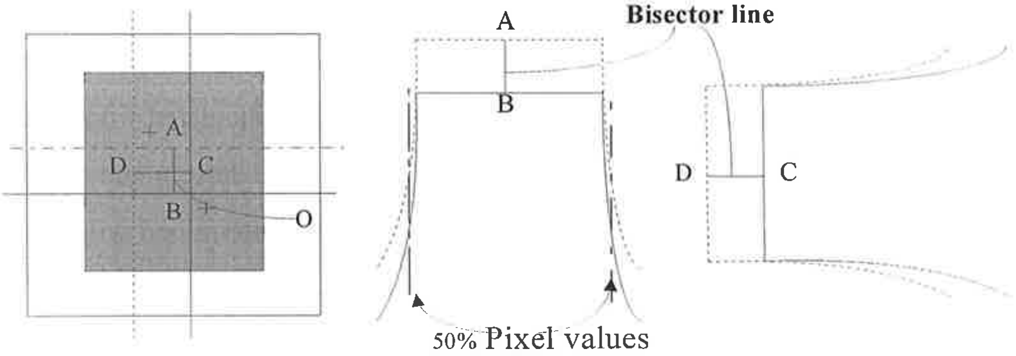

Image with markers **Cross Plane profiles** **In Plane profiles**

Figure 6.6. A schematic of the beam centre position determination. AB and CD are the bisector lines, and the intercept point, O, of AB and CD is the beam centre.

6.5 Marker position determination

Two markers are used to aid the mechanical alignment assessment test procedures developed in this chapter. Since the marker positions will be directly or indirectly used in the test procedures, the determination of the marker position must be accurate.

6.5.1. Edge detection and marker position

The pixel size of Beamview Plus images is 0.5×0.5 mm at the isocentre, i.e. 100 cm from the source. If a small marker were used to represent the marker's position, then the accuracy would be ± 1 pixel, which is ± 0.5 mm. However, the recommended limitation for collimator, gantry, and treatment couch rotational axes is ± 1 mm. In order to achieve sub-pixel accuracy in the marker position determination, a $2.5 \times 2.5 \times 2.0$ *cm* rectangular lead marker with machined edges was used. One corner of the marker was used to identify the position of the marker. The marker's position within an image was located by detecting two perpendicular edges of the marker. To detect the edges, two regions of interest about 2 × 1 cm (~ 40 × 20 pixels) were selected around the left and top edges of the marker image (see Figure 6.7a). The 50% pixel value points were calculated from the rows/columns (within the selected regions of interest) crossing the mentioned marker edges (between A and B, and between C and D on Fig. 6.7a). These points were fitted with a straight line for both edges respectively. The intersection point of these two lines defines the position of the marker, i.e. the corner of the maker. Figure 6.7b shows measured data (see table 6.1) used for determination of the marker position. The 50% pixel value was calculated using the equation (6.2) and is illustrated in figure 6.8. The 100% pixel value is an average of ROI 10 × 10 pixels within the edge region and the background is calculated from ROI 10 × 10 pixels outside the radiation field. Using this localization procedure, a sub-pixel accuracy can be achieved, i.e. one of the corners of the marker can be determined within ± 0.1 pixel in both image axes (x and y).

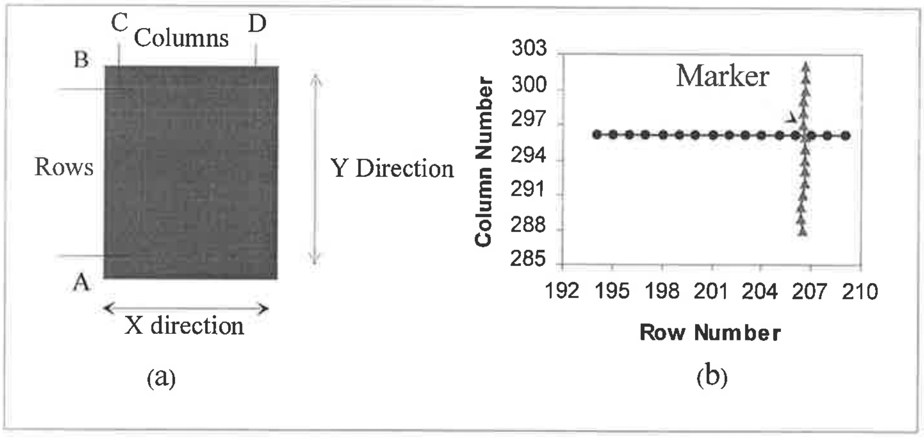

(a) (b)

Figure 6.7. (a) A schematic image of the marker and (b) the determination of the marker positions using pixels with pixel value corresponding to 50% intensity of the outside marker region.

Table 6.1. Sample marker edges data which are used to determine the marker position (Data are measured in pixel).

X Direction Edge		Y Direction Edge	
(X, Y) ± 0.1		(X, Y) ± 0.1	
195.0, 296.2	203.0, 296.1	206.5, 288.0	206.6, 296.0
196.0, 296.2	204.0, 296.1	206.4, 289.0	206.5, 297.0
197.0, 296.1	205.0, 296.1	206.4, 290.0	206.5, 298.0
198.0, 296.1	206.0, 296.1	206.5, 291.0	206.5, 299.0
199.0, 296.1	207.0, 296.1	206.6, 292.0	206.6, 300.0
200.0, 296.1	208.0, 296.1	206.6, 293.0	206.6, 301.0
201.0, 296.1	209.0, 296.0	206.6, 294.0	206.6, 302.0
202.0, 296.1	-- --	206.6, 295.0	-- --

6.5.2. Marker size determination

The 2.0 cm height of the lead markers provides a significant signal-noise-ratio in the edge detection. Different widths of marker have been used to measure the reproducibility of the marker edges and marker position. Ten measurements have been done. Reproducibility of measurement results (Table 6.2) shows that a 30 × 30 pixel size marker provides highly accurate and reproducible results in detecting the edge.

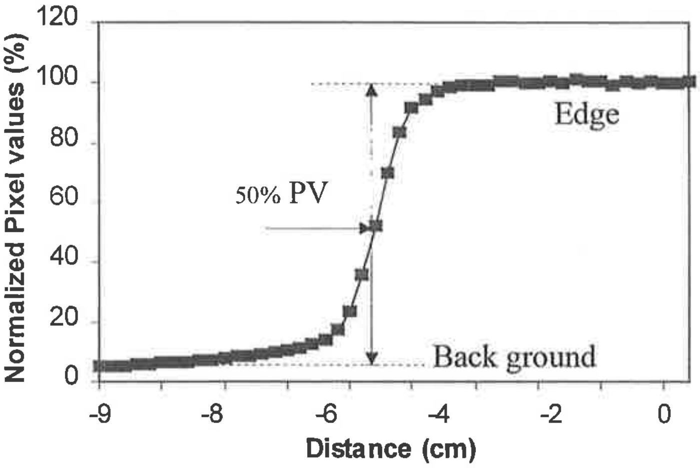

Figure 6.8. A schematic shows how to calculate the edge position. The pixel values are normalized using average pixel value from ROI 10 × 10 pixels in the centre of the marker.

Table 6.2. Reproducibility test of position determination for markers of various sizes; the standard deviation from 10 measurements is shown.

Marker size (pixel)	**10 × 10**	**20 × 20**	**30 × 30**	**40 × 40**
SD (pixel)	**2.00**	**0.41**	**0.20**	**0.15**

Due to the noise level and the divergence effect of the beam (beam non-uniformity), a larger marker does not provide significant improvement to the edge detection and a smaller size marker causes a larger standard deviation and lower reproducibility of determination of the marker position. From the pixel size of BEAMVIEW^{PLUS}, which is 0.5 mm per pixel, the marker size should be 1.5 cm. Because of the beam divergence, the pixels near the corners cannot be used to determine the edges, the marker size was chosen to be 2.5 cm.

6.6. Determination of the detector assembly shift during gantry rotation

Before the mechanical alignment can be assessed, a correction must be made for any possible image movement caused by factors not related to mechanical alignment of the linac. From the quality assurance procedures of EPIDs, the geometrical accuracy of the EPID is one of the most important criteria (see chapter 3). During the test procedure, the gantry will rotate 180°. However, as the gantry rotates, the EPID detector assembly can shift relative to the beam due to flexing in the mechanical structure of the detector assembly. Sagging of the EPID up to a few mm has been reported during gantry rotation (Murrer, *et al.* 2000). That causes the shift of the radiation area (phantom or patient images) relative to the origin of the image matrix (see Figure 6.9). Furthermore, the camera itself can shift or rotate at different gantry angles due to gravity or loose structures. As a result, the camera's view of the detector will change causing the image of the beam to shift relative to the origin of the image matrix. Although these shifts are not a problem of the misalignment itself, it will affect the image registration during the test procedure. Consequently, appropriate corrections must be performed. In our test procedure, this is done simultaneously with the test step one as explained in the following section. A common reference point must be selected for image registration during the test procedure; the origin of the image matrix was chosen in this study.

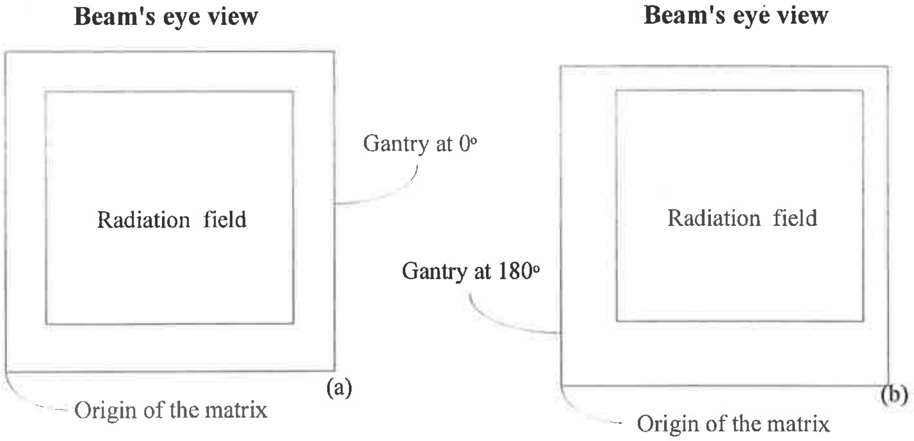

Figure 6.9. A schematic of image shifts. (a) an unshifted image (b) an image shifted due to EPID shift and camera shift/rotation .

6.7. A novel alignment test procedure with an EPID

The individual cases of mechanical misalignment as well as the set-up procedure are illustrated in Figure 6.10. Figure 6.10a shows the correct alignment observed when the gantry rotates from 0° to 180° angles. The gantry rotational axis is perpendicular to the plane of the figure and the collimator rotational axis is in the plane of the paper. Positions of the source and markers are indicated. Figure 6.10b illustrates collimator and gantry axes misalignment, the collimator axis shifts after the gantry rotates from 0° to 180°. Figure 6.10c illustrates jaw asymmetry and Figure 6.10d illustrates the effect of source displacement for gantry rotation from 0° to 180°.

In the first step (see Figure 6.11), the collimator rotation angle is set to 90°, the gantry angle to 0° and a marker, M', is placed on the couch (the central plane of the marker is placed at the isocentre plane, making the source to surface distances at gantry angles 0° and 180° equal). Another marker, M, is placed on top of the EPID detector screen. One image is acquired, then rotate the gantry to 180° and another image is acquired. With the positions of the markers, M and M', and radiation field centre, O, identified, the distances of M'O, and MO can be calculated (all the positions are relative to the origin of the EPID image matrix (x_0, y_0)). By comparing the distances M'O, and the positions of marker M' for the two images, the alignment problems can be evaluated.

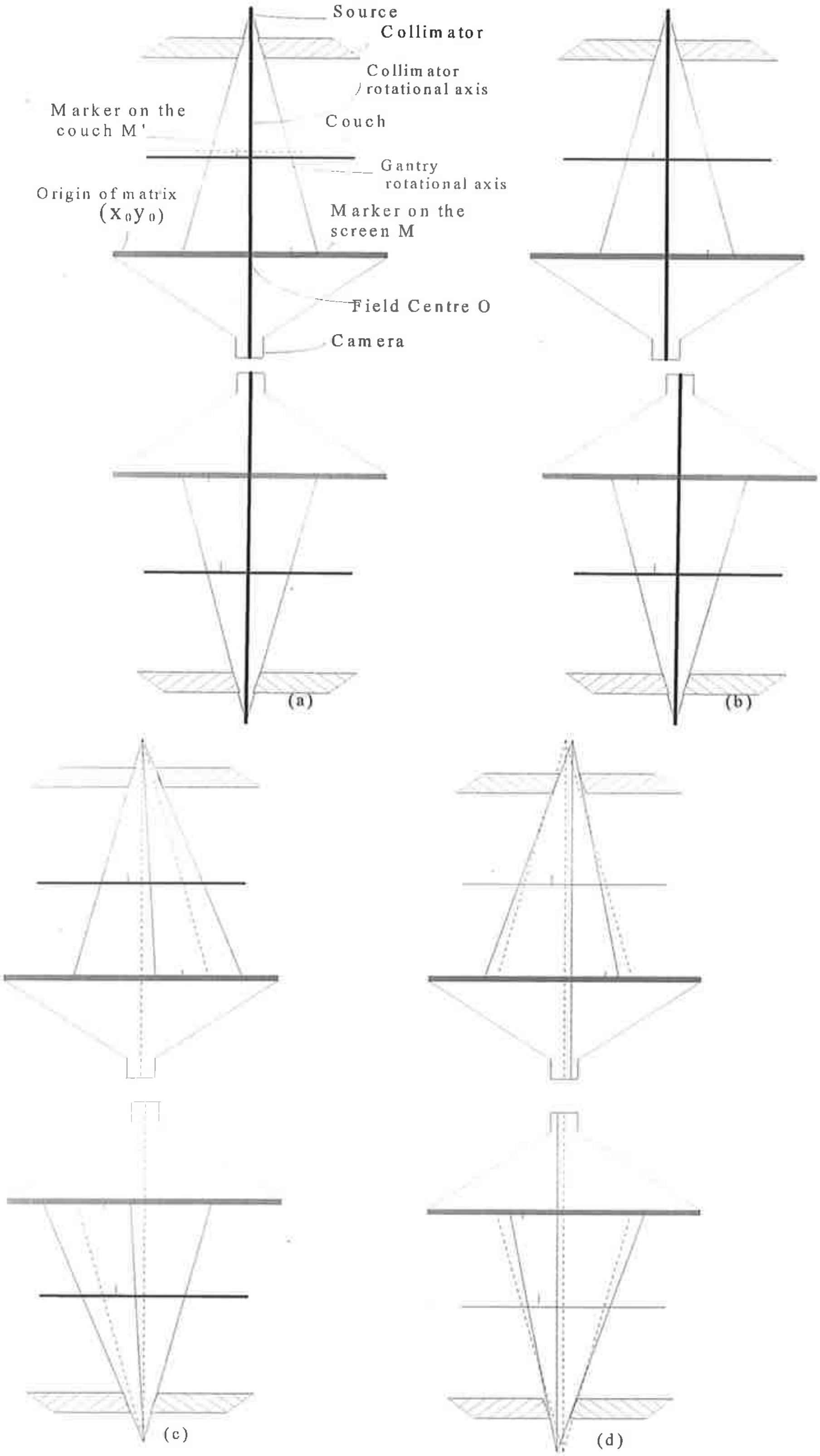

Figure 6.10. A schematic of beam alignment test using Beamview plus system; (a) correct alignment; (b) collimator and gantry axes intersection problems; (c) jaw symmetry problem; and (d) source position problem. Solid lines represent actual positions of axis and radiation field edges while dashed lines represent their ideal positions.

From figure 6.12, the difference of the distances M'O for the two images, ***d'***, is derived as:

$$d' = \sqrt{[(M'_{1x} - O_{1x}) - (O_{2x} - M'_{2x})]^2 + [(M'_{1y} - O_{1y}) - (M'_{2y} - O_{2y})]^2}, \tag{6.3}$$

where subscripts *1* and *2* correspond to the images acquired at gantry at 0° and 180°, respectively. The difference, ***d***, of the distances MO for the two images is calculated differently, using the geometrical distance only as marker M rotates with the EPID and its position relative to the origin of the EPID matrix does not change for two gantry positions.

$$d = \sqrt{(M_{1x} - O_{1x})^2 + (M_{1y} - O_{1y})^2} - \sqrt{(M_{2x} - O_{2x})^2 + (M_{2y} - O_{2y})^2}, \tag{6.4}$$

Note that ***d'*** is not the geometrical distance of M' to the beam centre in the two images because of the rotation. It is derived from the distance between M' and beam centre in the x and y directions separately. If the value of ***d'*** is greater than 0 mm and less than 2 mm, then one or more of the alignment problems has occurred, however, the mechanical alignment is within the recommend tolerance and no further action is required. It should also be noted that the calculation of the distance of M'O is independent of image shifts caused by EPID shift and camera shift/rotation. On the other hand, the positions of O and the distances MO will change for the two gantry positions if the EPID system is shifted. The amount of shift or rotation can be therefore determined from a comparison of the distances MO and the position O for the two images. This correction is then used for a calculation of the position of M'. The correction formula is as follows:

$$\begin{aligned} M'_{2xCor} &= (512 - M'_{2x}) + (O_{2x} - O_{1x}) \\ M'_{2yCor} &= M'_{2y} + (O_{2y} - O_{1y}) \end{aligned} , \tag{6.5}$$

where indices *1* and *2* have the same meaning as with equation (6.3). The term 512 comes from the gantry rotation, which makes the image rotate 180°. The Beam view plus image dimension is 512 × 480, so the value of 512 in equation (6.5) results from the array dimension.

If there is a problem with the collimator and gantry rotation axes, the position of the marker M' will change (after correction for the EPID shift/rotation with equation (6.4)).

However, the position of the marker M' is independent of the source position and/or jaw symmetry problems and the second step must be carried out to distinguish the causes of misalignment.

In the second step, set the gantry to 0° and the collimator to 90°, acquire one image, then rotate the collimator 180° away, i.e. 270°, and acquire another image. If the position of the radiation beam centre, O, has changed but the position of M' has not, then a jaw asymmetry problem has been identified. On the other hand, none of these parameters will change if there is a source position problem. The flow chart for the test procedure is described in Figure 6.11 and findings related to individual alignment problems are summarized in Table 6.3.

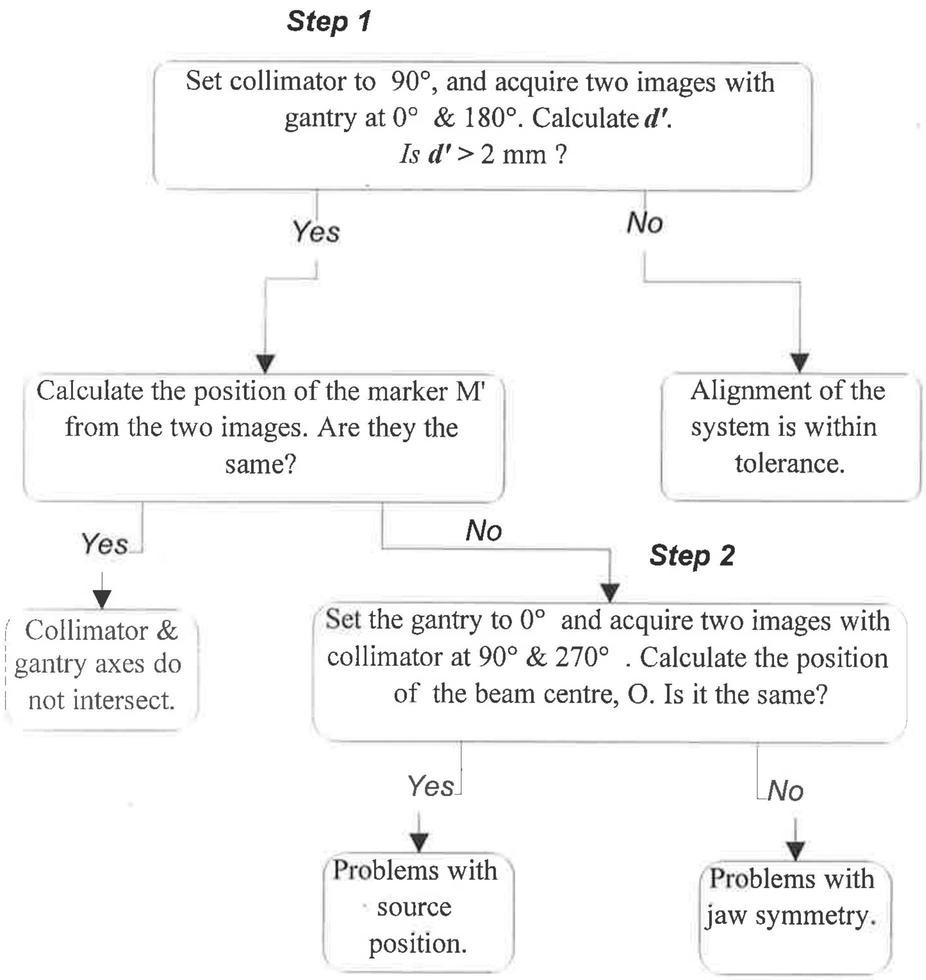

Figure 6.11. The flow chart for the test procedure.

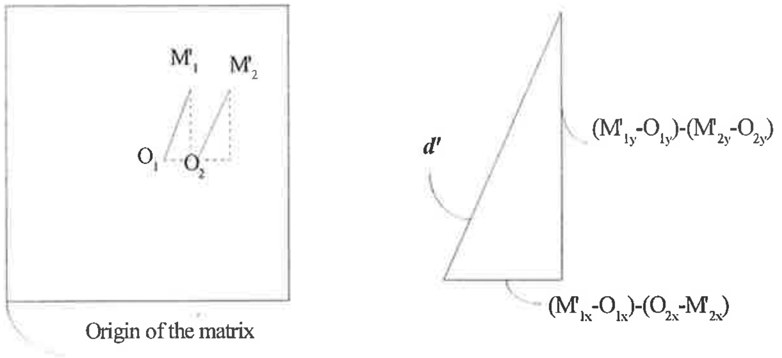

Figure 6.12. A schematic for the derivation of *d'*.

Table 6.3. Summary of mechanical alignment tests.

Problems	Pos. M	Pos. O	Pos. M'	D	d'	Dete.
Collimator at 90° and gantry rotates from 0° to 180°						
Camera Rotates and/or Shift	Y	Y	Y	N	N**	Y
EPID house and camera as one object shift	N	Y	Y	Y	N	Y
Collimator and gantry Axes not intersect	N	N	Y	N	Y	Y
Source position problem	N	N	N	N	Y	N**
Jaw asymmetry	N	N	N	N	Y	N**
Gantry at 180° and collimator rotates from 90° to 270°						
Camera Rotates or Shift	N	N	N	N	N	N
EPID house and camera as one object shift	N	N	N	N	N	N
Collimator and gantry Axes not intersect	N	N	N	N	N	N
Source position problem	N	N	N	N	N	Y
Jaw asymmetry	N	Y	N	Y	Y	Y

Note: Y means position or the distance have changed. Dete. means detectable.

** only the camera rotation problem.

During the test procedures, it is important that (a) the couch is not moved during the gantry rotation, (b) the gantry and collimator are set to within 0.1° of the required angles. A deviation of 0.1° from the intended gantry angle (0° or 180°) would cause about 1.75 mm beam displacement at the isocentre plane. This is an inherent accuracy of the gantry angle setting for the treatment units, not related to the test procedure.

The software involved in this study such as beam centre localization, marker positions determination, marker edges detection and Beaview^{PLUS} image reading were developed in Interactive Data analysis Language (IDL). These programs are PC based, easy to transfer between PCs and aimed to provide quick analysis the experiment data.

6.8. Results with a Siemens linear accelerator

6.8.1. EPID test results

The two-step procedure mentioned above was performed on a Siemens linear accelerator. Its mechanical alignment was estimated using 6 MV x-rays. The test results are presented in Table 6.4. The images are presented in Figures 6.13.

Table 6.4. The results of the beam alignment tests carried out. Data and errors are pixel numbers with 1 pixel ≈ 0.5 mm.

Gantry (± 0.1°)	Colli. (± 0.1°)	Beam Centre (X,Y)(± 0.1)	Marker M (X,Y)(± 0.1)	Marker M' (X,Y)(± 0.1)	*d* (±0.4)	*d'* (±0.4)
0.0°	90.0°	258.4,229.7	155.8,282.5	295.5, 206.6	0.5	2.2
180.0°	90.0°	255.1,241.0	151.6,290.8	295.2,205.3*		
180.0°	270.0°	255.4,239.3	151.6,290.6	295.7, 205.3*	N/A	

*** Positions were corrected for the shift of the EPID and the camera using equation (6.5).**

The results of the first measurement, intended to examine the status of the mechanical alignment of the Siemens accelerator, indicate that:

(1) The distance from marker M to the field centre, O, has changed by 0.3 ± 0.2 mm meaning that the EPID housing and camera have shifted as one object.

(2) The position of the beam centre, O, has changed approximately by 6.0 ± 0.1 mm from the gantry at 0° to 180° meaning that, apart from the EPID system shift, the camera itself, has moved inside the house of EPID during the gantry rotation.

(3) The field centre, O, has changed 0.85 mm from collimator at 90° to 270° indicating jaw asymmetry is within tolerance.

(4) The position of M' has changed by 0.75 ± 0.07 mm (after correcting for the EPID and camera shift) indicating that the collimator and gantry axes intersect within 0.75 mm circle from the isocentre.

(5) The distance M'O has changed by 1.1 ± 0.2 mm (*d'*) from gantry at 0° to 180° showing that the collimator and gantry axes intersection and source position are not ideal points, but are within 2 mm tolerance (AAPM, 1995). These results therefore mean that the mechanical alignment of the Siemens accelerator is acceptable.

Table 6.4 shows the test results for one measurement only; multiple tests (10 measurements) show reproducible results for this test procedure with the standard deviation of 0.5 pixel (0.25 mm).

6.8.2. Star shot results

A star shot has been commonly adopted by many radiotherapy centres (r.f. chapter 2). For comparison a star shot test, using radiographic film, was also performed to test the gantry rotational axis. The results show that the rotational axes of the gantry and collimator do not intersect but are within 2 mm tolerance, confirming the results of the EPID measurement.

6.8.3. Pre-set jaw asymmetry test

To test the procedure further, a jaw asymmetry of 2 mm was simulated by moving a single jaw. The findings of the procedure were compared with this preset value of asymmetry in order to assess the accuracy of the technique. The results are presented in Table 6.5.

The results, under the condition of simulated 2 mm jaw asymmetry, show:

(1) The difference, *d'*, of distance M'O is 5.5 ± 0.5 pixels reflecting there is a 2.75 ± 0.25 mm mechanical alignment problem (when considering the original minor discrepancy, this result agrees within the error with the setup value of 2 mm).

(2) The position of M' has changed by 0.50 ± 0.07 mm.

(3) With the collimator rotated 180°, the position of the beam centre, O, has changed by 2.15 ± 0.25 mm. The left and right field edges have shifted to the right by the same amount as the beam centre. These results agree well, within the error, with the pre-set value of jaw asymmetry of 2 mm thus confirming the accuracy of the technique described.

Table 6.5. The results of the measurement under the condition of 2 mm simulated jaw asymmetry (data are measured in pixels).

Gantry (±0.1°)	Colli. (±0.1°)	Beam Centre (X,Y)(± 0.1)	Marker M (X,Y)(± 0.1)	Marker M' (X,Y)(± 0.1)	*d* (±0.4)	*d'* (±0.4)
0.0°	90.0°	253.2, 238.9	202.4, 310.7	334.8, 183.6*	3.4	5.5
180.0°	90.0°	257.2, 227.3	205.2,302.4	334.5, 184.5		
180.0°	270.0°	260.9, 225.8	205.8, 302.4	334.9, 184.9	N/A	

* Positions were corrected for the shift of the EPID and the camera using equation (6.5).

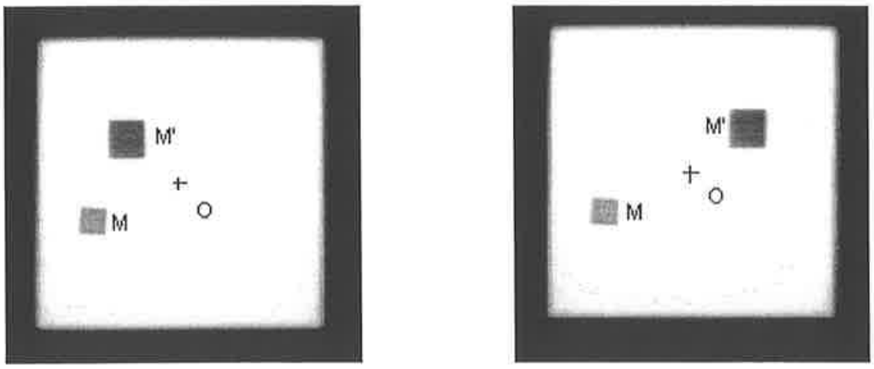

(a) (b)

Figure 6.13. EPID images with markers M and M' for (a) gantry at 180°, (b) gantry at 0°. From (a) and (b) an image shift can be identified in the horizontal direction.

6.9. Conclusion and discussion

The spit-field test assumes that the alignment problems which cause the radiation field to be displaced in the longitudinal direction (i.e. along a line parallel to the gantry rotational axis) will seldom result in shifts upon gantry rotation and are consequently of less clinical importance. Since the split-field test only detects lateral shifts, it cannot detect the sagging of the treatment head support which is illustrated in Fig. 6.1e. The reported technique in this chapter can detect the treatment head sagging problem, since it calculates the distances in two dimensions. However, further tests will be needed to distinguish it from the problem of the collimator and gantry rotational axes not intersecting.

The procedure described here provides a method for evaluating the mechanical alignment of a linear accelerator with a high degree of accuracy. It is simultaneously sensitive to all general causes of beam misalignment. Consequently, it is suitable for routine quality assurance. The whole test typically takes only about 10 minutes to perform, including image processing. There is no film processing and digitising procedures involved and the image analysis is virtually real time. Unlike some conventional methods, this procedure does not depend on the coincidence of the light and radiation fields.

This test can detect less than 2 mm deviation from jaw symmetry. Also the source position and gantry and collimator rotation axes intersection problems can be detected and quantified (i.e. it can be determined whether the overall mechanical alignment of the medical linear accelerator is within tolerance of 2 mm diameter circle). The cumulative accuracy obtained in this test is 0.25 mm. The position of marker M also provides information about the EPID shift/rotation (since an image shift of 6 mm was detected due to EPID movement for gantry at 90° and 270°) which should be taken into account when the device is used for confirmation of the correct patient set up.

Chapter 7

Assessment of Linac Mechanical and Radiation Isocentre with an Electronic Portal Imaging Device

7.1. Introduction

Regular checks on the performance of radiotherapy treatment units are essential and a variety of protocols have been published (AAPM, 1975 & 1994, Boyer, 1979, Essenburg, 1972, Lutz, 1981). These protocols identify that the determination of the mechanical and radiation isocentre must be accurate and unambiguous since both the position of the radiation field on patients and the positioning aids are referenced to the isocentre. This chapter discusses an accurate, simple and fast technique developed for the assessment and monitoring of the position of the mechanical and radiation isocentre with an EPID system.

The radiation isocentre is defined as the centre of the smallest sphere through which the axes of the gantry, collimator and couch pass for all angles of these motions (AAPM, 1995). This is illustrated in figure 7.1. The rotational axes of collimator and couch are within the paper plane and the gantry rotation axis is perpendicular to the paper plane. The mechanical isocentre is the centre of the smallest sphere through which the axes of the gantry & collimator pass for all angles of these motions. (Khan, 1992), see figure 7.2.

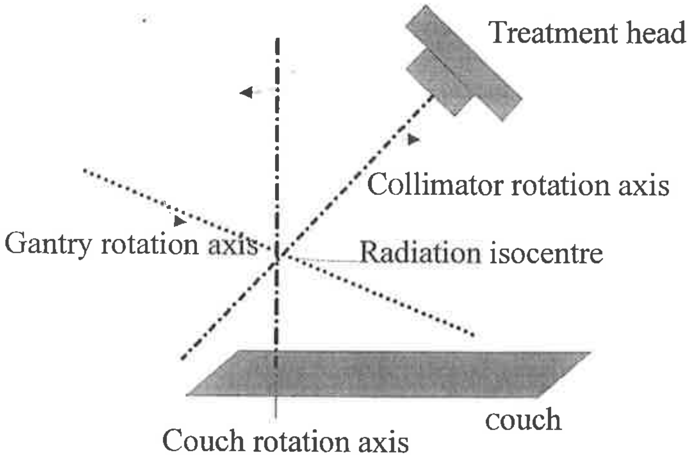

Figure 7.1. Definition of radiation isocentre.

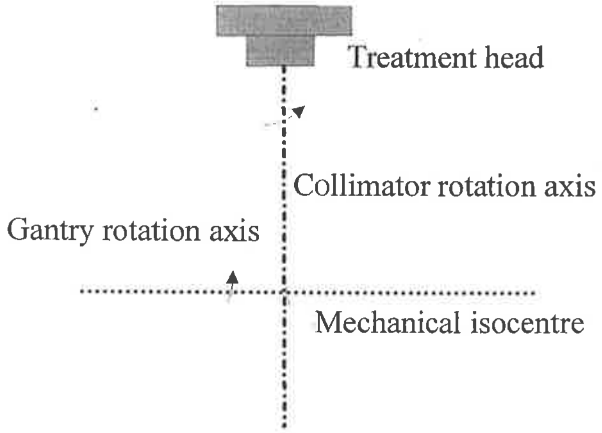

Figure 7.2. Definition of mechanical isocentre.

7.2. Conventional methods

The conventional methods used to determine the radiation and mechanical isocentre have been described by many authors (Khan, 1992, AAPM 1975, 1995, Green, 1997). The mechanical isocentre check is a measure of the coincidence of the tip of a front pointer installed on the collimator and the isocentre point marker typically mounted on the treatment couch (see chapter 2, figure 2.1). The radiation isocentre check involves exposing films at different gantry, collimator and couch rotation angles to produce "star shots", using jaws set to a narrow slit, from the collimator, gantry and treatment couch rotations. Lines drawn manually through the middle of the slit images define the intersection point(s) of the slit images. The spatial spread of the intersection points is determined by visual examination (see figure 7.3). The lines present the middle of the slit images with ~ 5 mm width at isocentre plane.

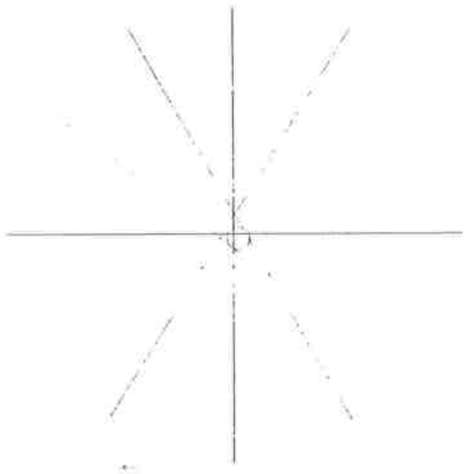

Figure 7.3. Schematic of "star shot" results. The lines represent exposures at gantry angles which are about 20° apart. The circle shows the uncertainty of the radiation isocentre.

The conventional method of using front pointers to decide the mechanical isocentre position, while simple in concept involves extensive measurements. Hudson (1988) developed a simple technique to check the mechanical isocentre position and size by measuring the displacement of the optical pointer on a flat scale on the surface of the treatment couch. The Hudson technique delineates the cross hair position on graph paper. The projection image of the cross hairs have a width ~2 mm at isocentre plane; this determines that the delineation lines will cause at least ~0.5 mm uncertainty.

The radiation isocentre determination using "star shots" involves exposing and developing several ready pack films and less quantitative measurements, i.e. less accurate as the centres of the slit images is determined subjectively by eye only. Furthermore, the radiation isocentre is measured separately for the gantry, collimator and couch rotations. It cannot be guaranteed that the three isocentres independently measured for the gantry, collimator and couch rotation will intersect within the recommended 2 mm diameter sphere. On the other side, mechanical isocentre measured with front pointers is determined from the collimator rotations and gantry rotations. If the light field and radiation field coincidence is confirmed the interception of the collimator, gantry rotation axes of radiation field can be determined. That means the radiation isocentre check depends on the radiation and light field coincidence.

7.3. Isocentre assessment with an EPID

In this chapter, the application of an EPID for radiation and mechanical isocentre co-incidence will be investigated. Compared with conventional methods, the assessment of the position of the mechanical isocentre and radiation isocentre using an EPID with a light/radiation scintillation detector screen, can be more accurate, quantitative, simple and fast.

7.3.1. Theory

7.3.1.1. Determination of the mechanical isocentre

The mechanical isocentre can be determined using the linear accelerator's optical system. The coincidence of the mechanical axis of the collimator assembly, the light beam axis and cross hairs must be maintained throughout test procedures. These can be tested by rotating the collimator 180° and checking the coincidence of (a) the light field edges and (b) the intersection of diagonals and the position of cross hairs (AAPM, 1975, Khan, 1992). Under these conditions, the assessment of the mechanical isocentre can be achieved by checking the optical isocentre (which is determined from the optical system) of the treatment unit.

The simple geometry for calculating the displacement between the isocentre at gantry 0° and at any angle ϑ is shown in Figure 7.4. The EPID detector screen is positioned in the assumed isocentric plane, i.e. 100 cm from source.

The difference of the cross hair positions between the gantry at 0° and any other angle, ϑ, can be calculated. The true distance Δd from mechanical isocentre is related to the measured distance ΔA from the images by (see Figure 7.4)

$$\Delta d = \Delta A \ \cos\vartheta, \tag{7.1}$$

where ϑ is the gantry rotation angle from vertical position. The vertical deviation from the isocentre can also be calculated from $\Delta A/\tan\vartheta$. ΔA is a more easily measured value than the value of Δd because of the amplification factor $1/\cos\vartheta$.

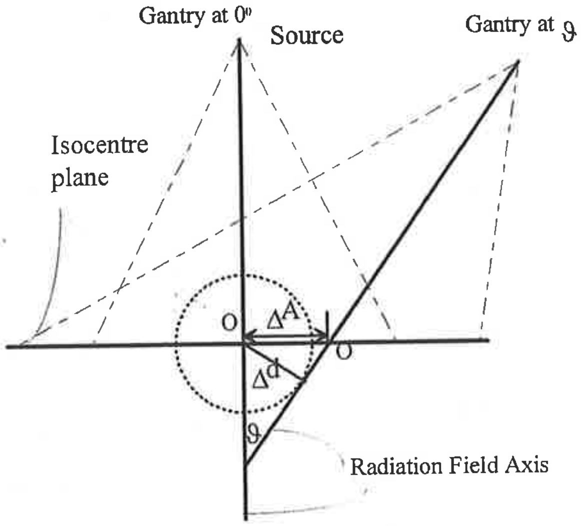

Figure 7.4. Schematic of calculating the displacements of cross hair position at different gantry angles.

The cross hair position can easily be located in each EPID light field image using a PC based program. The intensity distribution of a profile through the cross hairs in the light field images is close to being Gaussian. With a Gaussian function fitted to the cross hair profile, the cross hair position can be determined from the peak intensity position and the standard deviation. In order to increase the accuracy, 20 points of each side of the cross hairs were determined to fit a straight line. The intersection point of two lines fitted to the orthogonal cross hairs determined the intersection point of the cross hairs (see figure 7.5).

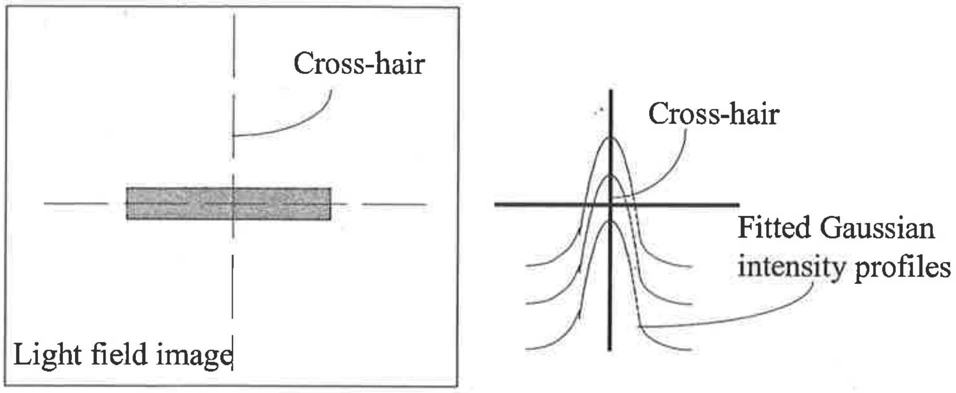

Figure 7.5. Determining cross hair position within a light field image.

7.3.1.2. Experimental determination of the radiation isocentre

The radiation isocentre was determined independently for the gantry, collimator, and treatment couch rotations using the radiation field directed to an EPID.

7.3.1.2.1. Collimator rotation measurements

The collimator rotation axis position was determined by examining the radiation field centre at different collimator angles. The radiation field centre was calculated from each image acquired at different collimator angular positions. These centre positions should be located within a circle 2 mm in diameter. To determine the radiation field centre, two beam profiles were plotted at the crossplane and inplane respectively (around the central part of the field). Connecting the two corresponding midpoints (inplane/crossplane) will form a bisector line. The intersection of the crossplane and inplane bisector lines indicates the position of the radiation beam centre (*Liu et. al,* 2000, also ref. Chapter 6).

7.3.1.2.2. Gantry rotation measurements

When radiation is present, the optical cross hairs cannot be seen in the EPID images, and the radiation field centres cannot be determined by locating the cross hair positions. However, the projected radiation field centre, O_{mes}, on BIS 710 detector plane can be located for each gantry rotation angle. The method was described by Liu *et al.* (2000). On the other hand, the expected projected radiation field centre, $O^{'}_{cal}$, can be calculated from the simple geometry shown in Figure 7.6. Consequently, the shift of the projected radiation field centres, between O_{mes} and $O^{'}_{cal}$, can be derived from the predicted and measured values. From the geometry of figure 7.6, using trigonometric functions the following equations can be derived:

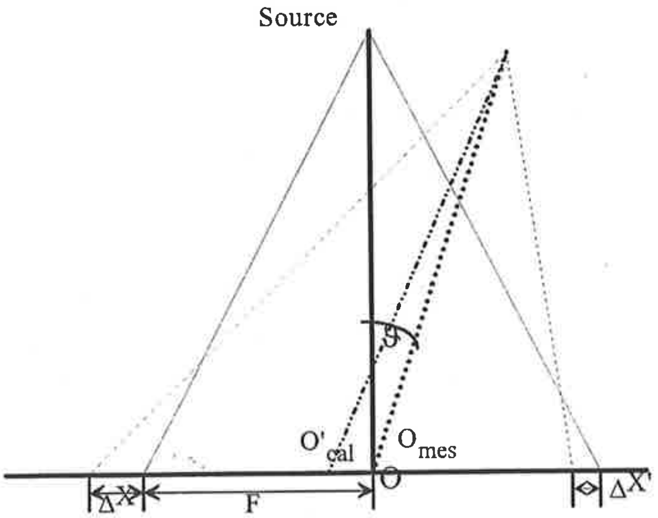

Figure 7.6. Geometry used to calculate the radiation field centre, $O^{'}_{cal}$, at gantry angular position θ. O is the radiation field centre at 0° gantry.

$$\Delta X = F\frac{S(1-\cos\theta)+F\sin\theta}{S\cos\theta - F\sin\theta} \tag{7.2}$$

$$\Delta X' = F\frac{S(\cos\theta - 1)+F\sin\theta}{S\cos\theta + F\sin\theta}, \tag{7.3}$$

where F is half the radiation field size in a horizontal plane measured at gantry angular position 0°. S is the source to surface distance (SSD). ΔX and $\Delta X'$ are the radiation field edge displacements in the horizontal direction (figure 7.7 and 7.8). The radiation field size, F' at gantry angle θ, is given by the following equation

$$F' = \Delta X + \Delta X' + F = \frac{F\cos\theta}{\cos^2\theta - F^2\sin^2\theta / S^2}, \tag{7.4}$$

If the S >> F and θ is small, equation (7.4) can be simplified to equation (7.5). In this paper S =100 cm, F = 7.5 cm and $\theta \le 60°$.

$$F' = \frac{F}{\cos\theta}, \tag{7.5}$$

The difference between equation (7.4) and (7.5) with these parameters is less than 0.1 mm. The ratio of field sizes calculated from equation (7.4) and (7.5) plotted against gantry angle is given in figure 7.9. Therefore the radiation field centre at the gantry angular position θ, can be calculated from the new field size *F'* using equation (7.7).

$$O = F + A\ , \tag{7.6}$$

$$O'_{cal} = F' + A - \Delta X\,, \tag{7.7}$$

where *A* is the left radiation field edges at 0° gantry and can be calculated from the 50% intensity values from the radiation images.

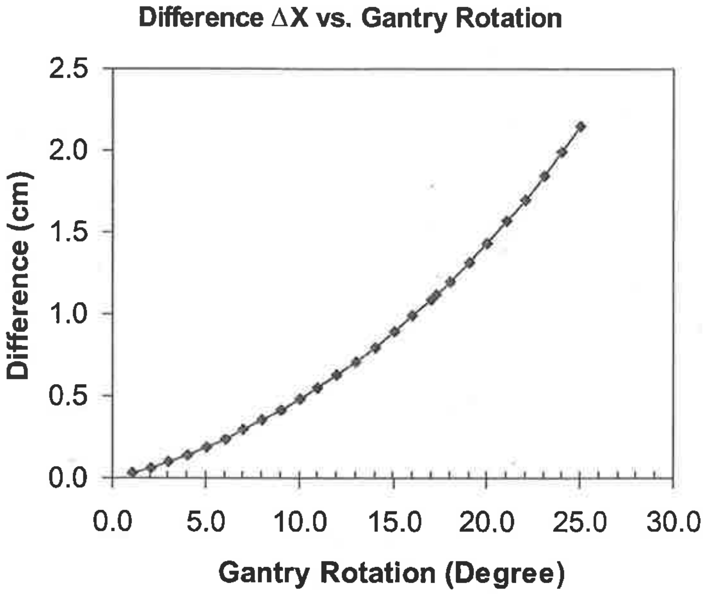

Figure 7.7. The radiation field shift ΔX with gantry angle. The field size is 15 cm and SSD is 100 cm.

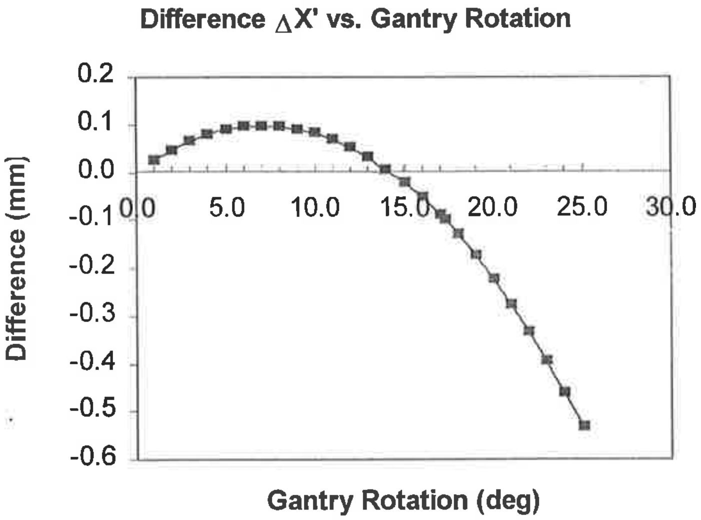

Figure 7.8. The radiation field shift *ΔX'* with gantry angle. The field size is 15 cm and SSD is 100 cm.

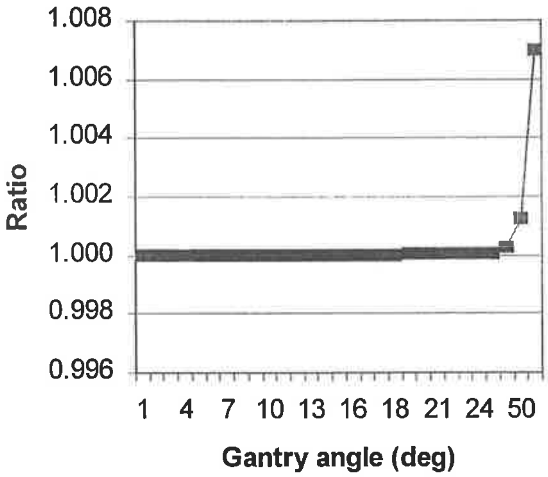

Figure 7.9. The ratio of field sizes calculated from equations (7.4) and (7.5) for a original field size 25 × 25 cm. It shows that for small gantry angles the two equations give the same results.

7.3.2 Experiment techniques

7.3.2.1. EPID and accelerator

The EPID used in this chapter is stand-alone video-based EPID, the Wellhöfer Dosimetrie BIS 710. Its detailed characteristics have been described in chapter 4. The manufacturer also provides a combined light and radiation scintillation detector screen designed to check light and radiation field coincidence. The current investigation and measurements were performed using 6 MV photon beams on a Siemens KD-2 linac (Siemens Medical Systems, Inc.).

7.3.2.2 Determination of the mechanical isocentre

1. Collimator rotation measurements

The BIS 710 was set up on the treatment couch (Figure 7.10) with a source to scintillation layer distance of 100 cm. The gantry was set to an angular position of 0°, and eight cross hairs images (light field images) were acquired at collimator rotational increments of 45° with the light field size at 20×15 cm^2 . The light field images were analysed and the cross hair positions were located within each image.

2. Gantry rotation measurements

With the collimator set at an arbitrary angular position, say 90°, cross hair images were acquired and stored at gantry rotational increments of 10° (on both clockwise and anti-clockwise directions). At the same time, graph paper was laid on the top of the BIS 710 detector screen and the cross hair positions were recorded at each gantry imaging position.

The cross hair positions were located within each image and ΔA was measured from the images and Δd was calculated using equation (7.1).

7.3.2.3 Determination of the radiation isocentre position

1. Collimator rotation measurements

Investigation of the radiation field centre position at different collimator angular positions shows any displacement of the collimator rotational axis during collimator rotation.

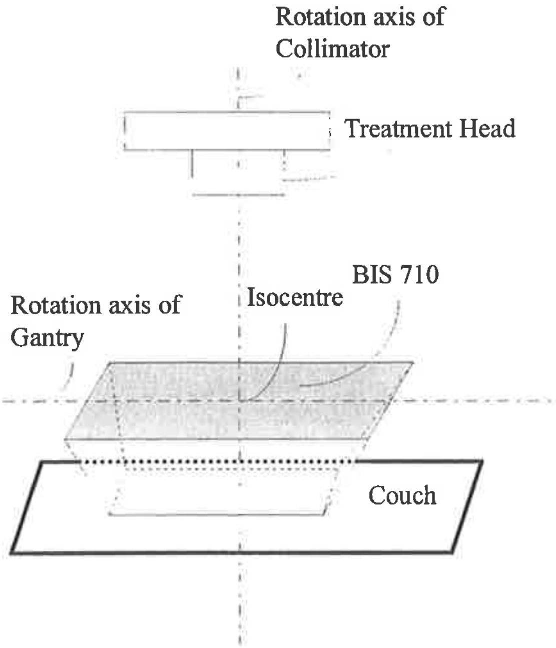

Figure 7.10. Schematic of the mechanical isocentre test set up geometry.

By keeping the placement of the EPID the same as in previous section (see Figure 7.10), an exposure is made with a radiation field size 15 × 20 cm. Images were acquired at collimator angle 0°, then with the collimator rotated through 360° in 90° steps (this selected step size makes the radiation field centre easier to calculate). The radiation field centre was determined from the inplane/crossplane profiles for each image.

2. Gantry rotation measurements

By monitoring the radiation field centre position at different gantry angles and then comparing with the theoretical (calculated) positions, the deviation of the gantry rotational axis position during rotation can be shown.

Radiation images were also acquired at each gantry angular position where light field images were acquired (c. f. S III. B.2). To avoid the image overlap, there is a limitation of gantry rotation step size in the "star shot" technique. Unlike the film technique with star shots, there is no limitation on the size of the gantry rotation step. However, images cannot be acquired when the gantry angle is larger than 60° (clockwise direction), or less than 300° (anti-clockwise direction) due to the BIS 710 setup position and the detector's physical size. After radiation images were acquired, the new field size could be calculated from equation (7.4) or (7.5). Then the field centres could be calculated as well as measured.

3. Treatment couch measurements

In order to investigate the treatment couch rotation axis position, a $2.5 \times 2.5 \times 1.0$ *cm* rectangular lead marker with machined edges was put on the top of the couch which was 100.5 cm away from the source. The marker was set at about 3 cm, an arbitrary distance to make measurements easier, away from the cross hairs centre. The BIS 710 was setup on the floor (Figure 7.11). Radiation images were acquired in steps of 15° in couch rotation. The marker's position within an image is located by detecting two perpendicular edges of the marker (Liu *et al.*, 2000, or ref. Chapter 4). The radiation centre can be determined from the inplane/crossplane beam profiles and is fixed during the couch rotation. The distances of the marker to the radiation field centre were calculated. The measured marker position should be located within a 2 mm loop centred at the radiation centre during the treatment couch rotation.

7.3.3 RESULTS AND DISCUSSION

7.3.3.1 Determination of the mechanical isocentre

1. Collimator rotation measurements

The cross hair positions for the collimator rotation are presented in Table 7.1. The fourth and fifth columns are the deviations of cross hair position from the mean position. The mean position is calculated by averaging the cross hair positions from all the images. Figure 7.12 show the distribution of cross hair positions at different collimator angles and the average (ideal position). The two dashed lines indicate a reference distance of 2 mm. The results demonstrated that all the cross hair positions were within a 1 mm diameter circle.

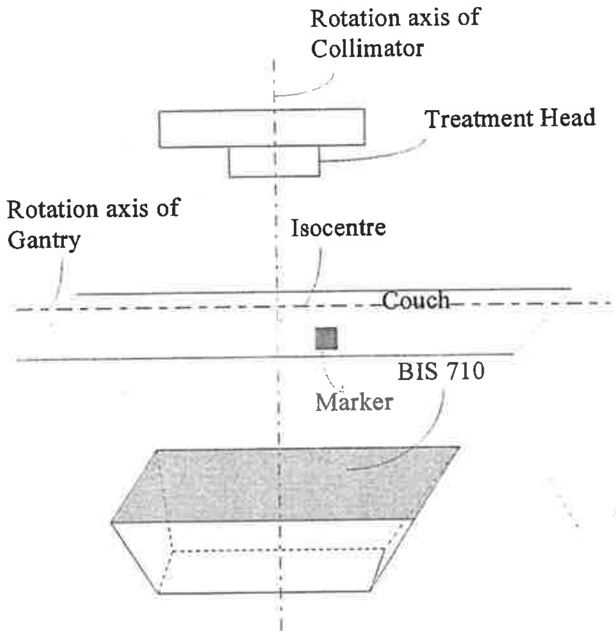

Figure 7.11. Schematic of BIS 710 setup geometry to test isocentre of the treatment couch.

Table 7.1. Cross hair positions at different collimator angles. Data are presented in pixels with 1 pixel = 0.6 mm.

Collimator	Cross hairs		Δx	Δy	Δd
ϑ	X (±0.3 pixel)	Y (±0.3 pixel)	(±0.3 pixel)	(±0.3 pixel)	(±0.3 pixel)
0°	249.5	248.1	-0.7	0.1	0.7
45°	250.0	248.0	-0.2	0.0	0.2
90°	250.0	247.5	-0.2	-0.5	0.7
135°	250.2	247.3	0.0	-0.7	0.7
180°	251.0	247.5	0.8	-0.5	0.9
225°	250.0	248.0	-0.2	0.0	0.2
270°	250.5	248.7	0.3	0.7	0.8
315°	250.2	248.5	0.0	0.5	0.5

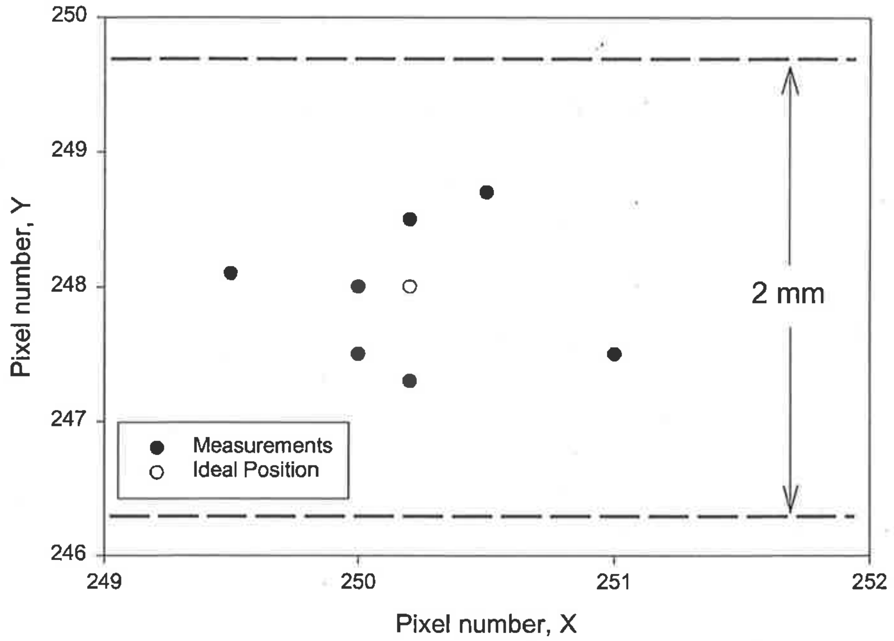

Figure 7.12. The scatter plots of cross hair positions (shown by diamond) at different collimator angles and the mean position (dot). Scale on both axes is pixel number.

2. Gantry rotation measurements

Example data for gantry rotations are given in Table 7.2. As a comparison, the graph paper recorded data are also shown in this table. The negative gantry angles indicate anti-clock wise gantry rotation. The graph paper data were determined by drawing the cross hair position and measuring the difference in positions between gantry angles ϑ and 0°. The accuracy achieved with this method is 0.5 mm. The fourth column in table 7.2 shows the cross hair positions in the direction perpendicular to the axis of the gantry rotation (in pixel numbers), and there is no displacement in the other direction (within the error). The mechanical isocentre of the tested accelerator was therefore within a sphere of diameter 2 mm, which is within the suggested tolerance (AAPM, 1995).

Table 7.2. Results of mechanical isocentre positions from BIS710 measurements (with 1 pixel = 0.6 mm) and graph paper (manual) measurements.

	Graph paper		BIS 710		
Gantry Angle ϑ	ΔA (± 0.5 mm)	Δd (±0.5mm)	Cross hair (± 0.3 pixel)	ΔA (± 0.3 pixel)	Δd (±0.3 pixel)
-60°	2.2	1.1	260.2	3.0	1.5
-50°	2.0	1.3	259.1	2.4	1.5
-40°	1.5	1.1	258.3	1.8	1.4
-30°	0.8	0.7	256.8	1.2	1.0
-20°	0.8	0.8	256.0	0.6	0.6
-10°	0.2	0.2	255.3	0.0	0.0
0°	0.0	0.0	255.2	0.0	0.0
10°	0.5	0.5	255.1	0.0	0.0
20°	1.0	0.9	253.9	-0.6	-0.6
30°	1.0	0.9	253.1	-1.2	-1.0
40°	1.8	1.4	253.2	-1.2	-0.9
50°	2.0	1.3	252.1	-1.8	-1.2
60°	2.2	1.1	249.9	-3.0	-1.5

7.3.3.2. Determination of the radiation isocentre position

1. Collimator rotation measurements

Example data for the determination of the radiation isocentre from collimator rotation are shown in Table 7.3. The values of Δx and Δy were calculated from the difference in the radiation field centre in the x and y directions from the mean positions, respectively. The value of Δd is the absolute value of radiation field centre displacement from the collimator angle 0°.

2. Gantry rotation measurements

Sample data for gantry rotations are given in Table 7.4. The values of d and d' in Table 4 are the displacements between the radiation field centres at gantry angular positions 0° and θ, as measured and calculated, respectively. If $\Delta d = d - d'$, then $\Delta d = \Delta A * \cos\theta$ gives us the distance from the isocentre. The results show that the radiation isocentre of the gantry for this machine is contained within a 2 mm diameter circle.

Table 7.3. Collimator rotation test results. Data are in pixels.

Collimator ϑ	Field Centre X (±0.1 pixel)	Field Centre Y (±0.1 pixel)	Δx (±0.2 pixel)	Δy (±0.2 pixel)	Δd (±0.2 pixel)
0°	250.2	244.7	-0.3	-0.1	0.3
90°	250.6	243.8	0.1	-1.0	1.0
180°	251.6	245.3	1.1	0.5	1.2
270°	249.9	245.2	-0.6	0.4	0.9
360°	250.3	245.0	-0.2	0.2	0.3

Table 7.4. Results of radiation isocentre position from BIS710 measurement. Data are in pixels (with 1 pixel = 0.6 mm).

Gantry angle ϑ	Centre (±0.5 pixel) (measured)	Centre (calculated)	d (±0.5 pixel) (measured)	d' (calculated)	Δd	ΔT Δd *cos*θ
-60°	251.0	256.4	8.5	13.3	4.8	2.4
-50°	246.8	250.4	4.3	7.3	2.9	1.9
-40°	244.9	247.4	2.4	4.4	1.9	1.5
-30°	243.9	245.8	1.5	2.7	1.2	1.1
-20°	243.3	244.4	0.9	1.3	0.5	0.4
-10°	242.8	243.8	0.4	0.7	0.4	0.4
0°	242.5	243.1	0.0	0.0	0.0	0.0
10°	242.0	241.2	0.4	-1.9	1.4	1.4
20°	241.5	240.3	1.0	-2.7	1.8	1.7
30°	240.7	239.2	1.8	-3.9	2.1	1.8
40°	239.2	237.5	3.2	-5.5	2.3	1.8
50°	236.7	234.6	5.8	-8.4	2.6	1.7
60°	231.2	228.6	11.3	-14.4	3.2	1.6

3. *Treatment couch rotation measurements*

The positions of the marker, *M*, and radiation field centre, *O* (see figure 7.13), were calculated from every image acquired at different treatment couch angles. The distance *MO* was calculated. The radiation field centre should remain the same during the rotation of the treatment couch and the measurement results confirm this. Plotting the positions of the marker around the radiation field centre position will give the treatment couch rotation axis information. The results show the positions of the marker are distributed within a annulus of 2 mm in width (as shown in Figure 7.13). This also means that the treatment couch rotation axis is located within a circle 2 mm in diameter during its rotation for this machine.

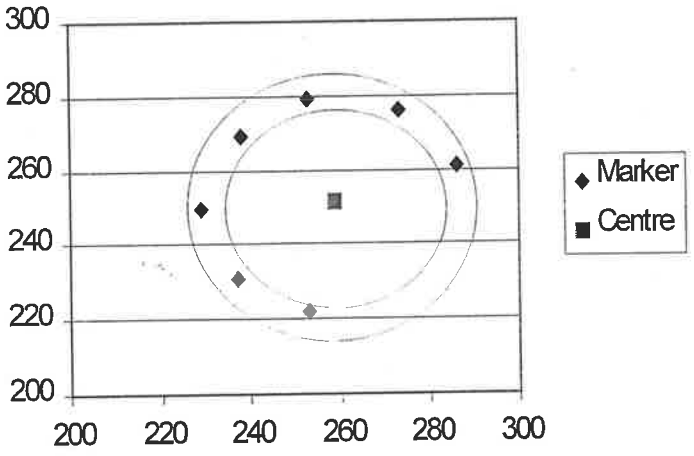

Figure 7.13. The scattered marker positions with couch rotation. The marker positions lie within a 2 mm annulus. Both axes are in pixels with 1 pixel ~ 0.6 mm.

The displacements of the distance of MO from the mean value of MO at different couch angles are plotted in figure 7.14. It shows that all the displacements are within ± 1 mm tolerance.

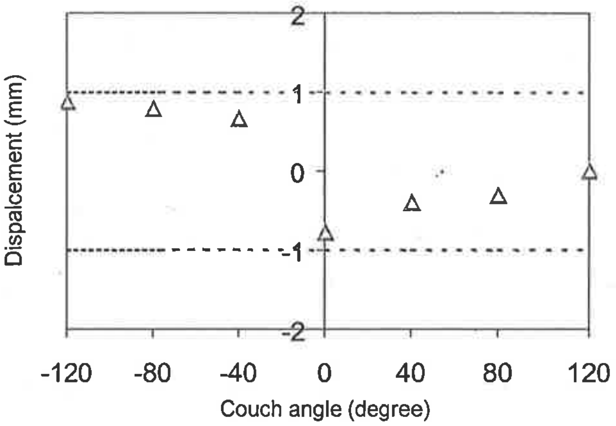

Figure 7.14. The displacement at each treatment couch angle.

Since the radiation isocentre was assessed separately from the gantry, collimator and couch rotations, the question arises how to determine whether the three isocentres intercept within a 2 mm diameter sphere. The conventional methods (e.g. star shots) cannot determine this because it depends on the mechanical isocentre test results and the coincidence of the light and radiation fields. However, coincidence of the three isocentres can be checked with this reported technique. Since the set-up geometry is the same for collimator and gantry rotation measurements, the isocentres derived from the collimator and gantry can be compared with each other. During the couch rotation measurements, an additional collimator rotation measurement can be made, then the isocentre can be derived from collimator and couch rotations and can be compared to each other. By comparing the isocentre measured from collimator/gantry check with the collimator/couch check the isocentre from the three separate measurements can be crosschecked.

Another important thing which needs to be noted is the set-up position of the EPID on the couch. Precise alignment to the front distance pointer or side lasers to 100 cm SSD is assumed. If there is 1 mm (x) shift up (shown in figure 7.15), the measured crosshair displacement, $\Delta A'$, will be larger than the real displacement, ΔA, because the BIS 710 detector will intersect the collimator axis at different level. From the geometry of figure 7.15 the following equation can be derived:

$$\Delta A^{'} = \Delta A + x\tan\theta \quad \text{mm}, \tag{7.8}$$

$$\Delta d^{'} = \Delta d + x\sin\theta\,. \tag{7.7}$$

This means that for gantry angles larger than 45° there will be larger than 1 mm uncertainty for ΔA if there is a 1 mm set up shift. The error for a true displacement of isocentre, Δd, is ~0.7 mm and the larger the angle the larger the error. This is a significant error and caution must be taken during the BIS set up.

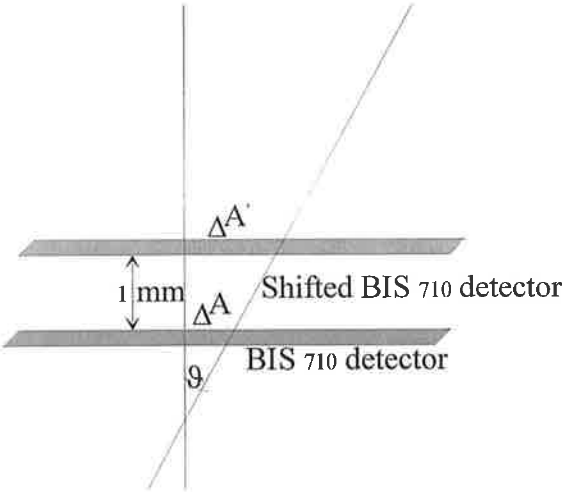

Figure 7.15. Schematic of a x = 1 mm set up displacement in of BIS introduces uncertainty of measurements.

7.3.4. Conclusions

A technique has been demonstrated which provides a simple approach to assessing the mechanical and radiation isocentres of a medical linear accelerator. The technique utilizes an EPID and provides an alternative to conventional techniques. When compared with conventional techniques, it is much easier to implement and faster to analyse and quantify the results by using a PC based program. It also minimizes human error, thereby increasing the measurement accuracy. The radiation isocentre check is independent of the coincidence of the light field and radiation field.

In practice a 0.3 mm accuracy for the collimator and couch radiation axes position check can be achieved over the full range of collimator and couch rotation angles. For the gantry rotation axis position check the maximum gantry angle used in this technique was ±60°. This is a limitation of the method. However, since the remaining part of the gantry rotation range is symmetrical with measured part of the range, the technique is adequate for routine diagnosis of the occurrence of problems. It should be noted that the accuracy of these new tests is dependent on the coincidence of the cross-wires with the axis of rotation of the collimator and the symmetry of the jaws.

It is concluded that the Wellhöfer BIS 710 can be used to assess the mechanical and radiation isocentre position in routine quality assurance checks.

Chapter 8

Conclusions and Possible Future Research

8.1. Conclusions

The aim of this thesis was to investigate the applications of electronic portal imaging devices (EPIDs) in radiotherapy quality assurance and to improve the efficiency and accuracy of QA. Although this investigation has only concentrated on video-based electronic portal imaging devices, such as the Wellhofer Dosimetrie BIS710 system and Siemens' Beamview^{PLUS}, the concepts and physics approach discussed can be implemented with any other type of EPID provide the spatial resolutions is better than 1 mm.

Prior to implementing EPIDs for radiotherapy quality assurance tests, their other clinical applications and characteristics were reviewed and investigated. Several techniques for using an EPID to carry out radiotherapy QA have been developed. The previous well-developed electronic portal imaging techniques have concentrated on verification of the setup geometry, such as the radiation beam size, shape and location relative to anatomical structures within the patient (van Herk *et al* 1988, Bijhold *et al* 1991b, Bel *et al* 1996, Meertens *et al* 1990 and Michalski *et al* 1993). Among them the patient set-up error measurements and on-line or off-line correction strategies have been implemented in many radiotherapy centres (Ezz *et al.* 1992, De Neve *et al.* 1993, Luchka and Shalev 1996, Bijhold *et al.*, 1992, Bel *et al.*, 1993, 1996). Also, their use for dosimetry has been investigated in the last few years. These dosimetric applications fall into two main categories: measurements of transmitted dose (i.e. two-dimensional dose maps) (Kirby *et al* 1995, Beollaard *et al* 1996, McNutt *et al* 1996) and the design of compensators to achieve the desired dose (Yin *et al* 1994, Roback and Gerbi 1995). Further investigation of the calibration accuracy and patient dose measurements is still needed due to Intensity Modulated Radiation Therapy (IMRT) becoming more widespread, and compensator design using EPIDs becoming less widely used.

A stand-alone EPID's characteristics have been investigated and the calibration curves (which describe the relationship between the incident monitor unit on the detector and output pixel values) were measured. The effect of the beam parameters, such as beam field size, dose rate, photon energy, and sampling times have been studied in a region of interest of 10 × 10 pixels around the central beam axis. The results demonstrate that the output pixel value is a linear function of the incident monitor units, which is expected for a video based portal imaging system (Leong 1986, Kirby and Williams 1993). The field size effect found for the BIS710 is similar to ion chamber measurements at smaller field sizes. However, the output pixel values increase more rapidly at larger field sizes due to design of the optical system within the BIS housng. The system was found to be insensitive to dose rate, but is energy dependent. A linear relationship has been shown for different sampling times below 1.8 s (but a non-linear relation is expected after 2 s). It is the energy dependence of the fluorescent screen/video based EPIDs and the effect of scattered radiation in the optical chain which hamper their accurate application in absolute dose measurements.

The QA techniques developed with EPIDs include mechanical alignment assessment, flatness and symmetry assessment, light and radiation isocentre assessment, photon beam energy constancy check, and light and radiation field coincidence tests. An EPID (BEAMVIEW^{PLUS}) mounted onto a gantry was used to detect and distinguish the causes of possible mechanical misalignment, such as source position displacement relative to the collimator rotational axis, collimator jaw asymmetry, or when the rotational axes of the gantry and the collimator do not intersect. It was shown that this technique provides a method for evaluating the mechanical alignment of a linear accelerator with a high degree of accuracy and the method is simultaneously sensitive to all general causes of beam misalignment (ref. Chap. 5). Consequently, the EPID is suitable for routine quality assurance.

As EPIDs have the ability to provide two-dimensional portal dose distribution information (at least for relative doses), it is possible to investigate the flatness and symmetry within a pre-defined area. A stand-alone EPID, i.e. a Beam Imaging System (BIS710), was used to investigate the flatness and symmetry of x-ray beams from linacs. Instead of determining the flatness and symmetry along the major axes only, this EPID allows the beam flatness and symmetry to be assessed within a two dimensional area and any "cold" or "hot" spot could be found. The method developed provides more information about the beam flatness and symmetry than a simple calculation of flatness and symmetry from the major axes. Indeed, it can be used as a secondary device to monitor the x-ray beam flatness and symmetry.

As it is essential to check the isocentre of the linac for patient set up, the mechanical and radiation isocentres were assessed using the BIS710. This study has demonstrated the feasibility of using the EPID to assess mechanical and radiation isocentres of a linear accelerator in a quick and efficient way with a higher degree of accuracy achieved as compared to more conventional methods, e.g. the star shot. The combined light and radiation sensitive scintillation detector provides digital and quantitative measurements that enable the light and radiation field coincidence to be checked. The light field edges can be difficult to detect accurately, because the light intensity is not uniform especially near the field edges. A relative uniform intensity of light field maybe needed in order to prove the accuracy, otherwise care must be taken when checking the coincidence of the light field and radiation field. Nevertheless it does provide a useful and quick check for light and radiation coincidence and the method compares well with the film technique for convenience and accuracy. The EPID was also used for checking x-ray energy constancy, and for enhanced dynamic wedge dose distribution checks.

The thesis concludes that EPIDs can be used for quality assurance after careful measurements of their inherent physical parameters. The work has demonstrated the feasibility of using an EPID to assess mechanical alignment, and the mechanical and radiation isocentres of a linear accelerator in a quick and efficient way with a higher degree of accuracy achieved as compared to more conventional methods. The EPID can be effectively used to assess and monitor the mechanical and radiation isocenters. EPIDs can also be used to provide quick dosimetric checks provided it is calibrated.

The variety PC-based softwares were developed for this thesis with IDL. This ensures that different formatted images and experimental data could be analysed easily.

8.2. Possible Future Research and Applications

The techniques developed in Chapter 4,5, and 6 could be used clinically, provided that the EPIDs are available and carefully calibrated. The techniques developed with EPIDs are not intended to substitute for all the conventional techniques and the gold standard devices used in medical physics. The techniques developed can improve efficiency and accuracy, and as secondary standard devices, the EPIDs can be used to do some routine quality assurance checks.

Possible future work with these devices might be:

(1) Electron beam flatness, symmetry, and energy constancy checks. Because of beam contamination, the electron energy constancy cannot be represented by one parameter. If a percentage depth dose can be obtained from a wedge-like phantom, then the depth of maximum dose, electron practical range, and the slope of the tail part of the percentage depth dose curve together might be able to provide a better index for electron energy.

(2) EPIDs can provide patient dose verifications especially for the IMRT treatment modality.

There are still a significant number of challenges to be faced for the full implementation of EPIDs in a more effective and accurate manner in radiotherapy.

Appendix A

Table 1. Regularly checked parameters and the corresponding tolerance limits for of medical accelerators as recommended by AAPM (AAPM, 1994).

Frequency	Procedure	Tolerance
Daily		
	Dosimetry	
	(1) X-ray output constancy	3%
	(2) Electron output constancy	3%
	Mechanical	
	(1) Localiztion lasers	2 mm
	(2) Distance indicator (ODI)	2 mm
	Safety	
	(1) Door interlock	Functional
	(2) Audio monitor	Functional
Monthly		
	Dosimetry	
	(1) X-ray output constancy	2%
	(2) Electron output constancy	2%
	(3) Backup monitor constancy	2%
	(4) X-ray central axis dosimetry parameter (PDD, TAR) constancy	2%
	(5) Electron central axis dosimetry parameter (PDD) constancy	2 mm @therapeutic depth
	(6) X-ray beam flatness constancy	2 %

(7) Electron beam flatness constancy	3%
(8) X-ray and electron symmetry	3%

Safety interlock

(1) Emergency off switches	Functional
(2) Wedge, electron cone interlocks	Functional

Mechanical

(1) Light/radiation field coincidence	2 mm or 1% on a side
(2) Gantry/collimator angle indicators	1 deg
(3) Wedge position	2 mm (2% change)
(4) Tray position	2 mm
(5) Applicator position	2 mm
(6) Field size indicator	2 mm
(7) Cross-hair centring	2 mm diameter
(8) Treatment couch position indicators	2 mm/1 deg
(9) Latching of wedges, blocking tray	Functional
(10) Jaw symmetry	2 mm
(11) Field light intensity	Functional

Annual

Dosimetry

(1) X-ray/electron output calibration constancy	2%
(2) Field size dependency of x-ray output constancy	2%
(3) Output factor constancy for electron applicators	2%
(4) Central axis dosimetry parameter (PDD, TAR) constancy	2%
(5) Off-axis factor constancy	2%
(6) Transmission factor constancy for all treatment accessories	2%
(7) Wedge transmission factor constancy	2%
(8) Monitor chamber linearity	1%
(9) X-ray output constancy vs gantry angle	2%

(9) Electron output constancy vs gantry angle	2%
(9) Off-axis factor constancy vs gantry angle	2%
(12) Arc mode	Mfrs. specs

Safety interlock

(1) Follow manufacturer's test procedures	Functional

Mechanical checks

(1) Collimator rotation isocenter	2 mm diameter
(2) Gantry rotation isocenter	2 mm diameter
(3) Couch rotation isocenter	2 mm diameter
(4) Coincidence of collimator, gantry, couch, axes with isocenter	2 mm diameter
(5) Coincidence of rotation and mechanical isocenter	2 mm diameter
(6) Table top sag	2 mm
(7) Vertical travel of table	2 mm

Appendix B

The programs developed in this thesis were coded with IDL® developed by Research System, Inc. Boulder, CO (Windows version 5.2), unless specified otherwise. The following list includes the major programs and source codes only. In the source codes, explanatory comments start and finish with “;”.

BIS_710.pro

This program manipulates BIS 710 images. It can be used for calculating average pixel values and the standard deviation within a ROI by moving and clicking a mouse. It can also be used to measure flatness, symmetry at main axes, to rotate the image at arbitrary angle, and to locate the centre of the image etc.

```
;Calculate the Average and Standard Diviation in Region of Interest
Function ROI_SD, NewIm, Subx, Suby,Mean, SD, win_num;

REPEAT Begin
 Ans1=1
 print, 'PLEASE PRESS LEFT MOUSE BUTTON TO SELECT THE ROI.'
 !Err=1
 wset,win_num
 WSHOW, Win_num
 WHILE(!Err EQ 1) DO BEGIN $
     Cursor,X,Y, /DEVICE, /DOWN; Waiting for push down the left button.
     PRINT,X,Y
 ENDWHILE

 IF (x GE subx/2) and (y GE Suby/2) THEN $
     ROI=EXTRAC(NewIm, x-subx/2,y-suby/2,subx,suby)   $
 ELSE $
     ROI=EXTRAC(NewIm, x,y,subx,suby)

 ;***** CALCULATE STANDARD DEVISION
 data=REFORM(roi, long(Subx*Suby))
 data=float(data)
 Result = MOMENT(data)
 Mean=result(0) & SD= result(1)^0.5
 print,'mean=', result(0),'varian=',result(1)
```

```
 junk=DIALOG_MESSAGE('DO you want to do another region?', /Question, /Cancel)
 IF Junk EQ 'Yes' Then Begin
      WSET,WIN_NUM
    WSHOW, win_num
 Endif
  Ans1=(Junk NE 'Yes') ; if junk='Yes' then Ans1=0 (FALSE),that means should repeat
 endrep $
UNTIL Ans1  ; Repeat mean until it is TRUE. 'SUN' NE 'FUN'=TRUE
return, Mean
END

FUNCTION FIELD_CENTRE, beam, Xsiz, Ysiz, Centre ; calculate the centre of beam
Xsiz=500
b=FLTARR(Xsiz)
;beam=REFORM(image[250,*]); This is the Coloumn profile,
for i=1,499 do b(i)=beam(i)-beam(i-1)
tem=max(b,ii)
tem=min(b,jj)
centre=(ii+jj)/2
Mean0=(beam(10)+beam(490))/2. ; back ground
Mean_c=0.
For i=0,4 do Mean_c=(beam(centre-2+i)+Mean_c)/2. ; mean of centre axis
c50=(Mean_c-Mean0)/2.+Mean0
Beam_FF=FLTARR(Xsiz/2)   ; first half of the profile
Beam_SF=FLTARR(Xsiz/2)   ; second half of the profile

for jj=0,Xsiz/2-1 do beam_FF[jj]=beam[jj] ;
for jj=Xsiz/2, Xsiz-1 do beam_SF[jj-Xsiz/2]=beam[jj] ;

a=min(ABS(beam_ff-c50),j) ; the nearest point to the 50% contour
IF(beam[J] LE c50) Then $
      c50l=j-(c50-beam[j])/(beam[j-1]-beam[j])
IF(beam[j] GT c50) Then begin
   IF(beam[j] NE beam[j+1]) Then $
           c50l=j+(beam[j]-c50)/(beam[j]-beam[j+1])
  IF(beam[j]  EQ beam[j+1]) Then $
          c50l=j+1+(beam[j]-c50)/(beam[j+1]-beam[j+2])
ENDIF

a=min(ABS(beam_Sf-c50),j) ; the nearest point to the 50% contour
IF(beam_sf[J] LE c50) Then $
      c50r=j-(c50-beam_sf[j])/(beam_sf[j-1]-beam_sf[j])
IF(beam_sf[j] GT c50) Then begin
   IF(beam_sf[j] NE beam_sf[j+1]) Then $
      c50r=j+(beam_sf[j]-c50)/(beam_sf[j]-beam_sf[j+1])
 IF(beam_sf[j]  EQ beam_sf[j+1]) Then $
```

```
     c50r=j+1+(beam_sf[j]-c50)/(beam_sf[j+1]-beam_sf[j+2])
ENDIF
C50R=c50r+Xsiz/2.
Centre=(C50l+c50r)/2.
Field_size=C50r-c50l
Return, Field_size
end

;PRO PD_EXAMPLE
cd,'C:\rsi\filmdata' ;data log directory
desc = [ '1\READ IMAGE' , $ ; that is a pull down button  1 start next
        '0\READ NEW DATA' , $ ; next is continuous pull down
        '3\ROTATION' , $ ; this is a sub-pull down and the last for 1
        '2\USER DEFINE DEGREE' , $; the pull down of 3 and the end of 3
        '1\SD' , $ ; same level of Read image and is a pull down
        '0\10 x 10' , $ ; of SD
        '0\20 x 20' , $ ; of SD
        '0\50 x 50' , $
        '2\CUSTOM SIZE' , $ ; of SD, but is the last of SD
        '1\PROFILES', $ ; Same level of Read ... and is pull down
        '0\IN PLANE', $
        '0\CROSS PLANE', $ ; of Profiles and the last (only) one
        '3\PRINT' , $ ; not pull down but same level of Read ...
        '0\IN PLANE' , $
        '2\CROSS PLANE', $
        '0\CENTRE' , $
        '1\FLAT & SYM', $
        '0\IN PLANE' , $ ; next is continuous pull down
        '2\CROSS PLANE' ,$
        '0\ROI' , $
        '2\DONE' ] ; the last button of the same level Read..


;Create the widget:
base = WIDGET_BASE()
EXTRA= WIDGET_BASE(base,/COLUMN)
menu   =   CW_PDMENU(base,   desc,   /RETURN_FULL_NAME,XOFFSET=0);,
XSIZE=500), /RETURN_FULL_NAME
text = WIDGET_TEXT(base,YOFFSET=25,XSIZE=83); ,UNITS=0) ;,FRAME=500
draw = WIDGET_DRAW(base, /FRAME,UVALUE = 'DRAW_WIN_EVENT', $
       RETAIN = 2,XSIZE=500,YSIZE =512);XSIZE=512,YSIZE =480)
WIDGET_CONTROL, /REALIZE, base
WIDGET_CONTROL,draw,Get_value=win_num
info={draw_wid:win_num,text:text}
WIDGET_CONTROL,base,Set_uvalue=info
```

```
;Provide a simple event handler:

REPEAT BEGIN

   ev = WIDGET_EVENT(base)
   WIDGET_CONTROL, ev.top, GET_UVALUE=info
 ITS=ev.value
;   PRINT, ev.value
 CASE ITS OF
     'READ IMAGE.READ NEW DATA' : $ ;this depend on the key words
/RETURN_FULL_NAME

 BEGIN

NewIm=READ_BIS(NewIm, Xsiz, Ysiz);, data_path)
                                                                ;
 NewIm=image

 WSET, info.draw_wid

 WSHOW,win_num

 Tvscl, NewIm

 END
     'READ IMAGE.ROTATION.USER DEFINE DEGREE' :                 $
     BEGIN
     Repeat begin
 An=1

 CONTI:
 junk=DIALOG_MESSAGE('Do you want to rotate the image?'$

, /Question, /Cancel)

 IF (junk EQ 'Yes') Then Begin
     WIDGET_CONTROL, info.text, SET_VALUE='Please input the degree: '
     read, angle
     Newim=ROT(NewIm, angle) ;, missing
     WSET, win_num;info.draw_wid
     WSHOW,win_num
     TVSCL,Newim; TV, congrid(NewIm,512, 512);

 ENDIF ELSE
 begin
         WIDGET_CONTROL, info.text, SET_VALUE='PLEASE CONTNIOUS'
```

```
          GoTO, CONTI
 ENDELSE

 junk=DIALOG_MESSAGE('Rotate Again?', /Question, /Cancel)
 An=(junk NE 'Yes')

 ;WIDGET_CONTROL, info.text, SET_VALUE='Please input the degree: '
  endrep $
 Until An
     WIDGET_CONTROL, info.text, SET_VALUE='END ROTATION'
     END
 'SD.10 x 10' :                                                        $
 BEGIN

 junk=DIALOG_MESSAGE('Do you want change the average Box Size?', /Question,
/Cancel)

 IF (junk EQ 'Yes') Then Begin
     Subx=10 & Suby=10
     Mean=ROI_SD(NewIm, Subx, Suby,Mean, SD, win_num)
WIDGET_CONTROL,info.text,SET_VALUE='Mean='+string(FORMAT='(F6.2)',Mean
)+ $

 '   SD=' + string(FORMAT='(F5.2)',SD)
ENDIF ELSE
 WIDGET_CONTROL, info.text, SET_VALUE='Continue the program!'
 END
      'SD.20 x 20': $
      BEGIN
     junk=DIALOG_MESSAGE('Do you want change the average Box Size?',
/Question, /Cancel)
     IF (junk EQ 'Yes') Then Begin

     Subx=20  &
     Suby=20

 Mean=ROI_SD(NewIm, Subx, Suby,Mean, SD, win_num);,mm,nn)

 WIDGET_CONTROL, info.text, SET_VALUE='  Mean = ' +
string(FORMAT='(F6.2)',Mean)+ $

     '   SD=' + string(FORMAT='(F5.2)',SD)

 ENDIF ELSE
 print, 'Continue the program!'
      END
```

```
  'SD.50 x 50': $
     BEGIN

 junk=DIALOG_MESSAGE('Do you want change the average Box Size?', /Question,
/Cancel)
 IF (junk EQ 'Yes') Then Begin
      Subx=50 &
      Suby=50
      Mean=ROI_SD(NewIm, Subx, Suby,Mean, SD, win_num);,mm,nn)

WIDGET_CONTROL, info.text, SET_VALUE='  Mean =  ' +
string(FORMAT='(F6.2)',Mean)+ $
      '   SD=' + string(FORMAT='(F5.2)',SD)
 ENDIF ELSE
print, 'Continue the program!'
       END
  'SD.CUSTOM SIZE': $
     BEGIN

 junk=DIALOG_MESSAGE('Do you want change the average Box Size?', /Question,
/Cancel)
      IF (junk EQ 'Yes') Then Begin
      Print, 'Please Input the Box Size:'

 READ, Subx, Suby; long(Subx),long(Suby)
 Mean=ROI_SD(NewIm, Subx, Suby,Mean, SD, win_num)
 WIDGET_CONTROL, info.text, SET_VALUE='  Mean  ' +
string(FORMAT='(F6.2)',Mean)+ $
      '   SD=' + string(FORMAT='(F5.2)',SD)
 ENDIF ELSE
 print, 'Continue the program!'
       END
 'FLAT & SYM.IN PLANE' : $
      BEGIN
 WIDGET_CONTROL, info.text, SET_VALUE='PRESS MOUSE BUTTON TO
SELECT ROW'

 !Err=1
 wset,win_num
 WSHOW, Win_num
 WHILE(!Err EQ 1) DO BEGIN $
 Cursor,X,Y, /DEVICE, /DOWN; Waiting for push down the left button.
 beam=reform(NEWIM[*,y])
 beam=MEDIAN(beam,11)
 sym=FLAT_SYm(beam, flat, sym)
```

```
 WIDGET_CONTROL, info.text, SET_VALUE='  Flatness is ' +
string(FORMAT='(F5.2,"%")',flat)+ $
 '   Symmetry is ' + string(FORMAT='(F5.2,"%")',Sym)
 wset,win_num
 WSHOW, Win_num
 ENDWHILE
 END
 'FLAT & SYM.CROSS PLANE' : $
 BEGIN

 WIDGET_CONTROL, info.text, SET_VALUE='PRESS MOUSE BUTTON TO
SELECT ROW'

 !Err=1
 wset,win_num
 WSHOW, Win_num
 WHILE(!Err EQ 1) DO BEGIN $
 Cursor,X,Y, /DEVICE, /DOWN; Waiting for push down the left button.
 beam=reform(NEWIM[X,*])
 beam=MEDIAN(beam,11)
 sym=FLAT_SYm(beam, flat, sym)

 WIDGET_CONTROL, info.text, SET_VALUE=' Flatness is  ' +
string(FORMAT='(F5.2,"%")',flat)+ $
 '   Symmetry is  ' + string(FORMAT='(F5.2,"%")',Sym)

 wset,win_num
 WSHOW, Win_num
 ENDWHILE
 END
 'CENTRE' : $
      BEGIN
      BEAM_x=reform(NewIm[*,250])
      FIELD_SIZ=FIELD_CENTRE(beam_X, Xsiz, Ysiz, YY_C); IS THE CENTRE OF
Y DIRECTION
      BEAM_y=reform(NewIm[YY_C,*])
      FIELD_SIZ=FIELD_CENTRE(beam_y, Xsiz, Ysiz, Y_Centre)
      print, FIELD_SIZ
      BEAM_x=reform(NewIm[*,Y_Centre])
      FIELD_SIZ=FIELD_CENTRE(beam_X, Xsiz, Ysiz, X_Centre)
      print, FIELD_SIZ
      WIDGET_CONTROL, info.text, SET_VALUE='   Field Centre (X,Y)   (   ' +
string(FORMAT='(F6.2)',X_Centre)+ $
      '   '+string(FORMAT='(F6.2)',Y_Centre)+'  )'
      END
```

```
 'PROFILES.IN PLANE': $;the row should be IN Plane,the column should be IN Plane
(BIS ONLY)

      BEGIN
      WIDGET_CONTROL, info.text, SET_VALUE='Please Input the Row Number:'
      READ, rown
      Beamx=NewIm(*, rown)
      for i=RowN+1, RowN+2 do beamx=beamx/2.+ NewIm(*,i)/2.
      beamx = SMOOTH(beamx,3)
      window, /free, xsize=500, ysize=500
      plot, beamx,YTITLE='Pixel Value', XTITLE='No. of ponits';,xrange=[0, 500]
      WSET, win_num
      WSHOW,win_num
      END
 'PROFILES.CROSS PLANE': $
      BEGIN
      WIDGET_CONTROL, info.text, SET_VALUE='Please Input the Column Number:'
      READ, Col_N
      Beamx=NewIm(Col_N,*)
      for i=Col_N+1, Col_N+2 do beamx=beamx/2.+ NewIm(Col_N,*)/2.
      beamx = SMOOTH(beamx,3)
      window, /free, xsize=500, ysize=500
      plot, beamx,YTITLE='Pixel Value', XTITLE='No. of ponits';,xrange=[0, 500]
      WSET, win_num
      WSHOW,win_num
      END
 'ROI' : $
      Begin
      WIDGET_CONTROL, info.text, SET_VALUE='Read the lower left Corner & Top
right corner:'
      read, LLX, LLY, TRX, TRY
      col=TRX-LLX
      row=TRY-LLY
      print,'Xsize(Column)= ',col, ' Ysize(Row)= ', row
      ROI=FLTARR(col,row)
      temp=FLTARR(xsiz,row)
 For i=0, row-1 Do begin
      temp[*,i]=Newim[*,i+LLY]
 For j=0, col-1 Do ROI[j,i]=temp[j+LLX,i]
      endfor

 window, /free, Xsize=col+20, Ysize=row+20
 TVSCL, ROI
 print, max(roi), min(roi)
 END
 'DONE': $
```

```
      BEGIN;
 junk=DIALOG_MESSAGE('Are you sure?', /Question, /Cancel)
  IF (junk EQ 'Yes') Then Begin
      print,'See you later!'
      WIDGET_CONTROL, ev.top, /destroy
  ENDIF ELSE
 print, 'Continue the program!'
      END
; WIDGET_CONTROL, /DESTROY, base
ENDCASE
END UNTIL ev.value EQ 'DONE'
WDELETE, 8
CD, 'C:\RSI\MYPRO'
END
; *************** PRINT OUT THE CALENDAER *********
set_plot, 'printer'
DEVICE, /landscape
CALENDAR,1 ,2000
DEVICE, /CLOSE
set_plot, 'win'
END ; End of the program.
```

BIS_read.pro
This is a function program. It reads BIS 710 images and records the header information such as the sampling time and sampling numbers etc.

```
Function READ_BIS, NewIm,Xsiz, Ysiz
 Xsiz=500l ;column
 Ysiz=500l ;row
File=''
FILE=PickFile(/READ,Filter='*.*');,
Path=data_path);'c:\rsi\tmp');bis\23mv');beamdata')
;header=256
ihdr ={BIS_header, $
      status:0, $ ; intarr(1), which equal two bytes
      extended: bytarr(8), $;strarr(8),
      rows:0, $ ;intarr(1), $
      colums:0, $ ;intarr(1), $
      firstid:0, $ ;intarr(1), $
      secondid:0b, $;;strarr(1),== byte
      name:bytarr(9),  $;strarr(9),
      year:0, $ ;intarr(1), $
      month:0b, $;bytarr(1),$;strarr(1),
      day:0b, $;bytarr(1),$;strarr(1), $
```

```
 hour:0b, $;bytarr(1),$;strarr(1), $
 minute:0b, $;bytarr(1),$;strarr(1), $
 second:0b, $;bytarr(1),$;strarr(1), $
 ix:0, $ ;intarr(1), $; size x in 1/100 mm
 iy:0, $ ;intarr(1), $; size y in 1/100 mm
 FielSiz_in:0, $ ;intarr(1), $; field size in inplane
 FielSiz_Cr:0, $ ;intarr(1), $; field size in crossplane
 SID:0, $ ;intarr(1), $;Source isocentre distance in cm.
 colli:0, $ ;collimator angle
 film_po:0, $ ; deviation perpendicular to measuring plane
 m_type:0, $; measuring type, 512 In/Cr, 1024 In/beam 2048 Cr/beam
 Film_or:0, $; film orientation, 1 emulsion opposite to source, 2 emulsion to source
 SSD:0, $; Source to Surface Distance
 radtype:0, $; Radiation Type
 energy:0, $; Energy/voltage: 0-50Mevoder kV*10
;others:bytarr(199) $
 film_plane:0, $;Film plane position
 phantom:0, $;phantom material
 acctyp:0, $;accessory
 acnu:0, $;accessory number
 fieldtyp:0, $;field type
 asy_jawx:0, $; asymmetry jaws
 asy_jawy:0, $;
 watersurface:0, $;
 isox:0, $;isocentre
 isoy:0, $;
 Hosp:bytarr(30), $; Hospital Name Strarr does not work here.
 Dept:bytarr(30), $ ; department
 therun:bytarr(20), $ ; therapy unit
 Ther_lable:bytarr(20), $
 physicist:bytarr(20), $
 u1:0., $ ; unknown tag
 u2:0., $ ; float array which equal two bytes
;    fNormierFactor:0., $ ; total 205 byte left 51 byte.
 type:0b, $; type of devices?;
 Devices:bytarr(10), $
 Tank_angle:0,$
 Tank:0,$
 Med_dev:0, $; mechanical device, 256 - Table Bis , 4096--Head Bis
 Ver_corr:0b, $; version of correction
 Correct:0b, $; Correction: 0--not corrected, 1-- corrected -Bis 1.35,
  ;2-- corrected -Bis 1.4 and later
 CCD_X: 0,$; CCD active region in X-direction
 CCD_Y: 0, $;CCD active region in X-direction
 Sample_time:0,$; CCD sampling time.
 Sample_No: 0,$; sample numbers
```

```
    Reserved:bytarr(20), $
    Offset:0, $ ;?
    ChekSum:0 $ ;not used
    } ; end of the header infor ; total 256 byte.
OPENR, UNIT, FILE, /GET_LUN
READu, unit,ihdr  ;
newim=intarr(Xsiz,Ysiz) ; image array
READu, unit,newim
NewIm=REVERSE(newim,2)
FREE_LUN, UNIT
;NewIm=MEDIAN(NewIm,11)
Return, NewIm
END
```

BIS_flat_sym.pro

This program automatically calculates the flatness and symmetry of the BIS 710 radiation field images. Firstly, it locates the edges of the radiation field. Secondly, it identifies the predefined area used to calculate the flatness and symmetry. Finally, it calculates the flatness and symmetry within this area.

```
;***** CALCULATE STANDARD DEVISION
Function MEAN_D, roi, Mean, subx, suby
 data=REFORM(roi, (Subx*Suby))
 data=float(data)
 Result = MOMENT(data)
 Mean=result(0) & SD= result(1)^0.5
;print,'mean=', result(0),'varian=',result(1)
Return, Mean
END


Function Edge, NewIm, Xisz,Ysiz, Left_Ed, Right_Ed, Bot_Ed, Top_Ed, X_centre,
Y_centre

;***** Calculate the rufe edge positions by differential *****
RowP=NewIm[*,250]
RowP=reform(RowP)
ColP=NewIm[250,*]
ColP=reform(ColP)
diff=FLTARR(500)
for i=1,499 do diff(i)=RowP(i)-RowP(i-1)
a=max(diff,ii)
Left_Ed=ii
a=min(diff,ii)
```

```
Right_Ed=ii
for i=1,499 do diff(i)=ColP(i)-ColP(i-1)
a=max(diff,ii)
Bot_Ed=ii
a=min(diff,ii)
Top_Ed=ii
X_centre=(Left_Ed+Right_Ed)/2
Y_centre=(Top_ed+Bot_Ed)/2
Print, X_centre,Y_centre
Return, newIm
END
;***** Finish Calculate the ruff edge positions *****
;***** Main axes, Inplane and cross plane, Flatness and symmetry calculation *****

Function IN_CROSS, NewIm, x1,x2, y1, y2,sym,flatness

IF ((Y2-Y1) LT 10.) then begin
 Siz=X2-X1
 xx=INDGEN(Siz)+X1
 yy=(y2+Y1)/2.;fix(k*xx+b); the line pass lower-right and top_left
 temp=reform(Newim[XX,YY])
ENDIF
IF ((X2-X1) LT 10.)  then begin
 Siz=Y2-Y1
 xx=(x2+x1)/2.
 yy=INDGEN(Siz)+Y1
 temp=reform(Newim[XX,YY])
ENDIF
result=size(temp)
Siz=result(1)
Sym=0.
For i= 0,Siz/2-1 do begin
      Ratio=ABS(float(temp(i))/temp(Siz-1-i)-1.)*100.
      IF  RATIO GE Sym THEN Sym=RATIO
ENDFOR
flatness=(float(max(temp))/min(temp)-1.)*100.
return, sym
end

;***** Diagonal Direction flatness and symmetry calculation *****

;***** Diagonal straight line pass two points. *****
Function AXIS_LINE, NewIm, x1,x2, y1, y2,sym,flatness
k=float(Y2-Y1)/(X2-X1)
b=Y2-k*X2
Siz=X2-X1
```

```
xx=INDGEN(Siz)+X1
yy=INTARR(Siz)
yy=fix(k*xx+b); the line pass lower-right and top_left
result=size(Newim[XX,YY])
temp=Newim[XX,YY]
Siz=result(1)
Sym=0.
For i= 0,Siz/2-1 do begin
      Ratio=ABS(float(temp(i))/temp(Siz-1-i)-1.)*100.
      IF  RATIO GE Sym THEN Sym=RATIO
ENDFOR
flatness=(float(max(temp))/min(temp)-1.)*100.
;plot, /noerase,posi=[0.,0.,1.,1.], xx,yy
return, sym
end


;****** MAIN PROGRAM

;******** Automatically find the four corner of the image ********
;set_plot, 'printer'
;DEVICE, /portrait
;Device,SCALE_FACTOR=10
NewIm=READ_BIS(NewIm,Xsiz, Ysiz)
;NewIm=image;_im20
;***** smooth the image MEDIAN FILTER
Newim=Median(newIm,11)
Window, 0, Xsize=Xsiz; Ysize=Ysiz
TVSCL,newim

NewIm=Edge(NewIm,Xisz,Ysiz,   Left_Ed,   Right_Ed,   Bot_Ed,   Top_Ed,   X_centre,
Y_centre) ; the rugh centre of the image X_centre Y_center
subx=10 & suby=10
;left edge detection ;***** the function is defined separately.
x=Left_Ed & y=250
Rex=LR_ED(NewIm,Rex,subx, suby, x, y,X_centre,Y_centre)

;Top edge dtection
x=250 & y=Top_ed
Rey=BT_ED(NewIm,Rey,subx, suby, x, y,X_centre,Y_centre)

;To determin the TOP--LEFT corner
x0=250 & y0=250
TOP_Lx=(rex(0)+rey(0)*rex(1)-rex(1)*rey(1)*X0-Y0*REX(1))/(1.-rex(1)*rey(1))
TOP_Ly=(rey(0)+rex(0)*reY(1)-REY(1)*X0-Y0*REY(1)*REX(1))/(1.+rey(1)*rex(1))
```

```
;To determin the TOP--Right corner
x=Right_Ed & y=250
Rex=LR_ED(NewIm,Rex,subx, suby, x, y,X_centre,Y_centre)
TOP_Rx=(rex(0)+rey(0)*rex(1)-rex(1)*rey(1)*X0-Y0*REX(1))/(1.-rex(1)*rey(1))
TOP_Ry=(rey(0)+rex(0)*reY(1)-REY(1)*X0-Y0*REY(1)*REX(1))/(1.+rey(1)*rex(1))

;To determin the BOTTOM--RIGHT corner
x=250 & y=Bot_ed
Rey=BT_ED(NewIm,Rey,subx, suby, x, y,X_centre,Y_centre)
BOT_Rx=(rex(0)+rey(0)*rex(1)-rex(1)*rey(1)*X0-Y0*REX(1))/(1.-rex(1)*rey(1))
BOT_Ry=(rey(0)+rex(0)*reY(1)-REY(1)*X0-Y0*REY(1)*REX(1))/(1.+rey(1)*rex(1))

;To determin the BOTTOM--LEFT corner
x=Left_Ed & y=250
Rex=LR_ED(NewIm,Rex,subx, suby, x, y,X_centre,Y_centre)
BOT_Lx=(rex(0)+rey(0)*rex(1)-rex(1)*rey(1)*X0-Y0*REX(1))/(1.-rex(1)*rey(1))
BOT_Ly=(rey(0)+rex(0)*reY(1)-REY(1)*X0-Y0*REY(1)*REX(1))/(1.+rey(1)*rex(1))
;******** Symmetry test******
Field_size=((Top_Rx-Top_Lx)+(Bot_Rx-Bot_Lx)+(Top_Ly-Bot_Ly)+(Top_Ry-
Bot_Ry))/4. ; field six of the beam, F
IF (ABS(Field_size-167.) LT 2.) OR (Field_size LT 165.) Then shifts=10./0.6   ; 17.
for F<10 cm dm=1 cm dd=2cm ;F>10 cm dm=0.1F dd=0.2F
IF Field_size GT 170. Then  shifts=0.11*Field_size ;170 is >10 cm field
;shifts=16 ; reference the figure in logbook.
Xf=Top_lx+(Top_rx-Top_lx)/2.+shifts*(Bot_ry-Bot_ly)/Field_size
Yf=Top_ly+(Top_ry-Top_ly)/2.-shifts*(Bot_rx-Bot_lx)/Field_size
Xh=Bot_lx+(Bot_rx-Bot_lx)/2.-shifts*(Bot_ry-Bot_ly)/Field_size
Yh=Bot_ly+(Bot_ry-Bot_ly)/2.+shifts*(Bot_rx-Bot_lx)/Field_size
Xe=Top_lx+(Bot_lx-Top_lx)/2.+shifts*(Top_ly-Bot_ly)/Field_size
Ye=Top_ly+(Bot_ly-Top_ly)/2.+shifts*(Bot_lx-Top_lx)/Field_size
Xg=Bot_rx+(Top_rx-Bot_rx)/2.-shifts*(Top_ry-Bot_ry)/Field_size
Yg=Bot_ry+(Top_ry-Bot_ry)/2.-shifts*(Top_lx-Bot_lx)/Field_size
Xa=Bot_lx+2.*shifts*(Top_rx-Bot_lx)/(2.^0.5*Field_size)
Ya=Bot_ly+2.*shifts*(Top_ry-Bot_ly)/(2.^0.5*Field_size)
Xb=Top_rx-2.*shifts*(Top_rx-Bot_lx)/(2.^0.5*Field_size)
Yb=Top_ry-2.*shifts*(Top_ry-Bot_ly)/(2.^0.5*Field_size)
Xc=Top_lx+2.*shifts*(Bot_rx-Top_lx)/(2.^0.5*Field_size)
Yc=Top_ly-2.*shifts*(Top_ly-Bot_ry)/(2.^0.5*Field_size)
Xd=Bot_rx-2.*shifts*(Bot_rx-Top_lx)/(2.^0.5*Field_size)
Yd=Bot_ry+2.*shifts*(Top_ly-Bot_ry)/(2.^0.5*Field_size)

; ***** calculate the flatness at he main axes, IN/Cross Plane, Two dignal directions
flatness=AXIS_LINE(NewIm, xa, xb, ya, yb,Dig_sym_BL_TR,Dig_flat_BL_TR)
flatness=AXIS_LINE(NewIm, xc, xd, yc, yd,DIG_SYM_TL_BR,Dig_flat_TL_BR)
flatness= IN_CROSS(NewIm, xe, xg, ye, yg,INPLANE_SYM,INLANE_FLATNESS)
flatness= IN_CROSS(NewIm, xh, xf, yh, yf,CRPLANE_SYM,CRLANE_FLATNESS)
```

```
print,FORMAT ='("Diagonal direction(Top-Left to Bottom-Right) Symmetry
:",F5.2,"%")', $
  DIG_SYM_TL_BR
print,FORMAT ='("Diagonal direction(Top-left to Bottom-Right) Flatness :",F5.2,"%")',
$
   Dig_flat_TL_BR
print,FORMAT ='("Diagonal direction(Bottom-Left to Top-Right) Symmetry
:",F5.2,"%")', $
  Dig_sym_BL_TR
print,FORMAT ='("Diagonal direction(Bottom-Left to Top-Right) Flatness:", F5.2,"%")',
$
  Dig_flat_BL_TR
print,FORMAT='("In-plane Symmetry and flatness:",F5.2,"%")', INPLANE_SYM,
INLANE_FLATNESS .
print,FORMAT ='("Cross-plane Symmetry and
Flatness:",F5.2,"%")',CRPLANE_SYM,CRLANE_FLATNESS
; ***** finish calculate the flatness at he main axes

;POLYFILL OF THE FLATNESS AREA
XX=[Xa, Xe, Xc, Xf, Xb, Xg, Xd, Xh]
YY=[Ya, Ye, Yc, Yf, Yb, Yg, Yd, Yh]
POLYFILL, XX, YY, COLOR = 12, /DEVICE
P= POLYFILLV(XX,YY,500,500); THE POINTS WITH THE FLATNESS AREA
SZ=SIZE(P)
FX=LONARR(SZ(1)) & FY=LONARR(SZ(1))
FLAT=FLTARR(500,500)
FF=LONARR(SZ(1))
FOR I=0L,SZ(1)-1 DO BEGIN
 ;put the pixel value within the flatness area to an array.
 FX(I)=P(I)/500
 FY(I)=P(I)-500*FX(I)
 FF(i)=NewIm[FY(I),FX(I)]
 FLAT[FY(I),FX(I)]=NewIm[FY(I),FX(I)]
ENDFOR
Row_n=INTARR(500)
II=0
JJ=0L
SYM=0.0
FOR I=P[0]/500,P[SZ(1)-1]/500 DO BEGIN ;THE ROW NUMBER
     FOR J=0L,SZ(1)-1 DO BEGIN
     IF FX(J) EQ I THEN BEGIN

II=II+1 ;IS THE NUMBER OF EACH ROW
 JJ=JJ+1 ;IS THE TOTAOL NUMBER OF ELEMENTS
     ENDIF
     ENDFOR
```

```
  Row_N(i)=ii
  FOR M=1,II/2-1 DO BEGIN ; fin the center of each row and get the ratio of both sidc
  RATIO=abs(FLOAT(NewIm[FY(II/2+JJ-II-M),I])/NewIm[FY(II/2+JJ-II+M),I]1.)*100.
      IF  RATIO GE SYM THEN SYM=RATIO
  ENDFOR
  II=0
ENDFOR

;Flatness is the ratio of max pixel value and min pixel value within AECFBGDHA
;***** find the maximum and minimum value of the flat area
temp=max(ff,jj); the point position in the image
ROI=EXTRAC(NewIm, FY(jj)-subx/2,FX(jj)-suby/2,subx,suby) ; that means from the
very top part
Mean=MEAN_D(roi,mean_MAX,subx,suby)
;***** find minimum value point position in the image and average over a 10*10
;***** to ensure the point sued to average are with in the flatness area.
temp=min(ff,jj) ;the minmum value of the point within the area
     For i=1,5 do begin
     IF FLAT[FY(JJ)-i,FX(jj)] EQ 0. then begin
     X_start=FY(jj)-i+1.
        I=5
     ENDIF Else X_start=FY(jj)-5
 ENDFOR
 For i=1,5 do begin
     IF FLAT[FY(JJ)+i,FX(jj)] EQ 0. then begin
     X_end=FY(jj)+i-1
     i=5
     ENDIF Else X_end=FY(jj)+5
 ENDFOR
 For i=1,5 do begin
     IF FLAT[FY(JJ),FX(jj)-i] EQ 0. then begin
     Y_start=FX(jj)-i+1
     i=5
     ENDIF Else Y_start=FX(jj)-5
 ENDFOR
 For i=1,5 do begin
     IF FLAT[FY(JJ),FX(jj)+i] EQ 0. then begin
     Y_end=FX(jj)+i-1
     i=5
     ENDIF Else Y_end=FX(jj)+5
 ENDFOR
X_l=X_end-FY(jj)
Y_l=Y_end-FX(jj)
if X_l LT subx/2 then X_start=FY(jj)-subx+X_L
if Y_l LT suby/2 then Y_start=FX(jj)-suby+Y_L
print, X_start, X_end, Y_start, Y_end
```

```
ROI=EXTRAC(Flat, X_start,Y_start,subx,suby) ; that means from the very top part
FOR i=0,99 DO IF ROI(i) EQ 0.0 then ROI(i)=temp
Mean=MEAN_D(roi,mean_MIN,subx,suby)
Flatness=MEAN_MAX/MEAN_MIN
Print, FORMAT = '("The Flatness Is (%) ", F5.2,"%")', (Flatness-1.0)*100.
Print, FORMAT = '("The Symetry  Is (%)", F5.2,"%")',SYM
Print, FORMAT = '("The Flatness from the rare data(%) ", F5.2,"%")',
(Float(max(ff))/min(ff)-1.)*100.
;DEVICE, /CLOSE
;set_plot, 'win'

;***** connect A B C D E F G H  to form the flatness area *****
;TVscl, newIm ; the connection must after
PLOTS,[Xa,Xe], [Ya,Ye],COLOR=12, /DEVICE
PLOTS,[Xe,Xc], [Ye,Yc],COLOR=12, /DEVICE
PLOTS,[Xc,Xf], [Yc,Yf],COLOR=12, /DEVICE
PLOTS,[Xf,Xb], [Yf,Yb],COLOR=12, /DEVICE
PLOTS,[Xb,Xg], [Yb,Yg],COLOR=12, /DEVICE
PLOTS,[Xg,Xd], [Yg,Yd],COLOR=12, /DEVICE
PLOTS,[Xd,Xh], [Yd,Yh],COLOR=12, /DEVICE
PLOTS,[Xh,Xa], [Yh,Ya],COLOR=12, /DEVICE
;***** connect the four corners *****
PLOTS,[Top_Lx, Top_Rx],[Top_Ly,Top_Ry],COLOR=12,/DEVICE
PLOTS,[Top_Rx, Bot_Rx],[Top_Ry,Bot_Ry],COLOR=12,/DEVICE
PLOTS,[Bot_Rx, Bot_Lx],[Bot_Ry,Bot_Ly],COLOR=12, /DEVICE
 ;Position at (0,0).
PLOTS,[Bot_Lx, Top_Lx],[Bot_Ly,Top_Ly],COLOR=12,/DEVICE;

;***** Diagonal straight line pass two points. *****
k1=float(Top_ry-Bot_ly)/(Top_rx-Bot_lx)
b1=Bot_ly-k1*Bot_lx
xx=FINDGEN(300)+80
yy=FLTARR(300)
yy=k1*xx+b1; the line pass lower-left and top right
k2=float(Top_ly-Bot_ry)/(Top_lx-Bot_rx)
b2=Bot_ry-k2*Bot_rx
xx2=FINDGEN(300)+80
yy2=FLTARR(300)
yy2=k2*xx2+b2; the line pass lower-right and top_left
plot, xx,yy,/Noerase,POS=[0., 0., 1.0,1.0],xrange=[0,500],yrange=[0,500],COLOR=12
oplot, xx2, yy2,COLOR=12
;DEVICE, /CLOSE
;set_plot, 'win'
END
```

BIS_film_cor_matrix.pro

This program calculates the BIS correction matrix using film images. First, it reads the digitised film image and resizes the image to fit the BIS image size. Second, film image and BIS 710 image are aligned by shifting and rotating the images. The ratio of the two images is saved into a file as a correction matrix.

```
File="
FILE=PickFile(/READ, Filter='*.bri', Path='c:\rsi\filmdata')
OPENR, UNIT, FILE, /GET_LUN
ihdr=bytarr(256); ihdr=bytarr(128) for *.img images.
READu, unit,ihdr  ;
Xsiz=716l;  film column
Ysiz=716l;  film row
image=intarr(Xsiz,Ysiz) ; image array
READu, unit, image ; end header for the film image.
image=REVERSE(image,2)
FREE_LUN, UNIT
temp = CONGRID(image, 493, 492) ; 493 comes from (716.*406.)/590.
film_re=ROT(temp,1.8)                                                    ;
406 is 25 cmm field size 590 is the image size of the film.
film_re=MEDIAN(film_re,11)

;***** Make resize film image to 500*500 and fit BIS images
N_25=fltarr(500,500)
N_25[0:6,*]=230.
  ; centre at x direction is 6 pixels less
;N_25[*,0:7]=210.
N_25[*,484:499]=210.                                                     ;
centre at x direction is 8 pixels less
N_25[7:499, 0:483]=film_re[*,8:491]

;***** compare the profiles with BIS images.
;Nb=reform(N_25[252,*])
;bb=reform(image[252,*])
;plot, Nb/1514.7
;oplot, bb/605.6, linestyle=2
;window, xsize=500, ysize=500
;Tvscl, N_25

;***** Read BIS image
BIS_image=READ_BIS(NewIm, 500, 500)

;***** Calculate the ratio
C_R=N_25/float(NewIm+0.01)
```

```
;OPENw, UNIT, 'Corr_im_25.dat', /GET_LUN
;printf, unit,C_R
;FREE_LUN, unit
end

;N_im25=FLTARR(500,500)
;N_im25[0:26,0:499]=318.
;N_im25[27:499,0:9]=188.0
;N_im25[27:478,10:476]=ABS(2445-Film_25)
;N_im25[478:499,10:499]=198.
;N_im25[27:478,476:499]=168.
;image=MEDIAN(image,11); smooth the image MEDIAN FILTER
END
```

Bvheader.pro

This program reads the BEAMVIEW^{PLUS} images, and digitized film images, opens the data array for further manipulation and records the header information.

```
Header=BYTARR(1200)
File=''
FILE=PickFile(/READ,Filter='*.dat', Path='c:\rsi\tmp');filmdata'); select files
OPENR, UNIT, FILE, /GET_LUN
READU, unit,header
FREE_LUN, UNIT
Group=STRARR(10)
GroupL=INTARR(10)
Group(0)=STRCOMPRESS('Group'+
STRING(header(1),/print)+STRING(header(0),/print))
GroupL(0)=Header(11)+12
print, Group(0),'
     ', 'Length=', GroupL(0)

I = 1
 ;Initialize index.a 1
HeaderL= GroupL(0)
Sum=Header(11)+12
WHILE (Group(i-1) NE 'Group 224 127' ) DO Begin
 Group(i)=STRCOMPRESS('Group'+ STRING(header(Sum+1),/print)$
       +STRING(header(Sum),/print))
 GroupL(i)=Header(Sum+11)+12
```

```
;Sum=Sum+GroupL(i)
 IF (Group(i) EQ 'Group 40 0') THEN BEGIN
     FOR J=0,50 DO BEGIN ; ELEMENT 16 DECIDE THE ROW No., ELEMENT 17
ECIDE THE COLUMN No.
        IF  (Header(Sum+J) EQ 0) AND (Header(Sum+J+1) EQ 16) THEN $
     Rows=LONG(Header(Sum+J+6)*256+Header(Sum+J+7))
     IF  (Header(Sum+J) EQ 0) AND (Header(Sum+J+1) EQ 17) THEN $
     Columns=LONG(Header(Sum+J+6)*256+Header(Sum+J+7))
     ENDFOR
;    Print, 'Rows =', Rows,'
     ', 'Columns =', Columns
 ENDIF
 Sum=Sum+GroupL(i)
 IF (Group(i) NE 'Group 224 127' )
 Then Begin
     print, Group(i),'
     ', 'Length=', GroupL(i)
 ENDIF ELSE BEGIN
     GroupL(i)=20
     print, Group(i),'
     ', 'Length=', GroupL(i)
 ENDELSE
 ;End of else clause.
 HeaderL= HeaderL+ GroupL(i)
 I = I + 1
Endwhile
Print,'THE HEADER LENGTH (BYTES) IS = ',  HeaderL
Print, 'Rows =', Rows,'
     ', 'Columns =', Columns
PRINT, 'THE FILE LENGTH (BYTES) IS = ',
LONG(ROWS*COLUMNS+HEADERL)
; IT SHOULD NOTE THAT IS A*B IS TOO LARGE WE MUST USE LONG TO
CONVERT IT, BUT FIRST WE
; SHOULD SET A=LONG(*****), B=LONG(*****) THEN USE LONG(A*B) TO
PRINT A*B
END
```

Flat_sym.pro

This program calculates the flatness and symmetry of BIS 710 radiation images of any extracted inplane or crossplane beam profiles.

```
Function Flat_sym, beam, Flatness, Sym, Cenre_P
Xsiz=500;693;767;
b=FLTARR(Xsiz)
;beam=REFORM(image[250,*]); This is the Column profile,
for i=1,Xsiz-1 do b(i)=beam(i)-beam(i-1)
tem=max(b,ii)
tem=min(b,jj)
centre=(ii+jj)/2
Mean0=(beam(10)+beam(Xsiz-10))/2. ; back ground
Mean_c=0.
For i=0,4 do Mean_c=(beam(centre-2+i)+Mean_c)/2. ; mean of centre axis
c50=(Mean_c-Mean0)/2.+Mean0
Beam_FF=FLTARR(Xsiz/2+1)   ; first half of the profile
Beam_SF=FLTARR(Xsiz/2+1)   ; second half of the profile
for jj=0,Xsiz/2-1 do beam_FF[jj]=beam[jj] ;
for jj=Xsiz/2, Xsiz-1 do beam_SF[jj-Xsiz/2]=beam[jj] ;
a=min(ABS(beam_ff-c50),j) ; the nearest point to the 50% contour
IF(beam[J] LE c50) Then $
 c50l=j-(c50-beam[j])/(beam[j-1]-beam[j])
IF(beam[j] GT c50) Then begin
   IF(beam[j] NE beam[j+1]) Then $
 c50l=j+(beam[j]-c50)/(beam[j]-beam[j+1])
 IF(beam[j]  EQ beam[j+1]) Then $
 c50l=j+1+(beam[j]-c50)/(beam[j+1]-beam[j+2])
ENDIF

a=min(ABS(beam_Sf-c50),j) ; the nearest point to the 50% contour
IF(beam_sf[J] LE c50) Then $
 c50r=j-(c50-beam_sf[j])/(beam_sf[j-1]-beam_sf[j])
IF(beam_sf[j] GT c50) Then begin
   IF(beam_sf[j] NE beam_sf[j+1]) Then $
 c50r=j+(beam_sf[j]-c50)/(beam_sf[j]-beam_sf[j+1])
 IF(beam_sf[j]  EQ beam_sf[j+1]) Then $
 c50r=j+1+(beam_sf[j]-c50)/(beam_sf[j+1]-beam_sf[j+2])
ENDIF
C50R=c50r+Xsiz/2.
Cenre_P=Fix((C50l+c50r)/2.)
Field_size=C50r-c50l
print, c50r, c50l
flat_l=0.8 * Field_size
shift_l=fix(flat_l/2)
```

```
;**** PLOT the figure with flatness part showed.
window, 8, Xsize=500, Ysize=500
xx1=FLTARR(120)
for i=0, 119 do xx1(i)=Cenre_P-shift_l
plot, float(beam)/beam(cenre_p);,yrange=[0.,1.2]
oplot, xx1,FINDGEN(120)
for i=0, 119 do xx1(i)=Cenre_P+shift_l
oplot, xx1,FINDGEN(120)

Sym=0.
For i= 0,shift_l do begin
     Ratio=ABS(float(beam(Cenre_P-i))/beam(Cenre_P+i)-1.)*100.
     IF  RATIO GE Sym THEN Sym=RATIO
ENDFOR
flatness=(float(max(beam[(Cenre_P-shift_l):(Cenre_P+shift_l)]))/min(beam[(Cenre_P-
shift_l):(Cenre_P+shift_l)])-1.)*100.
Print, FORMAT = '("The Flatness Is (%) ", F5.2,"%")',Flatness
Print, FORMAT = '("The Symetry  Is (%)", F5.2,"%")',SYM
print, 'Profile centre is ', Cenre_P
return, sym
end
```

Cross_hair.pro

This program reads BIS 710 light field image and locates the cross hair position.

Marker.pro

This function is written to locate the marker position within a BIS 710 image.

Couch.pro

Calculate the distance of the markers to the centre of the BIS 710 images. Then verifies the distances, which should be within 2 mm annulus.

BT_ed.pro

This function calculates the top/bottom edges of a radiation images by finding the 50% contour.

LR_ed.pro

This function calculates the left/right edges of a radiation images by finding the 50% contour.

References

AAPM (1975) American Association of Physicist in Medicine, Code of practice for x-ray therapy linear accelerators, Med. Phys., 2(3), 110-121.

AAPM (1984) Physical aspects of quality assurance in radiation therapy, AAPM report No. 13 (American Institute of Physics, New York)

AAPM (1993) Code of practice for accelerators, Report of task group 45 of the Radiation Therapy Committee of AMMP, Med. Phys., 21(7), 1093-1121

AAPM (1994) Comprehensive QA for radiation oncology: Report of AAPM Radiation Therapy Committee Task Group 40, Med. Phys., 21 (4), 581-619

Andreo P. (1991) Monte Carlo techniques in Medical radiarion physics, Phys. Med. Biol., 36, 861-920

Althof V.G.M., de Boer J.C.J, Huizenga H., Stroom J.C., Visser A.G., and Swanenberg B.N. (1996) Physical characteristics of a commercial electronic portal imaging device, Med. Phys., 23, 1845-1855

Antonuk L.E., Boudry J., Yorkston J., Wild C.F., Longo M.J. and Street R.A. (1990) Radiation-damage studies of amorphous-silicon photodiode sensors for applications in radiotherapy x-ray imaging, Nucl. Inst. Meth., A299, 143-146

Antonuk L.E., Boudry J., Huang W., McShan D.L., Morton E.J., Yorkston J., Longo M.J. and Street R.A. (1992) Demonstration of megavoltage and diagnostic x-ray imaging with hydrogenated amorphous silicon arrays, Med. Phys., 19, 1455-1466

Baily N.A., Horn R.A., Kampp T.D. (1980) Fluoroscopic visualization of megavoltage therapeutic x ray beams, Int. J. Radiat. Oncol. Biol. Phys., 6, 935-939

Bansal R., Staib L., Chen Z., Rangarajan A., Knisely J., Nath R., and Duncan J. (1999) A minimax entropy registration framework for patient setup verification in radiotherapy, Comput. Aided Surg., 4, 287-304

Bel A., van Herk M., Bartelink H. and Lebesque J.V. (1993) A verification procedure to improve patient set-up accuracy using portal images, Radiother.Oncol., 29, 253-260

Bel A., Vos P.H. and Rodrigus P.T. (1996) High-precision prostate cancer irradiation by clinical application of an off line patient stup verification procedure, using portal imaging, Int. J. Radiat. Oncol. Biol. Phys., 35, 321-332

Bijhold J., Gilhuijs K.G.A., van Herk M. and Meertens H. (1991a) Radiation field edge detection in portal images, Phys. Med. Biol., 36, 1705-1710

Bijhold J., van Herk M., Vijlbrief R. and Lebesque J.V. (1991b) Fast evaluation of patient set-up during radiotherapy by aligning features in portal and simulator images, Phys. Med. Biol., 36, 1665-1679

Bijhold J., Lebesque J.V., Hart A.A. and Vijlbrief R.E. (1992) Maximizing setup accuracy using portal images as applied to a conformal boost technique for prostatic cancer, Radiother. Oncol., 24, 261-271

Bissonnette J.P., Jaffray D., Fenster A. and Munro P. (1992) Physical characterisation and optimal magnification for portal imaging system, SPIE, 1651, 182-188

Bissonnette J.P., Jaffray D., Fenster A. and Munro P. (1994) Optimal radiographic magnification for portal imaging, Med. Phys., 21, 1435-1445

Bissonnette J.P., Cunningham I.A. and Munro P. (1997) Optimal phosphor thickness for portal imaging, Med. Phys., 24, 803-814

Beollaard R., van Herk M. Bijinheer B.J. (1996) The dose response relationship of a liquid-filled electronic portal imaging device, Med. Phys., 23, 1601-1611

Boyer, A.L. (1979) Verification of mechanical alignment and interlock operation, Presented at Electron Linear Accelerators in Radiation Therapy, AAPM Special Workshop, Washington, DC, 1979

Boyer A.L., Antonuk L., Fenster A., van Herk M., Meertens H., Munro P., Reinstein L.E. and Wong J. (1992) A review of electronic portal imaging devices (EPIDs), Med. Phys., 19, 1-16

Brahme A. (1993) Optimisation of radiation therapy and the development of multileaf collimation, Int. J. Radiat. Oncol. Biol. Phys., 25, 373-375

Burch S.E., Kearfott K.J., Trueblood J.H., Sheils W.C., Yeo J.I., Wang C.K. (1997) A new approach to film dosimetry for high energy photon beams: lateral scatter filtering, Med. Phys., 24, 775-783

Curtin-Savard A. and Podgorsak B. (1997) An electronic portal image device as a physics tool, Med. Dosimetry, 22, 101-105

Das I.J., Desobry G.E., McNeeley S.W., Cheng E.C. and Shultheiss T.E. (1998) Beam characteristics of a retrofitted double-focussed multileaf collimator, Med. Phys., 25, 1676-1684

De Neve W., van den Heuvel F., Coghe M., Verellen D., de Beukeleer M., Roelstraete A., de Roover P., Thon L. and Storme G. (1993) Interactive use of on-line portal imaging in pelvic radiotherapy, Int. J. Radiat. Oncol. Biol. Phys., 25, 517-524

Doi K., Holje, Loo L-N, Sandrik J.M., Jennings R.j., and Wagner R.F. (1982) MTF's and wiener spectra of radiographic screen-film system, HHS Publ. NO. 82-8187 (FDA)

Droege R.T. and Bjarngard B. (1979b) Metal screen-film detector MTF at megavoltage x-ray energies, Med. Phys., 6, 515-518

Eilertsen K., Skretting A., and Tennvassas T.L. (1994) Methods for fully automated verification of patient set-up in external beam radiotherapy with polygon shaped fields, Phys. Med. Biol. 39, 993-1012

Eilertsen K. (1997) Automatic detection of single MLC leaf positions with corrections for penumbral effects and portal imager dose rate characteristics", Phys. Med. Biol., 42, 313-334

Eilertsen K.(2000) 6th international workshop on electronic portal imaging, Brussels

Essenberg A., and Koziarsky A.(1972) Alignment of light localised beam and radiographic x-ray beam, Radiology, 104 (3), 716-719

Essers M. Hoogervorst BR. van Herk M. Lanson H. Mijnheer BJ. (1995) Dosimetric characteristics of a liquid-filled electronic portal imaging device, Int. J. Radiat. Oncl. Biol. Phys., 33 (5), 1265-72

Essers, M., Boellaard, R., van Herk, M., Lanson, H. and Mijnheer B. (1996) Transmission dosimetry with a liquid-filled electronic portal imaging device, Int. J. Radiat. Oncl. Biol. Phys., 34 (4), 931-941

Ezz A., Munro P., Porter A.T., Battista J., Jaffray D.A., Fenster A. and Osborne S. (1992) Daily monitoring and correction of radiation field placement using a video-based portal imaging system: a pilot study, Int. J. Radiat. Oncol. Biol. Phys., 22, 159-165

Gagel B., Schramm O., Harms W., Wenz F., van Kampen M., Wannenmacher M. and Eble M.J. (2000) The electronic portal image system Siemens Beamview plus system and the conventional verification films CEA-TVS and DU PONT CQL-7, a comparison of subjective visual image quality, 6th international workshop on electronic portal imaging, Brussels

Galvin J.M., Smith A.R., Moeller R.D., Goodman R.L., Powlis W.D., Rubenstein J., Solin L.J., Michael B., Needham M., Huntzinger C.J. and Kligerman M.M. (1992) Evaluation of a multileaf collimator design for a photon beam, Int. J. Radiat. Oncol. Biol. Phys., 23, 789-801

Galvin J.M., Smith A.R. and Lally B. (1993a) Characterization of a multileaf collimator system, Int. J. Radiat. Oncol. Biol. Phys., 25, 181-192

Galvin J.M., Chen X.-G. and Smith R.M. (1993b) Combining multileaf fields to modulate fluence distributions, Int. J. Radiat. Oncol. Biol. Phys., 27, 697-705

Galvin J.M. (1999) The Multileaf Collimator - A complete guide, AAPM Refresher Course, Nashville, USA.

Gao Q., Yin F.F., and Nie K. (1999) Treatment field shape verification using elliptic Fourier transform, Med. Phys., 26, 2415-2421

Gilhuijs K.G.A. and van Herk M. (1993) Automatic on-line inspection of patient setup in radiation therapy using digital portal images, Med. Phys., 20, 667-677

Gilhuijs K.G.A., van de Ven P.J.H., and van Herk M. (1995) Automatic three-dimensional inspection of patient setup in radiation therapy using portal images, simulator images, and computed tomography data, Med. Phys., 23, 389-399

Gilhuijs K.G.A., Drukker K., Touw A., van de Ven P.J.H. and van Herk M. (1996) Interactive three dimensional inspection of patient setup in radiation therapy using digital portal images and computed tomography data, Int. J. Radiat. Oncol. Biol. Phys., 34, 873-885

Greene D. and Williams P.C. (1997) *Linear accelerator for radiation therapy,* Bristol, UK: Institute of Physics Publishing

Hammond R., Suchowerska N., Manderson C. and Drew J. (1997) Portal image quality: electronic vs. film, Radiation therapist, 7, 98-102

Hanley J., Mageras G.S., Sun J., Kutcher G.J. (1995) The effects of out-of-plane rotations on two-dimensional portal image registration in conformal radiotherapy of the prostate, Int. J. Radiat. Oncol. Biol. Phys., 33, 1331-1343

Haoward-Flanders P. and Newbery G.R. (1950) A gantry type of mounting for high voltage x-ray therapy equipment, Br. J. Radiol., 23, 355-357

Heijimen B. J. M., Pasma K. L., Kroonwijk M. (1995) Portal dose measurement in radiotherapy using an electronic portal imaging device (EPID), Phys. Med. Biol., 40, 1943-1955.

Hilt G., Wolf D., and Aletti P. (1999) Reprocessing of control portal images for patient setup verification during treatment in external radiotherapy, Med. Phys., 26, 2539-2549

Hudson F.R. (1988) A simple isocenter checking procedure for radiotherapy treatment machines using the optical pointer, Med. Phys., 15, 72-73

IAEA (1987) Absorbed dose determination in photon and electron beams, International Atomic Energy Agency, Technical Rep., 277, Vienna

IEC (1989a) *Medical electron accelerators-functional performance characteristics,* International Electrotechnical Commission, Geneva, IEC publication 976

IEC (1989b) *Medical electron accelerators in the range 1 Mev-50 Mev-Guidelines for functional performance characteristics,* International Electrotechnical Commission, Geneva, IEC publication 977

ICRU (International Commission on Radiation Units and Measurements) (1962) Radiation Quantities and Units, ICRU report 14. Bethesda, Maryland.

ICRU (International Commission on Radiation Units and Measurements) (1976) Determination of the absorbed dose in patient irradiated by beams of x- or gamma -rays in radiotherapy procedures, ICRU rep. 24, Bethesda, Maryland

ICRU (International Commission on Radiation Units and Measurements) (1984) Determination of the absorbed dose in patient irradiated by beams of x- or gamma -rays in radiotherapy procedures, ICRU rep. 23, Bethesda, Maryland

ICRU (International Commission on Radiation Units and Measurements) (1984) Radiation dosimetry: Electron beams with energies between 1 and 50 MeV (report 35). Bethesda, Maryland.

Jaffray D.A., Battista J.J., Fenster A. and Munro P. (1994) X-ray scatter in megavoltage transmission radiography: Physical characteristics and influence on image quality, Med. Phys., 21, 45-60

Jaffray D.A., Chawla K., Yu C. and Wong J.W. (1995) Dual-beam imaging for online verification of radiotherapy field placement, Int. J. Radiat. Oncol. Biol. Phys., 33, 1273-1280

Jaffray D.A., Drake D.G., Chawla K. and Wong J.W. (1996) Characterization of a clinical fluoroscopic portal imager, Proceedings of the 4th International Workshop on electronic portal imaging, Amsterdam, The Netherlands.

James H.V., Atherton S., Budgell G.J., Kirby M.C., and Williams P.C. (2000) Verification of dynamic multileaf collimation using an electronic portal imaging device, Phys. Med. Biol., 45, 495-509

Johns H.E. and Cunningham J.R. (1983) The Physics of Radiology (4th edition), Charles C Thomas, Springfield, Illinois.

Jordan T.J. (1997) Megavoltage X-ray beams: 2-50 MV, Br. J. Radiol. (Supp.25), 62-105

Karzmark, C.J. and Morton R.J. (1981) *A primer on theory and application of linear accelerator in radiation therapy*, HHS publication (FDA), 82-8181

Khan F. (1994) *The physics of radiation therapy,* 2nd ed., Williams and Wilkins, Baltimore, USA.

Keller H., Fix M. and Rüegsegger P. (1998) Calibration of a portal imaging device for high-precision dosimetry: A Monte Carlo Study, Med. Phys., 25 (10), 1891-1902

Kirby, M.C. and Williams, P.C. (1993) Measurement possibilities using an electronic portal imaging device, Radiother. Oncol., 29, 237-243

Krell G., Tizhoosh H.R., Lilienblum T., Moore C.J., and Michaelis B. (1998) Enhancement and associative restoration of electronic portal images in radiotherapy, Int. J. Radiat. Oncol. Biol. Phys., 49, 157-171

Krieger H. and Petzold G.J. (1989) Strahlenphsik, Dosimetrie umd Strahlenschutz, B.G. teubner, Stuttgart, Germany

Kirby M.C. (1995) A multipurpose phantom for use with electronic portal image devices, Phys. Med. Biol., 40, 323-334

Kirby, M. C., and Williams, P. C. (1995) The use of an electronic portal Imaging Device for Exit Dosimetry and Quality Control Measurements, Int. J. Radiation Oncology Bio. Phys., 31 (3), 593-603,

Kruse J.J., Herman M.G. and Hagness C.R. (2000) Image quality and clinical efficiency of electronic and film portal images, 6th international workshop on electronic portal imaging, Brussels

Kubo H D, Shapiro E G and Seppi E J (1999) Potential and role of a prototype amorphous silicon array electronic portal imaging device in breathing synchronized radiotherapy Med. Phys., 26, 2410-2414

Lariviere P.D (1989) The quality of high energy x-ray beams, Br. J. of Radio. 62, 473-481

Leong J. (1986) Use of digital fluoroscopy as an on-line verification device in radiation therapy, Phys. Med. Biol., 31, 985-992

Liu G., van Doorn T. and Bezak E. (2000) Evaluation of the Mechanical alignment of a Linear Accelerator with an Electronic Portal Imaging Device (EPID), Australas. Phys. Sci. Eng. Med., 23, 74-80

Low D.A., Li Z. and Klein E.E. (1996) Verification of milled two-dimensional photon compensating filters using an electronic portal imaging device, Med. Phys., 23, 929-938

Luchka K. and Shalev S. (1996) Pelvic irradiation of the obese patient: A treatment strategy involving megavoltage simulation and intratreatment setup corrections, Med. Phys., 23, 1897-1902

Luchka K., Chen D. and Shalev S. (1996b) Assessing radiation and light field congruence with video based electronic portal imaging device, Med. Phys., 23 (7), 1240-1252

Lutz, W.R., Larsen R.D. and Bjarngard, B.E. (1982) Beam alignment tests for therapy accelerator, Int. J. Radiat. Oncl. Biol. Phys., 7, 1727-1731
Ma L., Geis P.B. and Boyer A.L. (1997) Quality assurance for dynamic multileaf Collimator modulated field using a fast beam imaging system, Med. Phys., 24 (8), 1213-1220

Ma L., Boyer A.L., Findley D.O., Geis P.B. and Mok E. (1998) Application of a video-optical beam imaging system for quality assurance of medical accelerators, Phys. Med. Biol., 43, 3469-3659

Mayer, R., Williams, A., Frankel, T., Cong, Y., Simons, S., Yang, N., and Timmerman, R. (1997) Two-dimensional film dosimetry application in heterogeneous materials exposed to megavoltage photon beams, Med. Phys., 24 (3), 455-460

McNutt T.R., Mackie T.R., Reckwerdt P. and Paliwal B.R. (1996) Modelling dose distributions from portal dose images using the convolution/superposition method, Med. Phys., 23, 1381-1392

Meertens H., van Herk M. and Weeda J. (1985) A liquid ionisation detector for digital radiography of therapeutic megavoltage photon beams, Phys. Med. Biol., 30, 313-321

Meertens H., van Herk M. and Weeda J. (1988) An inverse filter for digital restoration of portal images, Phys. Med. Biol., 33, 687-702

Meertens H., Bijhold J. and Strackee J. (1990) A method for the measurement of field placement errors in digital portal images, Phys. Med. Biol., 35, 299-323

Metcalfe P., Kron T. and Hoban P. (1997) *The physics of radiotherapy X-rays from linear accelerators*, Madison, Wisconsin, USA, Medical physics publishing

Michalski J. M., Wong J. W., Gerber R. L., Yan D., Cheng A., Graham M. V., Renna M. A., Sawyer P. J., and Perez C. A. (1993) The Use of On -Line Image Verification to Estimate the Verification in Radiation Therapy Dose Delivery, Int. J. Radiat. Oncol. Biol. Phys., 27, 707-716

Millar D., Chairman, Task Group 23 (1997), *Verification of the accuracy of computerised dose calculation systems for photon beams, Radiation Therapy Committee* (American Association of Physicists in Medicine, College Park, MD)

Morton E.J., Swindell W., Lewis D.G. and Evans P.M. (1991) A linear array, scintillation crystal-photodiode detector for megavoltage imaging, Med. Phys., 18, 681-691

Motz J.W. and Danos M (1978) Image information content and patient exposure, Med. Phys., 5, 8-22

Munro P., Rawlinson J.A. and Fenster A. (1987a) Therapy imaging: A signal-to-noise analysis of metal plate/film detectors, Med. Phys., 14, 975-984

Munro P., Rawlinson J.A. and Fenster A. (1987b) Therapy imaging: Limitations of imaging with high energy x-ray beams, Proc. SPIE 767, 178-184

Munro P., Rawlinson J.A. and Fenster A. (1990) A digital fluoroscopic imaging device for radiotherapy localization, Int. J. Radiat. Oncol. Biol. Phys., 18, 641-649

Munro P. (1997) On line portal imaging, *39th annual meeting American society for therapeutic radiology and oncology*, Orlando, Florida, USA

Munro P. and Bouius D.C. (1998) X-ray quantum limited portal imaging using amorphous silicon flat-panel arrays, Med. Phys., 25, 689-702

Murrer L., Kaatee R., de Boer J., Heijmen B. (2000) The 6th International Workshop on Electronic Portal Imaging, June 2000, Brussels, Belgium.

Nelson W. R., Hirayama H. and Rogers D. W. O. (1985) The EGS4 code system, Stanford Linear Accelerator, Stanford University, SLAC-265 UC-32

Owen B. (1991) A summary of high energy photon absorbed doe to water comparison Doc. CCEMI 9I)/91-92 (Bureau International des Poids et Mesures, Sevres)

Partridge M., Evans P.M. and Symonds-Tayler J.R. (1999) Optical scattering in camera-based electronic portal imaging, Phys. in Med. & Biol., 44 (10), 2381-2396

Perera T., Moseley J. and Munro P. (1999) Subjectivity in interpretation of portal films, Int. J. Radiat. Oncol. Biol. Phys., 45, 529-534

Petrascu O., Bel A., Linthout N., Verelllen D., Soete G., and Storme G. (2000) Automatic on-line electronic portal image analysis with a wavelet-based edge detector, Med. Phys., 27, 321-329

Pisciotta V., Wu X., Fiedler, Serago C., Calish-Watzich M., Schwade J., and Houdek P. (1992) A rapid method for electron beam energy check, Med. Phys., 19 (6), 1451-1453

Podgorsak E.B., Rawlinson J.A. and Johns H.E. (1975) X-ray depth dose from accelerators in the energy range from 10 to 32 MeV, *Am. J. Roentgeno.,* 123, 182-191

Que W. and Rowlands J.A. (1995) X-ray imaging using amorphous selenium: inherent spatial resolution, Med.Phys., 22, 365-374

Radcliffe, T., Barnea, G., Wowk, G., Rajapakshe, R., Shalev, S. (1993) Mento Carlo opimization of metal/phosphor screens at megavoltage energies, Med. Phys., 20, 1161-1169

Rajapakshe R.., Luchka K., and Shalev S. (1996) A quality control test for electronic portal imaging devices, Med. Phys. 23, 1237-1244

Rajapakshe R.., Shalev S. and Luchka K. (2000) Quality assurance of EPIDs system, 6th international workshop on electronic portal imaging, Brussels

Reinstein L.E.,. Durham M., Tefft M., Yu A., Glicksman AS. and Eaton W. (1984) Portal film quality: a multiple institutional study, Med. Phys., 11, 555-557

Remeijer P., Geerlof E., Ploeger L., Gilhuijs K.G.A., van Herk M., Bel A., and Lebesque J.V. (2000) 3-D portal image analysis in clinical practice: an evaluation of 2-D and 3-D analysis techniques as applied to 30 prostate cancer patients, Int. J. Radiat. Oncol. Biol. Phys., 46, 1281-1290

Roback D.M. and Gerbi B.j. (1995) Evaluation of electronic portal imaging device for missing tissue compensator design and verification, Med. Phys., 22, 2029-2034

Roberts, R. (1996) Portal imaging with film cassette combinations: what film should we use, British J. of Radiology, 69, 70-71

Shalev S., Lee T., Leszczynski K., Cosby S., Chu T., Reinstein L and Meek A. (1989) Video techniques for on-line portal imaging, Comput. Med. Imaging. Graph., 13, 217-226

Shalev S. (1995) Treatment Verification Using Digital Imaging, *Medical Radiology Radiation Therapy Physics*, Edited by A. R. Smith, Springer-verlay Berlin Heidelberg

Spirou S.V. and Chui C.S. (1994) Generation of arbitrary fluence profiles by dynamic jaws or multileaf collimators, Med. Phys., 21, 1031-1041

Shalev S. (1996) *Megavoltage Portal Imaging, Teletherapy: Present & Future*, Edited by J. Paita, T. R. Mackie, Advanced Medical Publishing, Madison, Wisconsin

Shalev S. (1997) *Portal Image Processing System, User's Guide*, MCTEF 1997

Swindell W., Morton E.J., Evans P.M. and Lewis D.G. (1991) The design of megavoltage projection imaging systems: Some theoretical aspects, Med. Phys., 18, 855-866

Swindell W. and Evans P.M.. (1996) Scattered radiation in portal images: a Monte Carlo simulation and a simple physical model, Med. Phys., 23(1), 63-73

Taborsky S.C., Lam W.C., Sterner R.E. and Skarda G.M. (1982) Digital imaging for radiation therapy verification, Opt. Eng., 21, 888-893

van Herk M. and Meertens M. (1988) A matrix ionisation chamber imaging device for on-line patient setup verification during radiotherapy, Radiother. Oncol., 11, 369-378 van Herk M. (1991) Physical aspects of a liquid-filled ionization chamber with pulsed polarizing voltage, Med. Phys., 18, 692-702

van Herk M., Bel A., Gilhuijs K.G.A., and Vijbrief R.E. (1993) A comprehensive system for analysis of portal images, Radiother. Oncol., 29, 221-229

van Herk M., Fenci W. and van Dalen A., (1995) Design and implementation of a high speed matrix ionisation chamber system, Med. Phys., 22, 991 (abstract)

Vigneault E., Pouliot J., Laverdiere J., Roy J., Dorion M. (1997) Electronic portal imaging device detection of radio-opaque markers for the evaluation of prostate position during megavoltage irradiation: a clinical study, Int. J. Radiat. Oncol. Biol. Phys., 37, 205-212

Visser A.G., Huizenga H., Althof V.G. and Swanenburg B.N. (1990) Performance of a prototype fluoroscopic radiotherapy imaging system, Int. J. Radiat. Oncol. Biol. Phys., 18, 43-50

Wang J.Z. and Fallone B.G. (1994) A robust morphological algorithm for automatic radiation field edge extraction and correlation of portal images, Med. Phys., 21, 237-244

Wellhofer Dosimetrie 1997, BIS710 *User Manual* (Schwarzenbruk: Wellhofer Dosimetrie)

Webb S. (1993*) The physics of three-dimensional radiation therapy*, Institute of Physics Publishing, Bristol, UK

Webb S. (1997) *The physics of conformal therapy – advances in technology*, Institute of Physics Publishing, Bristol, UK

WHO (World Health Organisation) (1988), *Quality assurance in radiotherapy,* Geneva.

Williamson J.F., Khan F.M. and Sharma S.C. (1981) Film dosimetry of megavoltage photon beams: a practical method of isodensity-to-isodose curve conversion, Med. Phys., 8, 94-98

Wong J.W., Binns W.R.., Cheng A.Y., Gear L.Y., Epstein J.W., Klarmann J. and Purdy J.A. (1990) On-line radiotherapy imaging with an array of fibre-optic reducers, Int. J. Radiat. Oncol. Biol. Phys., 18, 1477-1484

Wowk B. and Shalev S. (1993) Grooved phosphor screens for on-line portal imaging, Med. Phys., 20, 1641-1651

Wowk B., Radcliffe T., Leszczynski K. W., Shalev S. and Rajapakshe R. (1994) Optimisation of metal/phosphor screens for on-line portal imaging, Med. Phys., 21, 227-235

Yeboah C. and Pistorius S. (2000) Monte Carlo studies of the exit photon spectra and dose to a metal/phosphor portal imaging screen, Med. Phys., 27 (2), 330-339

Yin F.F., Schell M.C. and Rubin P. (1994) Input/output characteristics of a matrix ion-chamber electronic portal imaging device, Med. Phys., 21, 1447-1454

Yin F.F., Schell M.C. and Rubin P. (1994) A technique of automatic compensator design for lung inhomogeneity correction suing electronic portal imaging device, Med. Phys., 21, 1729-11734

Yorkston J., Antonuk L.E., Seraji N., Huang W., Siewerdsen J. and El-Mohri Y. (1994) Evaluation of the MTF for a-Si:H imaging arrays, Proc. SPIE, 2163, 141-149

Zhao W. and Rowlands J.A. (1992) Large-area solid state detector for radiology using amorphous selenium, Proc. SPIE 1651, 134-143

Zhao W. and Rowlands J.A. (1993) Digital radiology using self-scanned readout of amorphous selenium, Proc. SPIE 1896, 114-120

Zhou S. and Verhey L.J. (1994) A robust method of multileaf collimator (MLC) leaf configuration verification, Phys. Med. Biol., 39, 1929-1947

Zhu, Y., Jiang, X.Q. and van Dyk, J. (1995) Portal dosimetry using a liquid ion chamber matrix: dose response studies, Med. Phys., 22, 1101-1106

Zhu Y., Kirov A., Mishra V., Meigooni A., and Williamson J.f. (1997) Quantitative evaluation of radiochromic film response for two-dimensional dosimetry, Med. Phys., 24 (2), 223-231